Geochronological and geochemical constraints on the origin of the Paleoproterozoic Union Island Group mafic magmatism, East Arm Basin, N.W.T.

by

Alex I-Fan Sheen

A thesis submitted in partial fulfillment of the requirements for the degree of

Master of Science

Department of Earth and Atmospheric Sciences

University of Alberta

ABSTRACT

The Slave craton underwent widespread extension during the Paleoproterozoic. In the southern Slave craton, this extension is manifest in multiple periods of continental mafic magmatism emplaced between 2.3–2.2 Ga and prior to 2.0–1.9 Ga calc-alkaline magmatism of the Taltson and Thelon zones along the Slave-Rae boundary. During this time the East Arm basin of Great Slave Lake was formed and now preserves a protracted sedimentary and volcanic record along the southeastern margin of the Slave craton. Within the East Arm basin package, the Union Island Group represents voluminous mafic volcanism with subordinate interbedded carbonate/shale sedimentary strata. Previous stratigraphic interpretations posit that the ca. 1928 Ma Wilson Island Group is the base of the East Arm basin stratigraphy, and that the Union Island Group is younger. This relationship is however equivocal; the Wilson Island Group is structurally isolated, and new field observations indicate that the Union Island Group was deposited unconformably on Archean granitic basement, the latter considered to be derived from the nearby Slave craton.

We report the first U–Pb baddeleyite crystallization age, 2042.7±3.0 Ma, for a diabase body which intrudes volcaniclastic horizons belonging to the Union Island Group lower basalt unit; the diabase intrusion is geochemically identical to flows of the lower basalt unit and is therefore interpreted as a feeder to these flows. The diabase crystallization age demonstrates that the Union Island Group is the oldest identified supracrustal package in the East Arm basin and that the East Arm basin is ~115 Myr older than previously thought. Our new stratigraphic interpretation is supported by detrital zircon provenance age distribution in two Union Island Group sedimentary samples. These detrital zircons are dominated by 2.76–2.56 Ga ages reflecting prominent input from the Archean basement. The youngest detrital zircons have ages indistinguishable from the emplacement age of the diabase. Zircon ages from the 1.9–2.0 Ga Taltson and Thelon magmatism, are absent from the

Union Island Group sedimentary rocks while being prominent in all other strata of the East Arm basin; further confirming that the Union Island Group is the oldest strata in the East Arm basin.

The Union Island Group contains two stratigraphically and geochemically distinct mafic volcanic packages. The lower magmatism is predominantly alkaline, is characterized by high enrichment levels of incompatible elements and a large compositional range (108–438 ppm Zr, 13–62 ppm Nb), and preserves an OIB-like chemical signature. The upper magmatism, in contrast, is tholeiitic, displays much lower levels of incompatible elements with a uniform composition (83–101 ppm Zr, 2–4 ppm Nb), and has a DM-like chemical signature. Both packages display overlapping depleted time-integrated $\varepsilon_{Nd(i)}$ values (+1.1 – +3.2). Petrological modeling suggests that the lower magmatism originated from interaction between upwelling asthenosphere and a depleted mantle reservoir; the upper magmatism was produced by decompression melting of the shallow mantle consisting mostly of the depleted reservoir. The petrogenesis established in this study is consistent with a continental rift origin for the Union Island Group magmatism and is further supported by geochemical similarities with Proterozoic and Phanerozoic rift successions.

Combing geochronological and geochemical findings, we propose that the Union Island Group represents an incipient rift sequence during the ca. 2043 Ma rifting at the southern margin of the Slave craton. The proposed tectonic model is consistent with the break-up of the Slave craton from a pre-Laurentia supercontinent during the 2.23–2.01 Ga period. Our conclusions further suggest an intraplate origin for the Taltson and Thelon magmatism, and that the Slave craton and the Rae domain were a contiguous crustal unit as early as ca. 2043 Ma.

PREFACE

Research presented in this study is part of a larger project investigating the origin and evolution of the East Arm basin, a collaboration between the University of Alberta and the Northwest Territories Geological Survey.

The unconformity between the Union Island Group and the Archean basement, shown in Fig. 2.4b, was discovered by L. Ootes and A. Bekker during additional fieldwork in the Union Island area. The photograph of the unconformity was taken by L. Ootes.

Geochemical studies presented in this thesis include re-analysis of samples originally presented in the late Stephen Goff's 1984 Ph.D. thesis, entitled *The magmatic and metamorphic history of the East Arm of the Great Slave Lake, N.W.T.* Standard materials WGB-1, TDB-1, and SY-2 were provided by Bruce Kjarsgaard at the Geological Survey of Canada.

U–Pb purification of baddeleyite fractions #1 and #2 of sample LH14-27 was done by Dr. Larry Heaman, with ID-TIMS analysis conducted by James LeBlanc. U–Pb detrital zircon LA-ICPMS study of sample LH15-EA51 was conducted by Madisen Janzen as a research assistant under Dr. Larry Heaman; the detrital zircon study is included in this thesis with her consent.

All ideas presented in this thesis are my own, although they have been developed through discussions with my supervisor, Dr. Larry Heaman. All writing and figures presented here are my own work.

ACKNOWLEDGEMENTS

Funding for this project was supported by the Polar Continental Shelf Program, the Natural Sciences and Engineering Research Council of Canada (NSERC) Discovery Grants Northern Research Supplements Program (RGPNS; Grant #444185, to L. Heaman). Additional funding was supported by the Canada Graduate Scholarship-Master's (CGS M) from NSERC, the Walter H. Johns Graduate Fellowship and Eugene Brody Graduate Scholarship from the University of Alberta, and the Graduate Student Scholarship from Student Aid Alberta.

First and foremost, I would like to thank my supervisor Dr. Larry Heaman for the incomparable opportunity to explore the Precambrian puzzle and for his unfailing guidance and support over the past three years. His encouragement motivated me to explore beyond what was envisioned at the start of the project, learning with excitement the numerous facets of research in the process; the abundance of information included in this thesis—big and small—is a testament to this. Through relentless edits, comments, and discussions Larry has immensely helped me develop the skills to communicate academic research. I am equally grateful for his guidance during fieldwork and for the maxim that good research is one that uncovers more questions.

Secondly, I would like to thank Luke Ootes for his fabulous mentorship in the field and for his far-reaching support in every aspect of the fieldwork and other parts of the project. Luke's wealth of knowledge in everything Slave (and beyond) helped me grasp the significance of our findings and realize, at the same time, how one craton alone holds far more wonders and mysteries than one could possibly ever comprehend. Luke has also provided valuable feedback and suggestions regarding figures in chapters 1 and 2. Also, we owe Luke a big one for locating the Union Island Group basal unconformity.

I would also like to thank the Heaman geochronology research group for training me, formally or informally, on the various sample preparation and processing protocols: Barry Herchuk, for teaching me to keep things clean at all times and without whose reminder to rinse thoroughly I would never had recovered enough baddeleyite for dating; James LeBlanc, for helping me overcome the anxiety of remotely operating the large and delicate TIMS instrument; Madisen Janzen and Barry Shaulis, for everything zircon-related (and for being wonderful field

companions); Ilona Ranger and Stephanie Nichols, for heartwarming moral support and the odd mantle-related chit-chats.

Robert Creaser and Chiranjeeb Sarkar provided laboratory training for the tracer isotope studies. Thank you also to the following people for other various training, analysis, and logistics associated with this project: Lisa Budney, Diane Caird, Andy DuFrane, Nathan Gerein, Marilyn Huff, Mark Labbe, Andrew Locock, Martin von Dollen, and Barbara Ziger. Extra shoutout to Shyra Craig for never being annoyed whenever I came to sign out the mill room keys.

Bruce Kjarsgaard of the GSC provided valuable mentorship during fieldwork and in subsequent geochemical discussions. Other members of the field parties deserve a special thank you as well: Andrey Bekker, Jordan Burke, Murray Gingras, and Jesse Reimink.

Thank you to my family for always being there for me. Many friends have also poured out unending moral support in high times and in low. As it would take another thesis just to thank you all, I will give special shoutouts to the following few: Ricky, for being the best ever roommate and my moral compass; Devon, for your perpetual optimism and humour; Mike, for your candid sincerity that I can only aspire to possess; and Megan and Joel, for all our musical escapades.

And lastly—cheesy as it may sound—thank you to all the wonderful people I have met in Edmonton over the last three years. As a good friend puts it, hibernation is common during the long northern winters, but once you've found people to hibernate with, you're golden.

TABLE OF CONTENTS

LIST OF TABLES

LIST OF FIGURES

1 INTRODUCTION

The Paleoproterozoic Eon (2.5–1.6 Ga) is characterized by widespread mafic magmatism across previously stabilized Archean crustal domains (Amelin et al., 1995; Heaman, 1997; Isley and Abbott, 1999). In the Slave craton, for example, no less than fourteen Paleoproterozoic mafic dyke swarms have been identified (Buchan et al., 2010). The abundance of mafic magmatism emplaced in the Slave craton during the 2.2–2.0 Ga time period has been interpreted to reflect the protracted Paleoproterozoic extension and subsequent break-up of a Neoarchean supercraton, Sclavia (Bleeker, 2003).

The East Arm basin is situated on the southern flank of Slave craton and largely comprises Paleoproterozoic supracrustal successions (Figs 1.1, 1.2). The deformed nature of the East Arm basin, in addition to the general lack of geochronological constraints on the depositional age of the basal stratigraphy, has contributed to several contrasting tectonic models, including a fold belt, a failed rift, and a collisional back-arc (Hoffman, 1969, 1973, 1987, 1988b). Many studies have interpreted the lowest stratigraphic unit in the East Arm basin to be the ca. 1.93 Ga Wilson Island Group (Bowring et al., 1984), which is thought to relate to the 1.99–1.91 Ga Slave-Rae collision (Bowring et al., 1984; Hoffman, 1987, 1988b; Kjarsgaard et al., 2013a; Fig. 1.3). However, the Wilson Island Group is structurally isolated from the Archean basement (Hoffman, 1981, 1988a), therefore its stratigraphic relationship is unclear. The Union Island Group, a package of mafic volcanic and intrusive rocks with subordinate sedimentary strata of conglomerate, quartz arenite, dolomite, mudstone, and black shale, unconformably overlies Archean basement (Thorstad, 1976; Hoffman et al., 1977, 1988a). The Union Island Group has been conventionally interpreted to post-date the Wilson Island Group (Hoffman 1969, 1973; Hoffman et al., 1974, 1977; Kjarsgaard et al., 2013a) based on correlating metamorphic fabrics, and that the Wilson Island Group has been metamorphosed to a higher grade than the rest of basin stratigraphy (Hoffman et al., 1977; Johnson, 1990). This stratigraphic relationship is however equivocal due to the lack of any preserved stratigraphic contact between the two groups.

In light of the uncertainties in the conventional stratigraphic model of the East Arm basin, this study aims to constrain the timing and origin of mafic magmatism of the Union Island Group using high-precision isotope dilution thermal ionization mass spectrometry (ID-TIMS) U–Pb

baddeleyite geochronology, laser ablation inductively coupled plasma mass spectrometry (LA-ICP-MS) U–Pb detrital zircon geochronology, whole-rock geochemistry, Nd and Sr isotope geochemistry, and petrological modeling. These new findings are combined to address the early history of the East Arm basin with respect to contemporaneous major tectonic events in and around the Slave craton.

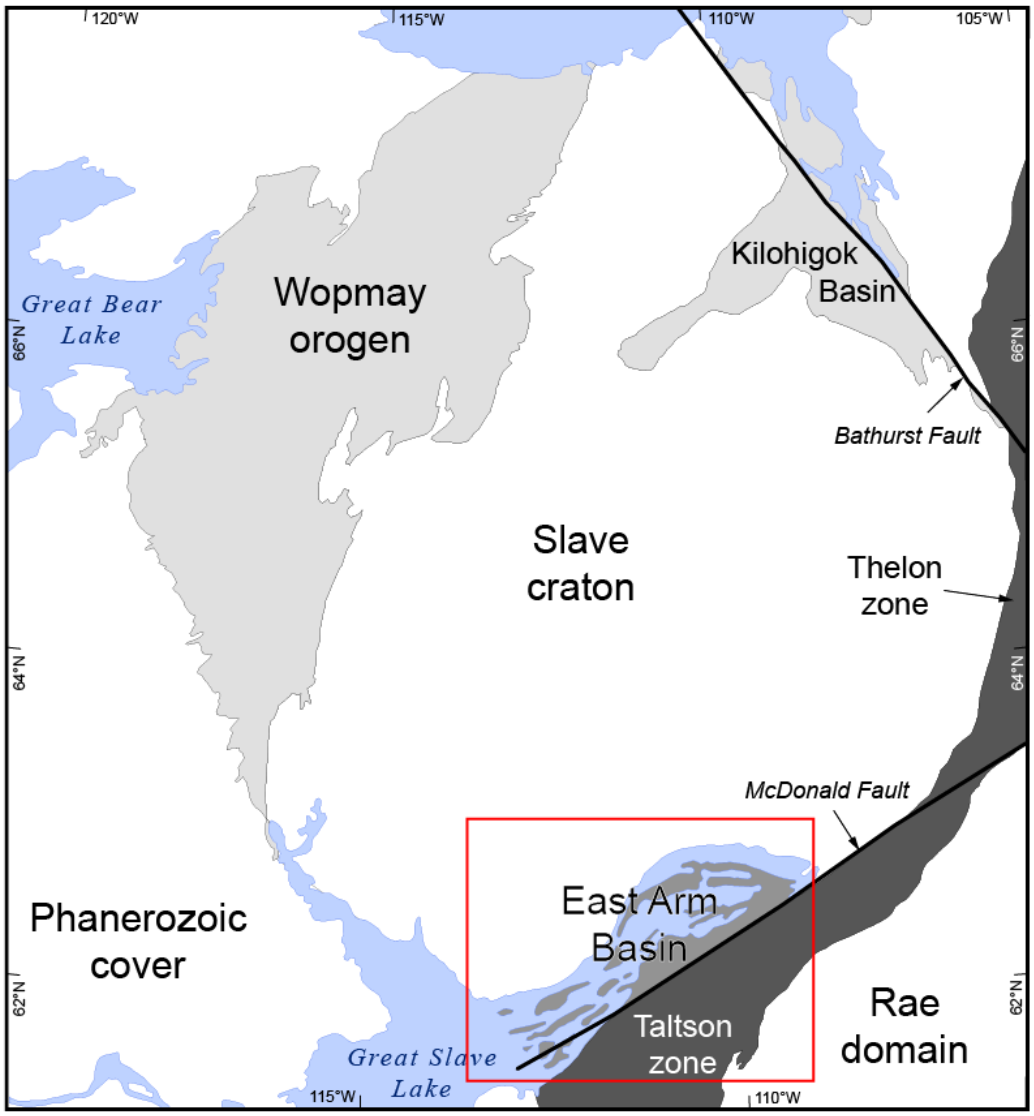

Figure 1.1. Map of the Slave craton, showing the location of the East Arm basin and other surrounding major tectonic domains. Modified after Buchan et al. (2010).

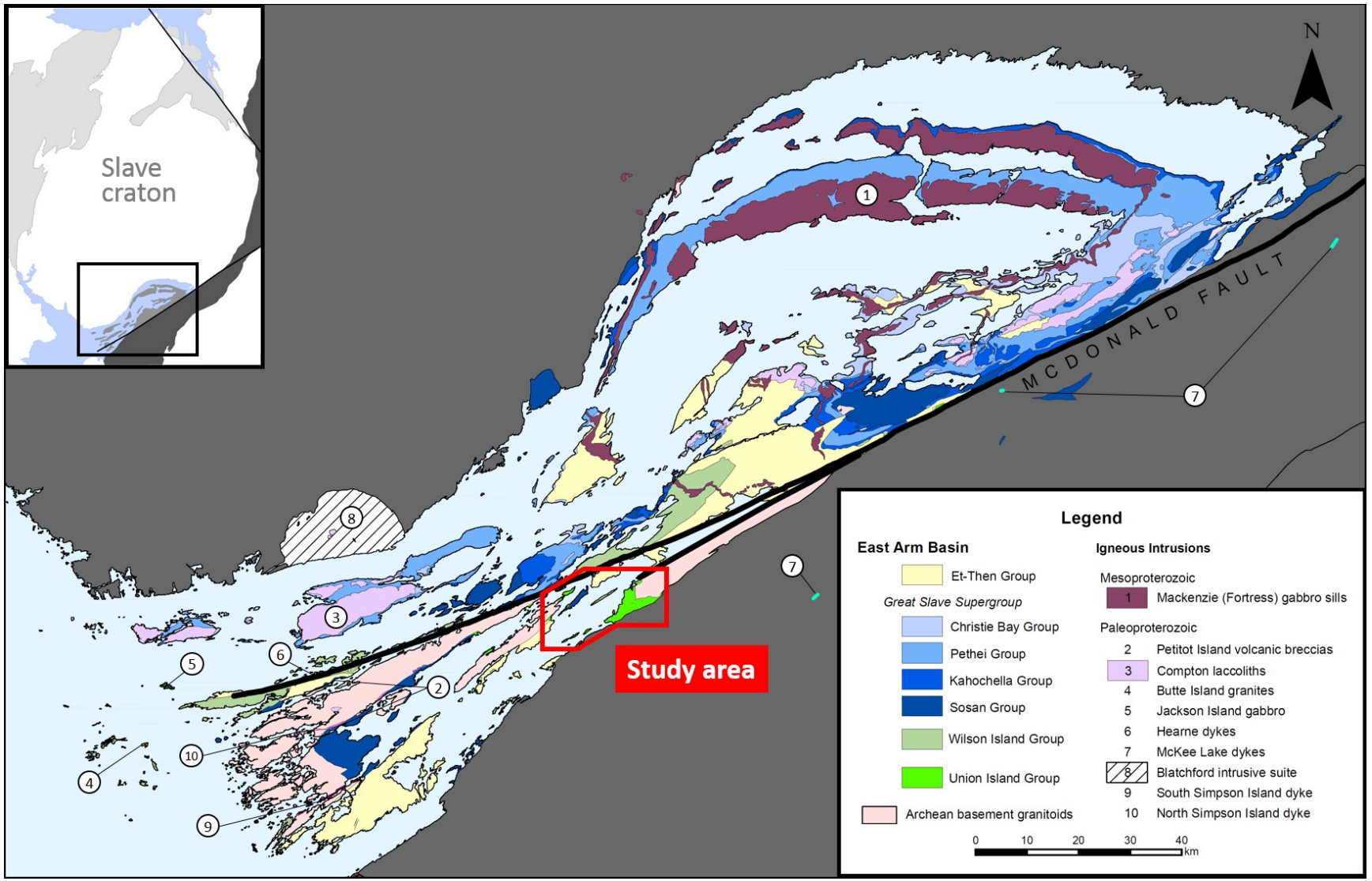

Figure 1.2. Geologic map of the East Arm basin, showing Paleoproterozoic igneous intrusions. Study area is denoted by the red box. Modified after Hoffman et al. (1977) and Kjarsgaard et al. (2013b).

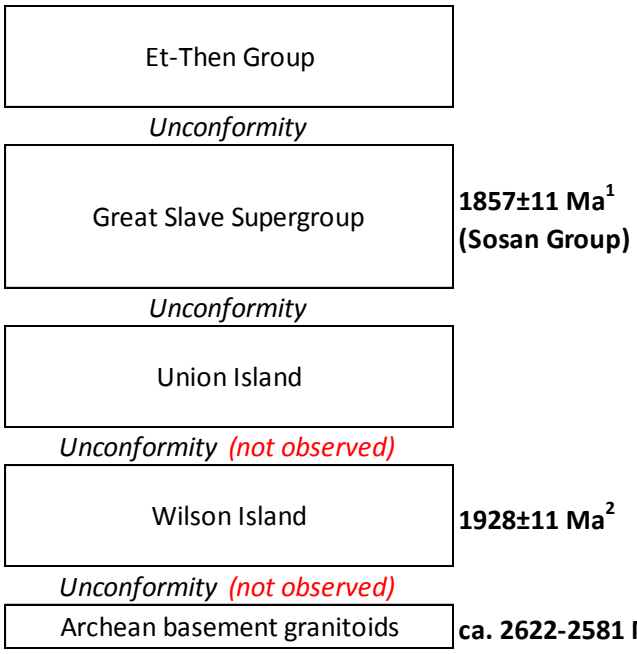

Figure 1.3. The conventional stratigraphic model of the East Arm basin as adopted by Hoffman (1969, 1973), Hoffman et al. (1974, 1977), and Kjarsgaard et al. (2013a). The Wilson Island Group is structurally isolated from the rest of the basin strata. Age data from [1]Kjarsgaard et al. (2013a), [2]Bowring et al. (1984), and [3]Kjarsgaard et al. (2013b).

2 BACKGROUND

2.1 Regional geology

The East Arm basin corresponds to the eponymous geographic region of the Great Slave Lake, N.W.T. (Fig. 1.2). Surficial extent of the basin measures ~100 km by ~300 km. The East Arm basin is bound to the northwest by the Slave craton. To the south, the basin is bound by mylonite zones associated with the ca. 1.9 Ga Great Slave Lake shear zone (GSLsz; Hanmer et al., 1992; Hoffman, 1987), which is partly separated from the basin by the post-1.86 Ga northeast-southwest trending McDonald Fault (Bowring et al., 1984). Stratigraphic thickness of the basin ranges from ~10 km in the southeast to ~2 km in the northwest (Hoffman, 1969). The basin strata are generally gently dipping towards the Slave craton, but become tightly folded in a synclinal structure towards the GSLsz. Inliers of felsic Archean crust occur in the southwestern portion of the basin (Thorstad, 1976; Hoffman et al., 1977; Janzen, 2015), between the McDonald Fault and the southern shore of the Great Slave Lake.

The stratigraphy of the East Arm basin is Paleoproterozoic in age and has been subdivided into four units (in order of decreasing age): Wilson Island Group, Union Island Group, Great Slave Supergroup, and Et-Then Group (Fig. 1.3; Hoffman, 1968, 1969, 1988a). Sedimentary and volcanic rocks of the Union Island Group and the Wilson Island Group have a relatively limited surficial exposure and show varying degrees of deformation and metamorphism prior to deposition of the younger Great Slave Supergroup, which consists of marine and fluvial sequences with intervening volcanic strata (Hoffman, 1968). Both the Wilson Island Group and the Great Slave Supergroup were folded into an anticlinal structure prior to further deposition of the Et-Then Group (Johnson, 1990).

Volcanic ages associated with the East Arm basin

A felsic volcanic rock of the Wilson Island Group (reported as a felsite in Bowring et al., 1984) has been dated at 1928±11 Ma and represents the oldest known volcanism thus far in the East Arm basin. A ca. 1857 Ma age for intermediate volcanic rocks of the Sosan Group is the only other reported age of volcanism within the basin stratigraphy (Kjarsgaard et al., 2013a).

Regional Paleoproterozoic igneous intrusions and their relation to the East Arm basin

The East Arm basin and its surrounding region host a number of Paleoproterozoic igneous intrusions (Table 2.1; Fig. 2.1). The central and southern regions of the Slave craton are intruded by the ca. 2231 Ma Malley dykes, ca. 2210 Ma Mackay dykes, and the ca. 2126–2108 Ma Indin dykes. In the southeastern end of North Simpson Island, the basement is cut by a 050°–070°-trending, ca. 2219 Ma diabase dyke ("Simpson Island dyke" or "Easter Island dyke" in previous reports; interpreted to be a Mackay dyke by Kjarsgaard et al. (2013a); hereafter referred to as "North Simpson Island dyke"; Mumford et al., 2012). Another 050°-trending diabase dyke cuts the basement ~10 km to the southeast ("Mid-Aphebian diabase dyke" of Goff, 1984 and Goff et al., 1982; hereafter referred to as "South Simpson Island dyke") and is geochemically correlated with mafic dykelets cutting the North Simpson Island dyke (Goff, 1984). Uranium–lead baddeleyite geochronology in this study constrains the emplacement age of the South Simpson Island dyke to be 2217–2198 Ma (Appendix C).

The ca. 2193–2164 Ma Southwest Slave magmatic province (SWSMP) consists of the Big Spruce, Squalus Lake and Blatchford alkaline intrusive suites, as well as the Duck Lake mafic sill and Dogrib dyke swarm (Bleeker and Hall, 2007; Mumford, 2013). In the GSLsz immediately south of the McDonald Fault, the ca. 2038 Ma, ENE-trending McKee Lake dykes cut both deformed and undeformed granites that share similar lithological attributes as basement inliers observed in the East Arm basin (Pehrsson et al., 1993). The NNE-trending ca. 2027–2023 Ma Lac de Gras swarm extends into the southern part of the Slave craton (Buchan et al., 2010).

The Wilson Island Group is intruded by the ENE-trending, ca. 1901 Ma Hearne dykes (Bleeker et al., 2008) and the ca. 1895 Ma Butte Island epizonal granites (Bowring et al., 1984; Kjarsgaard et al., 2013a). Several other ENE-trending diabase dykes have been observed to cut Archean inliers in the East Arm basin (Kjarsgaard et al., 2013b) and are interpreted to be Hearne dykes based on orientation (Kjarsgaard et al., 2013b), although the dykes' relationship with basin stratigraphy is unclear. Gabbro intrusions on Jackson Island, in the western tip of the basin, are coeval with the Hearne dykes (Kjarsgaard et al., 2013a). The ca. 1872–1861 Ma Compton monzodiorite laccoliths intrude the Christie Bay and Pethei groups of Great Slave Supergroup (Bowring et al., 1984; Hoffman, 1988a), with cogenetic monzodiorite stocks intruding the Blatchford intrusive suites in Slave craton. The Petitot Island breccia dykes intrude the Archean basement in close association

Table 2.1. Paleoproterozoic igneous intrusions in the East Arm basin and in the southern Slave craton.

DOMAIN/Name	Age (Ma)	References
EAST ARM BASIN		
N. Simpson Island dyke	2219 ± 3.7	Mumford et al. (2012)
S. Simpson Island dyke*	2217 - 2198	this study
Wilson Island Group felsic volcanism	1928 ± 11	Bowring et al. (1984)
Hearne dykes	1901 ± 4	Buchan et al. (2010)
SLAVE CRATON		
Malley dykes	2231 ± 2	Buchan et al. (2012)
Mackay dykes	2208 ± 5	LeCheminant and van Breemen (1994)
Dogrib dykes	2193 ± 2	Mitchell et al. (2014)
Blatchford Lake intrusive suite	2185 - 2176	Bowring et al. (1984), Sinclair et al. (1994), Mumford et al. (2012), Mumford (2013)
Big Spruce intrusive suite	2188 ± 16	Cavell and Baadsgaard (1986)
Duck Lake sill	2181 ± 2	Bleeker and Kamo (2003)
Squalus Lake intrusion	2180 ± 1	Villeneuve and van Breemen (1994)
Indin dykes	2126 - 2108	Buchan et al. (2016)
Lac de Gras dykes	2023 ± 2	Buchan et al. (2009)
Blatchford stocks	1892 ± 4	Mumford and Cousens (2014)
Ghost dykes	1885	Buchan et al. (2016)
GREAT SLAVE LAKE SHEAR ZONE		
McKee Lake dykes	2038 ± 3	Pehrsson et al. (1993)
Granite intrusions	1978 ± 5	van Breemen et al. (1990)
	1976 ± 5	van Breemen et al. (1990)
	1960	Hanmer et al. (1992)
	1924	Hanmer et al. (1992)

* Data summarized in Appendix C of this study.

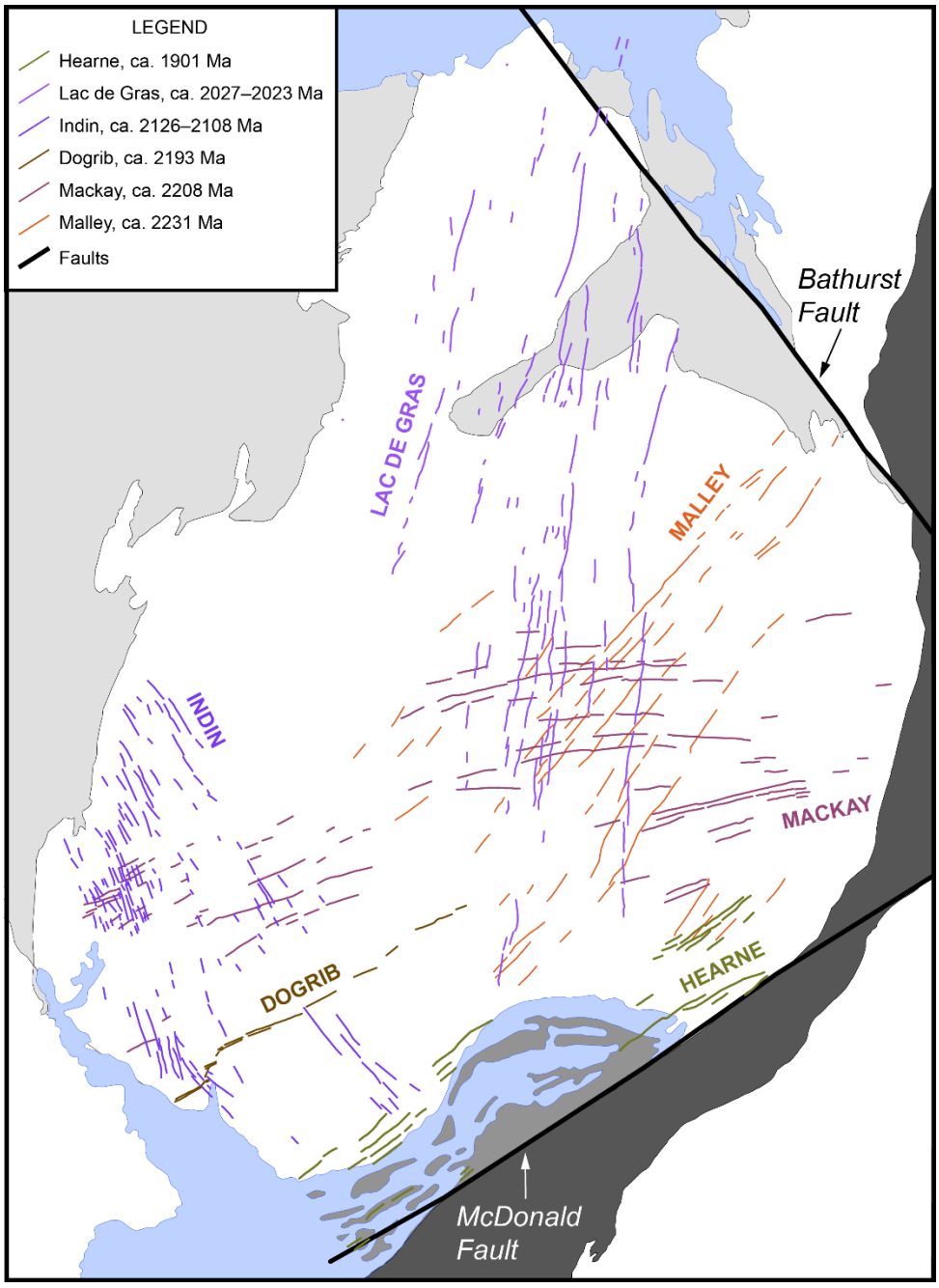

Figure 2.1. Map of Paleoproterozoic mafic dyke swarms in the Slave craton. Modified after Buchan et al. (2010). Age data references are listed in Table 2.1.

with the North and South Simpson Island dykes, but are interpreted to postdate the Sosan Group of the Great Slave Supergroup (Badham, 1979).

Although Mesoproterozoic in age, mafic dykes and sills associated with the ca. 1267 Ma Mackenzie igneous event (LeCheminant and Heaman, 1989) are regionally extensive and intrude the entirety of basin stratigraphy, more prominently in the northeastern portion of the basin.

2.2 Geology of the Union Island Group

The Union Island Group outcrops in a ~25 km by ~10 km area south of the McDonald Fault in the southwestern portion of the basin (Fig. 2.2). Outcrops are distributed in two separate areas, one along the southern shore of Great Slave Lake (hereafter referred to as "mainland area") and the other on islands north and northeast of Union Island (hereafter referred to as "Union Island area").

2.2.1 Previous work

Rocks of the Union Island Group were initially mapped and described by Stockwell (1932; 1936a, 1936b), Henderson (1939), Stockwell et al. (1968), and Reinhardt (1970), and then studied in more detail as part of the East Arm basin stratigraphy by Hoffman (1968; 1969). Thorstad (1976) and Hoffman et al. (1977) published the first stratigraphic division of the Union Island Group, along with detailed lithological and structural descriptions. The first geochemical and isotopic analyses of igneous units of the Union Island Group were presented by Goff et al. (1982) and Goff (1984). This is followed by a more recent geochemical survey by Kjarsgaard et al. (2013a).

2.2.2 Stratigraphy

The Union Island Group comprises marine basinal to platform sequences with intervening mafic volcanic and intrusive rocks. Combining previous studies and observations during field work associated with this study, we recognize six stratigraphic units within the Union Island Group (Fig. 2.3; Thorstad, 1976; Hoffman, 1977):

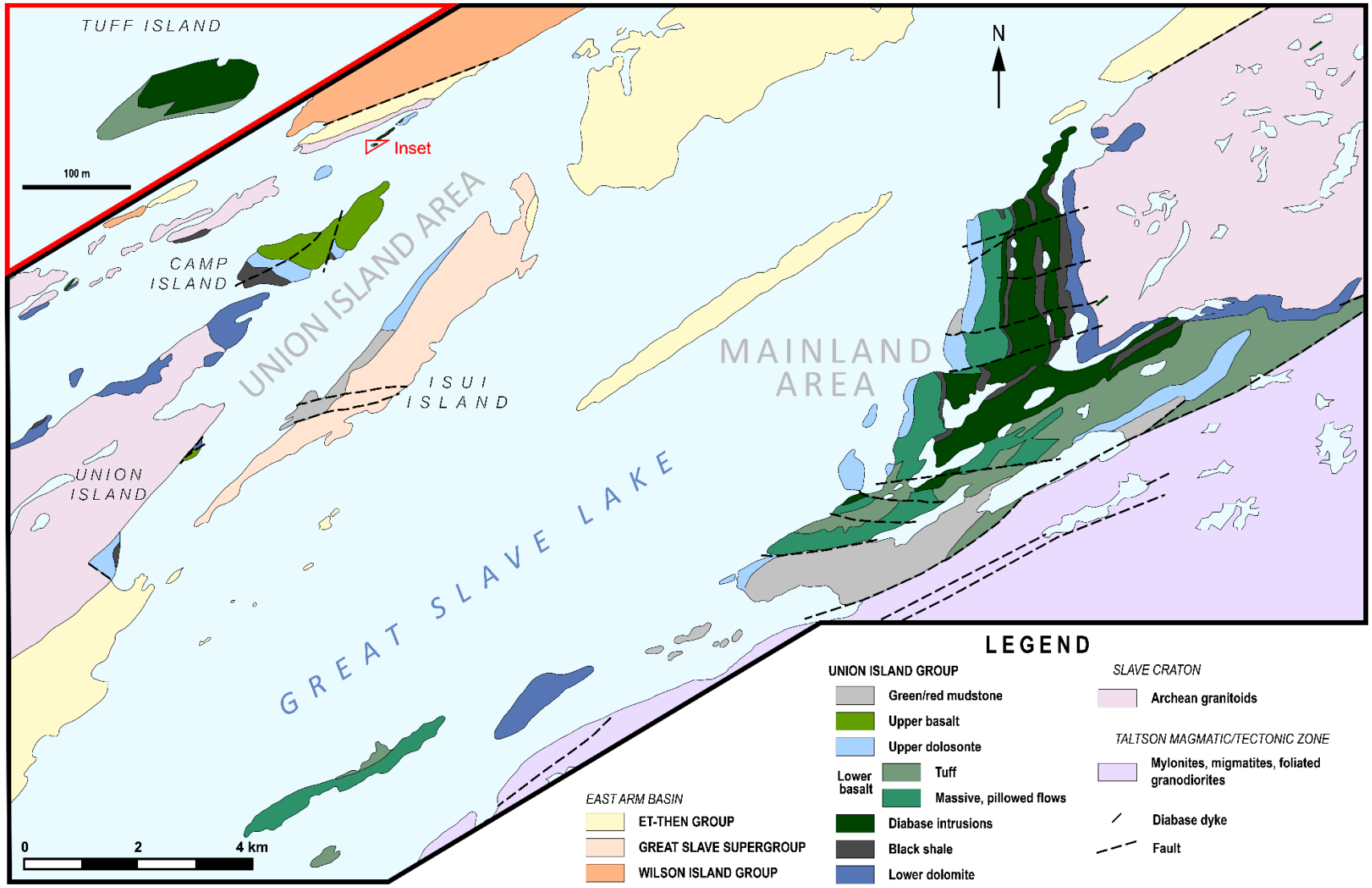

Figure 2.2. Geologic map of the Union Island Group. Geology after Thorstad (1976), Hoffman et al. (1977), and Goff (1984).

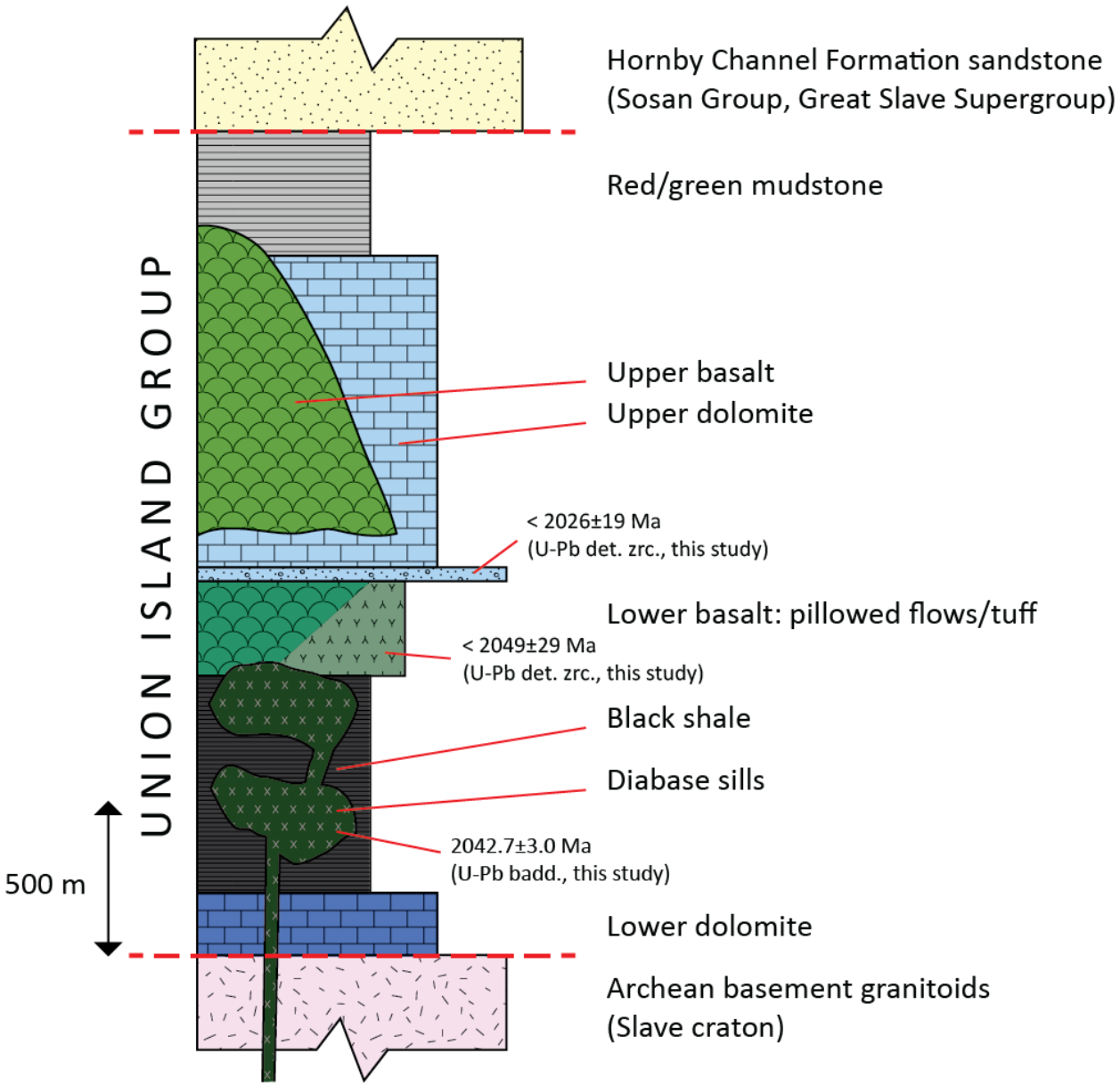

Figure 2.3. A simplified stratigraphic column of the Union Island Group, based on Thorstad (1976) and Goff (1984). Geochronology results from this study are labeled.

1) Lower dolomite

The lower dolomite unit is generally massive (Fig. 2.4a) and contains irregular cherty beds and lenses, in addition to pelitic layers that exhibit micaceous parting. Thorstad (1976) described radial axial dolomite veins as a characteristic of the lower dolomitic unit.

The lower dolomite unit is basal to the Union Island Group and unconformably overlies Archean basement. The exposed unconformity was identified during field work for this study on the northeastern tip of Union Island; other exposures of the unconformity have been reported by Thorstad (1976) and Hoffman et al. (1977). The unconformity exposure on Union Island consists of a regolith profile of weathered granites preserved as quartz grains held in a calcareous matrix (Fig. 2.4b). At the base of the lower dolomite unit Thorstad (1976) and Hoffman et al. (1977) identified a discontinuous section of quartz conglomerate, with granule- to pebble-sized clasts. We identified another unconformity with Archean basement on an island just south of the northeastern tip of North Simpson Island. At this site the observed younging sequence is arenite, quartzite, dolomite, the latter interpreted to be part of the lower dolomite unit. The lower dolomite unit has an exposed apparent thickness of ~200 m.

2) Black shales

The black shale unit consists of massive to laminated carbonaceous black shale interbedded with laminated dolomitic mudstone (Fig. 2.4c). Pyrite occurs in disseminated and nodular forms throughout the unit (Thorstad, 1976). A local occurrence of a one-inch thick massive pyrite bed was observed during fieldwork of this study (Fig. 2.4d). The black shale unit has an exposed lateral thickness of ~500 m.

3) Lower basalts

The ~300 m thick lower basalt unit outcrops almost exclusively in the mainland area where it overlies the black shale unit. The unit contains pillowed and massive basalt flows which are locally plagioclase-phyric (Figs 2.4e, f), as well as interflows of mafic-intermediate volcaniclastic rocks and tuff beds. Goff (1984) described the basalt flows as having massive bases and pillowed tops. Pillowed basalt flows in the upper section of the unit commonly contain inter-pillow cavity infills and cross-cutting dolomitic veins (Fig. 2.4g). Flow-top breccias on top of the basalt flows grade upwards into massive lapilli tuffs (Goff, 1984). An outcrop of massive tuff with well-preserved

Figure 2.4a. Union Island Group lower dolomite, showing generally massive and buff-weathering appearance. Sediment reworking is reflected in fluid-fractured clasts. On a small island north of Union Island, near collection site of samples LH14-EA22A, B.

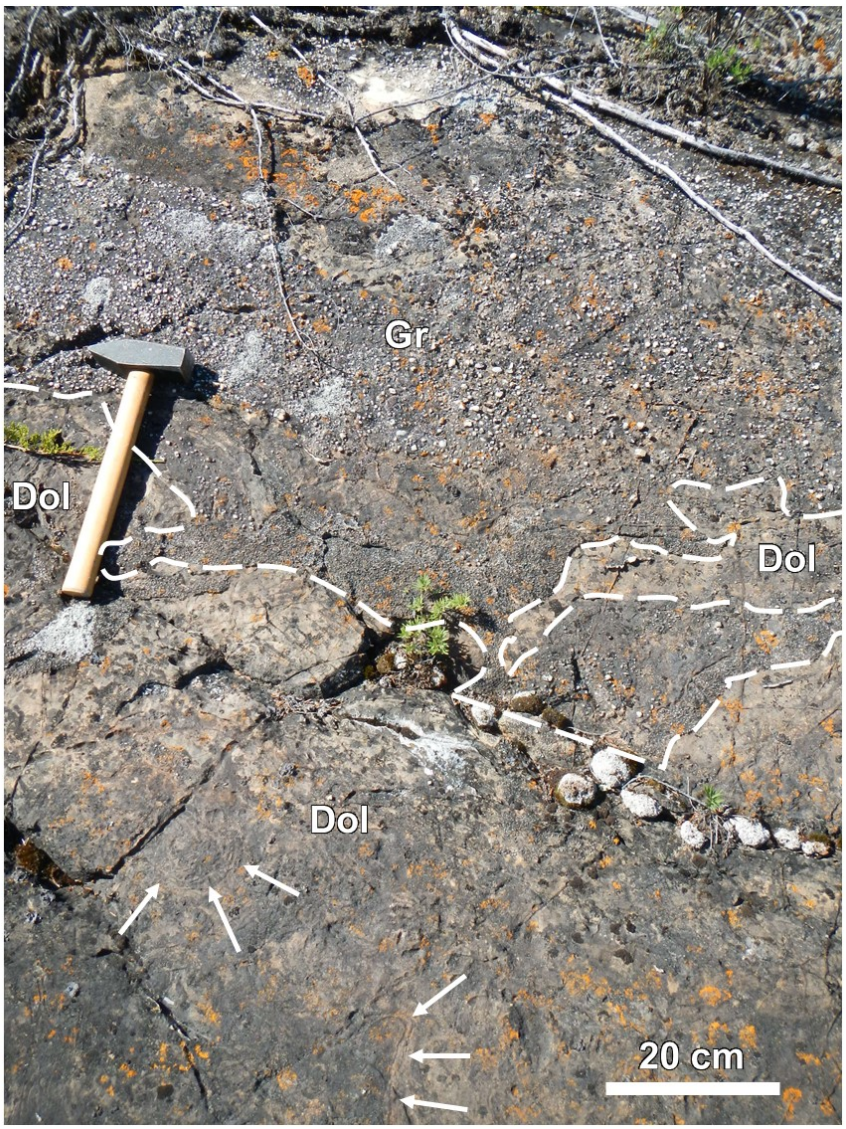

Figure 2.4b. Unconformity (dashed line) between the Union Island Group and the Archean basement. Massive calcareous strata of the lower dolomite unit (Dol) overlies weathered basement granite (Gr); the granite in this picture has been reduced to quartz grains held in a calcareous matrix. Stromatolitic structures in the dolomite are indicated by white arrows. The way up is indicated by the shaft of the hammer. Northeastern tip of Union Island. Photo by L. Ootes.

Figure 2.4c. Black shale unit, containing a calcareous block (centre). Rusting pyrite (orange) is visible at the tip of the hammer. Southwestern shore of Camp Island.

Figure 2.4d. Massive pyrite bed (grey to white) within black shale unit. Pen for scale is ~15 cm long. Southwestern side of Camp Island.

Figure 2.4e. Pillowed flow in lower basalt unit. Mainland area. Sample LH14-EA07 was collected from the partially exposed pillow to the left of the hammer.

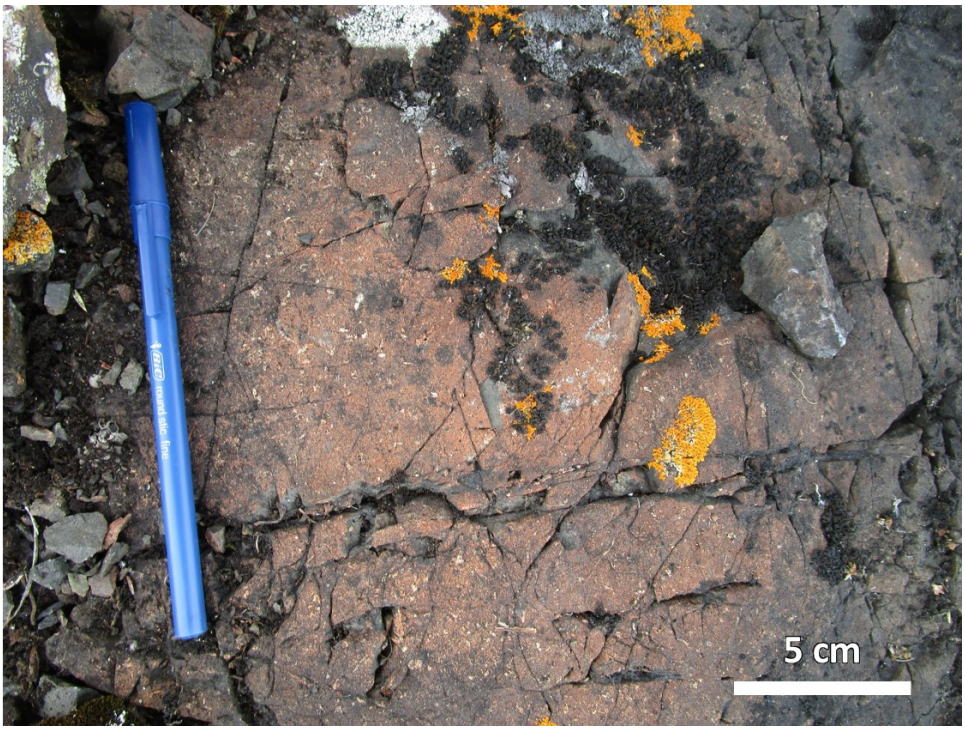

Figure 2.4f. Basalt flow containing white porphyritic plagioclase, lower basalt unit. Mainland area. Near collection site of sample LH15-EA14.

Figure 2.4g. Hydrothermal infill of carbonate minerals in fractures and cavities (red arrow) in the lower basalt unit. Mainland area.

interflow sediments occurs on a small island northeast of Union Island (hereafter referred to as Tuff Island; Figs 2.2, 2.4h). A larger extent of massive, unsorted tuff in the southern limb of the mainland area contains lenses of dolomite and tuffaceous mudstone (Thorstad, 1976).

4) Upper dolomite

The ~200 m thick upper dolomitic unit overlies the lower basalt unit in the mainland area and is conformable over the black shale unit in the Union Island area. The unit is well-bedded (Fig. 2.4i), contrasting with the generally massive lower dolomitic unit (Thorstad, 1976). Grain size of the unit ranges from silt- to sand-sized. Red and green mudstones occur as interbeds. Stromatolitic intervals occur in the northeastern part of Union Island.

5) Upper basalts

The upper basalt unit occurs only in the Union Island area, largely restricted to a 3-km-long island northeast of Union Island (hereafter referred to as "Camp Island"). The unit outcrops as a ~1000-m-thick sequence of well-preserved pillowed basalt flows (Fig. 2.4j) intercalated with flow-top breccias. Thin beds of interflow sedimentary horizons are also reported (Thorstad, 1976). Pillowed basalts that were observed along the southern shore and northeastern tip of the island display a wide range of morphologies, from amoeboid-like to lava-tube-like shapes to pillowed flows (Fig. 2.4l), commonly with thick selvages. Some flows contain shelf structures (Fig. 2.4m), indicating paleohorizontal direction. Internal cavities and interstices are filled with hydrothermal carbonate minerals and quartz, although the unit overall appears less altered compared to the lower basalt unit observed during fieldwork.

6) Red/green mudstones

The ~400-m-thick mudstone unit overlies the upper dolomitic unit, the upper basalt unit and massive tuffs of the lower basalt unit, all with apparently conformable contacts (Thorstad, 1976). The mudstone is well-laminated with alternating mudstone and siltstone intervals plus their dolomitic variants. Soft-sediment deformation features such as convolute bedding and micro-faults are common (Fig. 2.4n). The basal portion of the unit is characterized by black shale, concretionary mudstone and dolomitic beds, while graded bedding becomes more common up-section. The mudstone unit is unconformably overlain by quartzite of the basal Hornby Channel Group of the Great Slave Supergroup.

Figure 2.4h. Interflow sedimentary bed (red arrow) in tuff sequence, lower basalt unit. The bed shows normal grading. Collection site of sample LH15-EA51. Tuff Island.

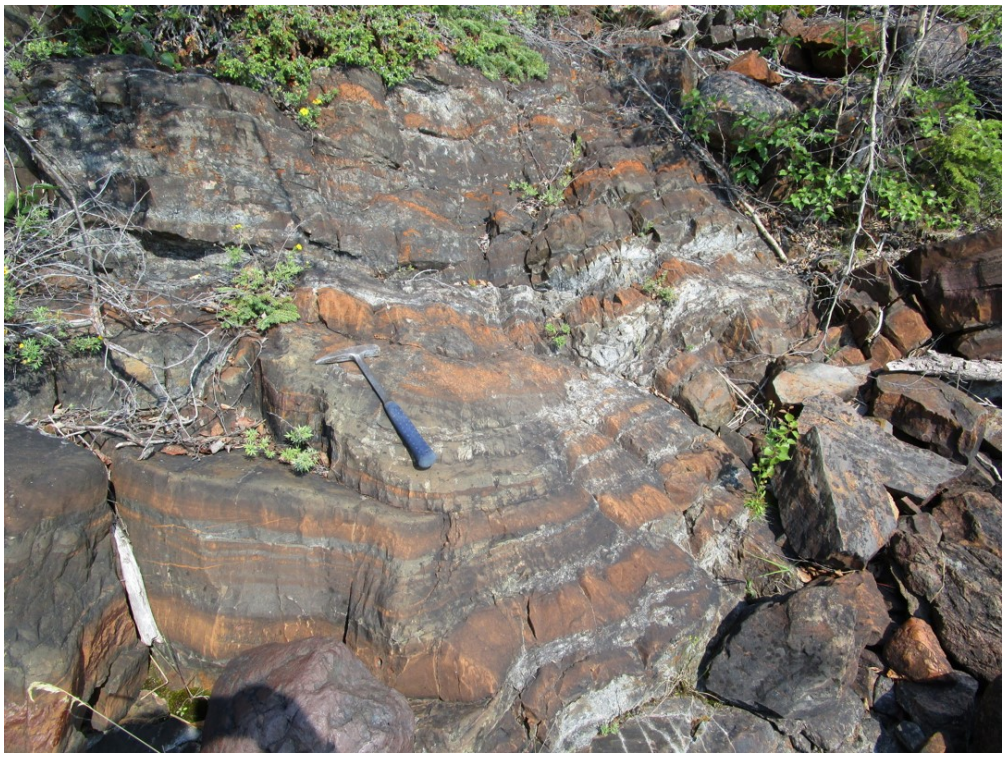

Figure 2.4i. Fine-grained dolomitic beds (orange) interlayered with silt- to sand-sized clastic beds (grey), upper dolomite unit. South shore of Camp Island. Younging up. Hammer for scale is ~40 cm long.

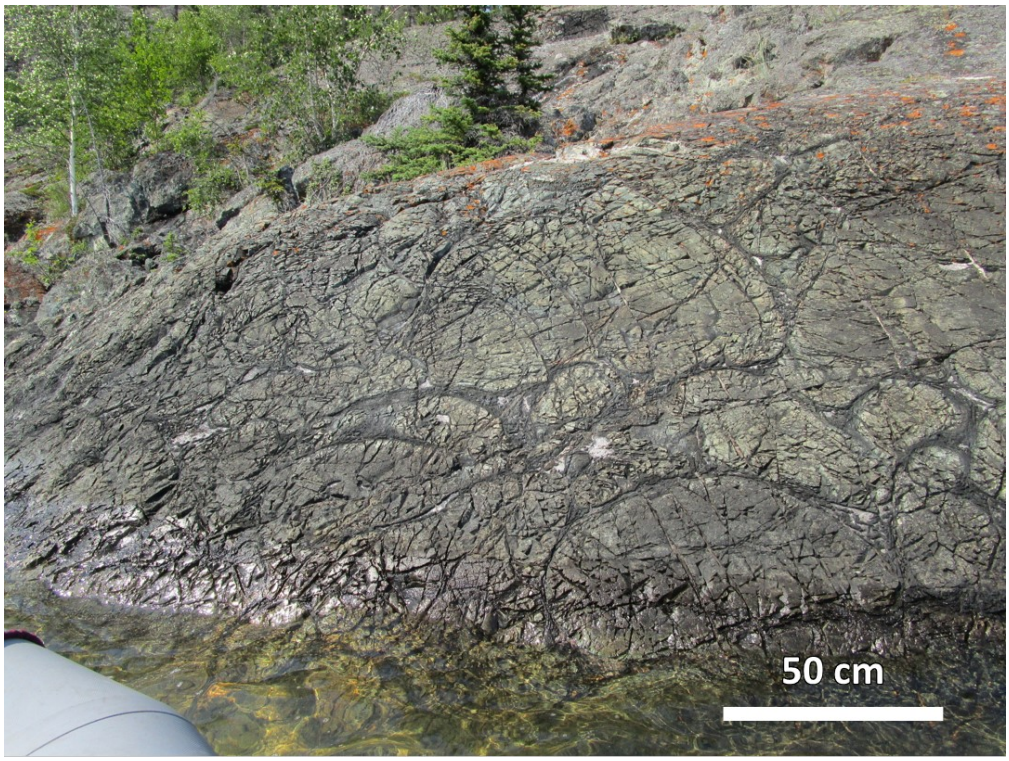

Figure 2.4j. Pillowed flows in the upper basalt unit. Note the devitrified pillow rims and grey-white infill of inter-pillow cavities by hydrothermal carbonate minerals. Southern shore of Camp Island.

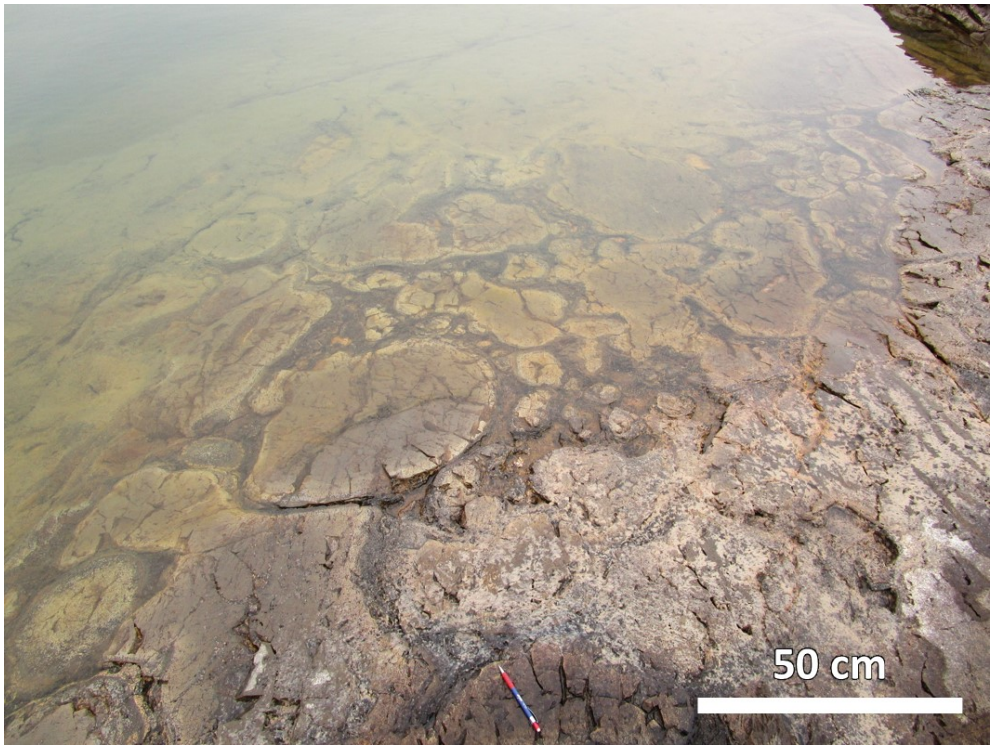

Figure 2.4k. Amoeboid habit of pillowed flows in the upper basalt unit, here partially underwater. Note the light-coloured rims indicative of basalt alteration. Northeastern tip of Camp Island.

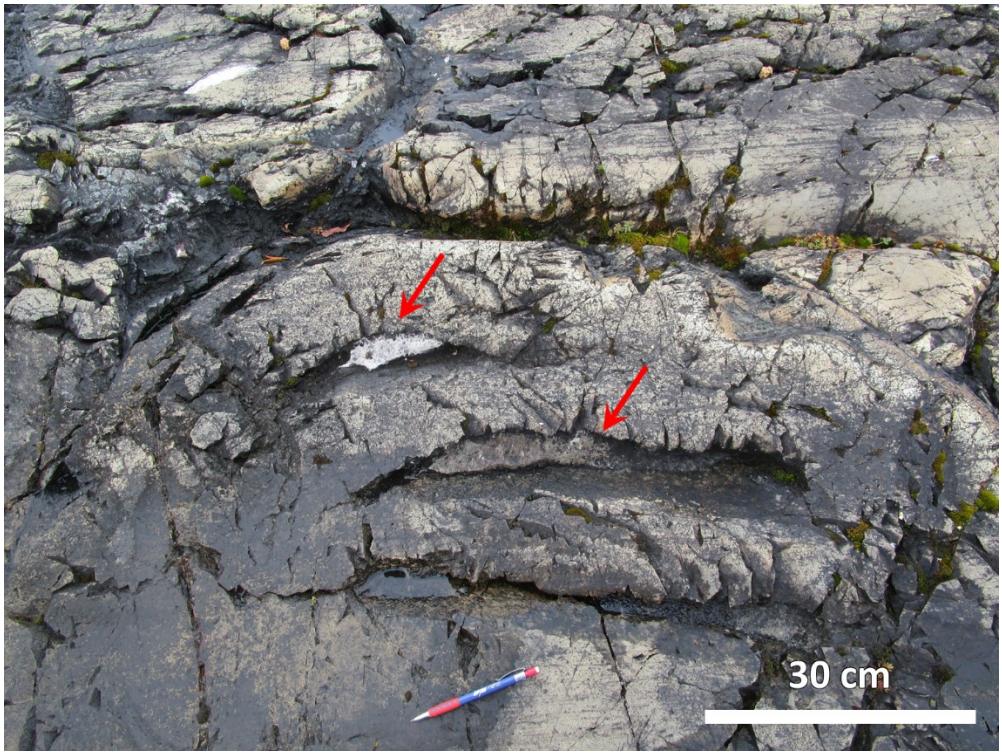

Figure 2.4l. Shelves (red arrows) within a pillow in the upper basalt unit. Note the infill of white carbonate minerals which has partly weathered away. Northeastern tip of Camp Island.

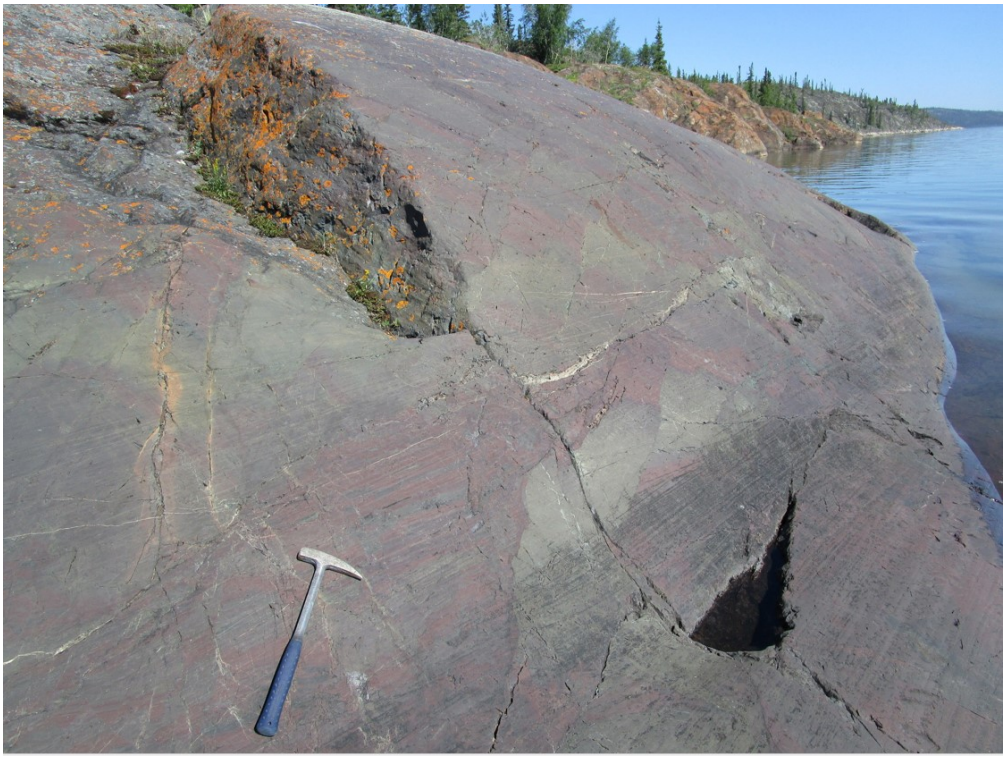

Figure 2.4m. Finely laminated beds of the red and green mudstone unit, showing micro-faults. Northeastern part of Union Island, view northeast. Hammer for scale is ~40 cm long.

Figure 2.4n. Columnar joining (red arrows) on a diabase sill in the mainland area. View towards northwest.

Figure 2.4o. Close-up view of the weathered surface of a diabase sill, with distinguishable light-coloured plagioclase laths.

Union Island Group diabase sills and dykes

Diabase sills intrude the black shale and lower basalt units in the mainland area (Fig. 2.1), with estimated thicknesses of up to 200 m (Goff, 1984). At least two sills are identified (Thorstad, 1976). These display chill margins and columnar jointing (Goff, 1984; Fig. 2.4o). Near one of the chill margin sampled in this study, both the diabase and black shale exhibit shearing that may have resulted from regional deformation.

The diabase ranges from black to black-green on fresh surfaces and weathers orange, often with discernable white plagioclase (Fig. 2.4p). The sills show generally coarsening grain size from margins towards centre.

Three correlative diabase dykes (sec. 4.1) cut the Archean basement and range 2–25 m in thickness and 040–060^{o} in trend. Two of these intrude the basement within ~200 m from the recessive basal unconformity of the lower dolomite unit; the third (LH14-07) occurs ~5 km northeast of the mainland area exposures. Only the center of one of these dykes (LH14-22B) is slightly magnetic.

Another correlative diabase body (sec. 4.1) intrudes the volcaniclastic sequences on Tuff Island (Fig. 2.2) the geometry of this intrusion remains unclear such that it was not possible to identify if it is a sill or a dyke. This diabase body is strongly magnetic.

2.2.3 Deformation and metamorphism

Strata of the Union Island Group are folded along a northeast-southwest trending axis. This is evident as a southwest-facing anticlinal structure in the mainland area. In the Union Island area the upper basalts are preserved in an anticlinal fold structure with axial trace striking to the northeast. Many of the dolomitic carbonate outcrops in the Union Island area preserve a northeast-striking, steeply dipping foliation that is axial planar to M-folds. As the area of the Union Island Group is bisected by the McDonald fault, numerous fault-related fractures occur in the mainland area.

The Union Island Group is metamorphosed to lower-greenschist facies. This is typified in the mafic units, where a characteristic assemblage of actinolite-chlorite-epidote-titanite is the predominant transformed mineralogy (sec. 3.4). Plagioclase is commonly altered to sericite or

albite. Abundant carbonate-rich veins and mineral replacement by carbonates suggest alteration by hydrothermal fluids (Thorstad, 1976; Goff, 1984; sec. 3.4).

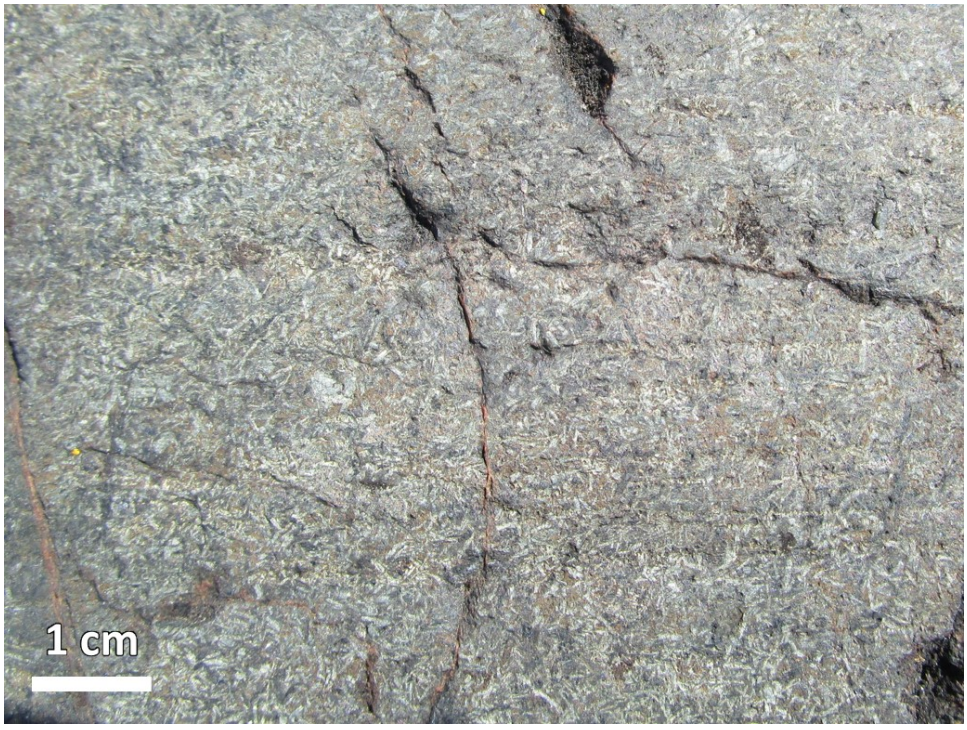

Figure 2.4p. Close-up view of a relatively unweathered surface of the diabase intrusion on Tuff Island. White laths of plagioclase are distinguishable alongside black pyroxene and orange-weathering metal oxides. Collection site of sample LH15-EA58.

3 METHODOLOGY

3.1 Sampling Strategy

Fieldwork was conducted in the East Arm area for a combined duration of eighteen days during the 2014 and 2015 field seasons. The principal goals of fieldwork were 1) to evaluate stratigraphic interpretations for the Union Island Group, both internally and relative to the rest of the stratigraphy in the East Arm basin, by verifying observations in previous mapping studies (e.g., Thorstad, 1976) and possibly updating with new observations, and 2) to collect specimens from the igneous units of the Union Island Group for geochemical and geochronological analysis, and from the sedimentary units for detrital zircon geochronology analysis. Location and description of all 45 samples collected are presented in Fig. 3.1 and Table 3.1. In general, at least 1 kg (fist-sized) was collected for each volcanic sample; a minimum of 5 kg was collected for each intrusive sample to maximize the amount of baddeleyite crystals available for geochronological analysis.

Union Island Group volcanic units

Given that the Union Island Group lower basalt unit may represent the earliest-known surficial expression of mafic magmatism in the East Arm basin, a high-resolution investigation into compositional variations of successive lava flows can yield insights into magmatic processes and the origin of the Union Island Group mafic magmatism. We collected nine basalt samples (LH15-EA06 to LH15-EA14) at a 10 m interval along the uppermost 90 m of the lower basalt unit exposed in the mainland area. The outcrop is continuously exposed along the shoreline of Great Slave Lake. The sampled flows overlie a layer of dolomitic, clay- to silt-sized interflow sediment and terminate at an upper unconformity, which is truncated by a quartz pebble conglomerate bed that is in turn overlain by the upper dolomite unit. Eight additional samples (LH15-EA16 to LH15-EA23) were collected from an outcrop of pyroclastic rocks 5 km to the southwest.

A previously undescribed outcrop of well-preserved tuffs and interflow sediments was surveyed on Tuff Island (Fig. 3.1) and was interpreted as belonging to the lower basalt unit based on the observation that it is intruded by a diabase body; the diabase is geochemically identical to sills intruding the lower Union Island Group strata in the mainland area (sec. 4.1.7). Eight samples were collected from the tuff sequence (LH14-26A, B, LH15-EA51–LH15-EA56) for petrographic and

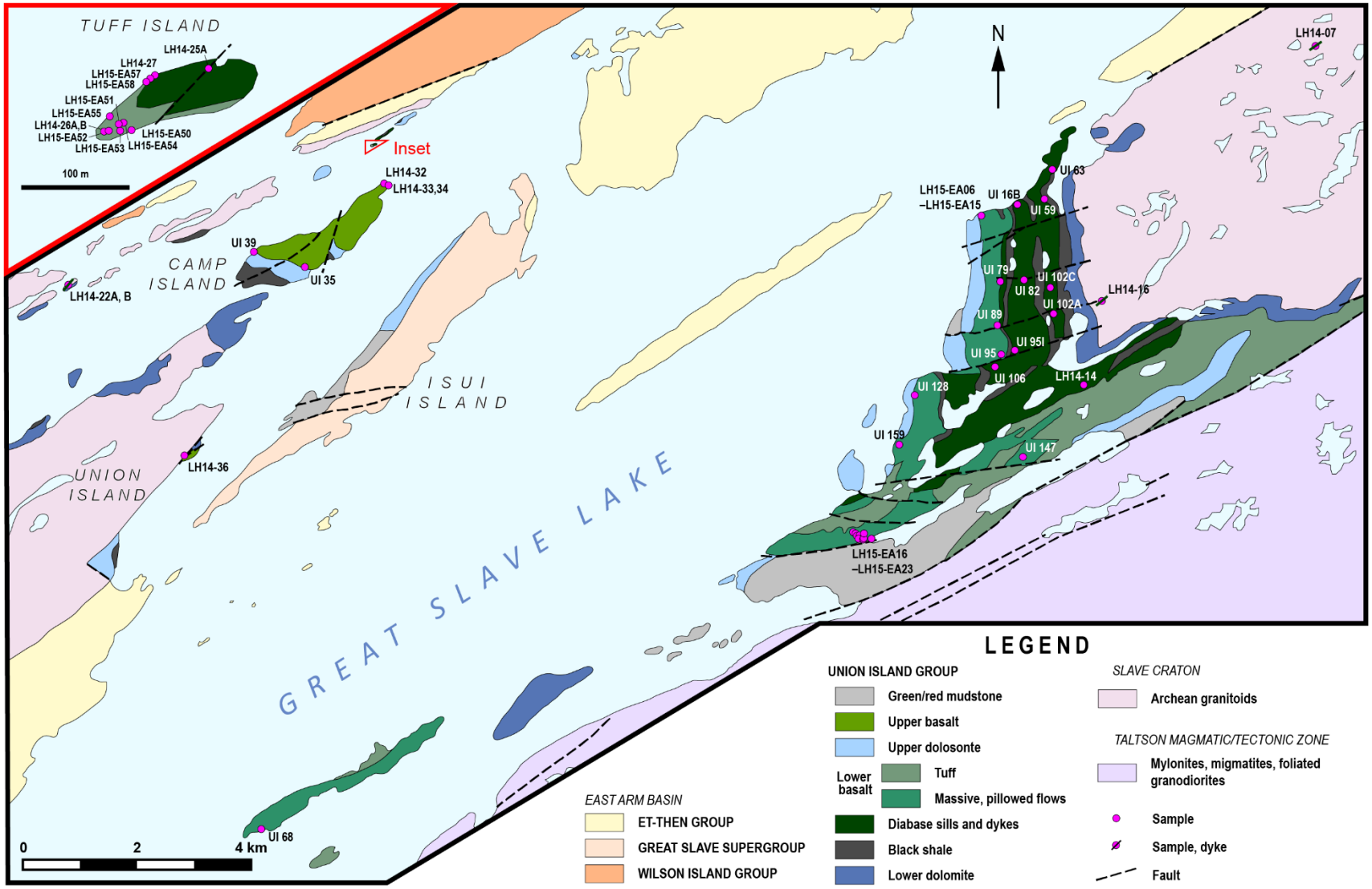

Figure 3.1. Geologic map of the Union Island Group, showing locations of samples collected in this study ("LH" series) and archive samples selected for analysis ("UI" series).

Table 3.1. List of Union Island Group samples collected during field work of this study, with location coordinates and collection notes.

Sample Number	Unit	Lithology	Latitude	Longitude	Notes
LH14-07B	Diabase intrusions	Diabase dyke	62° 02. 53 N	111° 27.23 W	Dyke center, trend 050-060, width 25m, cuts basement granitoid, some dyke splaying
LH14-14	Diabase intrusions	Diabase sill	61° 59.46 N	111° 31.70 W	Coarse-grained, visible greenschist alteration, with carbonate veins, fractures
LH14-16	Diabase intrusions	Diabase dyke	62° 00.21 N	111° 31.40 W	Dyke, trend 050, width 2-3m, cuts basement granitoid; vesicular with spherical pit weathering; overall colour transitions to grey 15m east of sample site, showing black spheroids; ~200m from recessive unconformity
LH14-22A	Diabase intrusions	Diabase dyke	62° 00.41 N	111° 50.74 W	Dyke margin, trend 040, width 12m, cuts basement granitoid; non-magnetic; fairly altered internally despite lacking apparent deformation; ~30m from recessive unconformity
LH14-22B	Diabase intrusions	Diabase dyke	62° 00.41 N	111° 50.74 W	Dyke centre of LH14-22A, slightly magnetitc; alteration sic.
LH14-25A	Diabase intrusions	Diabase	62° 01.71 N	111° 44.09 W	NE of landing, medium-grained, highly fractured, moderately magnetic
LH14-26A	Lower basalt	Tuff	62° 01.73 N	111° 44.95 W	
LH14-26B	Lower basalt	Tuff	62° 01.73 N	111° 44.95 W	
LH14-27	Diabase intrusions	Diabase	62° 01.69 N	111° 44.99 W	Collected from landing site; moderately magnetic
LH14-32	Upper basalt	Basalt	62° 01.33 N	111° 44.88 W	Possibly syn-volcanic dyke, contact not demonstrated, possibly ponded flow
LH14-33	Upper basalt	Basalt	62° 01.31 N	111° 44.77 W	Possibly syn-volcanic dyke, gradational boundary into pillowed flows
LH14-34	Upper basalt	Basalt	62° 01.32 N	111° 44.76 W	Same as sample LH14-33
LH14-36	Upper basalt	Basalt	61° 58.86 N	111° 48.72 W	Pillowed flow, contains carbonate veins
LH15-EA01	Diabase intrusions	Diabase sill	62°00.271 N	111°32.394 W	Lower sill, coarse-grained centre; bag 1 contains grabs within 5-10m radius, bag 2 contains broken fragments from a single boulder collected at specified coordinates
LH15-EA02	Diabase intrusions	Diabase sill	62°00.264 N	111°32.445 W	W (upper) side of lower sill, distance from actual margin indeterminate
LH15-EA04	Diabase intrusions	Diabase sill	see notes		E (lower) margin of lower sill, fine-grained, ~20cm from sheared contact, ~30cm upslope from LH15-EA03
LH15-EA05	Lower basalt	Basalt	62°01.023 N	111°33.665 W	Clay- to silt-sized dolomitic interflow sediments below LH15-EA06
LH15-EA06	Lower basalt	Basalt	see notes		10m SW of LH15-EA05
LH15-EA07	Lower basalt	Basalt	62°01.017 N	111°33.692 W	Pillow centre
LH15-EA08	Lower basalt	Basalt	62°01.008 N	111°33.703 W	
LH15-EA09	Lower basalt	Basalt	62°00.998 N	111°33.705 W	Coordinates taken from a slightly higher elevation due to steep slope
LH15-EA10	Lower basalt	Basalt	62°00.995 N	111°33.677 W	
LH15-EA11	Lower basalt	Basalt	62°00.987 N	111°33.678 W	Contains black amygdules of secondary chlorite
LH15-EA12	Lower basalt	Basalt	62°00.980 N	111°33.682 W	
LH15-EA13	Lower basalt	Basalt	62°00.965 N	111°33.677 W	Plagioclase-phyric, weathers black
LH15-EA14	Lower basalt	Basalt	62°00.955 N	111°33.678 W	Small cm-scale flow banding, possibly reflecting magmatic shear
LH15-EA15	Upper dolomite	Qtz. pebble conglomerate	10m SW of LH15-EA14		Directly above unconformity between upper dolomite and lower basalt
LH15-EA16	Lower basalt	Volcanoclastics	61°58.155 N	111°36.070 W	
LH15-EA17	Lower basalt	Volcanoclastics	61°58.144 N	111°36.019 W	Contains visible dissemintated grey-silver metal oxides
LH15-EA18	Lower basalt	Volcanoclastics	61°58.124	111°35.990 W	

Table 3.1. (continued)

Sample Number	Unit	Lithology	Latitude	Longitude	Notes
LH15-EA19	Lower basalt	Volcanoclastics	61°58.129	111°35.939 W	
LH15-EA20	Lower basalt	Volcanoclastics	61°58.102	111°35.950 W	
LH15-EA21	Lower basalt	Volcanoclastics	61°58.091	111°35.846 W	Contains amygdules and black carbonate veins
LH15-EA22	Lower basalt	Volcanoclastics	30m N of LH15-EA21		
LH15-EA23	Lower basalt	Volcanoclastics	61°58.147	111°35.854 W	
LH15-EA51	Lower basalt	Tuff	see inset of sample map		Normally-graded interflow sediments, largest clasts ~2mm
LH15-EA52	Lower basalt	Tuff	see inset of sample map		Contains 3mm thick layer containing vesicular basalt fragments (1mm)
LH15-EA53	Lower basalt	Tuff	see inset of sample map		
LH15-EA54	Lower basalt	Tuff	see inset of sample map		
LH15-EA55	Lower basalt	Tuff	see inset of sample map		Right by shore
LH15-EA56	Lower basalt	Tuff	see inset of sample map		
LH15-EA57	Diabase intrusions	Basaltic breccia	see inset of sample map		Vesicular breccia lens (5cm x 40cm) within diabase; surrounding diabase shows fractures infilled by breccia matrix; 1m~ away from diabase-tuff boundary
LH15-EA58	Diabase intrusions	Diabase	see inset of sample map		5m SW from LH14-27 along shore

detrital zircon provenance study (sec. 4.2.2). An additional sample was collected from a lens of vesicular basaltic breccia cutting the diabase body.

Four samples were collected from the upper basalt unit on Camp Island and in the northeastern part of Union Island (LH14-32–LH14-34, LH14-36; Fig. 3.1). Samples include centers of pillowed basalts and linear dyke-like structures within pillowed flows, interpreted to be syn-volcanic dykes.

Union Island Group diabase sills and dykes

Four samples of Union Island Group diabase sills were collected in the mainland area (LH14-14, LH15-EA01, LH15-EA02, LH15-EA04; Fig. 3.1). Three additional samples were collected from the diabase intrusion on Tuff Island (LH14-25, LH14-27, LH15-EA58); the geometry of the Tuff Island diabase remains unclear such that it was not possible to demonstrate in the field if the body is a sill or a dyke.

As there exist several known Paleoproterozoic mafic dyke swarms in the East Arm basin and its surrounding area, collection was also made of other mafic dyke bodies observed during fieldwork, including some that were previously mapped. Due to the reconnaissance nature of this portion of the fieldwork, a margin-center pair was not collected for every mafic dyke surveyed. Three of these dykes (LH14-07, LH14-14, LH14-22) were subsequently interpreted as likely feeder dykes to the Union Island Group basalt package based on their similar whole-rock geochemistry (sections 4.1, 5.1).

Union Island Group sedimentary units

A quartz pebble conglomerate (LH15-EA15) was collected from the base of the upper dolomite unit for LA-ICPMS U–Pb detrital zircon geochronology (sec. 4.2). In addition, a layer of dolomitic interflow sediment was sampled at the base of the lower basalt geochemical transect.

Archive samples

In addition to field collection, eighteen igneous specimens were selected from the extensive Union Island Group thesis collection of S. Goff (1984) archived at the Department of Earth and Atmospheric Sciences, University of Alberta. Archive samples (denoted by sample numbers beginning with "UI") were selected based on sample freshness (i.e. lack of visible alteration and

weathering), volume available for analysis, and corresponding field location with the aim of expanding existing sample coverage.

Analytical sample selection

As all rocks of the East Arm basin have been subjected to lower greenschist-facies metamorphism and hydrothermal alteration (Thorstad, 1976; Goff, 1984), care was taken in selecting fresh specimens wherever possible. Samples with significant internal heterogeneity were excluded from whole-rock chemical analyses, as were those with abundant hydrothermal veins and visible signs of deformation.

For each diabase intrusion, the coarsest portion was sampled for U–Pb age dating to maximize the size of potential baddeleyite and/or zircon crystals and therefore the precision of analytical results. Fine-grained chilled margin samples were also collected for whole-rock chemical analysis as these may record the most primitive magma composition during the early stage of intrusion (e.g., Skelhorn et al., 1979; Upton et al., 1985; Kuehner, 1986).

3.2 Sample preparation

Samples for whole-rock chemical analysis were crushed following standard techniques. Care was taken to remove weathered surfaces, visible alteration crusts and veins. Cut rock chips (0.5–0.7 cm thick) were crushed to at least 200 mesh (<74 μm) using a tungsten carbide puck mill.

For U–Pb ID-TIMS geochronology, petrographic thin sections of diabase samples were first screened under petrographic microscope for the presence of baddeleyite or zircon. Igneous baddeleyite may contain magmatic zircon overgrowths, or is itself altered to zircon during metamorphism (Heaman and LeCheminant, 1993). Therefore, select thin sections were further examined under electron microprobe via secondary electron (SE) and backscatter electron (BSE) imagery to determine the morphology and paragenesis of baddeleyite crystals (secs 3.4.3, 3.4.4).

Sample LH14-27, which contains the largest and least zircon-rimmed baddeleyite crystals, was selected for a U–Pb ID-TIMS study. A separate portion of this sample was crushed in a similar fashion as samples for chemical analysis, but at a coarser grain size in order to preserve baddeleyite crystals. To separate baddeleyite crystals, the sample powder was first passed over a Wilfley Table at a slow feed rate (~0.2 kg/hr), then the heavy mineral fraction is further passed under a Frantz

Isodynamic Separator to remove the abundant, magnetic ilmenite and Ti-magnetite phases. Methylene iodide heavy liquid separation was bypassed due to the small size of the baddeleyite crystals (<60 μm). During separation procedures in this study, it was discovered that ~90% of all separated baddeleyite grains remained on metal surfaces of the Frantz Isodynamic Separator (e.g. feed trough), and that optimal recovery was achieved by rinsing these machine components with ethanol into petri dishes. A total of ~140 baddeleyite grains, measuring at least 20 μm in length, was separated from two batches of sample powder, each weighing ~0.2 kg before separation. Individual multi-grain fractions of baddeleyite were then selected via hand-picking under stereoscopic microscope; preference was given to grains that were intact, inclusion-free, and exhibited minimal zircon overgrowth.

Extraction of detrital zircon grains from sedimentary samples followed the same procedures as those for separating baddeleyite, except that a steel disk mill was used for crushing in order to obtain a coarser grind, and that standard Wilfley Table and methylene iodide heavy liquid density separation techniques were used. Approximately 1 kg of the sample rock was processed. From the hand-picked zircon fraction, a random population of ~200 grains was selected and mounted in epoxy. The mounts were polished first using a Carborundum 400B grit silicon carbide wet sandpaper, followed by 1 μm and 0.3 μm alumina on pellon polishing cloth, such that most zircon grains were exposed. Cathodoluminescent (CL) imagery of the polished zircons was taken using a Zeiss Axioscope 40 microscope to survey zircon morphology and for determining the placement of primary beam for spot analyses.

3.3 Analytical protocols

All analyses in this study, except for whole-rock element abundances, were conducted at the Department of Earth and Atmospheric Sciences, University of Alberta, with isotopic analysis done at the Canadian Centre of Isotopic Microanalysis.

3.3.1 Elemental geochemistry

Major-, minor-, and trace-element abundances were determined for 50 whole-rock samples via ICP (major, minor, and some trace elements) and ICP-MS analysis (trace elements) of lithium borate infused glasses at the Activation Laboratories Ltd., Ancaster, ON. The analytical package

4LITHORES was selected for all samples. Relative errors in three submitted blind standards are summarized in Table 3.2.

3.3.2 Sr and Nd tracer isotope analysis

Sample powders for isotope dilution tracer isotope analysis were weighed (4.4–4.9 mg), then dissolved in a 2:1 mixture of 16M HNO_3:48% HF, added ^{87}Rb–^{84}Sr and ^{149}Sm–^{150}Nd spikes, for 48 hours. This was followed by dissolution in 6 mL 12N HCl for 24 hours on a hotplate at 110–120ºC. Dissolved samples were dried down, then converted to 1 mL 2M HCl for chromatography separation. Rb–Sr and REE fractions were obtained separately through cation exchange resin (BioRad AG 50W-X8, 100–200 mesh) columns before being further purified through additional chemistry columns. Rb–Sr was collected in 2.5M HCl. Strontium was further purified from this fraction by elution with 0.05M HNO_3 through Sr spec resin (Eichrom 50–100 μm) columns. Rubidium was purified from the 3M HNO_3 and 7M HNO_3 wash of the Sr column and was collected through cation exchange resin (Eichrom AG 50W-X8) columns. REE fractions were collected in 6M HCl in the same procedures that separated the Rb–Sr fraction. Samarium and neodymium were further purified from the REE fraction through Ln spec resin (Eichrom 50–100 μm) columns by elution with 0.5M HCl and 0.25M HCl, respectively.

Rubidium isotopic ratios were measured on Micromass Sector 54 thermal ionization mass spectrometer. Purified Rb fractions were dried down with H_3PO_4, then dissolved in 10 μL Milli-Q water. Between 10% and 50% of sample solution was loaded on a Ta filament, with the loaded amount determined based on ICP-MS Rb concentrations in order to optimize the measured signal and minimize the error propagation from spiking. Samples were loaded at 1 A current, then 2 μL TaF activating complex is added onto the filament. Filament current is then slowly increased to 2 A until samples are dry. Measurements were taken at 1.4–1.5 V on Faraday cups. Analytical error is 0.03% based on analysis of the RbCl standard NBS984.

Strontium isotopic ratios were measured on a Thermo Fisher Scientific Triton Plus multi-collector thermal ionization mass spectrometer. Loading procedure is similar to that for Rb fractions, with the exception that samples were dissolved in 4 μL $TaCl_5$+HF activator complex before loading onto outgassed Re filaments. Measurements were made using Faraday detectors (10^{11} ohm amplifiers) at filament temperatures between 1380°C and 1420°C. Data were reduced offline in an Excel-based program. To measure the accuracy of the mass spectrometer, the Sr standard

Table 3.2. Major, minor, and trace element analyses of standard materials WGB-1, TDB-1, and SY-2, with associated relative errors and repeatability values.

Analyte Symbol	SiO_2	Al_2O_3	$Fe_2O_{3(T)}$	MnO	MgO	CaO	Na_2O	K_2O	TiO_2	P_2O_5	LOI
Unit Symbol	%	%	%	%	%	%	%	%	%	%	%
Detection Limit	0.01	0.01	0.01	0.001	0.01	0.01	0.01	0.01	0.001	0.01	
Analysis Method	FUS-ICP	FUS-ICP	FUS-ICP	FUS-ICP	FUS-ICP	FUS-ICP	FUS-ICP	FUS-ICP	FUS-ICP	FUS-ICP	FUS-ICP
WGB-1											
Published value (2σ)	*49.1±0.8*	*11.15±0.27*	6.71±0.14*	*0.143±0.014*	9.4±0.19*	*15.78±0.85*	*2.15±0.08*	0.94±0.04*	*0.84±0.07*	*0.099±0.034*	3.6-4.0
Analysis 1	49.56	10.66	6.45	0.13	9.46	16.47	2.09	0.88	0.88	0.07	3.81
Analysis 2	48.47	11.12	6.26	0.14	9.22	16.29	2.13	0.91	0.88	0.09	3.73
Relative error	1%	0-4%	4-7%	6-8%	1-2%	3-4%	1-3%	3-6%	5%	9-29%	0-2%
Repeatability	1%	2%	1%	1%	1%	1%	1%	2%	0%	13%	1%
TDB-1											
Published value (2σ)	50.2	*13.6±0.40*	14.4±0.29*	*0.204±0.010*	*5.9±0.3*	*9.6±0.7*	*2.2±0.1*	*0.89±0.08*	*2.3±0.2*	*0.23±0.05*	0.3
Analysis 1	50.26	13.48	14.38	0.20	5.64	9.81	2.23	0.87	2.39	0.22	0.39
Analysis 2	50.99	13.38	14.19	0.19	5.7	9.83	2.21	0.88	2.36	0.23	0.34
Relative error	0-2%	1-2%	0-1%	4-6%	4-3%	2%	0-1%	1-2%	2-4%	0-4%	13-30%
Repeatability	1%	0%	1%	1%	1%	0%	0%	1%	1%	2%	7%
SY-2											
Published value (2σ)	60.11±0.86	12.04±0.46	6.31±0.34	0.32±0.02	2.69±0.24	7.96±0.30	4.31±0.26	4.45±0.22	0.15±0.04	0.43±0.06	1.08±0.24
Analysis	60.53	12.11	6.26	0.31	2.6	7.98	4.38	4.54	0.14	0.43	1
Relative error	1%	1%	1%	3%	3%	0%	2%	2%	8%	0%	7%

For standards WGB-1 and TDB-1, certified values are denoted by asterisk (*), provisional values are denoted italic font, and remaining values are informational ranges or values (Canadian Certified Reference Materials Project, 1994, 1997). Published values for SY-2 are taken from compilation by Gladney and Roelandts (1990).

$$\text{Relative error} = \frac{|\text{literature value} - \text{analysis value}|}{\text{literature value}} \times 100\%$$

Table 3.2. (continued)

Analyte Symbol	Sc	Be	V	Cr	Co	Ni	Cu	Zn	Ga	Ge	As	Rb	Sr	Y	Zr
Unit Symbol	ppm	ppm	ppm	ppm	ppm	ppm	ppm	ppm	ppm	ppm	ppm	ppm	ppm	ppm	ppm
Detection Limit	1	1	5	20	1	20	10	30	1	0.5	5	1	2	0.5	1
Analysis Method	FUS-ICP	FUS-ICP	FUS-ICP	FUS-MS	FUS-MS	FUS-MS	FUS-MS	FUS-MS	FUS-MS	FUS-MS	FUS-MS	FUS-MS	FUS-ICP	FUS-MS	FUS-ICP
WGB-1															
Published value (2σ)	*44±4*	0.2-0.8	*222±17*	291±13*	*29.8±1.7*	*76±7*	*106±9*	*31.5±8.5*	11-13	0.2-7	1.5-5	*19.5±1.5*	*118±9*	*14.6±2.7*	*44±16*
Analysis 1	40	< 1	224	270	26	70	100	30	11	2	< 5	17	106	14.4	56
Analysis 2	39	< 1	228	290	26	70	90	30	11	1.9	< 5	17	105	14.1	54
Relative error	9-11%		1-3%	0-7%	13%	8%	6-15%	5%	8%	44-47%		13%	10-11%	1-3%	23-27%
Repeatability	1%		1%	4%	0%	0%	5%	0%	0%	3%		0%	0%	1%	2%
TDB-1															
Published value (2σ)	*36±3*	1.5	*471±21*	251±13*	*47±4*	92±6*	323±15*	155±11*	*21±2*	1	*2.5±0.5*	*23±2*	*230±24*	*36±4*	*156±20*
Analysis 1	35	1	445	220	43	90	320	150	21	1.6	< 5	20	213	33.9	164
Analysis 2	36	1	446	230	44	80	320	160	22	1.5	< 5	20	219	34.6	164
Relative error	0-3%	33%	5-6%	8-12%	6-9%	2-13%	1%	3%	0-5%	50-60%		13%	5-7%	4-6%	5%
Repeatability	1%	0%	0%	2%	1%	6%	0%	3%	2%	3%		0%	1%	1%	0%
SY-2															
Published value (2σ)	7.0±1.2	22±10	50±16	9.5±5.8	8.6±2	9.9±7.6	5.2±4.4	248±30	29±6	1.3	17.3±4.2	217±30	271±28	128±34	280±48
Analysis	7	25	49	< 20	8	< 20	< 10	270	29	1.5	16	215	277	129	298
Relative error	0%	14%	2%		7%			9%	0%	15%	8%	1%	2%	1%	6%

Analyte Symbol	Nb	Mo	Ag	In	Sn	Sb	Cs	Ba	La	Ce	Pr	Nd	Sm	Eu	Gd
Unit Symbol	ppm	ppm	ppm	ppm	ppm	ppm	ppm	ppm	ppm	ppm	ppm	ppm	ppm	ppm	ppm
Detection Limit	0.2	2	0.5	0.1	1	0.2	0.1	3	0.05	0.05	0.01	0.05	0.01	0.005	0.01
Analysis Method	FUS-MS	FUS-MS	FUS-MS	FUS-MS	FUS-MS	FUS-MS	FUS-MS	FUS-ICP	FUS-MS	FUS-MS	FUS-MS	FUS-MS	FUS-MS	FUS-MS	FUS-MS
WGB-1															
Published value (2σ)	*8±4*	*1.2±0.5*	0.1-1			*2±0.4*	*0.52±0.15*	*851±61*	*8.7±1.1*	14-20	2.3-2.6	*9.9±0.9*	*2.8±0.3*	*1.27±0.06*	2.5-3.5
Analysis 1	5.1	< 2	< 0.5	< 0.1	4	1.9	0.4	849	7.72	16	2.12	9.47	2.4	1.16	2.61
Analysis 2	3.8	< 2	< 0.5	< 0.1	4	1.9	0.4	831	7.74	16.2	2.16	9.48	2.63	1.2	2.75
Relative error	36-53%					5%	23%	0-2%	11%	5-6%	12-13%	4%	6-14%	6-9%	9-15%
Repeatability	15%				0%	0%	0%	1%	0%	1%	1%	0%	5%	2%	3%
TDB-1															
Published value (2σ)	11	*1.6±0.7*	0.5	0.2	*2±1*	*1±0.4*		241±13*	*17±2*	41±4*	6	*23±1*	*6±0.2*	*2.1±0.1*	7
Analysis 1	11	< 2	< 0.5	< 0.1	2	0.6	0.4	235	16.7	39.4	5.2	23.5	6.22	1.95	6.44
Analysis 2	11.7	< 2	< 0.5	< 0.1	3	0.5	0.4	235	16.2	38.6	5.1	23.5	6.04	2.02	6.34
Relative error	6%				50%	50%		2%	2-5%	4-6%	13-15%	2%	1-4%	4-7%	8-9%
Repeatability	3%				20%	9%	0%	0%	2%	1%	1%	0%	1%	2%	1%
SY-2															
Published value (2σ)	29±12	1.8±3.2	1.1±2	<0.5	5.7	0.25±0.2	2.4±0.6	460±100	75±18	175±70	18.8±3.4	73±22	16.1±2	2.42±0.66	17±3.6
Analysis	29.8	< 2	< 0.5	< 0.1	6	< 0.2	2.6	473	72.1	168	20.1	75.4	15.8	2.53	15.9
Relative error	3%						8%	3%	4%	4%	7%	3%	2%	5%	6%

Table 3.2. (continued)

Analyte Symbol	Tb	Dy	Ho	Er	Tm	Yb	Lu	Hf	Ta	W	Tl	Pb	Bi	Th	U
Unit Symbol	ppm	ppm	ppm	ppm	ppm	ppm	ppm	ppm	ppm	ppm	ppm	ppm	ppm	ppm	ppm
Detection Limit	0.01	0.01	0.01	0.01	0.005	0.01	0.002	0.1	0.01	0.5	0.05	5	0.1	0.05	0.01
Analysis Method	FUS-MS	FUS-MS	FUS-MS	FUS-MS	FUS-MS	FUS-MS	FUS-MS	FUS-MS	FUS-MS	FUS-MS	FUS-MS	FUS-MS	FUS-MS	FUS-MS	FUS-MS
WGB-1															
Published value (2σ)	*0.5±0.1*	2.5-3.5	*0.52±0.07*	1.2-1.8	0.15-0.30	*1.42±0.18*	0.20-0.36	*1.5±0.2*	0.3-1	1-3.5		4-14	0.1-2	*1±0.1*	*0.75±0.1*
Analysis 1	0.45	2.74	0.51	1.4	0.202	1.33	0.204	1.4	0.25	1.4	0.17	6	< 0.1	1.04	0.7
Analysis 2	0.49	2.9	0.57	1.55	0.212	1.39	0.218	1.4	0.39	< 0.5	0.15	8	< 0.1	1.11	0.87
Relative error	2-10%	3-9%	2-10%	3-7%	6-10%	2-6%	22-27%	7%	40-62%			11-33%		4-11%	7-16%
Repeatability	4%	3%	6%	5%	2%	2%	3%	0%	22%		6%	14%		3%	11%
TDB-1															
Published value (2σ)	*1.2±0.1*	*8±1*	*1.3±0.4*	4	*0.6±0.1*	*3.4±0.4*	*0.52±0.06*	*5±0.5*	*0.8±0.2*	0.6		17±3	0.8	2.7±0.3*	*1±0.1*
Analysis 1	1.02	6.46	1.24	3.46	0.492	3.05	0.477	4.7	0.66	0.8	< 0.05	14	< 0.1	2.68	0.91
Analysis 2	1.08	6.47	1.26	3.49	0.484	3.09	0.483	4.6	0.68	0.8	< 0.05	14	< 0.1	2.72	1.1
Relative error	10-15%	19%	3-5%	13-14%	18-19%	9-10%	7-8%	6-8%	15-18%	33%		18%		1%	9-10%
Repeatability	3%	0%	1%	0%	1%	1%	1%	1%	1%	0%		0%		1%	9%
SY-2															
Published value (2σ)	2.5±1.8	18±6	3.8±1.2	12.4±3.4	2.1±0.4	17	2.7±0.8	7.7±2.0	2.01±0.36	0.76	1.5±0.6	85±16	2±6	379±58	284±18
Analysis	2.96	20.1	4.43	14.4	2.32	17.6	3	9.1	1.43	0.8	1.14	202	< 0.1	376	283
Relative error	18%	12%	17%	16%	10%	4%	11%	18%	29%	5%	24%	138%		1%	0%

Table 3.3. Primary, secondary standards, analytical errors and repeatability for measuring Rb–Sr isotopes, Sm–Nd isotopes, and determining U–Pb model ages.

Analytical Method		ID-TIMS				MC-ICP-MS			ID-TIMS				
Standard Name		$^{87}Sr/^{86}Sr$	2 S.E.	$^{87}Rb/^{86}Sr$	%SD Error	$^{147}Sm/^{144}Nd$	$^{143}Nd/^{144}Nd$	2 S.E.	$^{207}Pb/^{206}Pb$ model age (Ma)	Error (Ma)	Isochron age (Ma)	Error (Ma)	%Disc
NBS987[a]	literature	0.710249											
	measured	0.71025	0.000017										
		0.71027	0.000015										
BHVO-2[b]	literature	0.703478					0.512979						
	measured	0.70350	0.00002	3.67	0.53								
	measured	0.70348	0.00002	3.27	0.75								
	measured					0.1503	0.512993	0.000010					
	measured					0.1502	0.513006	0.000019					
NBS984[a]	literature			0.38470									
	measured			0.38483	0.52								
JNdi[a]	literature						0.512103						
	measured						0.512086	0.000032					
IN1[b]	literature										2059.60	0.35	
	measured[c]										2057.5	1.2	
	measured[d]								2061.9	0.6			-7.58
	measured[d]								2058.1	0.7			-0.23
	measured[d]								2055.8	1.5			0.04
Primary standard analytical error[e]		0.0003-0.0029%		0.03%			0.003%						
Secondary standard analytical error[e]		0.001-0.004%					0.003-0.005%				0.10%		
Repeatability[f]		0.002%		5.7%		0.001%	0.001%		0.12%				

a. Primary standards

b. Secondary standards

c. Regression result of three U–Pb analyses

d. Individual U–Pb analysis

e. Standard analytical error $= \frac{|\text{literature value} - \text{measured value}|}{\text{literature value}} \times 100\%$

f. Repeatability $= \frac{\text{standard deviation } (\sigma) \text{ of all measured values}}{\text{mean of all measured values}} \times 100\%$

NBS987 (100 ng) was analyzed along with the samples at the beginning of each day of analysis; 200 measurements were taken at filament temperatures between 1390°C and 1400°C. Two analyses of NBS987 (100 ng) yielded mean $^{87}Sr/^{86}Sr$ ratios of 0.710265±0.000017 (2 standard errors; n=191) and 0.710277±0.000015 (2 standard errors; n=193), with associated relative errors of 0.0029% and 0.0003%, respectively, compared to the literature value of 0.710249 (Table 3.3). Isotopic ratios of Sm and Nd were measured using a Thermo Fisher Scientific Neptune Plus multi-collector inductively-coupled plasma mass spectrometer (MC-ICP-MS). Purified sample fractions were evaporated to dryness, dissolved in 9.5 mL 2% HNO_3; a greater-than-usual amount of 2% HNO_3 was necessary to dilute the Nd signal within optimal measurement range. 1 mL of the sample solution was taken for aspiration into plasma. Offline corrections were made based on measurements of the primary standard JNd1.

In addition to the primary standards analyzed on each instrument, two replicates of the Hawaiian basalt standard BHVO-2 was processed alongside each analytical batch as a secondary standard. Analytical errors and repeatability associated with both primary and secondary standards are summarized in Table 3.3.

3.3.3 Isotope dilution thermal-ionized mass spectrometry (ID-TIMS)

Uranium-lead analysis of baddeleyite follows protocols similar to those outlined in Heaman et al. (2002) and Heaman (2009). Selected baddeleyite fractions, ranging <0.5–0.9 μg, were cleaned in 4N HNO_3, then rinsed sequentially with Milli-Q water and acetone. Baddeleyite fractions were weighed prior to being transferred into TFE Teflon digestion vessels except where the grains were too small (<40 μm). A ^{205}Pb–^{235}U tracer solution was added to each sample before dissolution in a ~15:1 mixture of 48% HF and 7N HNO_3 for 48 hours at 190°C. Dissolved samples were dried down on hotplate before an additional dissolution cycle with 3.1N HCl at 190°C for 24 hours. The samples were loaded directly from dissolution vessels into anion-exchange resin columns for chromatographic purification of U and Pb, following protocols outlined in Heaman et al. (2002). Chromatography separation was omitted for baddeleyite fractions weighing <0.5 pg. For mass spectrometer analyses, sample solutions were dried down, then dissolved in a mixture of 4uL silicic acid and 0.1N H_3PO_4 before loading onto outgassed Re filaments. Uranium and lead isotopic ratios were measured on a Thermo Fisher Scientific Triton Plus MC-TIMS, using secondary electron multiplier (SEM) detector mode (Sarkar et al., 2015) at temperature ranges of 1200–

1295°C (Pb) and 1290–1350°C (U). Age calculations were carried out in Isoplot 4.15 (Ludwig, 2003), using decay constants of 1.55125×10^{-10} yr^{-1} (^{238}U) and 9.8485×10^{-10} yr^{-1} (^{235}U) , and a $^{238}U/^{235}U$ ratio of 137.88.

Three fractions from the Phalaborwa baddeleyite standard IN1 were analyzed alongside the unknowns to ensure analytical accuracy. Analyses of standard IN1 are presented in Table 3.4 and Figure 3.2. The three fractions yielded $^{207}Pb/^{206}Pb$ ages of 2061.9±1.2 Ma, 2058.1±1.3 Ma, and 2055.8±3.0 Ma (1σ), with a weighted mean of 2059.9±6.7 Ma (2σ). These compare well with the literature value of 2059.60±0.35 Ma (2σ; Heaman, 2009). The three analyses are between 0.04% and -7.58% discordant, with fraction #1 being reversely discordant outside the analytical errors; the reverse discordance is most likely due to incomplete dissolution of baddeleyite fragments.

3.3.4 Detrital zircon dating

Uranium–lead isotopic analysis of detrital zircons was conducted using laser-ablation multi-collector inductively-coupled plasma mass spectrometry (LA-MC-ICPMS) following procedures modified from Simonetti et al. (2005). The instrument setup consisted of a New Wave UP-213 laser ablation system interfaced with a Nu plasma 1 MC-ICPMS. The laser was operated at 4 Hz with a beam diameter of 30 μm. Each spot analysis represents the average of 60 1-second readings. Zircon reference material LH94-15 (Ashton et al., 1999) was analyzed between sets of 10 unknown analyses in order to monitor and correct for U–Pb fractionation, reproducibility, and instrument drift. Zircon standard OG1 (Stern et al., 2009) was analyzed as a blind standard between every ten analyses (Table 3.5). Analysis of OG1 during analytical session of sample LH15-EA51 yielded seven analysis with a weighted mean $^{207}Pb/^{206}Pb$ age of 3465.4±6.3 Ma (2σ; MSWD=0.68), identical with the reported ID-TIMS age of 3465.4±0.6 Ma (Stern et al., 2009). Analysis of OG1 during analytical session of sample LH15-EA15 yielded nine out of ten analysis with a weighted mean $^{207}Pb/^{206}Pb$ age of 3462.2±5.1 Ma (2σ; MSWD=1.03), also identical with the reported ID-TIMS age for OG1.

All data were reduced offline using an Excel-based program, where unknowns were normalized to the in-house zircon standard LH94-15. Data were not corrected for common Pb due to the difficulty in resolving transient isobaric contributions of ^{204}Hg present in the Ar gas from ^{204}Pb present in either the crystal and/or the blank. For sample LH15-EA51, the effect of common Pb correction is negligible due to low measurements of ^{204}Pb overall (10–129 cps). However, some

Table 3.4. TIMS U–Pb analysis of baddeleyite standard IN1. Associated errors are given in 1σ.

Fraction	Weight (µg)	U (ppm)	Th (ppm)	Pb (ppm)	Th/U	TCPb (pg)	$^{206}Pb/^{204}Pb$	$^{206}Pb/^{238}U$	$^{207}Pb/^{235}U$	$^{207}Pb/^{206}Pb$	$^{206}Pb/^{238}U$	$^{207}Pb/^{235}U$	$^{207}Pb/^{206}Pb$	%Disc
1 (4)	40.3	556	7	219	0.01	2.7	213456	0.4055 ± 5	7.121 ± 10	0.12737 ± 4	2194.4 ± 2.4	2126.7 ± 1.3	2061.9 ± 0.6	-7.6
2 (2)	2.4	669	9	246	0.01	2.4	15861	0.3770 ± 5	6.606 ± 10	0.12709 ± 5	2062.2 ± 2.4	2060.1 ± 1.3	2058.1 ± 0.7	-0.2
3 (2)	4.6	429	3	157	0.01	3.1	15185	0.3755 ± 5	6.571 ± 11	0.12692 ± 11	2055.1 ± 2.3	2055.4 ± 1.5	2055.8 ± 1.5	0.04

All atomic ratios are corrected for spike (composition), estimated blank (0.5 pg U, 1.0 pg Pb), and initial common lead (Stacey and Kramers, 1975).
Number in parentheses refers to the number of baddeleyite grains analysed; TCPb refers to total common Pb present in the analysis.
Age calculations based on decay constants of Jaffey et al. (1971); $^{206}Pb/^{238}U$ and $^{207}Pb/^{206}Pb$ ages corrected for initial disequilibrium in $^{230}Th/^{238}U$ using a Th/U (magma) ratio of 3.
Model Th/U ratio estimated from radiogenic $^{208}Pb/^{206}Pb$ ratio and $^{207}Pb/^{235}U$ age.

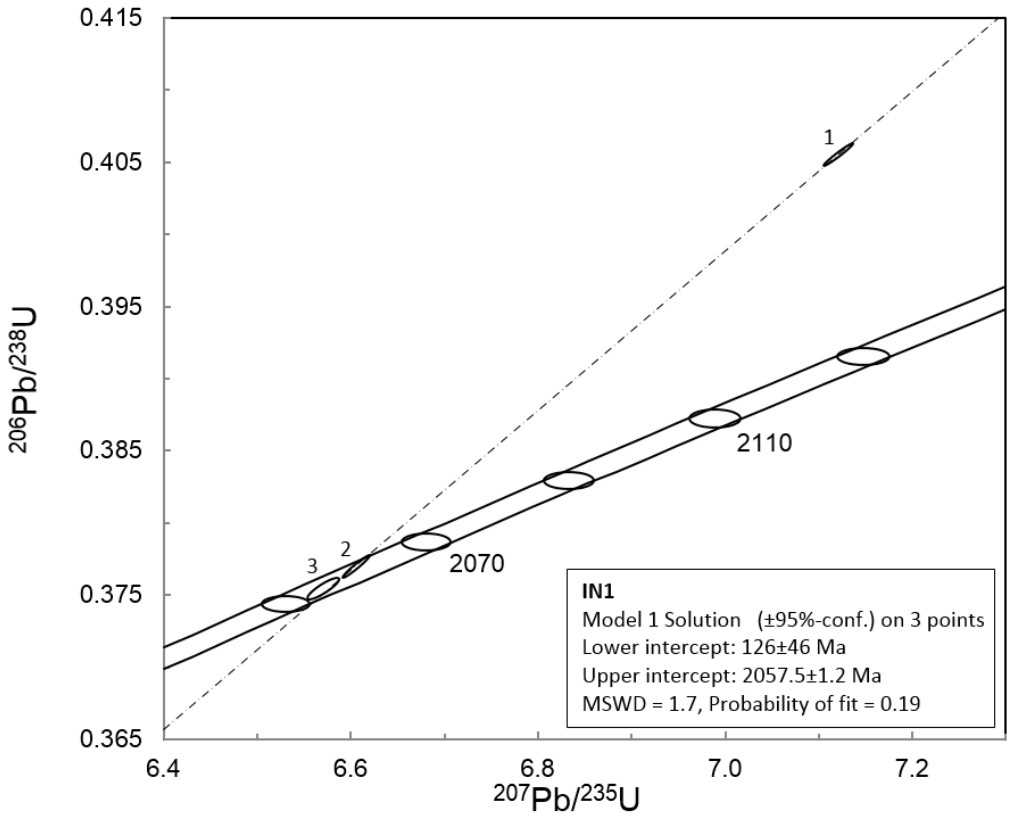

Figure 3.2. Concordia plot of U–Pb results for baddeleyite standard IN1.

Table 3.5. U–Pb LA-ICPMS results of secondary zircon standard OG1 analyzed during the analytical session of a) sample LH15-EA51 and b) sample LH15-EA15. Analysis that does not agree with the literature $^{207}Pb/^{206}Pb$ value of 3465.4±0.6 Ma (Stern et al., 2009) is struck out.

a.

	Apparent Ages (Ma)						
Spot name	$^{207}Pb/^{206}Pb$	2 σ	$^{207}Pb/^{235}U$	2 σ	$^{206}Pb/^{238}U$	2 σ	Disc (%)
OG1-1	3473	16	3452	46	3415	124	2.2
OG1-2	3468	16	3465	52	3460	141	0.3
OG1-3	3472	16	3476	41	3485	110	-0.5
OG1-4	3461	16	3459	44	3455	118	0.2
OG1-5	3457	16	3451	45	3440	120	0.7
OG1-6	3461	16	3476	44	3503	119	-1.6
OG1-7	3458	16	3414	39	3340	100	4.4

b.

	Apparent Ages (Ma)						
Spot name	$^{207}Pb/^{206}Pb$	2 σ	$^{207}Pb/^{235}U$	2 σ	$^{206}Pb/^{238}U$	2 σ	Disc (%)
OG1-1	3461	16	3450	36	3431	96	1.1
OG1-2	3462	15	3455	46	3445	125	0.6
OG1-3	3466	16	3461	37	3453	97	0.5
~~OG1-4~~	~~3444~~	~~16~~	~~3411~~	~~39~~	~~3356~~	~~103~~	~~3.3~~
OG1-5	3455	16	3463	49	3477	132	-0.8
OG1-6	3477	15	3480	44	3484	119	-0.2
OG1-7	3466	15	3452	50	3427	134	1.5
OG1-8	3451	16	3295	44	3044	107	14.8
OG1-9	3465	16	3465	53	3465	143	0.0
OG1-10	3454	17	3455	39	3456	104	0.0

grains in sample LH15-EA15 have high measured ^{204}Pb (maximum 2757 cps), indicating high common Pb content. To avoid erroneous $^{207}Pb/^{206}Pb$ zircon ages resulting from high common Pb content, we exclude from discussion those grains from sample LH15-EA15 with ^{204}Pb greater than 1000 cps.

3.4 Petrography of the Union Island Group mafic igneous rocks

A total of 69 petrographic thin sections were made for the purpose of determining the lithology, mineralogy and textures of Union Island Group igneous and sedimentary rocks. Due to the altered nature of the mafic igneous rocks, eight samples (LH14-14, LH14-33, LH14-27, LH15-EA11, LH15-EA12, UI68D, UI79B, and LH15-EA23) were analyzed using X-ray powder diffraction (XRD) to confirm the mineral assemblages observed in thin sections. Mineralogical characteristics of each studied unit are outlined below.

3.4.1 Lower basalt

The lower basalt unit is divided into two distinct textural groups. Group A contains fine-grained (<1 mm), sericitized plagioclase in matrix that has been entirely altered to chlorite and dolomite (Fig. 3.3a). Large (up to 10 mm), altered plagioclase and clinopyroxene antecrysts are observed in sample LH15-EA12 (Fig. 3.3b). Group B consists of plagioclase and clinopyroxene phenocrysts in glomeroporphyritic to intergranular textures (Fig. 3.3c). Larger clinopyroxene crystals locally develop subophitic texture around plagioclase laths. In all samples, plagioclase is commonly skeletal and variably sericitized. Clinopyroxene show patchy to complete alteration to feathery chlorite. Titanium-bearing oxide phases, up to 9 modal percent, include finely acicular ilmenite and sawtooth-like or skeletal Ti-magnetite with ilmenite exsolution lamellae (Fig. 3.3d). In some cases, oxide minerals show euhedral titanite overgrowths. The devitrified groundmass commonly contains epidote, with patches of fine chlorite and carbonate minerals throughout. Some samples contain veins and amygdules that are filled with chlorite, dolomite, and quartz. Olivine, although identified by XRD, is not observed in any of the thin sections. Accessory minerals include zircon (Fig. 3.3e), rutile, and apatite.

3.4.2 Upper basalt

Most of the upper basalt samples show fine-grained textures (<1 mm) similar to the second textural group of the lower basalt, although clinopyroxene is present. Samples from the centre of pillowed

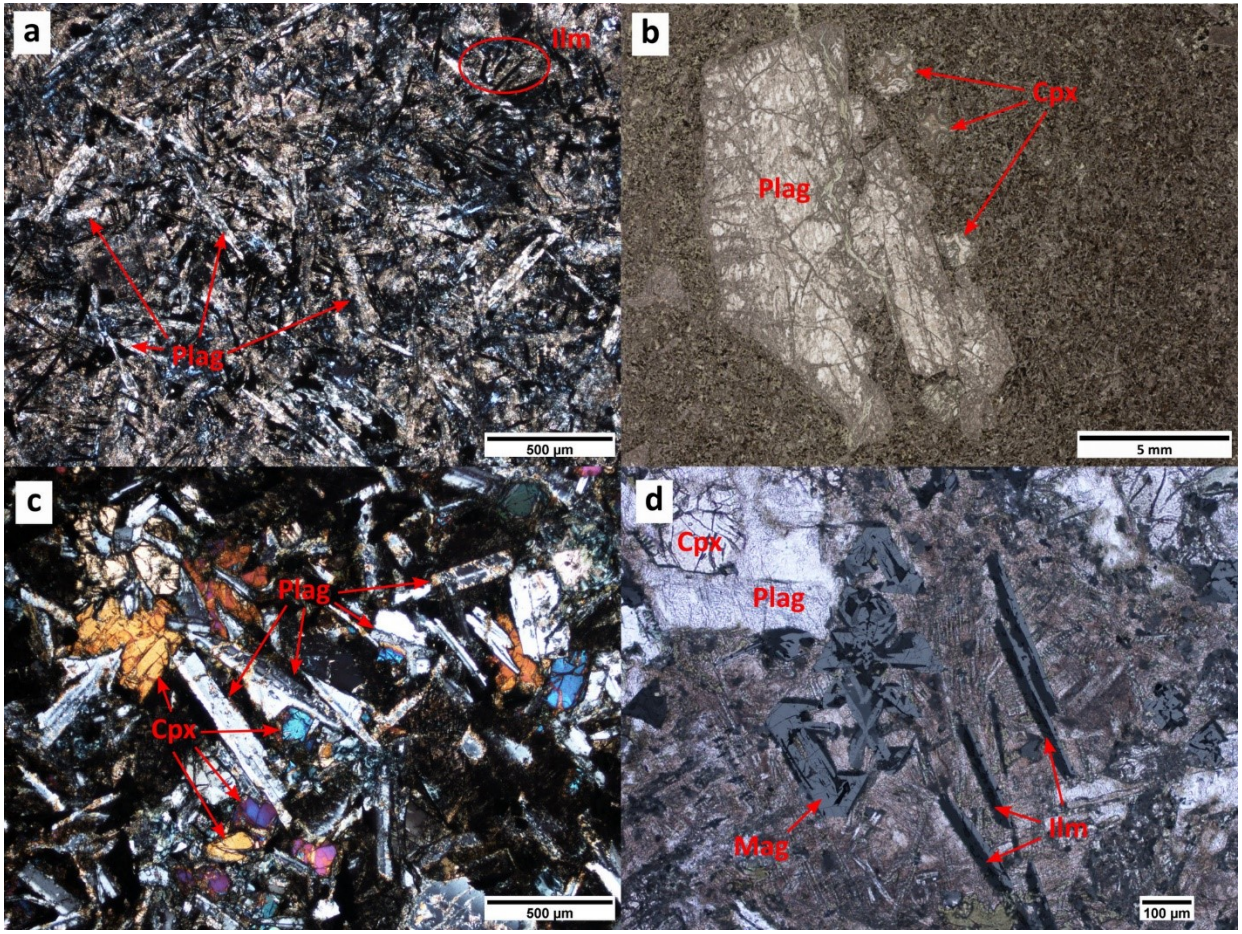

Figure 3.3. Photomicrographs of Union Island Group mafic units. a) Lower basalt unit (LH15-EA07b); fine-grained texture typical of type A lava flows; metal oxides are dominated by acicular ilmenite; cross-polarized light. b) Lower basalt unit (LH15-EA12); large plagioclase and clinopyroxene antecrysts in type A flow; plagioclase is strongly sericitized and equant clinopyroxene is replaced by concentric growths of chlorite and dolomite, plane-polarized light. c) Lower basalt unit (LH15-EA08); glomeroporphyritic texture in type B lava flows; cross-polarized light. d) Lower basalt unit (LH15-EA13); skeletal magnetite with darker-coloured lamellae of exsolved ilmenite; laths of ilmenite-magnetite on right; plane-polarized light with reflected light.

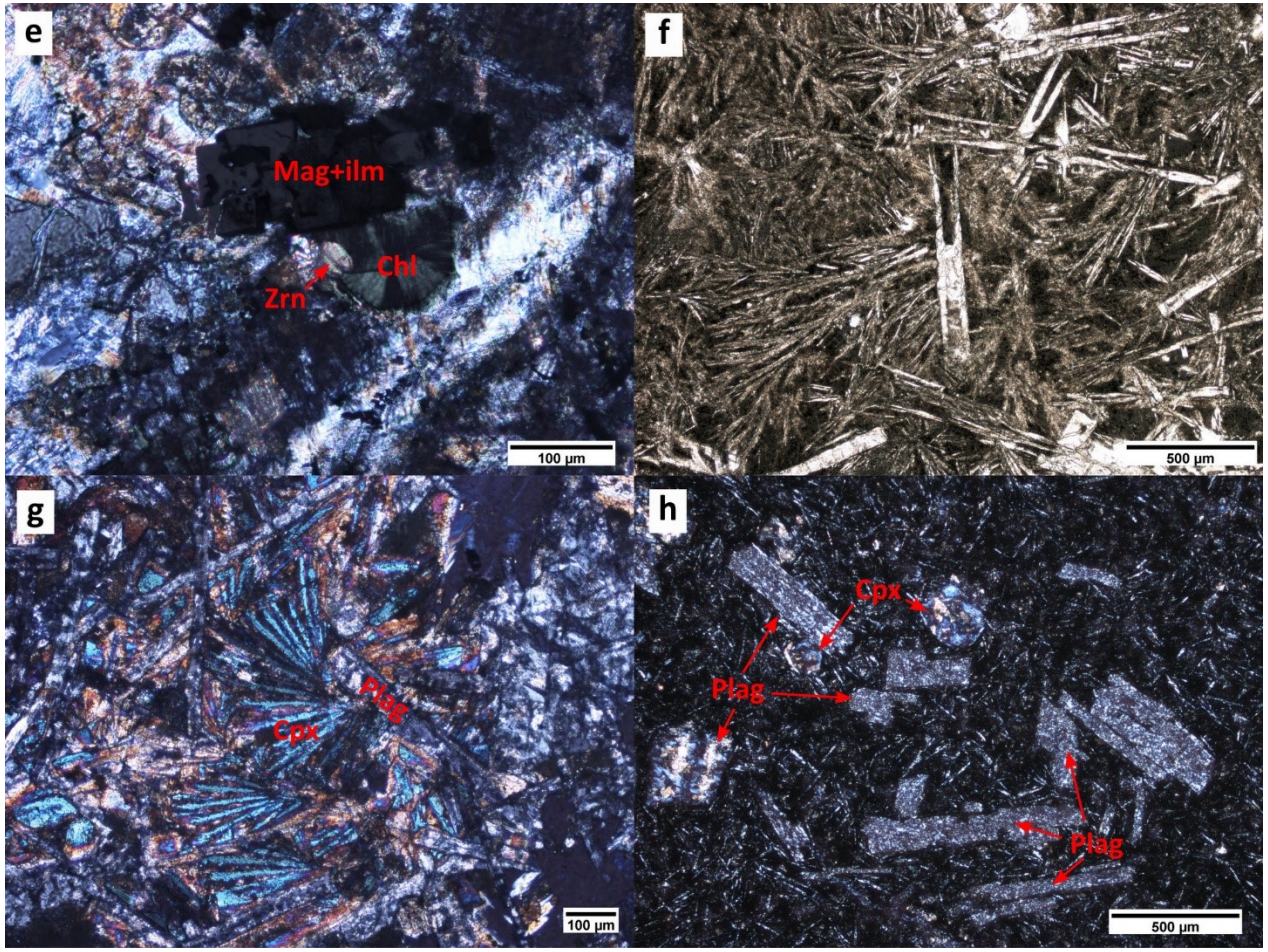

Figure 3.3. (continued) Photomicrographs of Union Island Group mafic units. e) Lower basalt unit (LH15-EA13); zircon in chloritized glass; cross-polarized light. f) Upper basalt unit (UI39); quenched texture in pillow flows, shown by swallow-tail habit of plagioclase, with a secondary population showing radiating, acicular growth; plane-polarized light. g) Upper basalt unit (LH14-33); quenched texture in pillowed flow shown by radiating growth of acicular clinopyroxene from plagioclase faces; cross-polarized light. h) Upper basalt unit (UI35A); porphyritic flow with plagioclase and clinopyroxene phenocrysts; plagioclase is entirely replaced by sericite and quartz, and clinopyroxene by chlorite and dolomite; cross-polarized light.

flows show a quenched texture with radial and dendritic clusters of fine plagioclase (Fig. 3.3f) and clinopyroxene (Fig. 3.3g). Rounded to lath-like clinopyroxene are extensively chloritized. Veins and amygdules are filled with fine chlorite and coarse dolomite. One specimen (UI35A) exhibits a distinct porphyritic texture (Fig. 3.3h), in which euhedral plagioclase and clinopyroxene phenocrysts have been extensively replaced by sericite, chlorite, and quartz; the glassy matrix is devitrified.

3.4.3 Diabase sill and dykes

The diabase intrusions exhibit ophitic to subophitic textures (Fig. 3.3i). Euhedral olivine has been completely replaced by fine chlorite. Plagioclase, extensively sericitized, is moderately sodic ($An_{35–45}$) and is altered to albite and epidote. Flow orientation of plagioclase is observed in one sill sample (LH14-14). Titanaugite, sometimes displaying compositional zoning, is altered to fine chlorite and epidote, and displays alteration rims of green actinolite and brown amphibole (Fig. 3.3j). Secondary amphibole also occurs as minor euhedral crystals where clinopyroxene has been completely replaced by chlorite and actinolite (Fig. 3.3k). Resorbed Ti-magnetite contains ilmenite exsolution lamellae (Fig. 3.3l) and breaks down further to yield euhedral or fine titanite overgrowth. Trace biotite occurs as alteration product of chlorite. Accessory minerals include apatite, zircon, baddeleyite, allanite, and pyrite.

In all diabase samples screened under SE and BSE imaging, baddeleyite occurs as 10–100 μm, brown to dark brown blades embedded in a chloritized glass (Figs 3.4, 3.5a). Larger crystals tend to be isolated crystals, whereas smaller crystals form clusters. Most blades are fractured such that the largest intact pieces of baddeleyite are usually ~40 μm in length. In BSE imagery, almost all baddeleyite crystals display metamorphic zircon overgrowth. Zircon overgrowths occur as irregularly-shaped rims enclosing baddeleyite fragments that have been broken down (Fig. 3.5b). Some zircon overgrowth also occurs as small, subhedral grains extending away from the baddeleyites (Fig. 3.5c), or as anhedral infill in fractured baddeleyite crystals. In some cases entire laths of baddeleyite have been replaced by polycrystalline zircon aggregates (Fig. 3.5d). These latter types of zircon overgrowth indicate crystallization during metamorphism (Heaman and LeCheminant, 1993).

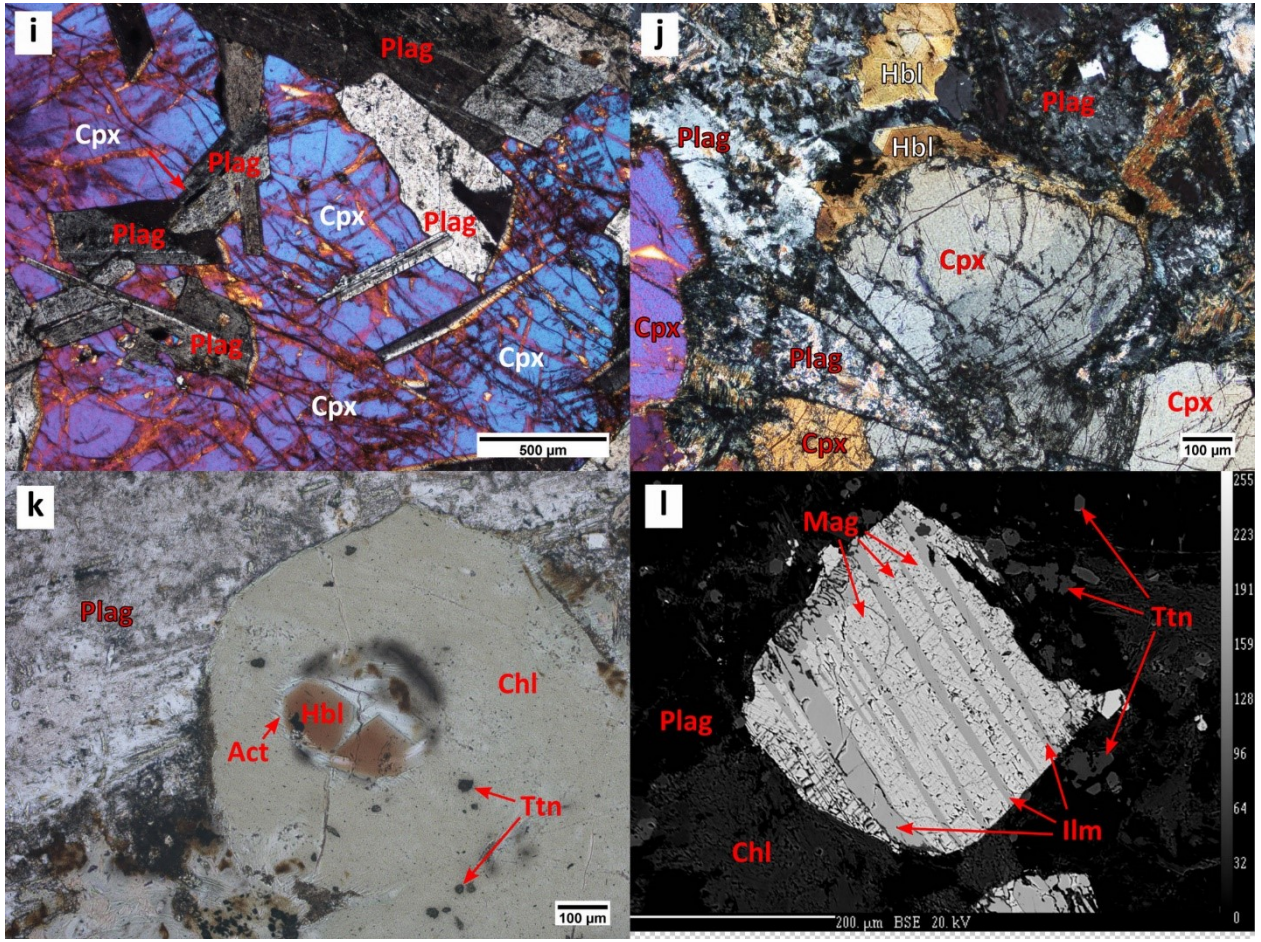

Figure 3.3. (continued) Photomicrographs of Union Island Group mafic units. i) Diabase sill (UI82); ophitic texture typical in both mainland sills; cross-polarized light. j) Diabase dyke (LH14-07B); marginal alteration of clinopyroxene to pleochroic hornblende; cross-polarized light. k) Diabase sill (UI102A); euhedral hornblende with green actinolite alteration rim at the core of chloritized clinopyroxene; plane-polarized light. l) Diabase intrusion (LH14-25); resorbed Ti-magnetite (light grey) with ilmenite exsolution lamellae (medium grey); euhedral titanite (dark grey) formed from breakdown of the magnetite; microprobe back-scattered electron image.

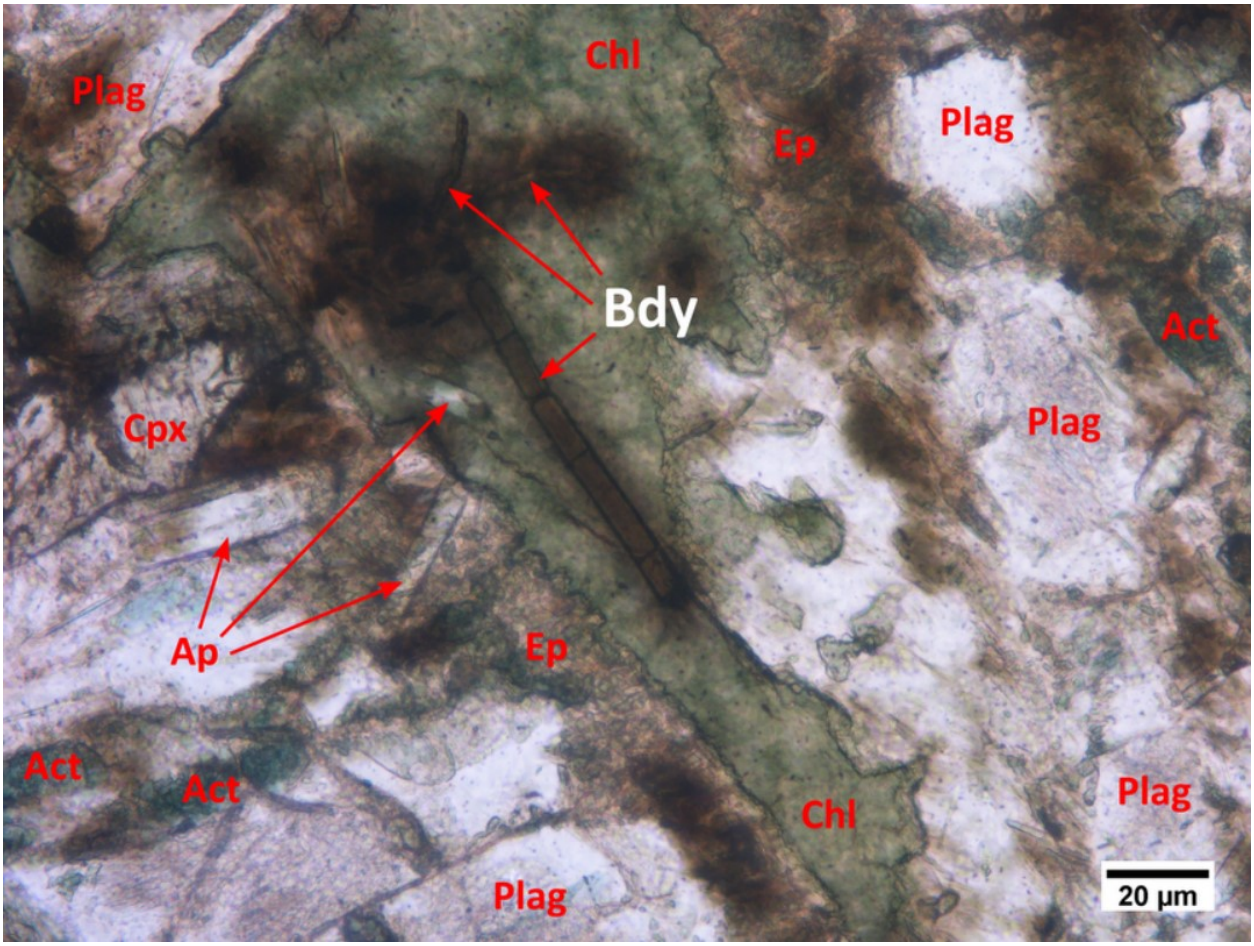

Figure 3.4. Fractured baddeleyite blades in chloritized interstitial glass between altered plagioclase and clinopyroxene. Unfractured length of the blade in centre is ~80 µm. Sample LH14-27. Plane-polarized light.

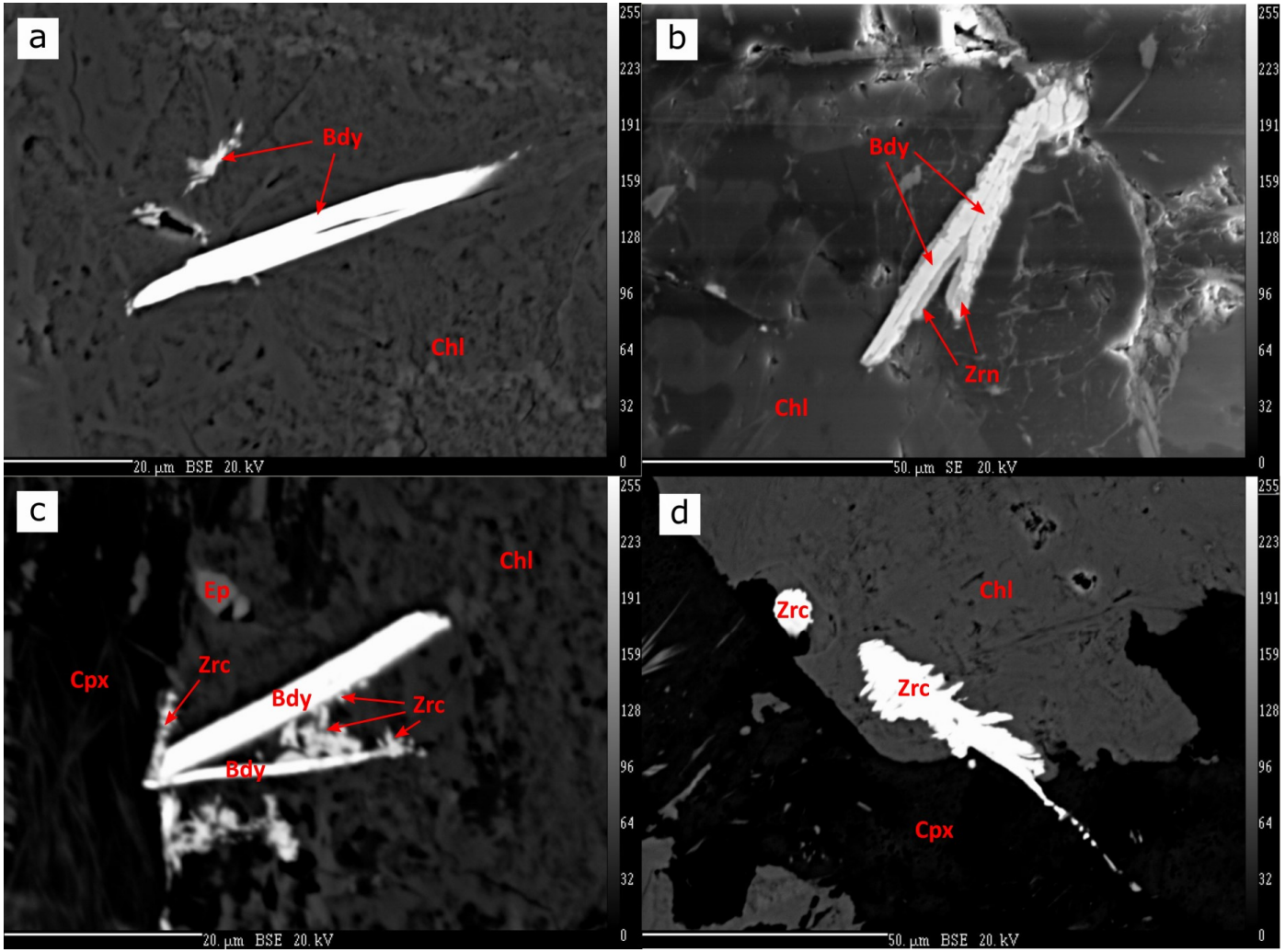

Figure 3.5. Electron microprobe imagery of baddeleyite morphology in Union Island Group diabase intrusions. a) Pristine baddeleyite blade (centre) with almost no zircon overgrowth (sample LH14-27); back-scattered electron image. b) Baddeleyites with metamorphic zircon overgrowth rims (sample LH14-25); secondary electron image. c) Baddeleyites with fine metamorphic zircon overgrowth (sample LH14-27); back-scattered electron image. d) Baddeleyites that have been entirely replaced by metamorphic zircon overgrowth (sample UI102A); back-scattered electron image.

3.4.4 Hand sample characterization of geochronology samples

Diabase intrusion LH14-27

Sample LH14-27 was collected from a diabase body which intrudes a thinly bedded volcaniclastic sequence on Tuff Island. We interpret these tuffs and interflow sediments at this location to belong to the lower basalt unit based on similar occurrences reported in the mainland area and that tuff sequences are absent from the upper basalt unit (Thorstad, 1976).

The sample is black-coloured in fresh surfaces and weathers dark green. White plagioclase laths, ranging 2–3 mm in length, are visible on the sample surface (Fig. 2.4p). Petrographically, the sample has a crystallization order of plagioclase>clinopyroxene>metal oxides. Olivine or pseudomorphs suggesting primary olivine are absent. Plagioclase, which dominates the samples at 60 modal percent, ranges from lath-shaped to tabular and is >80% sericitized and extensively fractured. Titanaugite (10–15 modal %) is ~1 cm large and shows ophitic texture with plagioclase. The clinopyroxene has been extensively altered to a chlorite+epidote±amphibole assemblage (~30 modal %). Secondary actinolite-amphibole produced by clinopyroxene breakdown occurs as ~0.3 mm idioblastic clusters mantled by a fine chlorite matrix, and are highly pleochroic. Metal oxides (5 modal %) occur mostly as skeletal, 0.5–1.0 mm Ti-bearing magnetite with exsolution lamellae of ilmenite. Resorbed boundaries are common. Titanite occurs as small euhedral crystals or blobs of fine-grained masses from the breakdown of the oxides. Accessory minerals include apatite, baddeleyite, and pyrite.

Baddeleyite occurs mostly in chloritized interstitial glass. Brown to dark-brown blade-shaped crystals, ranging 15–50 μm in length, occur individually or in clusters (Figs 3.5a, c). Blades are often fractured, with only minor metamorphic zircon overgrowth observed on the smaller blades (<20 μm).

Interflow sediment LH15-EA51

Sample LH15-EA51 (Fig. 2.4h) is a dark, 3-cm-thick interflow sediment layer collected from a thinly bedded tuff sequence on Tuff Island (Fig. 3.1). Bedding of the sediments are normally graded, with the largest clast size being ~1 mm and fining upwards into siltstone. The sediment clasts are angular to subangular, and consist of quartz, feldspar, fragments of tuff, basalt, and dolomite, plus trace biotite.

Quartz pebble conglomerate LH15-EA15

Sample LH15-EA15 (Fig. 3.6) was collected from a layer of quartz pebble conglomerate at the base of the upper dolomite unit in the mainland area (sample location is shown in Fig. 3.1). The contact between the upper dolomite and the underlying lower basalt is recessive at this location, such that the nature of the contact could not be determined. A separate occurrence of quartz pebble conglomerate grading upwards into quartzite was reported by Thorstad (1976) and was interpreted as a local channel fill.

The sample is clast-supported and consists of moderately sorted, rounded to sub-rounded clasts of predominantly white quartz (~95%) and minor dolomite and basalt (Fig. 3.6b). Quartz clasts range from 0.5–3 cm in diameter, while smaller grains are closely packed in the dolomitic matrix. All quartz grains display fractures and the sample shows some micro-faulting. Basaltic clasts are small (0.3–0.7 mm) and contain white plagioclase flecks (< 0.5 mm).

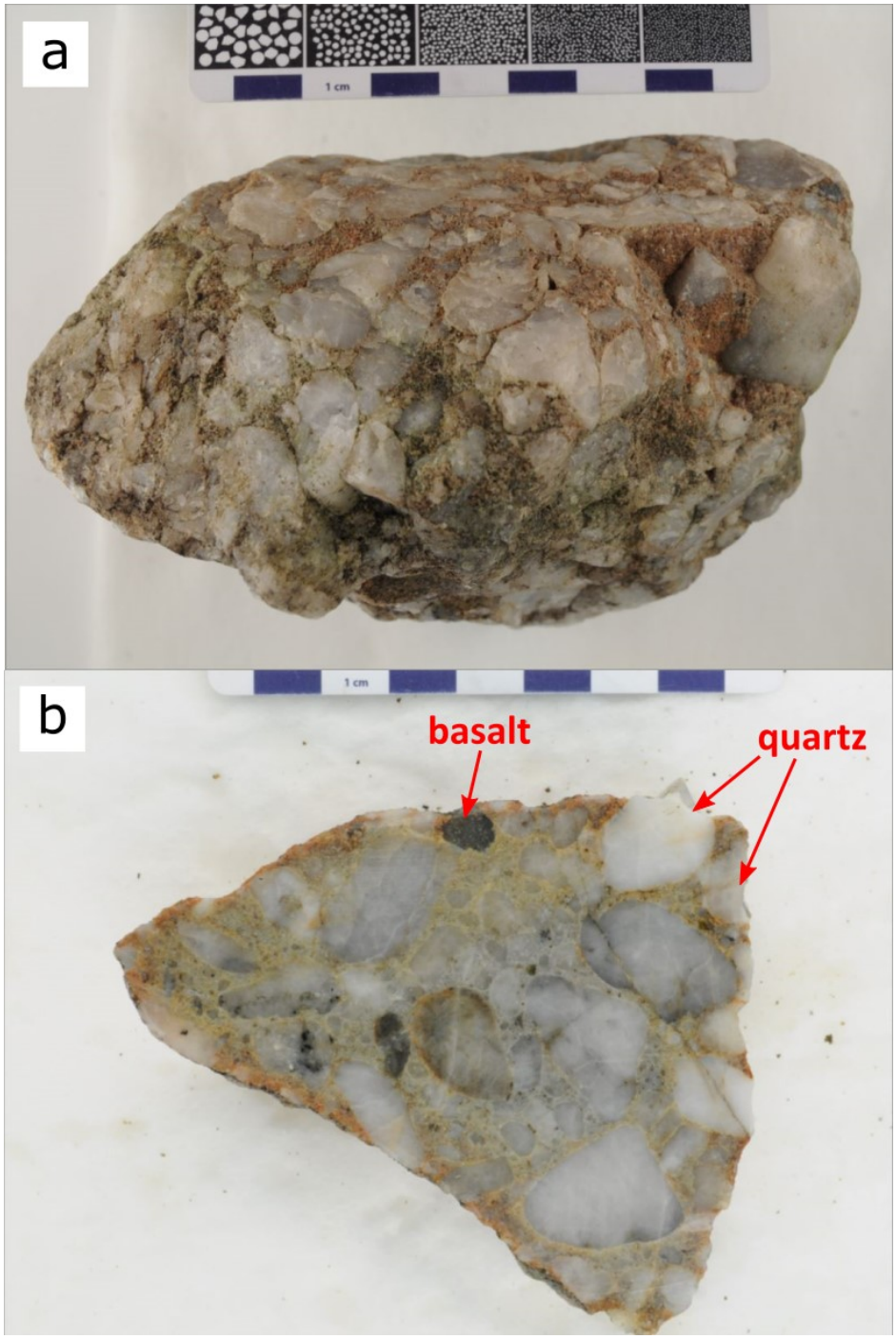

Figure 3.6. Photographs of quartz pebble conglomerate sample LH15-EA15. a) Coarse quartz clasts with orange-weathering dolomitic cement. b) Poorly-sorted quartz clasts and occasional small basalt clasts that show white plagioclase flecks.

4 RESULTS

4.1 Geochemistry

Major, minor, and trace element abundances are reported in Table 4.1. In both field observations and in petrographic thin sections, mafic rocks of the Union Island Group show signs of lower greenschist-facies metamorphism, deformation, and hydrothermal alteration. It is therefore necessary, prior to any meaningful discussion of geochemical data, to evaluate how much post-magmatic processes have influenced the chemistry of the rocks with respect to their original composition.

The loss-on-ignition content (LOI) measures the amount of volatile phases and is more appropriate than the chemical index of alteration (CIA) as a proxy for the degree of chemical alteration in the case of the Union Island Group mafic rocks, where hydrous minerals such as amphibole, chlorite, and serpentine make up the alteration products. Overall, the Union Island Group mafic rocks have LOI values ranging 2–12%. We evaluate the mobility of select elements during chemical alteration with bivariate plots illustrating the pattern of these elements versus LOI contents (Fig. 4.1). Alkali elements such as K_2O and large ion lithophile elements (LILE) such as Rb, Sr, and Ba can be easily mobilized during hydrothermal alteration and metamorphism. These elements show negative correlation with LOI, suggesting that they were mobile post-eruption and have been removed from the rocks. This may be due to interaction between basaltic glass and seawater (Menzies and Seyfried, 1979) and/or post-depositional folding and faulting of the Union Island Group strata (Thorstad, 1974). In contrast, high field strength elements (HFSE; represented here by Nb and TiO_2) and rare earth elements (REE; represented here by La and Sm/Yb ratio) display trends independent of LOI, suggesting that these elements have remained relatively undisturbed during chemical alteration and therefore are more likely to reflect the original magma composition. Other major alkali elements (Na_2O, CaO), which are fluid-mobile, show weak to no correlation with LOI.

Mafic igneous rocks of the Union Island Group are classified on the Zr/Ti versus Nb/Y plot (Fig. 4.2; Pearce, 1996). This classification scheme is more robust for altered Precambrian rocks as it employs only incompatible elements which are less fluid-mobile relative to silica and alkali contents. The lower basalt unit and the diabase intrusions plot as a coherent, approximately linear array, which falls mostly within the alkali basalt field ($Nb/Y > 0.8$; n=34) and partly crosses into

Table 4.1. Whole-rock geochemistry data of Union Island Group mafic units. Analytical methods are described in chapter 3.

	Analyte	SiO_2	Al_2O_3	$Fe_2O_{3(T)}$	MnO	MgO	Mg#*	CaO	Na_2O	K_2O	TiO_2	P_2O_5
	Method	FUS-ICP	FUS-ICP	FUS-ICP	FUS-ICP	FUS-ICP		FUS-ICP	FUS-ICP	FUS-ICP	FUS-ICP	FUS-ICP
UNIT/Sample Number	Unit	%	%	%	%	%		%	%	%	%	%
DIABASE INTRUSIONS												
LH14-14		46.00	14.52	14.11	0.22	8.25	54	6.86	2.46	1.58	1.58	0.18
LH14-25		47.95	13.39	17.45	0.20	4.09	32	5.87	2.89	1.55	3.57	0.46
LH14-27		44.54	14.47	17.83	0.26	5.13	36	5.89	2.25	2.38	3.52	0.38
UI16B		45.05	14.74	14.97	0.18	6.62	47	6.97	1.93	1.10	2.40	0.27
UI59A		48.74	13.73	14.90	0.20	5.80	44	6.61	2.48	1.23	2.80	0.37
UI63		46.97	15.12	12.61	0.19	8.21	56	7.47	2.07	2.17	1.83	0.18
UI82		47.83	13.25	15.96	0.25	5.19	39	7.15	4.01	0.27	2.64	0.32
UI95I		47.65	14.71	14.05	0.18	6.38	47	6.25	3.58	0.96	2.30	0.28
UI102B		46.71	14.66	14.88	0.19	6.48	46	6.46	3.33	1.21	2.38	0.31
UI102C		47.06	11.50	16.71	0.23	4.36	34	8.63	2.77	1.26	4.47	0.30
UI106		48.46	12.55	15.52	0.20	4.85	38	8.20	2.06	0.88	3.53	0.44
LH15- EA01-2		47.70	14.69	14.13	0.21	5.44	43	8.16	3.26	1.15	3.04	0.30
LH15- EA02		47.22	13.85	15.90	0.21	4.68	37	7.59	2.53	1.62	3.21	0.40
LH15- EA04		47.32	15.53	14.63	0.17	4.44	38	7.45	2.76	0.93	2.78	0.34
LH15- EA58		45.31	14.70	17.21	0.26	4.40	34	4.75	2.32	2.09	3.52	0.38
LH14-07B		47.87	13.72	14.57	0.28	6.04	45	9.37	2.38	1.16	2.21	0.25
LH14-22A		44.71	14.16	13.73	0.09	9.47	58	3.04	1.75	0.37	2.99	0.37
LH14-22B		44.95	13.55	16.93	0.22	5.87	41	5.86	1.95	1.79	2.71	0.32
LH14-16		41.73	14.81	11.04	0.18	5.99	52	6.54	1.09	3.63	2.78	0.34
LOWER BASALT												
UI68A		42.95	13.44	16.47	0.17	4.40	35	6.98	0.87	1.36	2.64	0.37
UI68D		44.44	12.51	12.10	0.13	3.52	37	9.98	1.00	1.53	2.17	0.26
UI79B		46.92	13.73	12.10	0.15	4.40	42	5.87	3.67	0.87	3.30	0.54
UI89E		46.74	14.24	13.61	0.17	5.37	44	4.90	3.54	0.32	2.55	0.34
UI95A		51.31	13.02	15.40	0.24	3.77	33	4.91	2.57	0.99	3.02	0.44
UI95D		48.46	12.83	10.77	0.16	4.37	45	6.30	3.37	0.71	2.59	0.39
UI128A		47.05	12.87	13.96	0.15	3.19	31	9.44	2.92	0.66	2.50	0.37
UI147		58.12	12.91	12.13	0.11	3.32	35	1.55	3.90	0.33	3.11	0.50
LH15- EA06		44.89	13.13	14.02	0.13	4.53	39	8.35	2.67	0.38	3.10	0.45
LH15- EA07B		39.58	13.63	16.17	0.22	4.42	35	8.72	3.23	0.33	3.01	0.41
LH15- EA08		48.58	13.68	14.06	0.33	4.40	38	8.22	2.43	2.16	2.47	0.32
LH15- EA09		49.02	13.71	14.76	0.25	4.89	40	8.27	2.37	2.08	2.41	0.31
LH15- EA10		51.49	14.22	11.55	0.20	4.77	45	5.63	2.31	0.84	2.63	0.34
LH15- EA11		40.84	13.74	13.12	0.18	4.20	39	9.65	3.67	0.27	3.05	0.41
LH15- EA12		42.60	14.95	17.00	0.13	5.61	40	5.62	2.40	0.91	3.43	0.46
LH15- EA13		49.17	13.75	15.08	0.24	4.65	38	6.50	2.40	2.02	2.49	0.33
LH15- EA14		49.84	13.60	14.35	0.23	4.48	38	7.40	2.15	2.49	2.56	0.33
LH15- EA16		45.72	13.76	14.45	0.18	5.28	42	7.03	3.55	0.50	2.43	0.29
LH15- EA17		47.55	13.83	13.78	0.21	5.06	42	7.51	3.93	0.48	2.43	0.29
LH15- EA18		41.10	14.03	13.84	0.26	3.69	35	10.33	3.19	1.20	3.17	0.43
LH15- EA19		48.41	14.40	15.67	0.16	4.07	34	2.19	2.60	2.22	3.33	0.44
LH15- EA20		48.87	12.88	14.66	0.17	3.54	32	5.52	2.83	0.78	2.93	0.38
LH15- EA21		53.06	10.62	13.61	0.18	4.87	41	4.12	1.76	1.07	3.03	0.34
LH15- EA22		47.06	14.38	13.65	0.13	5.62	45	4.96	1.72	2.29	2.91	0.38
LH15- EA23		46.47	13.05	15.65	0.21	4.91	38	3.85	3.39	0.80	2.96	0.44
UPPER BASALT												
LH14-32		47.00	15.99	11.27	0.17	7.15	56	8.37	2.19	2.26	1.71	0.14
LH14-33		45.73	15.35	12.16	0.16	7.68	56	8.84	2.88	0.99	1.69	0.14
LH14-34		48.22	15.60	9.87	0.14	6.67	57	8.16	3.91	0.35	1.68	0.13
LH14-36		46.01	15.52	10.69	0.14	5.52	51	7.23	4.86	0.40	1.62	0.13
UI39		46.43	15.49	12.65	0.19	5.71	47	9.06	3.30	1.03	1.68	0.15
UI35A		41.86	16.47	24.63	0.13	6.49	34	0.71	0.04	0.79	1.70	0.14
Detection Limit		0.01	0.01	0.01	0.001	0.01		0.01	0.01	0.01	0.001	0.01

*Mg# is calculated from $Mg^{2+}/(Mg^{2+}+Fe^{2+})\times100$ on a molar basis, and where Fe^{2+} is assumed to represent all Fe present in $Fe_2O_{3(T)}$ analysis.

Table 4.1. (continued)

UNIT/Sample Number	LOI FUS-ICP %	Total FUS-ICP %	Sc FUS-ICP ppm	Be FUS-ICP ppm	V FUS-ICP ppm	Cr FUS-MS ppm	Co FUS-MS ppm	Ni FUS-MS ppm	Cu FUS-MS ppm	Zn FUS-MS ppm	Ga FUS-MS ppm	Ge FUS-MS ppm
DIABASE INTRUSIONS												
LH14-14	3.44	99.23	22	1	214	240	75	130	70	230	21	1.9
LH14-25	3.37	100.80	31	3	397	100	51	120	210	200	26	1.4
LH14-27	2.42	99.08	26	2	565	80	83	130	190	160	27	1.6
UI16B	5.38	99.61	31	2	303	60	60	60	120	70	24	2.0
UI59A	3.59	100.40	26	2	294	80	67	80	90	100	23	1.4
UI63	3.51	100.30	26	1	245	120	75	190	20	120	20	1.4
UI82	2.86	99.74	36	2	334	130	52	40	120	70	21	1.6
UI95I	3.75	100.10	29	2	291	60	61	90	90	80	22	1.6
UI102B	3.63	100.20	20	1	235	70	67	120	90	150	21	1.3
UI102C	2.30	99.60	41	2	470	20	55	< 20	120	150	24	1.8
UI106	3.24	99.93	31	2	357	60	68	30	100	160	25	1.9
LH15- EA01-2	2.60	100.70	31	2	342	180	57	100	100	130	23	1.6
LH15- EA02	1.99	99.20	29	2	323	90	56	70	110	160	24	1.6
LH15- EA04	3.65	99.99	26	2	288	90	71	120	80	150	24	1.5
LH15- EA58	4.15	99.10	26	3	499	70	57	110	70	160	26	1.6
LH14-07B	2.08	99.91	36	2	342	70	55	90	180	220	21	1.6
LH14-22A	8.07	98.75	37	2	465	40	39	100	< 10	120	24	1.7
LH14-22B	4.68	98.82	35	1	408	50	53	90	90	240	22	1.9
LH14-16	11.91	100.00	26	3	284	110	55	110	90	80	23	1.0
LOWER BASALT												
UI68A	10.23	99.88	32	2	334	30	62	60	120	130	23	1.7
UI68D	11.66	99.31	32	2	304	50	54	70	120	100	20	1.5
UI79B	8.19	99.73	29	2	264	20	50	< 20	150	330	24	1.1
UI89E	8.17	99.97	32	2	300	50	37	40	170	70	24	1.2
UI95A	4.35	100.00	30	3	317	40	59	< 20	170	110	25	1.5
UI95D	8.53	98.49	31	2	301	40	58	40	100	60	21	0.9
UI128A	7.48	100.60	32	3	326	30	66	50	150	100	21	1.2
UI147	4.44	100.40	29	2	305	30	41	< 20	140	380	20	1.2
LH15- EA06	8.49	100.10	29	2	286	40	42	50	170	140	24	1.8
LH15- EA07B	9.70	99.41	30	3	310	40	49	50	160	130	27	1.5
LH15- EA08	2.16	98.81	34	2	336	50	70	60	140	140	22	1.8
LH15- EA09	1.96	100.00	34	2	332	60	61	60	140	110	24	2.0
LH15- EA10	6.08	100.10	34	2	342	40	52	50	160	230	23	1.3
LH15- EA11	10.42	99.55	29	2	309	40	42	40	90	110	26	1.4
LH15- EA12	6.66	99.77	36	4	347	120	55	260	140	120	29	2.9
LH15- EA13	3.16	99.80	33	2	332	40	55	50	140	120	22	1.7
LH15- EA14	2.06	99.49	34	2	342	40	46	50	140	120	22	2.0
LH15- EA16	7.20	100.40	31	2	306	60	49	60	140	130	23	1.5
LH15- EA17	5.23	100.30	31	2	304	50	51	50	140	120	22	1.7
LH15- EA18	8.21	99.47	32	3	340	40	49	40	160	180	25	1.4
LH15- EA19	5.15	98.64	34	3	352	30	48	50	190	70	25	0.8
LH15- EA20	6.78	99.34	30	3	310	30	47	40	150	210	24	1.5
LH15- EA21	6.22	98.88	26	2	350	< 20	26	20	60	490	20	1.3
LH15- EA22	7.49	100.60	34	2	383	50	41	50	80	130	21	1.1
LH15- EA23	6.97	98.70	32	4	337	30	51	40	170	90	26	1.5
UPPER BASALT												
LH14-32	3.17	99.42	31	< 1	332	320	59	110	50	70	21	2.0
LH14-33	4.02	99.63	31	< 1	330	320	63	110	60	110	21	1.4
LH14-34	3.60	98.36	30	1	332	330	44	100	30	80	20	1.9
LH14-36	8.19	100.30	29	1	316	310	56	110	60	130	20	1.2
UI39	3.98	99.68	30	1	308	280	65	110	20	70	21	1.4
UI35A	7.72	100.70	22	1	239	220	107	120	< 10	110	21	2.6
Detection Limit		0.01	1	1	5	20	1	20	10	30	1	0.5

Table 4.1. (continued)

UNIT/Sample Number	As FUS-MS ppm	Rb FUS-MS ppm	Sr FUS-ICP ppm	Y FUS-MS ppm	Zr FUS-ICP ppm	Nb FUS-MS ppm	Mo FUS-MS ppm	Ag FUS-MS ppm	In FUS-MS ppm	Sn FUS-MS ppm	Sb FUS-MS ppm	Cs FUS-MS ppm
DIABASE INTRUSIONS												
LH14-14	< 5	47	406	17.0	108	13.0	< 2	< 0.5	< 0.1	< 1	< 0.2	0.5
LH14-25	< 5	57	298	39.4	308	43.2	< 2	0.8	0.1	2	< 0.2	6.0
LH14-27	8	104	370	32.5	250	36.4	< 2	0.7	0.1	1	< 0.2	6.7
UI16B	< 5	32	258	26.0	197	26.6	< 2	< 0.5	< 0.1	2	< 0.2	1.2
UI59A	< 5	39	328	26.1	182	22.4	< 2	< 0.5	< 0.1	1	< 0.2	1.5
UI63	< 5	69	448	19.4	130	17.2	< 2	< 0.5	< 0.1	1	< 0.2	1.9
UI82	< 5	3	298	31.4	200	25.8	< 2	< 0.5	0.1	2	< 0.2	0.6
UI95I	< 5	25	358	26.9	188	25.5	< 2	< 0.5	< 0.1	2	< 0.2	1.4
UI102B	< 5	20	423	22.3	155	18.9	< 2	< 0.5	< 0.1	1	< 0.2	0.8
UI102C	< 5	28	462	29.5	196	26.5	< 2	< 0.5	0.1	2	< 0.2	3.5
UI106	< 5	19	272	34.1	226	27.6	< 2	< 0.5	0.1	2	< 0.2	1.1
LH15- EA01-2	< 5	28	424	23.0	145	17.6	< 2	< 0.5	< 0.1	1	< 0.2	1.6
LH15- EA02	< 5	45	429	29.3	193	23.0	< 2	< 0.5	0.1	1	< 0.2	4.7
LH15- EA04	< 5	23	378	25.1	161	18.6	< 2	< 0.5	< 0.1	1	0.6	1.9
LH15- EA58	< 5	72	326	32.8	253	35.4	< 2	< 0.5	0.1	2	0.4	4.6
LH14-07B	< 5	37	303	25.2	162	19.2	< 2	0.6	0.1	1	< 0.2	1.0
LH14-22A	< 5	18	40	26.8	174	22.8	< 2	0.6	< 0.1	2	< 0.2	0.5
LH14-22B	< 5	62	215	27.8	150	20.4	< 2	< 0.5	0.1	1	< 0.2	1.9
LH14-16	< 5	138	47	22.6	159	19.1	< 2	< 0.5	< 0.1	2	< 0.2	1.4
LOWER BASALT												
UI68A	< 5	35	134	34.6	277	38.5	< 2	< 0.5	< 0.1	3	0.4	0.6
UI68D	< 5	52	215	28.0	174	23.9	< 2	< 0.5	< 0.1	2	< 0.2	0.8
UI79B	19	13	142	47.4	438	62.1	< 2	0.7	0.2	4	0.4	0.6
UI89E	< 5	5	185	29.2	259	39.1	< 2	< 0.5	< 0.1	2	< 0.2	0.5
UI95A	< 5	24	288	45.0	375	54.0	< 2	0.6	0.1	3	< 0.2	3.3
UI95D	6	8	128	30.4	264	35.5	< 2	< 0.5	< 0.1	2	0.2	0.1
UI128A	< 5	20	302	36.9	269	37.2	< 2	< 0.5	< 0.1	2	< 0.2	1.5
UI147	< 5	2	89	40.2	370	54.5	< 2	0.5	< 0.1	3	< 0.2	0.4
LH15- EA06	9	6	120	40.7	340	51.6	< 2	< 0.5	0.1	3	< 0.2	0.4
LH15- EA07B	< 5	8	160	42.0	343	49.8	< 2	0.5	0.1	3	< 0.2	0.6
LH15- EA08	< 5	49	306	37.1	201	25.5	< 2	< 0.5	0.1	2	< 0.2	2.4
LH15- EA09	< 5	49	293	35.6	238	29.5	< 2	< 0.5	0.1	2	< 0.2	2.6
LH15- EA10	< 5	28	232	37.1	260	34.0	< 2	< 0.5	0.1	2	< 0.2	2.0
LH15- EA11	< 5	5	179	34.9	350	50.0	2	< 0.5	< 0.1	1	< 0.2	0.2
LH15- EA12	< 5	14	99	74.5	394	59.2	< 2	0.5	0.2	19	< 0.2	0.8
LH15- EA13	< 5	63	329	36.1	251	32.7	< 2	< 0.5	< 0.1	2	< 0.2	3.4
LH15- EA14	< 5	58	327	36.8	256	33.8	< 2	< 0.5	0.1	2	< 0.2	2.2
LH15- EA16	< 5	17	224	34.0	232	35.1	2	< 0.5	< 0.1	2	0.6	2.2
LH15- EA17	< 5	11	264	32.3	243	33.9	< 2	< 0.5	0.1	2	< 0.2	2.1
LH15- EA18	< 5	22	318	42.2	355	50.2	< 2	< 0.5	0.1	3	< 0.2	4.0
LH15- EA19	29	30	215	38.2	338	47.3	2	0.5	0.1	3	0.3	1.4
LH15- EA20	16	9	188	39.6	321	45.8	< 2	< 0.5	< 0.1	2	0.3	0.5
LH15- EA21	6	19	187	33.8	208	24.7	< 2	< 0.5	0.1	2	0.3	1.3
LH15- EA22	17	44	214	33.2	239	31.0	< 2	< 0.5	0.1	2	0.3	0.8
LH15- EA23	10	16	211	46.2	335	34.1	< 2	< 0.5	0.2	3	0.3	3.9
UPPER BASALT												
LH14-32	< 5	68	755	16.2	95	2.8	< 2	< 0.5	< 0.1	< 1	< 0.2	0.6
LH14-33	< 5	26	569	16.9	92	2.6	< 2	< 0.5	< 0.1	< 1	< 0.2	0.8
LH14-34	< 5	10	352	16.0	93	2.0	< 2	< 0.5	0.1	< 1	< 0.2	0.6
LH14-36	< 5	9	271	15.4	90	1.8	< 2	< 0.5	< 0.1	< 1	0.4	0.4
UI39	< 5	33	411	15.6	101	3.9	< 2	< 0.5	< 0.1	< 1	< 0.2	0.4
UI35A	8	29	10	11.8	99	4.0	< 2	< 0.5	< 0.1	< 1	0.5	0.7
Detection Limit	5	1	2	0.5	1	0.2	2	0.5	0.1	1	0.2	0.1

Table 4.1. (continued)

UNIT/Sample Number	Ba FUS-ICP ppm	La FUS-MS ppm	Ce FUS-MS ppm	Pr FUS-MS ppm	Nd FUS-MS ppm	Sm FUS-MS ppm	Eu FUS-MS ppm	Gd FUS-MS ppm	Tb FUS-MS ppm	Dy FUS-MS ppm	Ho FUS-MS ppm	Er FUS-MS ppm
DIABASE INTRUSIONS												
LH14-14	1125	18.6	40.1	5.07	21.7	4.52	1.77	4.18	0.61	3.50	0.66	1.80
LH14-25	420	49.6	106.0	13.00	53.6	11.40	3.63	9.97	1.51	8.50	1.60	4.30
LH14-27	939	39.8	87.0	10.90	44.4	9.13	2.84	8.07	1.15	6.71	1.30	3.57
UI16B	324	26.5	60.6	7.44	31.7	6.72	2.27	6.43	0.97	5.33	0.99	2.61
UI59A	348	26.3	59.6	7.45	32.5	6.83	2.35	6.75	0.92	5.30	0.95	2.59
UI63	792	17.6	39.4	4.95	20.9	4.62	1.70	4.51	0.67	3.85	0.73	1.90
UI82	286	28.3	64.1	8.10	35.0	7.92	2.34	7.19	1.02	6.15	1.12	3.07
UI95I	285	25.4	57.2	7.21	30.4	6.89	2.15	6.27	0.93	5.34	0.95	2.66
UI102B	1104	22.7	52.1	6.67	28.9	6.47	1.91	5.70	0.83	4.60	0.82	2.22
UI102C	671	26.7	61.3	7.87	34.4	7.64	2.77	7.13	1.07	6.05	1.08	2.87
UI106	285	33.7	77.3	9.69	42.0	9.34	2.96	8.40	1.22	6.84	1.21	3.19
LH15- EA01-2	336	20.7	48.8	6.55	29.6	6.41	2.31	6.02	0.90	4.95	0.87	2.35
LH15- EA02	723	29.1	66.6	8.52	37.5	8.66	2.63	7.60	1.15	6.33	1.10	2.95
LH15- EA04	598	24.6	56.7	7.25	31.8	7.03	2.44	6.17	0.96	5.26	0.94	2.38
LH15- EA58	603	39.0	86.1	10.60	43.1	9.41	2.17	7.91	1.27	6.92	1.26	3.32
LH14-07B	747	23.9	54.0	6.69	29.0	6.22	2.13	6.06	0.93	5.40	1.01	2.78
LH14-22A	36	27.2	59.2	7.59	32.4	7.05	1.58	6.57	0.97	5.90	1.09	3.11
LH14-22B	568	22.1	50.7	6.68	29.3	6.85	2.30	6.73	1.01	5.69	1.09	2.95
LH14-16	421	21.8	50.4	6.50	28.1	5.93	1.81	5.41	0.82	4.66	0.83	2.20
LOWER BASALT												
UI68A	305	35.6	79.3	9.61	40.1	8.49	2.24	7.07	1.14	6.52	1.28	3.52
UI68D	423	24.2	54.4	6.89	28.1	6.24	2.00	6.21	0.96	5.48	0.98	2.63
UI79B	198	60.8	133.0	15.80	63.6	12.50	2.98	10.60	1.70	9.54	1.73	4.67
UI89E	149	35.1	77.4	9.05	36.6	7.41	1.58	6.02	0.98	5.45	1.05	3.04
UI95A	531	52.7	114.0	13.60	54.6	11.10	2.86	10.20	1.59	8.87	1.61	4.19
UI95D	161	14.2	36.3	5.18	23.7	5.70	1.48	5.56	0.93	5.54	1.06	3.00
UI128A	568	31.5	71.9	8.99	37.4	8.04	2.45	7.62	1.22	7.12	1.32	3.55
UI147	61	38.0	86.7	10.80	45.3	9.71	2.39	9.06	1.41	7.97	1.50	4.02
LH15- EA06	203	26.0	72.6	10.80	47.0	10.70	3.06	9.68	1.51	8.42	1.57	4.20
LH15- EA07B	194	56.7	115.0	13.30	53.9	11.40	2.11	10.20	1.52	8.16	1.59	4.15
LH15- EA08	1571	28.1	65.2	8.49	36.9	8.56	2.45	8.39	1.29	7.37	1.40	3.76
LH15- EA09	1046	37.4	82.9	9.94	39.7	8.56	2.48	7.56	1.22	7.07	1.35	3.58
LH15- EA10	342	31.5	70.5	8.95	36.9	8.41	2.51	7.93	1.27	7.59	1.40	3.81
LH15- EA11	221	18.8	45.3	5.91	24.9	5.77	1.67	6.15	1.02	6.31	1.25	3.77
LH15- EA12	549	53.6	135.0	20.30	98.8	26.80	13.50	23.80	3.26	16.10	2.74	6.42
LH15- EA13	2113	28.3	67.0	8.80	37.2	8.75	2.31	8.05	1.27	7.26	1.36	3.82
LH15- EA14	1837	28.7	69.2	9.14	37.4	8.69	2.61	8.13	1.28	7.44	1.39	3.70
LH15- EA16	209	37.7	81.6	10.10	40.3	8.84	2.60	7.96	1.20	6.92	1.30	3.30
LH15- EA17	187	34.9	77.3	9.70	38.9	8.74	2.45	7.72	1.15	6.61	1.23	3.35
LH15- EA18	389	54.1	120.0	14.60	57.2	12.20	3.74	10.60	1.66	9.31	1.63	4.25
LH15- EA19	1326	44.5	101.0	12.40	49.4	10.30	2.21	8.78	1.36	8.02	1.48	4.06
LH15- EA20	313	45.4	99.4	12.20	48.4	10.30	2.49	9.40	1.45	8.34	1.57	4.14
LH15- EA21	318	29.5	68.1	8.71	36.3	8.46	2.17	7.82	1.22	6.94	1.34	3.52
LH15- EA22	690	29.6	69.3	9.20	38.6	8.54	2.85	8.06	1.21	6.87	1.29	3.70
LH15- EA23	205	59.0	125.0	15.10	59.8	12.80	3.78	11.10	1.72	9.29	1.74	4.60
UPPER BASALT												
LH14-32	1680	9.9	23.3	3.14	15.3	3.82	1.43	3.94	0.59	3.37	0.62	1.71
LH14-33	400	10.2	24.0	3.30	15.6	4.44	1.63	4.06	0.60	3.40	0.63	1.83
LH14-34	110	8.7	23.2	3.31	15.4	3.73	1.45	3.81	0.60	3.49	0.64	1.68
LH14-36	124	9.9	23.9	3.31	15.5	3.56	1.24	3.79	0.60	3.37	0.61	1.73
UI39	375	7.6	19.3	2.70	12.4	3.22	1.10	3.65	0.55	3.17	0.58	1.58
UI35A	38	2.8	8.6	1.29	7.3	2.37	0.57	2.27	0.39	2.33	0.44	1.25
Detection Limit	3	0.05	0.05	0.01	0.05	0.01	0.01	0.01	0.01	0.01	0.01	0.01

Table 4.1. (continued)

UNIT/Sample Number	Tm FUS-MS ppm	Yb FUS-MS ppm	Lu FUS-MS ppm	Hf FUS-MS ppm	Ta FUS-MS ppm	Tl FUS-MS ppm	Pb FUS-MS ppm	Bi FUS-MS ppm	Th FUS-MS ppm	U FUS-MS ppm
DIABASE INTRUSIONS										
LH14-14	0.240	1.47	0.229	2.6	1.02	< 0.05	28	< 0.1	1.56	0.38
LH14-25	0.584	3.50	0.528	7.1	3.21	0.09	14	< 0.1	5.54	1.30
LH14-27	0.486	2.99	0.437	6.1	2.58	0.40	10	< 0.1	4.51	1.05
UI16B	0.357	2.17	0.331	5.0	1.73	< 0.05	< 5	< 0.1	2.85	0.65
UI59A	0.344	2.18	0.317	4.9	1.28	< 0.05	< 5	< 0.1	2.14	0.49
UI63	0.263	1.66	0.244	3.4	1.05	0.20	< 5	< 0.1	1.67	0.39
UI82	0.415	2.68	0.440	5.4	1.74	< 0.05	< 5	< 0.1	2.86	0.63
UI95I	0.357	2.40	0.363	4.9	1.58	< 0.05	< 5	< 0.1	2.76	0.62
UI102B	0.290	1.87	0.281	4.1	1.22	< 0.05	< 5	< 0.1	1.80	0.42
UI102C	0.374	2.34	0.362	5.3	1.65	< 0.05	< 5	< 0.1	2.21	0.54
UI106	0.438	2.76	0.416	6.2	1.73	0.09	< 5	< 0.1	2.69	0.62
LH15- EA01-2	0.317	2.02	0.315	3.7	1.27	0.06	< 5	< 0.1	1.67	0.36
LH15- EA02	0.389	2.34	0.367	4.7	1.60	0.15	< 5	< 0.1	2.28	0.50
LH15- EA04	0.333	2.24	0.345	4.1	1.41	0.11	< 5	< 0.1	2.09	0.44
LH15- EA58	0.467	2.96	0.420	6.3	2.64	0.26	26	< 0.1	4.26	0.93
LH14-07B	0.399	2.36	0.355	3.9	1.52	< 0.05	51	< 0.1	2.19	0.58
LH14-22A	0.418	2.55	0.383	4.3	1.66	< 0.05	< 5	< 0.1	2.04	0.67
LH14-22B	0.396	2.48	0.354	3.7	1.51	0.14	38	< 0.1	1.83	0.46
LH14-16	0.292	1.78	0.274	4.3	1.23	0.52	< 5	< 0.1	1.86	0.47
LOWER BASALT										
UI68A	0.497	3.13	0.494	7.0	2.45	0.14	10	< 0.1	4.25	1.05
UI68D	0.373	2.34	0.352	4.6	1.60	0.08	< 5	< 0.1	2.34	0.54
UI79B	0.644	4.08	0.621	10.9	3.67	< 0.05	< 5	< 0.1	8.20	1.84
UI89E	0.432	2.74	0.436	6.7	2.23	< 0.05	< 5	< 0.1	4.53	1.10
UI95A	0.596	3.76	0.562	9.3	3.38	< 0.05	< 5	< 0.1	6.72	1.62
UI95D	0.425	2.79	0.416	6.4	2.69	< 0.05	< 5	< 0.1	4.86	1.25
UI128A	0.481	3.11	0.488	7.0	2.36	< 0.05	6	< 0.1	3.84	0.94
UI147	0.548	3.47	0.528	9.5	3.12	< 0.05	27	< 0.1	6.74	1.44
LH15- EA06	0.589	3.68	0.534	8.6	3.64	< 0.05	15	< 0.1	6.76	2.11
LH15- EA07B	0.590	3.83	0.586	8.4	3.44	< 0.05	< 5	< 0.1	6.67	1.63
LH15- EA08	0.526	3.30	0.498	5.1	2.23	0.22	15	< 0.1	4.02	0.98
LH15- EA09	0.499	3.14	0.451	6.1	2.35	0.28	9	< 0.1	3.93	0.95
LH15- EA10	0.531	3.40	0.490	6.6	2.48	0.17	27	< 0.1	4.16	0.96
LH15- EA11	0.542	3.53	0.578	8.5	3.44	< 0.05	< 5	< 0.1	6.78	1.58
LH15- EA12	0.821	4.94	0.704	9.6	4.03	< 0.05	6	< 0.1	7.58	1.82
LH15- EA13	0.521	3.30	0.499	6.4	2.35	0.30	8	< 0.1	3.95	0.93
LH15- EA14	0.534	3.56	0.530	6.2	2.41	0.23	< 5	< 0.1	4.01	1.01
LH15- EA16	0.468	3.08	0.472	5.9	2.33	0.10	< 5	< 0.1	4.39	0.99
LH15- EA17	0.456	3.00	0.452	5.8	2.36	0.07	< 5	< 0.1	4.42	1.05
LH15- EA18	0.615	3.91	0.585	8.9	3.68	0.07	< 5	< 0.1	6.70	1.56
LH15- EA19	0.570	3.74	0.575	8.5	3.64	0.13	< 5	< 0.1	7.07	1.73
LH15- EA20	0.564	3.58	0.570	8.0	3.22	< 0.05	9	< 0.1	6.28	1.55
LH15- EA21	0.494	3.32	0.513	5.1	1.97	0.08	117	< 0.1	3.33	0.72
LH15- EA22	0.512	3.12	0.449	5.7	2.10	0.31	< 5	< 0.1	3.23	0.70
LH15- EA23	0.638	3.97	0.609	6.4	3.08	0.09	< 5	< 0.1	6.59	1.58
UPPER BASALT										
LH14-32	0.229	1.34	0.197	2.4	0.24	0.75	< 5	< 0.1	0.59	0.10
LH14-33	0.256	1.52	0.218	2.6	0.23	0.12	6	< 0.1	0.60	0.12
LH14-34	0.227	1.31	0.191	2.3	0.23	< 0.05	< 5	< 0.1	0.58	0.13
LH14-36	0.235	1.37	0.201	2.2	0.19	< 0.05	25	< 0.1	0.57	0.09
UI39	0.216	1.34	0.210	2.9	0.23	0.22	< 5	< 0.1	0.77	0.13
UI35A	0.185	1.22	0.182	2.6	0.24	0.08	< 5	< 0.1	0.75	0.65
Detection Limit	0.005	0.01	0.002	0.1	0.01	0.05	5	0.1	0.05	0.01

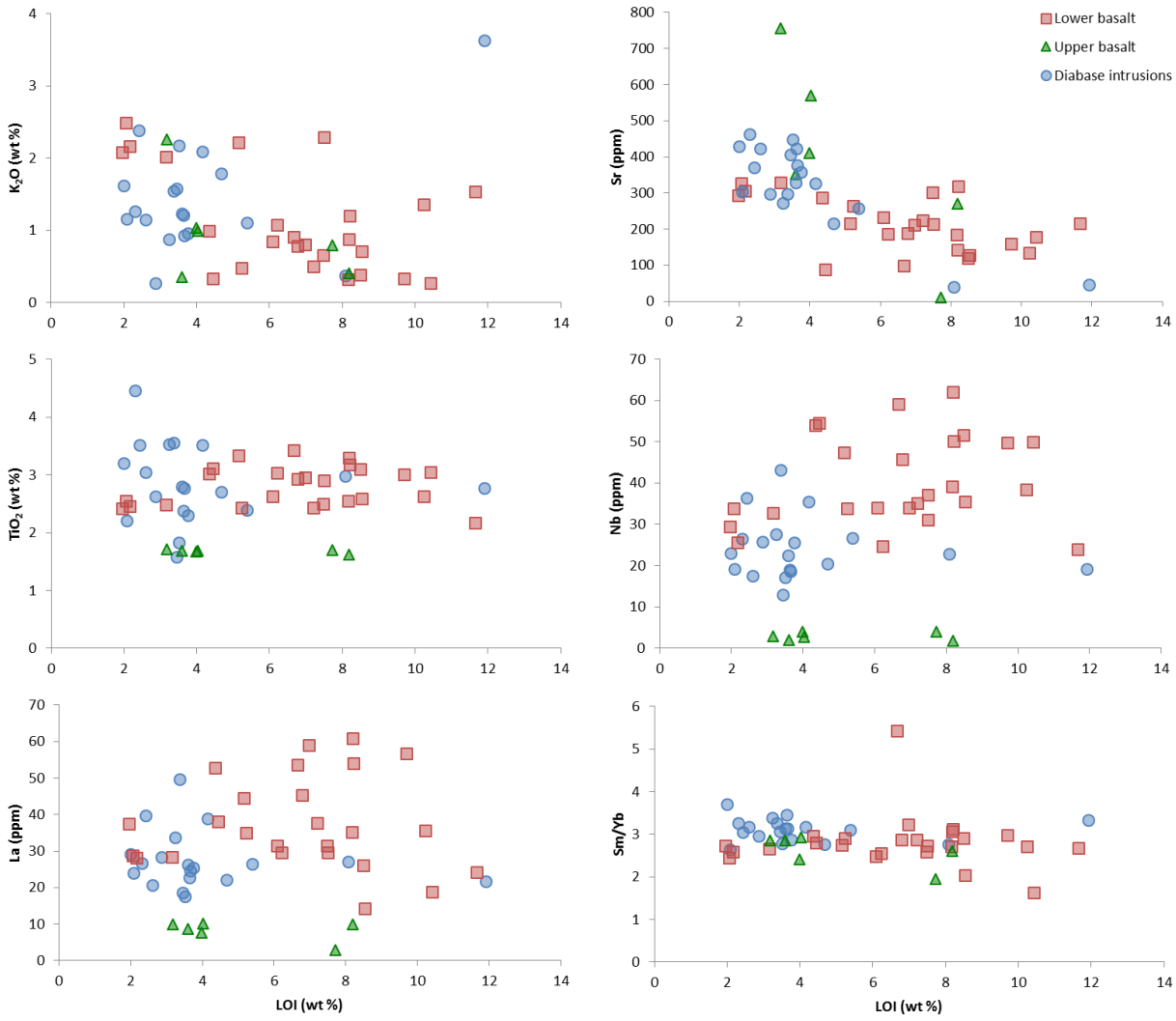

Figure 4.1. Bivariate plots of select major and trace elements against loss-on-ignition content (LOI).

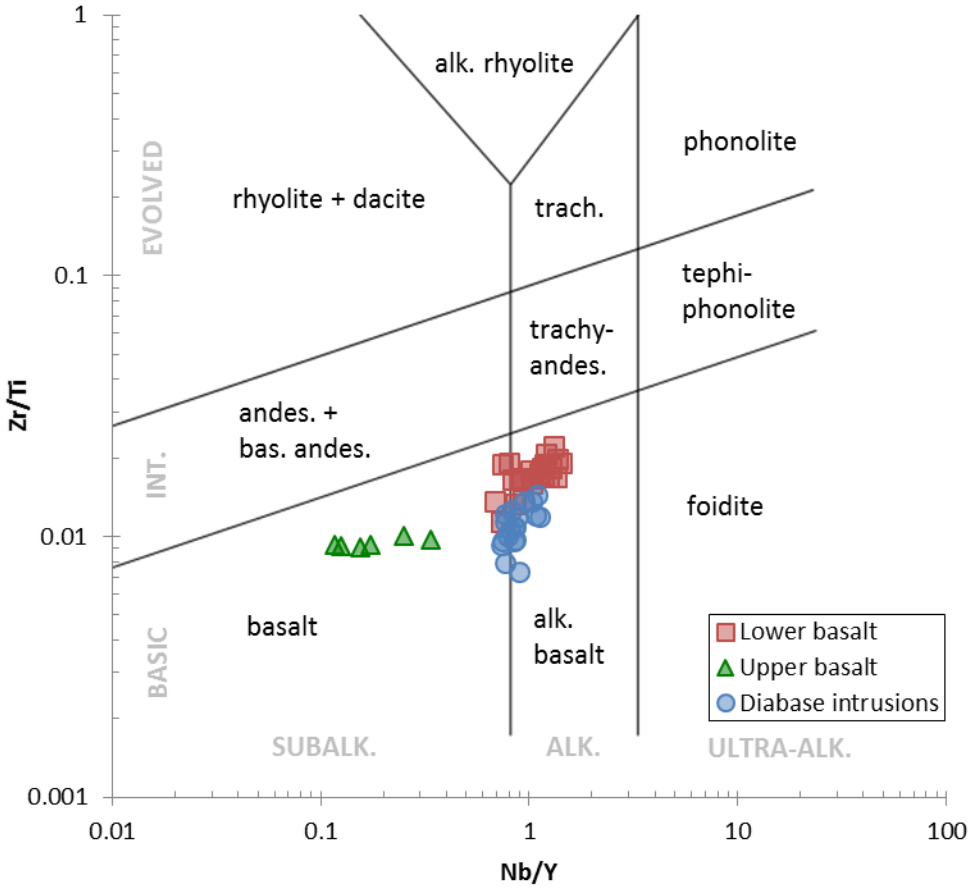

Figure 4.2. Zr/Ti vs. Nb/Y igneous classification (Pearce et al., 1996) of Union Island Group mafic units.

the subalkaline basalt field (Nb/Y < 0.8; n=10). The diabase tends to have higher Zr/Ti and Nb/Y ratios than the lower basalt unit. The upper basalt unit plots in the subalkaline basalt field and forms a linear trend with varying Nb/Y values (0.1–0.3) over a relatively constant Zr/Ti ratio (~0.01).

Significant compositional overlap between the diabase intrusions and the lower basalt unit is described below.

4.1.1 Major elements

Select Fenner diagrams for the Union Island Group mafic units are presented in Fig. 4.3. The lower basalt unit has Mg# ranging from 30 to 45, and displays a fairly constant range of SiO_2 (40–55 wt%). Al_2O_3 (12–15 wt%) and MgO (3–6 wt%) decrease with decreasing Mg#, while $Fe_2O_{3(T)}$ (11–17 wt%), TiO_2 (2.2–3.2 wt%), and P_2O_5 (0.26–0.54 wt%) increases (Table 4.2).

Samples of the upper basalt unit can be further subdivided into a low-Mg# (~35) and a mid-Mg# (45–55) group. No rocks of the upper basalt unit have Mg# in the range of 35–45. The gap is also present in geochemical data previously reported by Goff (1984) and Kjarsgaard et al. (2013a); thus it is unlikely to have been caused by sampling bias and may be a real compositional gap. Combined with analyses by Kjarsgaard et al. (2013a), the upper basalt unit shows a narrower range of SiO_2 content (39–48 wt%) compared to the lower basalt unit, but has generally higher Al_2O_3 (15–17 wt%), lower $Fe_2O_{3(T)}$ (<13 wt%), TiO_2 (1.5–1.7 wt%), and P_2O_5 (0.12–0.15 wt%), and a larger range of MgO (1–8 wt%).

The diabase intrusions show a greater range of Mg# (32–58). A dyke margin sample (LH14-22A) has the highest Mg# value (58) of all Union Island Group samples. The larger range of Mg# of the diabase suggests a higher degree of magma fractionation. The diabase intrusions have similar major element trends as those of the lower basalt unit, with 40–58 wt% SiO_2, 11–15 wt% Al_2O_3, 3–6 wt% MgO, 11–17 wt% $Fe_2O_{3(T)}$, 1.6–4.5 wt% TiO_2, and 0.18–0.46 wt% P_2O_5.

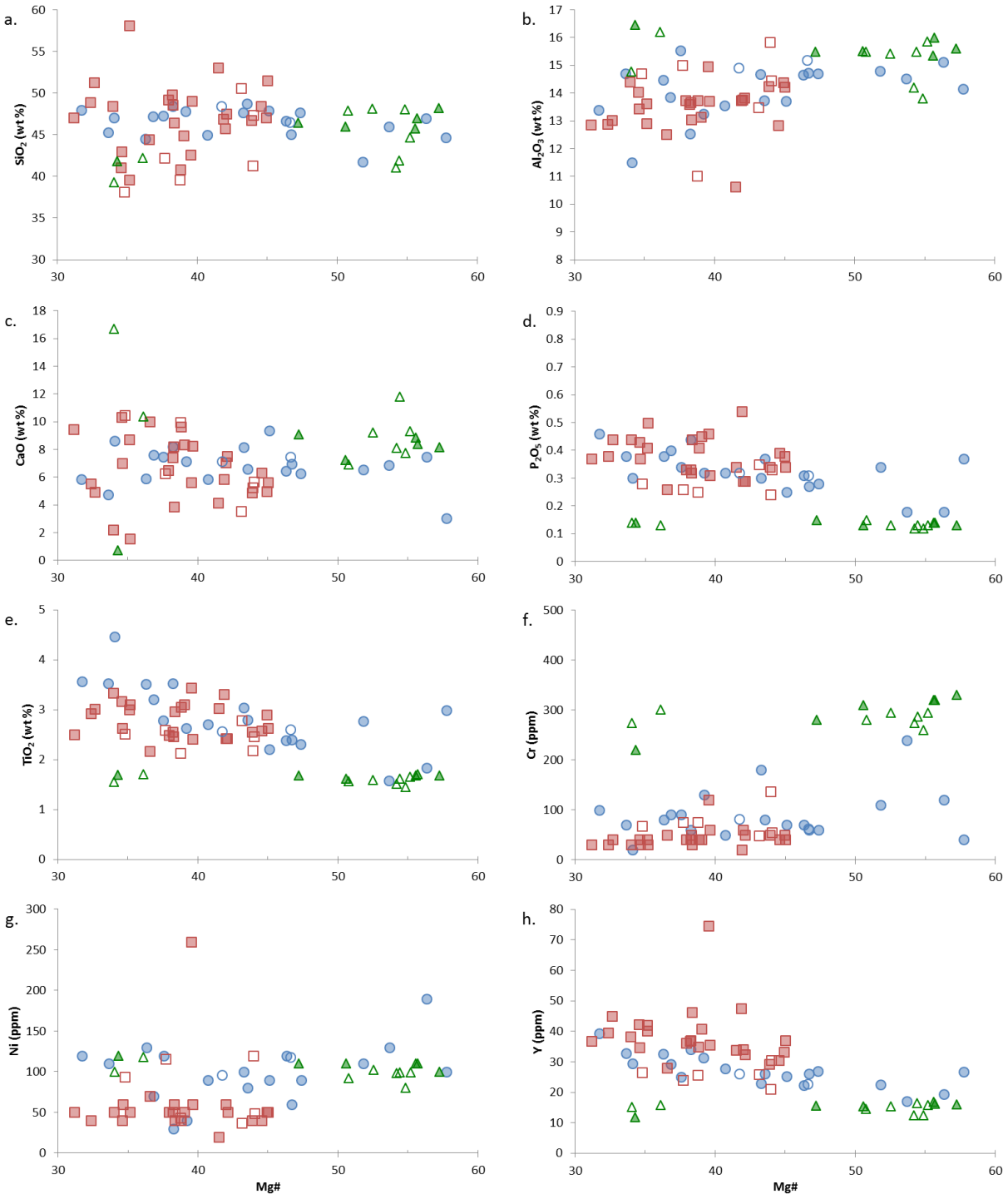

Figure 4.3. Fenner diagrams of select major, minor and trace elements for the Union Island Group mafic units. Analyses below detection limit are not plotted. See Figure 4.2 for symbol legend. Open symbols are analyses reported by Kjarsgaard et al. (2013a).

Table 4.2. Summary of key geochemical parameters of Union Island Group mafic units. For each parameter, the total range of values is given, followed by the mean in brackets.

		Lower basalt	Upper basalt	Diabase intrusions
n		25	14[a]	19
Mg#		30-45 (38)	34-57 (50)	32-58 (43)
Al_2O_3	wt%	11-15 (13)	14-16 (15)	12-16 (14)
MgO	wt%	3-6 (4)	2-8 (6)	4-9 (6)
$Fe_2O_{3(T)}$	wt%	11-17 (14)	7-14 (11)[b]	11-18 (15)
TiO_2	wt%	2.2-3.4 (2.8)	1.5-1.7 (1.6)	1.5-4.5 (2.9)
P_2O_5	wt%	0.26-0.54 (0.38)	0.12-0.15 (0.13)	0.18-0.46 (0.33)
Ni	ppm	20-260 (58)[c]	80-120 (103)	30-190 (100)[d]
Cr	ppm	20-120 (50)[d]	220-330 (289)	20-240 (89)
Zr	ppm	174-438 (293)	83-101 (93)	108-308 (186)
Nb	ppm	24-62 (41)	2-4 (3)	13-43 (24)
La	ppm	14-61 (37)	8-10 (9)[b]	18-50 (28)
La/Sm_N		1.3-3.2 (2.5)	1.5-1.8 (1.6)[b]	2.1-2.8 (2.4)
Gd/Yb_N		1.4-4.0 (2.1)	2.2-2.4 (2.3)[b]	2.1-2.7 (2.4)

a. Includes eight analyses from Kjarsgaard et al. (2013a), except for La, La/Sm_N, and Gd/Yb_N.
b. Excludes sample UI35A, which shows REE mobility due to alteration (discussed in Appendix A).
c. Excludes four samples below l.o.d. (20 ppm).
d. Excludes one sample below l.o.d. (20 ppm).

4.1.2 Compatible trace elements

All three Union Island Group mafic units show a positive correlation between Cr content and Mg# (Fig. 4.3f). The lower basalt unit has lower Cr levels (<20–120 ppm) compared to the upper basalt unit (220–330 ppm). All lower basalt unit samples have Ni contents below 70 ppm except for LH15-EA12, which contains an anomalously high Ni level of 260 ppm. Nickel content of the upper basalt unit (80–100 ppm) is higher than the lower basalt unit. The diabase intrusions have Cr content ranging 30–240 ppm and Ni content ranging 30–190 ppm. Both the lower basalt unit and the diabase display positive correlation between Ni and Mg#, whereas the upper basalt unit maintains a constant, narrower range of Ni (80–120 ppm; Fig. 4.3g).

4.1.3 Incompatible trace elements

With respect to immobile incompatible elements (e.g., HFSE, Y, Ti, P), the lower basalt unit and the diabase intrusions display a wide range of enrichment levels that increases with decreasing Mg# (e.g., Figs 4.3d, e, h). The upper basalt unit is only moderately enriched in immobile incompatible elements and maintains a narrow composition range. For example, Zr and Nb contents of the lower basalt unit vary between 174–439 ppm and 24–62 ppm, respectively, whereas the upper basalt unit displays a much narrower range of 90–101 ppm Zr and 2–4 ppm Nb, respectively (Fig. 4.4). The diabase intrusions have Zr (108–308 ppm) and Nb (13–43 ppm) contents that overlap those of the lower basalt unit. Incompatible element ratio Zr/Nb is nearly identical for both the lower basalt unit (7–10; average 7.3) and the diabase intrusions (7–9; average 7.8).

The upper basalt unit displays a uniform composition with respect to most incompatible element ratios (e.g. La/Sm_N; Table 4.2), however it displays an apparent large range in Zr/Nb ratios. Samples UI39 and UI35A in this study, together with eight analyses reported by Kjarsgaard et al. (2013a), have a restricted Zr/Nb range of 23–26. In contrast, samples LH14-32, LH14-33, LH14-34, and LH14-36 have Zr/Nb ratios ranging between 34 and 50 (Table 4.3). Blind re-analysis of these four samples returned a much smaller Zr/Nb range of 37–41, which remains distinctly separate from other upper basalt unit samples. We ruled out the possibility of sampling bias, since three of these four samples come from the same area as some of the samples collected by Kjarsgaard et al. (2013a), with the fourth sample from a previously unsampled locality. We attribute this discrepancy in Zr/Nb ratios to analytical imprecision when measuring low amounts

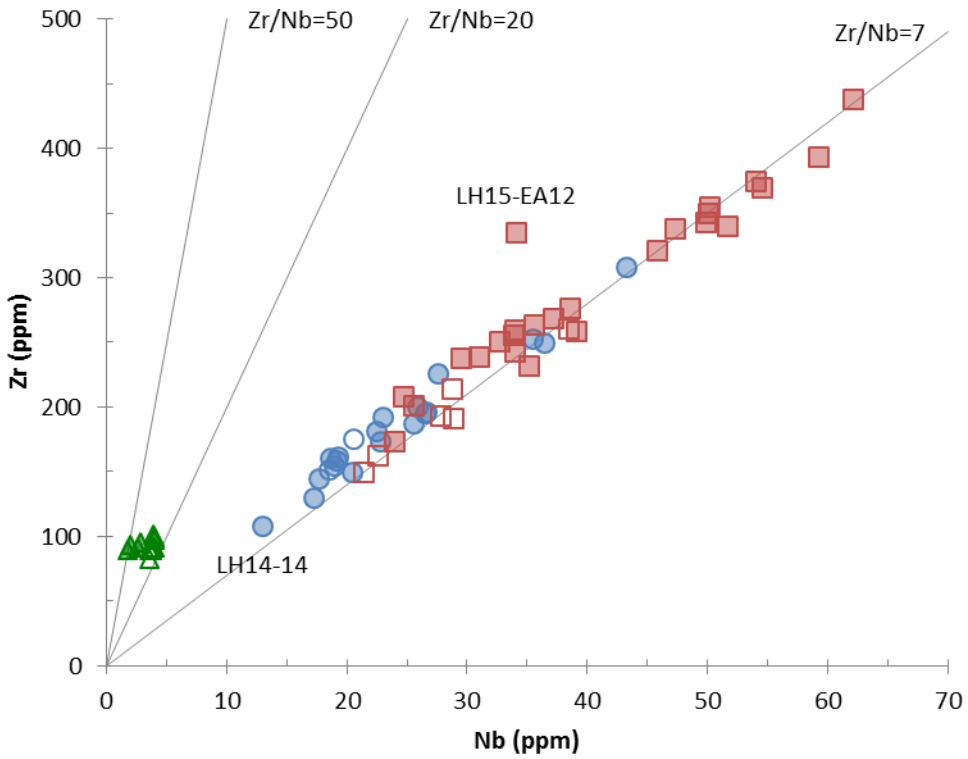

Figure 4.4. Zr vs. Nb plot for Union Island Group mafic units. See Figure 4.2 for symbol legend. All samples from the lower basalt unit and the diabase intrusions follow a well-defined trend with Zr/Nb ratios between 6.6 and 9.8, except for sample LH15-EA12 (discussed in Appendix A). A Zr/Nb=7 line is shown for reference.

Table 4.3. Zr and Nb analysis and calculated Zr/Nb ratios of upper basalt samples.

Sample	Zr (ppm)	Nb (ppm)	Zr/Nb
LH14-32	95	2.8	34
LH14-32 repl	101	2.7	37
LH14-33	92	2.6	35
LH14-33 repl	100	2.6	38
LH14-34	93	2.0	47
LH14-34 repl	102	2.5	41
LH14-36	90	1.8	50
LH14-36 repl	98	2.4	41
UI39	101	3.9	26
UI35A	99	4.0	25
KIA09-001A*	89.9	3.6	25
KIA09-001B*	82.5	3.6	23
KIA09-002*	91	3.7	25
KIA09-003*	91.8	4.0	23
KIA09-004A*	97.6	4.0	24
KIA09-004B*	91.6	3.7	25
KIA09-005*	90	3.8	24
KIA09-006*	91.9	3.9	24

"repl" indicates replicate analysis.
* Data from Kjarsgaard et al. (2013a).

of Nb which is characteristic in all upper basalt samples (2–4 ppm; Fig. 4.4). Blind analyses of the low-Nb standard reference material WGB-1 (8±4 ppm Nb; provisional value; 2σ) returned relative errors of 36% and 53%, with a repeatability of 15%. Repeatability associated with the re-analyzed four samples, which have even lower Nb content (1.8–2.8 ppm), ranges from 0% to 14%. In contrast, the four re-analyses of Zr levels have lower repeatability values of 3–5%. Therefore, we consider the discrepancy in Zr/Nb ratios between the four re-analyzed samples and the rest of the upper basalt unit samples to be a result of analytical imprecision of measuring low amounts of Nb. As a restricted Zr/Nb range of 23–26 is represented by ten analyses from two independent studies (Kjarsgaard et al., 2013a; this study), we interpret this as a more accurate representation of Zr/Nb ratios of the upper basalt unit.

4.1.4 Rare earth elements (REE)

All three Union Island Group mafic units display fractionated chondrite-normalized rare earth element (REE) profiles with LREE enrichment over HREE (Fig. 4.5). The lower basalt unit and the diabase intrusions display a wide range of enrichment levels (18–61 ppm La); LREE are highly fractionated (average La/Sm_N: 2.5) and HREE are moderately fractionated (average Gd/Yb_N: 2.2). Slightly negative Eu anomaly, reaching a minimum Eu*/Eu value of 0.7, is observed for a few samples of the lower basalt unit and of the diabase intrusions.

The upper basalt is distinguished from the other two units by being less enriched in REE overall (8–10 ppm La) and having less fractionated LREE (average La/Sm_N: 1.6).

4.1.5 Other high field strength elements (HFSE)

Primitive mantle normalized incompatible-element plots further highlight the marked compositional difference between the two basalt units and the compositional similarity between the lower basalt unit and the diabase intrusions (Fig. 4.6). The lower basalt unit displays an enrichment order of $Ta_N > La_N \cong Nb_N \cong Th_N$ (average $Th/Nb_N = 1.1$), whereas the upper basalt unit is characterized by depletion of Nb and Ta relative to Th and La (average $Th/Nb_N = 2.0$). In addition, the lower basalt unit displays a slightly negative Ti anomaly (average Ti/Ti* = 0.7), which is absent in the upper basalt unit (average Ti/Ti* = 1.1). The diabase intrusions display similar incompatible element enrichment profiles with the lower basalt unit, with an average Th/Nb_N ratio of 0.9 and an average Ti/Ti* ratio of 0.9.

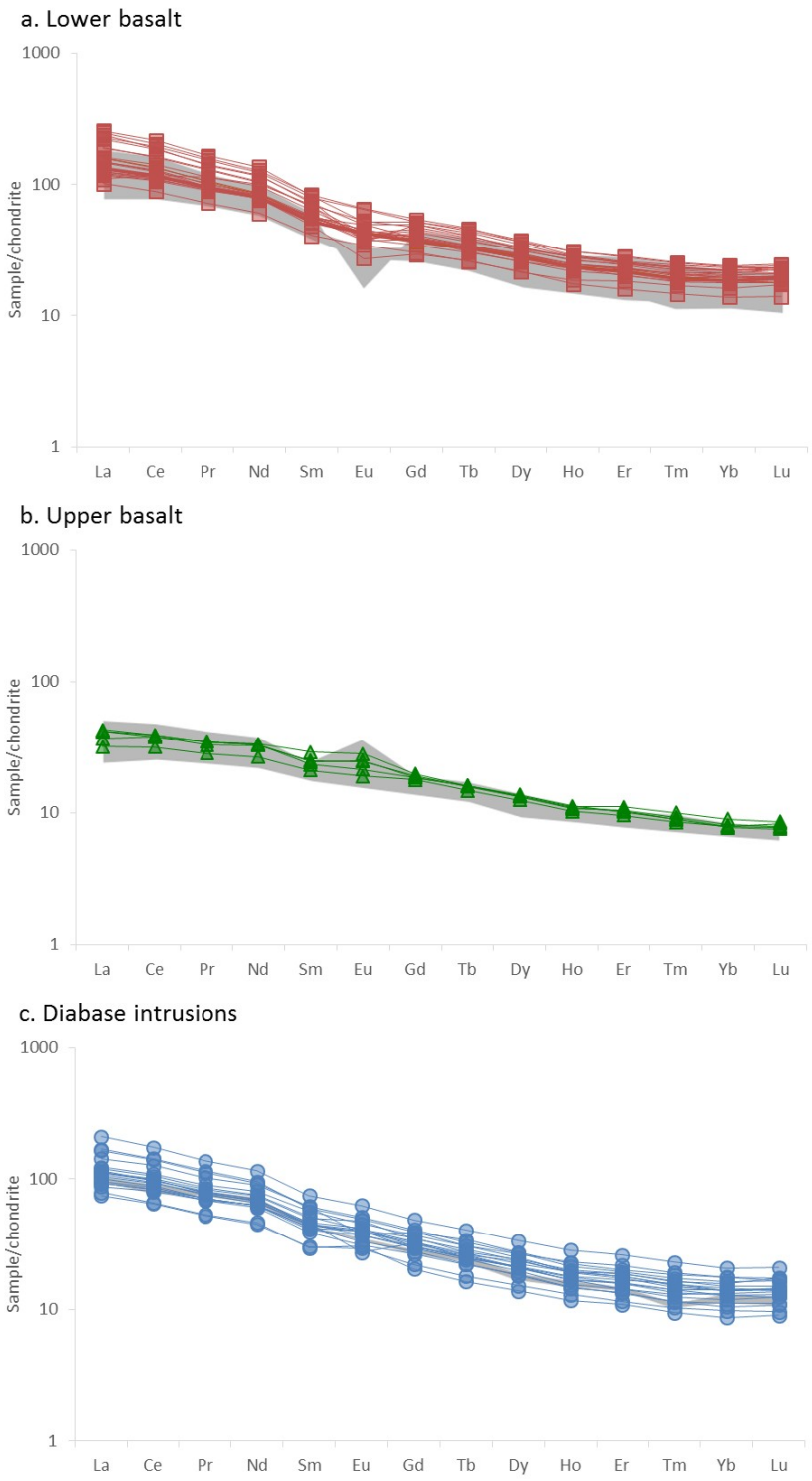

Figure 4.5. Chondrite-normalized rare earth element plots for the Union Island Group mafic units: a) lower basalt, b) upper basalt, and c) diabase intrusions. Grey band represents geochemical data from Kjarsgaard et al. (2013a). Sample LH15-EA12, which shows anomalous REE enrichment (discussed in Appendix A), is excluded from diagram a. Chondrite data from Sun and McDonough (1989).

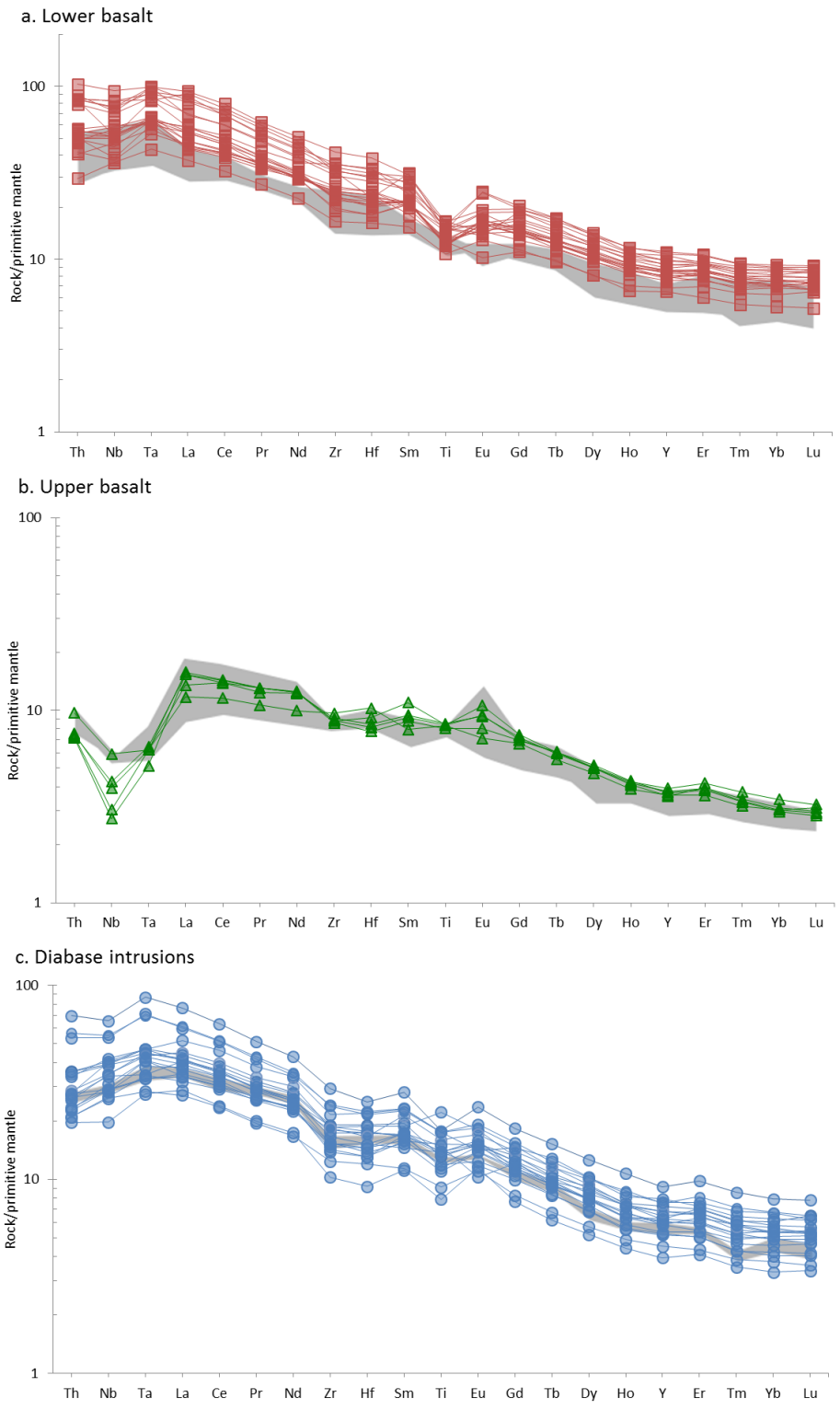

Figure 4.6. Incompatible element multi-element plots for Union Island Group mafic units. Normalization is relative to primitive (pyrolite) mantle (McDonough and Sun, 1995). Shaded area represents analysis reported in Kjarsgaard et al. (2013a).

Fractionation between REE and the rest of HFSE is observed for a few samples from both the lower and upper basalt units; this is discussed in more detail in Appendix A.

4.1.6 Geochemical transect of the lower basalt unit

Nine samples of the lower basalt package were collected along a transect where the lower basalts are continuously exposed in the mainland section. These nine transect samples are subdivided into two geochemically distinct types based on the abundances of select HFSE (Table 4.4; Fig. 4.7). Type A, including samples LH15-EA06, LH15-EA07B, LH15-EA11, and LH15-EA12, is characterized by having higher Hf (8.4–9.6 ppm) and Ta (3.4–4.0 ppm) contents relative to the less enriched type B (LH15-EA08 to LH15-EA10, LH15-EA13, and LH15-EA14; Hf: 5.1–6.6 ppm; Ta: 2.2–2.5 ppm; Fig. 4.8). We further note that this distinct gap in HFSE contents is also exhibited by the remainder of samples from the lower basalt unit. This second-order distinction implies that two geochemical subgroups of lava exist in the lower basalt unit. In the transect, each lava type is represented by at least two flows, alternating in the order of A_1, B_1, A_2, B_2 from bottom to top. Samples LH15-EA16 to LH15-EA23, collected on a continuously exposed, ~200 m × ~100 m outcrop south of the transect, also contain both type A and B lavas in close vicinity of each other. Thus, alternating layers of both lava types most likely extends through the entire lower basalt unit.

Within the sampled transect, type A lavas are finer-grained overall (<1 mm) and contain a more isotropic texture, whereas type B lavas are marked by coarser grain sizes (1–4 mm) and weakly glomeroporphyritic textures. Samples within flows B_1 and A_2 show slight increase in incompatible element enrichment levels; Hf increases from 5.1 ppm to 6.6 ppm in flow B_1, and 8.5 ppm to 9.6 ppm in flow A_2.

4.1.7 Internal geochemical variations of Union Island Group diabase sills and dykes

Of the diabase sills intruding the mainland Union Island Group strata, samples from stratigraphically lower positions tend to display the most primitive compositions (e.g., UI63), whereas those from stratigraphically higher positions tend to display the most evolved compositions (e.g., UI106). This stratigraphic correlation suggests progressive magma evolution with decreasing depth of sill emplacement. The diabase intrusion on Tuff Island (LH14-25, LH14-27, LH15-EA58) has the most evolved composition of all diabase samples, with sample LH14-25

Table 4.4. Geochemical summary of samples from the lower basalt unit transect.

Lava Type*	Stratigraphic Depth (m below upper unconformity)	Mg#	Zr (ppm)	Hf (ppm)	Ta (ppm)
B_2	10	39	340	8.6	3.64
B_2	20	35	343	8.4	3.44
A_2	30	38	201	5.1	2.23
A_2	40	40	238	6.1	2.35
B_1	50	45	260	6.6	2.48
B_1	60	39	350	8.5	3.44
B_1	70	40	394	9.6	4.03
A_1	80	38	251	6.4	2.35
A_1	90	38	256	6.2	2.41

*Number in subscript denotes sequence of lava layers.

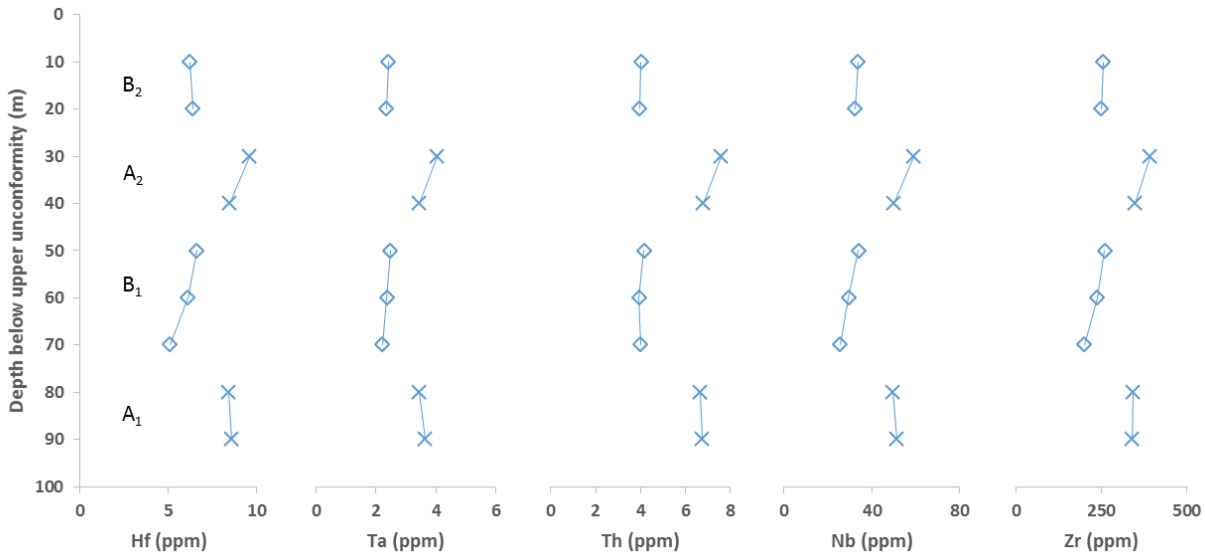

Figure 4.7. Plot of select HFSE abundances versus stratigraphic height for lower basalt transect samples. A type lavas are represented by X, and B type lavas are represented by open symbols.

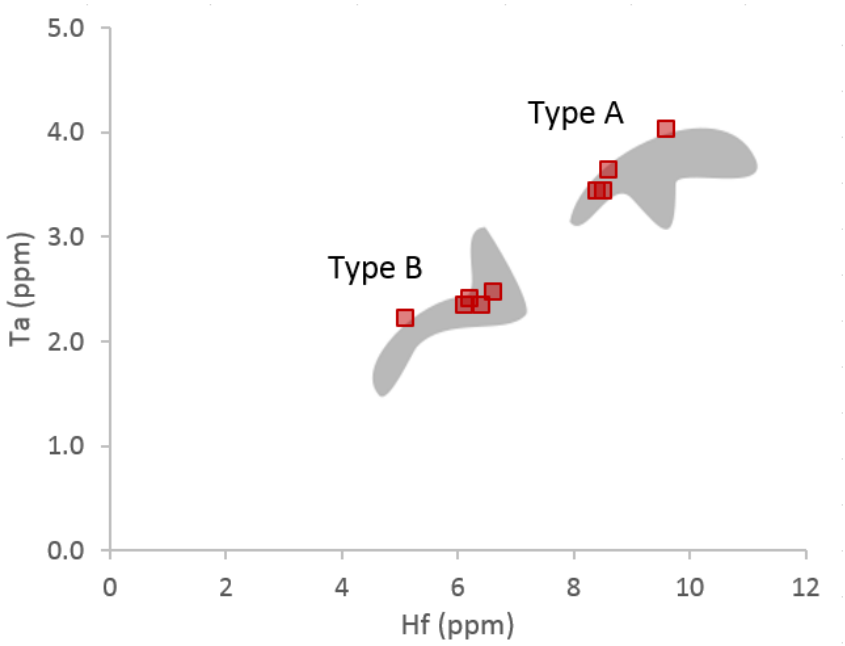

Figure 4.8. Ta vs. Hf content for lower basalt unit transect samples (n=9). Grey fields represent distribution of all lower basalt unit samples.

Table 4.5. Geochemical summary for centre-margin sample sets of diabase sills and dykes.

Sample Name	Sample Type	Mg#	Cr (ppm)	Zr (ppm)	Sc/Y
LH15-EA01-2	Sill centre	43	180	145	1.3
LH15-EA02	Sill upper margin	37	90	193	1.0
LH15-EA04	Sill lower margin	38	90	161	1.0
LH14-22A	Dyke margin	58	40	174	1.4
LH14-22B	Dyke centre	41	50	150	1.3

having 308 ppm Zr, 43 ppm Nb, and a Mg# of 32. These may represent a stratigraphically higher portion of the sill complex that is not preserved in the mainland area, or a separate intrusive body of highly evolved liquids related to the emplacement of the mainland sills.

A centre-margin sample set from one of the mainland sills indicates internal geochemical variation within the sill body (Table 4.5). The coarse centre (LH15-EA01-2) has higher Mg#, Cr, and Sc/Y ratio, and lower incompatible element enrichment than both the upper (LH15-EA02) and lower margins (LH15-EA04). Th/Nb ratio is lower at the sill centre (0.09), compared with the margins (0.10 and 0.11).

The margin of a Union Island Group diabase dyke cutting the Archean basement (LH14-22A) is significantly more primitive than its respective dyke centre (LH14-22B) and has a higher Mg# (58; highest of all Union Island Group samples), slightly higher incompatible element enrichment levels, and a pronounced negative Eu anomaly (Eu/Eu*=0.7). The two samples do not differ in Th/Nb ratio.

4.2 Geochronology

4.2.1 Diabase intrusion LH14-27

Uranium-lead isotope analyses for eight small multi-grain (2–8 grains) baddeleyite fractions from diabase intrusion LH14-27 are presented in Table 4.6. Most of these baddeleyite fractions have Th/U ratios typical for igneous baddeleyite (<0.1; Heaman and LeCheminant, 1993), although fractions #1, #4, and #7 have slightly elevated values (0.13–0.15). Total common Pb contents for all fractions are generally low (<3 pg). All analyses are between 3% and 10% discordant, which indicates a significant component of lead loss occurred. $^{207}Pb/^{206}Pb$ model ages for all analyses range between 2056 Ma and 2029 Ma. A Concordia plot (Fig. 4.9a) shows that the analyses display some scatter but generally follow a linear trend that defines an upper intercept age of 2042±20 Ma (MSWD=11.7). Four baddeleyite fractions (#2, 5, 7, 8) have identical $^{207}Pb/^{206}Pb$ dates within analytical uncertainty and define a regression line with an upper intercept date of 2042±8.0 Ma (2σ; MSWD = 0.34). These four fractions have a weighted mean $^{207}Pb/^{206}Pb$ age of 2042.7±3.0 Ma (2σ; MSWD = 0.23; Fig. 4.9b), which we interpret as the best estimate for the time of baddeleyite crystallization in diabase intrusion LH14-27.

Table 4.6. TIMS U–Pb analysis of baddeleyite fractions for diabase intrusion LH14-27. Associated errors are reported at 1σ.

Fraction	Weight (µg)	U (ppm)	Th (ppm)	Pb (ppm)	Th/U	TCPb (pg)	$^{206}Pb/^{204}Pb$	$^{206}Pb/^{238}U$	$^{207}Pb/^{235}U$	$^{207}Pb/^{206}Pb$	$^{206}Pb/^{238}U$ (Ma)	$^{207}Pb/^{235}U$ (Ma)	$^{207}Pb/^{206}Pb$ (Ma)	%Disc
1 (5)	0.9	137	19	49	0.14	2.0	1386	0.3485 ± 9	6.024 ± 19	0.1254 ± 2	1927.5 ± 4.3	1979.4 ± 2.7	2030.4 ± 2.8	5.9
2 (8)	0.9	135	13	50	0.10	2.4	1131	0.3583 ± 9	6.227 ± 19	0.1261 ± 2	1974.1 ± 4.4	2008.3 ± 2.7	2043.7 ± 2.8	4.0
3 (3)	0.5	249	24	89	0.10	1.4	2038	0.3568 ± 9	6.244 ± 19	0.1269 ± 2	1966.8 ± 4.3	2010.7 ± 2.7	2056.1 ± 2.6	5.0
4 (7)	0.5	464	63	170	0.13	2.9	1792	0.3577 ± 6	6.194 ± 13	0.1256 ± 1	1971.4 ± 3.1	2003.6 ± 1.8	2037.1 ± 1.7	3.8
5 (6)	0.5*	208	23	70	0.11	1.3	1730	0.3354 ± 10	5.830 ± 21	0.1261 ± 2	1864.3 ± 4.8	1950.8 ± 3.1	2044.1 ± 3.3	10.1
6 (3)	0.5*	306	34	110	0.11	1.7	2024	0.3576 ± 8	6.165 ± 16	0.1250 ± 2	1971.0 ± 3.8	1999.5 ± 2.3	2029.2 ± 2.2	3.3
7 (2)	0.5*	100	15	36	0.15	1.8	619	0.3399 ± 19	5.896 ± 41	0.1258 ± 5	1886.0 ± 9.0	1960.6 ± 6.0	2040.4 ± 6.7	8.7
8 (5)	0.5*	307	28	111	0.09	2.9	1168	0.3525 ± 8	6.118 ± 17	0.1259 ± 2	1946.3 ± 3.8	1992.8 ± 2.4	2041.4 ± 2.4	5.4

All atomic ratios are corrected for spike (composition), estimated blank (0.5 pg U, 1.0 pg Pb), and initial common lead (Stacey and Kramers, 1975).

Number in parentheses refers to the number of baddeleyite grains analysed; TCPb refers to total common Pb present in the analysis.

Weights were estimated for fractions #5–8 (marked by asterisk) based on similarity in grain count and grain size to fractions #3 and #4.

Age calculations based on decay constants of Jaffey et al. (1971); $^{206}Pb/^{238}U$ and $^{207}Pb/^{206}Pb$ ages corrected for initial disequilibrium in $^{230}Th/^{238}U$ using a Th/U (magma) ratio of 3.

Model Th/U ratio estimated from radiogenic $^{208}Pb/^{206}Pb$ ratio and $^{207}Pb/^{235}U$ age.

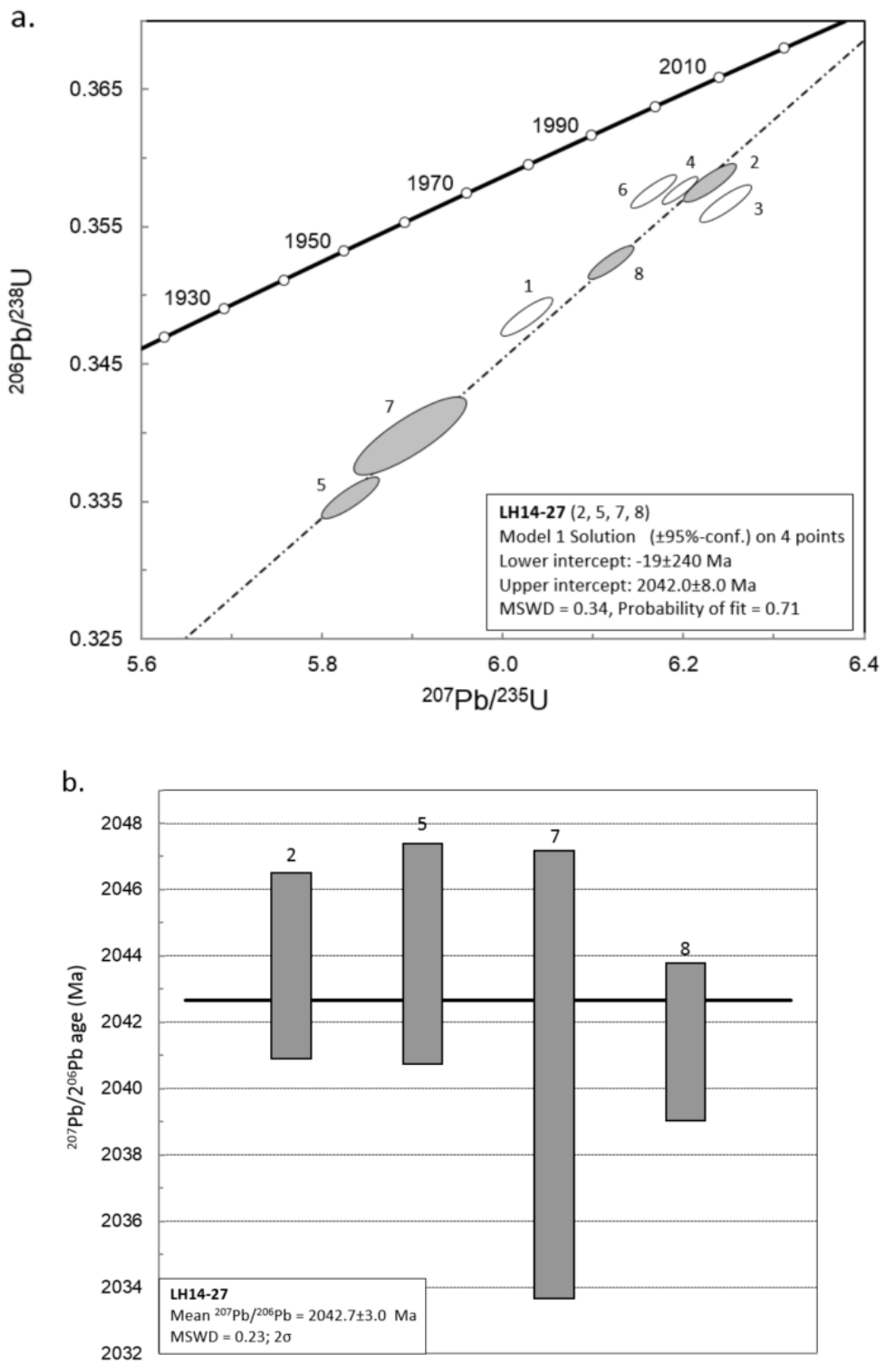

Figure 4.9. U–Pb baddeleyite results for diabase intrusion LH14-27. a) Concordia plot of all eight analyses, with a regression line based on fractions 2, 5, 7, 8 (filled ellipses). b) Weighted mean $^{207}Pb/^{206}Pb$ age plot for fractions 2, 5, 7, 8.

4.2.2 Interflow sediment LH15-EA51

U–Pb LA-MC-ICPMS detrital zircon ages were determined for interflow sediment sample LH15-EA51, collected from volcaniclastic beds on Tuff Island, are reported in Table 4.7. A total of 36 zircon grains were analyzed, yielding a mean age of 2627 Ma and a median age of 2656 Ma, with a standard deviation of 105 Ma (1σ). With one exception (grain #5), all zircon dates are Neoarchean and range between 2704 Ma and 2570 Ma, forming two prominent peaks at 2676±8 Ma and 2603±10 Ma (2σ; Fig. 4.10). This distribution pattern is broadly identical to that of granite crystallization ages within Neoarchean domains of the Slave craton (Geological Survey of Canada, 2013), which include the 2635–2620 Ma Defeat suite, the 2615–2608 Ma Concession suite, the ca. 2596 Ma Prosperous suite, the 2586–2584 Ma Morose granite, the 2585-2581 Ma Contwoyto suite, and the ca. 2582 Ma Yamba suite (van Breemen et al., 1992; Davis and Bleeker, 1999).

Only one zircon grain yielded a Proterozoic $^{207}Pb/^{206}Pb$ age, at 2049±29 Ma (2σ; 4.6% discordant). As this is the youngest zircon analyzed in this sample, we interpret 2049±29 Ma to be the maximum deposition age for this interflow sediment.

4.2.3 Quartz pebble conglomerate LH15-EA15

U–Pb LA-MC-ICPMS detrital zircon ages in conglomerate sample LH15-EA15, located at the base of the upper dolomite unit, are reported in Table 4.8. A total of 81 zircon grains were analyzed (n=88 before ^{204}Pb screening; not screened for discordance). The vast majority of zircon ages range between 2761 Ma and 2558 Ma, forming two prominent peaks at 2607±3 Ma and 2692±4 Ma (2σ; Fig. 4.10). This age distribution, like that of sample LH15-EA51, is similar to Neoarchean granite crystallization ages of the Slave craton.

Three zircon grains (grains #2, 3, and 51) are distinctively younger than the rest of the population, with $^{207}Pb/^{206}Pb$ dates of 2141±37 Ma (35% discordant), 2029±20 Ma (6% discordant), and 2026±19 Ma (4.3% discordant) (2σ). The two youngest ages are identical within analytical uncertainty and also identical with the youngest zircon age from sample LH15-EA51 (grain #5; 2049±29 Ma; 2σ); these identical zircon ages suggest provenance from the same source. We interpret 2026±19 Ma to be the maximum deposition age for the conglomerate bed and hence a maximum deposition age estimate for the upper dolomite unit. High discordance of the 2141±37 Ma zircon grain suggests that its $^{207}Pb/^{206}Pb$ age may have been significantly affected by Pb loss.

Table 4.7. LA-ICPMS U–Pb analysis for detrital zircon grains from interflow sediment sample LH15-EA51.

Spot name	^{206}Pb (cps)	^{204}Pb (cps)	^{207}Pb/^{206}Pb	2 σ	^{207}Pb/^{235}U	2 σ	^{206}Pb/^{238}U	2 σ	ρ
LH15-EA51-1	679585	129	0.1822	0.0019	11.74	0.33	0.4671	0.0122	0.928
LH15-EA51-2	265945	28	0.1839	0.0019	13.56	0.61	0.5347	0.0236	0.974
LH15-EA51-3	214787	28	0.1771	0.0018	12.39	0.48	0.5074	0.0189	0.963
LH15-EA51-4	155982	40	0.1761	0.0019	12.72	0.54	0.5239	0.0216	0.968
LH15-EA51-5	12035	31	0.1264	0.0021	6.22	0.23	0.3570	0.0119	0.897
LH15-EA51-6	304554	45	0.1754	0.0019	10.69	0.42	0.4421	0.0167	0.962
LH15-EA51-7	403747	24	0.1713	0.0018	11.13	0.46	0.4712	0.0191	0.969
LH15-EA51-8	399313	42	0.1810	0.0019	13.32	0.46	0.5336	0.0176	0.954
LH15-EA51-9	196448	40	0.1759	0.0019	12.26	0.41	0.5057	0.0158	0.947
LH15-EA51-10	302467	35	0.1810	0.0019	12.91	0.42	0.5171	0.0158	0.946
LH15-EA51-11	48421	18	0.1821	0.0022	12.85	0.65	0.5117	0.0252	0.970
LH15-EA51-12	224932	37	0.1821	0.0019	12.93	0.39	0.5147	0.0144	0.937
LH15-EA51-13	186561	51	0.1820	0.0019	13.06	0.39	0.5207	0.0146	0.939
LH15-EA51-14	189284	29	0.1849	0.0019	12.79	0.41	0.5016	0.0153	0.947
LH15-EA51-15	156758	10	0.1841	0.0019	13.45	0.67	0.5298	0.0256	0.977
LH15-EA51-16	171952	24	0.1747	0.0018	12.29	0.51	0.5103	0.0206	0.968
LH15-EA51-17	69383	18	0.1856	0.0022	13.80	0.53	0.5391	0.0199	0.953
LH15-EA51-18	198561	17	0.1821	0.0019	13.40	0.42	0.5336	0.0159	0.942
LH15-EA51-19	112824	30	0.1823	0.0020	12.77	0.51	0.5079	0.0195	0.963
LH15-EA51-20	272126	38	0.1734	0.0018	11.71	0.37	0.4898	0.0148	0.944
LH15-EA51-21	187806	49	0.1838	0.0019	12.65	0.47	0.4994	0.0180	0.961
LH15-EA51-22	222930	61	0.1829	0.0019	12.28	0.54	0.4868	0.0207	0.971
LH15-EA51-23	167384	51	0.1829	0.0019	12.41	0.52	0.4919	0.0199	0.968
LH15-EA51-24	280916	67	0.1796	0.0019	12.12	0.48	0.4895	0.0189	0.964
LH15-EA51-25	94187	32	0.1734	0.0018	12.20	0.50	0.5104	0.0203	0.966
LH15-EA51-26	357523	54	0.1787	0.0018	12.11	0.34	0.4914	0.0128	0.930
LH15-EA51-27	178102	33	0.1734	0.0019	11.92	0.45	0.4987	0.0182	0.960
LH15-EA51-28	160617	17	0.1823	0.0019	12.62	0.76	0.5022	0.0299	0.985
LH15-EA51-29	129146	58	0.1837	0.0019	13.13	0.53	0.5185	0.0203	0.966
LH15-EA51-30	156668	45	0.1743	0.0019	11.48	0.43	0.4778	0.0172	0.958
LH15-EA51-31	135257	43	0.1825	0.0019	12.58	0.48	0.5000	0.0185	0.961
LH15-EA51-32	247842	51	0.1743	0.0018	11.83	0.53	0.4925	0.0215	0.972
LH15-EA51-33	130057	45	0.1750	0.0019	11.87	0.41	0.4919	0.0163	0.953
LH15-EA51-34	381195	71	0.1770	0.0018	11.56	0.55	0.4736	0.0220	0.976
LH15-EA51-35	233447	77	0.1750	0.0018	11.99	0.40	0.4972	0.0158	0.949
LH15-EA51-36	78559	42	0.1725	0.0019	11.76	0.38	0.4942	0.0152	0.939

Table 4.7. (continued)

Spot name	Apparent Ages (Ma) $^{207}Pb^*/^{206}Pb^*$	2 σ	$^{207}Pb^*/^{235}U$	2 σ	$^{206}Pb^*/^{238}U$	2 σ	Disc (%)
LH15-EA51-1	2673	17	2584	26	2471	53	9.1
LH15-EA51-2	2689	17	2719	42	2761	98	-3.3
LH15-EA51-3	2626	17	2635	36	2645	80	-0.9
LH15-EA51-4	2616	18	2659	39	2716	91	-4.7
LH15-EA51-5	2049	29	2008	32	1968	56	4.6
LH15-EA51-6	2610	18	2496	36	2360	74	11.4
LH15-EA51-7	2570	17	2534	38	2489	83	3.8
LH15-EA51-8	2662	17	2702	32	2756	73	-4.4
LH15-EA51-9	2614	18	2625	31	2638	67	-1.1
LH15-EA51-10	2662	17	2673	30	2687	67	-1.1
LH15-EA51-11	2672	20	2669	47	2664	107	0.4
LH15-EA51-12	2673	17	2674	28	2677	61	-0.2
LH15-EA51-13	2671	17	2684	28	2702	62	-1.4
LH15-EA51-14	2698	17	2664	30	2620	66	3.5
LH15-EA51-15	2690	17	2711	46	2741	107	-2.3
LH15-EA51-16	2603	17	2627	38	2658	87	-2.6
LH15-EA51-17	2704	19	2736	36	2780	83	-3.5
LH15-EA51-18	2672	17	2708	29	2757	66	-3.9
LH15-EA51-19	2674	18	2663	37	2648	83	1.2
LH15-EA51-20	2591	17	2582	30	2570	64	1.0
LH15-EA51-21	2687	17	2654	35	2611	77	3.4
LH15-EA51-22	2679	17	2626	40	2557	89	5.5
LH15-EA51-23	2680	17	2636	38	2579	85	4.6
LH15-EA51-24	2649	17	2614	37	2568	81	3.7
LH15-EA51-25	2590	18	2620	38	2659	86	-3.2
LH15-EA51-26	2641	17	2613	26	2577	55	3.0
LH15-EA51-27	2590	18	2598	35	2608	78	-0.8
LH15-EA51-28	2674	17	2652	55	2623	127	2.3
LH15-EA51-29	2686	17	2689	38	2693	86	-0.3
LH15-EA51-30	2599	18	2563	34	2518	74	3.8
LH15-EA51-31	2676	17	2649	35	2614	79	2.8
LH15-EA51-32	2599	17	2591	41	2581	92	0.8
LH15-EA51-33	2606	18	2594	32	2579	70	1.3
LH15-EA51-34	2625	17	2569	44	2499	95	5.8
LH15-EA51-35	2606	17	2604	31	2602	68	0.2
LH15-EA51-36	2582	19	2585	30	2589	65	-0.3

Disc = Discordance relative to origin = 100% * (($^{207}Pb/^{206}Pb$ age - $^{206}Pb/^{238}U$ age)/($^{207}Pb/^{206}Pb$ age))

Table 4.8. LA-ICPMS U–Pb analysis for detrital zircon grains from quartz pebble conglomerate sample LH15-EA15. Samples with high common Pb content are excluded (struck out values) using a filter of ^{204}Pb > 1000 cps (n=7).

Spot name	^{206}Pb (cps)	^{204}Pb (cps)	$^{207}Pb/^{206}Pb$	2 σ	$^{207}Pb/^{235}U$	2 σ	$^{206}Pb/^{238}U$	2 σ	ρ
LH15-EA15-1	260711	34	0.1749	0.0018	11.25	0.43	0.4663	0.0173	0.965
LH15-EA15-2	407349	154	0.1332	0.0029	4.69	0.29	0.2553	0.0146	0.935
LH15-EA15-3	3275058	261	0.1409	0.0019	12.66	0.47	0.6515	0.0226	0.929
LH15-EA15-4	209035	87	0.1741	0.0018	9.73	0.38	0.4055	0.0154	0.963
LH15-EA15-5	449978	45	0.1730	0.0018	11.90	0.53	0.4989	0.0214	0.973
LH15-EA15-6	151706	43	0.1762	0.0019	11.95	0.54	0.4920	0.0215	0.972
LH15-EA15-7	233814	85	0.1749	0.0018	9.59	0.43	0.3977	0.0175	0.974
LH15-EA15-8	302318	34	0.1770	0.0018	12.14	0.47	0.4977	0.0184	0.964
LH15-EA15-9	357199	39	0.1748	0.0018	12.11	0.62	0.5027	0.0254	0.981
LH15-EA15-10	139841	56	0.1762	0.0019	10.08	0.41	0.4147	0.0162	0.966
LH15-15-11	194423	112	0.1798	0.0019	8.62	0.40	0.3477	0.0158	0.975
~~LH15-15-12~~	~~242552~~	~~1119~~	~~0.2056~~	~~0.0030~~	~~3.50~~	~~0.40~~	~~0.1233~~	~~0.0141~~	~~0.992~~
LH15-15-12A	182323	28	0.1860	0.0019	12.77	0.69	0.4980	0.0265	0.981
LH15-15-13	207224	221	0.1839	0.0032	11.05	0.65	0.4357	0.0244	0.956
LH15-15-14	137776	42	0.1752	0.0018	12.29	0.53	0.5090	0.0215	0.971
LH15-15-15	188997	42	0.1840	0.0019	13.45	0.59	0.5302	0.0226	0.972
~~LH15-15-16~~	~~433486~~	~~2757~~	~~0.2405~~	~~0.0031~~	~~4.52~~	~~0.23~~	~~0.1363~~	~~0.0068~~	~~0.968~~
LH15-15-17	286654	157	0.1854	0.0023	10.36	0.48	0.4053	0.0181	0.962
LH15-15-18	228313	54	0.1750	0.0018	12.21	0.49	0.5059	0.0198	0.968
LH15-15-19	160565	100	0.1758	0.0019	10.18	0.36	0.4202	0.0140	0.951
LH15-15-20	194506	76	0.1822	0.0019	6.60	0.30	0.2627	0.0118	0.975
LH15-EA15-21	136429	86	0.1830	0.0019	7.95	0.35	0.3150	0.0137	0.973
LH15-EA15-22	441339	83	0.1700	0.0018	11.65	0.45	0.4969	0.0183	0.961
LH15-EA15-23	366544	83	0.1730	0.0018	11.63	0.45	0.4874	0.0184	0.965
LH15-EA15-24	165862	113	0.1721	0.0019	6.40	0.77	0.2698	0.0323	0.996
LH15-EA15-25	199716	905	0.1926	0.0021	2.95	0.18	0.1110	0.0067	0.984
LH15-EA15-26	200050	276	0.1810	0.0019	6.37	0.38	0.2553	0.0149	0.984
~~LH15-EA15-27~~	~~519174~~	~~1201~~	~~0.1997~~	~~0.0024~~	~~10.26~~	~~0.38~~	~~0.3725~~	~~0.0130~~	~~0.944~~
LH15-EA15-28	231853	114	0.1812	0.0018	12.69	0.62	0.5080	0.0243	0.978
LH15-EA15-29	209602	131	0.1736	0.0019	7.50	0.43	0.3130	0.0176	0.982
LH15-EA15-30	94039	126	0.1824	0.0020	12.43	0.58	0.4943	0.0224	0.973
LH15-EA15-31	43168	91	0.1826	0.0021	12.82	0.53	0.5091	0.0202	0.960
~~LH15-EA15-32~~	~~326072~~	~~2272~~	~~0.2386~~	~~0.0068~~	~~4.29~~	~~0.31~~	~~0.1305~~	~~0.0088~~	~~0.920~~
LH15-EA15-33	270026	366	0.1864	0.0019	8.95	0.41	0.3484	0.0154	0.974
LH15-EA15-34	111028	491	0.2161	0.0026	6.29	0.63	0.2111	0.0209	0.993
LH15-EA15-35	44236	123	0.1778	0.0020	11.48	0.53	0.4683	0.0210	0.969
LH15-EA15-36	145449	119	0.1768	0.0019	11.57	0.49	0.4746	0.0194	0.968
LH15-EA15-37	220134	284	0.1982	0.0035	13.07	0.58	0.4783	0.0195	0.919
LH15-EA15-38	377345	142	0.1744	0.0018	5.75	0.30	0.2392	0.0123	0.981
~~LH15-EA15-39~~	~~282354~~	~~2577~~	~~0.2084~~	~~0.0024~~	~~9.23~~	~~0.42~~	~~0.3213~~	~~0.0140~~	~~0.966~~
LH15-EA15-40	313223	295	0.1759	0.0020	4.82	0.39	0.1985	0.0158	0.990
LH15-EA15-41	120283	147	0.1751	0.0019	11.73	0.52	0.4859	0.0210	0.971
LH15-EA15-43	102841	13	0.1879	0.0019	12.29	0.52	0.4741	0.0194	0.971
LH15-EA15-44	229762	268	0.1898	0.0026	10.31	0.44	0.3939	0.0161	0.948
LH15-EA15-45	311121	7	0.1846	0.0019	12.73	0.55	0.4999	0.0208	0.972
LH15-EA15-46	390489	20	0.1757	0.0022	12.95	0.58	0.5348	0.0231	0.960
LH15-EA15-47	166997	56	0.1742	0.0022	9.96	0.69	0.4148	0.0281	0.983
LH15-EA15-48	210294	78	0.1917	0.0022	9.30	0.69	0.3519	0.0257	0.988
LH15-EA15-49	224820	666	0.2008	0.0023	5.76	0.29	0.2083	0.0102	0.974
LH15-EA15-50	330938	0	0.1884	0.0019	13.35	0.60	0.5138	0.0224	0.974

Table 4.8. (continued)

Spot name	^{206}Pb (cps)	^{204}Pb (cps)	$^{207}Pb/^{206}Pb$	2 σ	$^{207}Pb/^{235}U$	2 σ	$^{206}Pb/^{238}U$	2 σ	ρ
LH15-EA15-51	69397	0	0.1250	0.0014	6.00	0.24	0.3479	0.0135	0.958
LH15-EA15-52	240651	32	0.1803	0.0019	7.25	0.35	0.2916	0.0136	0.977
LH15-EA15-53	256577	126	0.1922	0.0024	8.83	0.51	0.3333	0.0186	0.975
LH15-EA15-54	165425	2	0.1776	0.0018	8.75	0.32	0.3574	0.0125	0.959
LH15-EA15-55	720016	34	0.1737	0.0019	11.34	0.44	0.4736	0.0175	0.960
LH15-EA15-56	213249	9	0.1739	0.0018	4.72	0.29	0.1970	0.0118	0.986
LH15-EA15-57	272203	17	0.1766	0.0019	9.37	0.47	0.3846	0.0189	0.977
LH15-EA15-58	129201	0	0.1831	0.0019	12.33	0.57	0.4885	0.0221	0.974
LH15-EA15-59	268939	367	0.1832	0.0019	6.34	0.26	0.2510	0.0101	0.969
LH15-EA15-60	247678	503	0.1966	0.0038	3.31	0.31	0.1223	0.0110	0.977
LH15-EA15-61	242830	0	0.1754	0.0026	10.32	0.46	0.4267	0.0180	0.943
LH15-EA15-64	279493	160	0.1873	0.0026	11.89	0.66	0.4605	0.0247	0.967
LH15-EA15-65	211360	0	0.1758	0.0018	12.21	0.62	0.5038	0.0250	0.979
LH15-EA15-66	143540	0	0.1747	0.0018	9.15	0.36	0.3801	0.0146	0.966
LH15-EA15-67	131409	24	0.1806	0.0019	5.72	0.30	0.2299	0.0118	0.980
LH15-EA15-68	428101	65	0.1610	0.0019	16.36	0.93	0.7371	0.0409	0.979
LH15-EA15-69	289158	123	0.1887	0.0027	12.15	0.58	0.4670	0.0211	0.953
LH15-EA15-70	302150	0	0.1977	0.0020	14.39	0.62	0.5278	0.0223	0.973
LH15-EA15-71	151897	0	0.1818	0.0019	4.57	0.36	0.1825	0.0143	0.992
LH15-EA15-72	280459	0	0.1807	0.0018	12.39	0.50	0.4971	0.0195	0.967
~~LH15-EA15-73~~	~~288151~~	~~2491~~	~~0.2493~~	~~0.0030~~	~~7.94~~	~~0.45~~	~~0.2309~~	~~0.0128~~	~~0.977~~
LH15-EA15-74	235082	0	0.1749	0.0018	11.55	0.45	0.4790	0.0179	0.965
LH15-EA15-75	228960	102	0.1863	0.0021	9.74	0.44	0.3794	0.0168	0.969
LH15-EA15-76	354952	514	0.1941	0.0030	10.88	0.77	0.4065	0.0282	0.976
LH15-EA15-77	125398	14	0.1893	0.0024	10.74	0.39	0.4114	0.0140	0.936
LH15-EA15-78	261857	0	0.1791	0.0019	9.95	0.51	0.4028	0.0203	0.979
~~LH15-EA15-79~~	~~176296~~	~~2251~~	~~0.2772~~	~~0.0059~~	~~1.75~~	~~0.15~~	~~0.0457~~	~~0.0037~~	~~0.966~~
LH15-EA15-80	292410	78	0.1774	0.0024	10.69	0.82	0.4373	0.0328	0.984
LH15-EA15-81	127305	14	0.1754	0.0035	5.79	0.35	0.2393	0.0136	0.943
LH15-EA15-82	101772	0	0.1861	0.0019	13.06	0.59	0.5089	0.0226	0.975
LH15-EA15-83	333374	0	0.1831	0.0019	11.27	0.75	0.4463	0.0292	0.988
LH15-EA15-84	170899	0	0.1248	0.0013	6.08	0.24	0.3534	0.0134	0.963
LH15-EA15-85	577271	53	0.1731	0.0017	7.25	0.53	0.3036	0.0220	0.991
LH15-EA15-86	56454	0	0.1866	0.0020	12.84	0.53	0.4989	0.0200	0.966
LH15-EA15-87	379148	0	0.1750	0.0018	11.49	0.53	0.4761	0.0215	0.976
LH15-EA15-88	160801	0	0.1857	0.0020	12.13	0.55	0.4735	0.0207	0.972
LH15-EA15-89	442065	0	0.1788	0.0022	12.23	0.50	0.4958	0.0194	0.953
LH15-EA15-90	149872	9	0.1824	0.0021	11.89	0.43	0.4729	0.0162	0.950

Table 4.8. (continued)

Spot name	Apparent Ages (Ma) $^{207}Pb^*/^{206}Pb^*$	2 σ	$^{207}Pb^*/^{235}U$	2 σ	$^{206}Pb^*/^{238}U$	2 σ	Disc (%)
LH15-EA15-1	2605	17	2544	35	2468	75	6.4
LH15-EA15-2	2141	37	1765	50	1466	74	35.2
LH15-EA15-3	2239	24	2655	35	3234	88	-56.9
LH15-EA15-4	2597	18	2410	36	2194	70	18.3
LH15-EA15-5	2587	17	2597	41	2609	91	-1.1
LH15-EA15-6	2617	17	2601	41	2579	92	1.7
LH15-EA15-7	2606	17	2397	41	2159	80	20.1
LH15-EA15-8	2625	17	2615	35	2604	79	1.0
LH15-EA15-9	2604	17	2613	47	2625	108	-1.0
LH15-EA15-10	2618	17	2442	37	2237	73	17.2
LH15-15-11	2651	17	2298	42	1924	75	31.6
~~LH15-15-12~~	~~2872~~	~~23~~	~~1526~~	~~87~~	~~750~~	~~81~~	~~78.0~~
LH15-15-12A	2707	17	2663	50	2605	113	4.6
LH15-15-13	2688	28	2527	53	2331	109	15.8
LH15-15-14	2608	17	2627	40	2652	91	-2.1
LH15-15-15	2690	17	2712	41	2742	94	-2.4
~~LH15-15-16~~	~~3123~~	~~21~~	~~1734~~	~~42~~	~~823~~	~~39~~	~~78.1~~
LH15-15-17	2701	21	2467	42	2193	83	22.1
LH15-15-18	2606	17	2620	37	2639	84	-1.6
LH15-15-19	2613	18	2452	32	2262	63	15.9
LH15-15-20	2673	17	2059	40	1504	60	48.9
LH15-EA15-21	2680	17	2225	39	1765	67	38.9
LH15-EA15-22	2558	18	2576	35	2601	79	-2.0
LH15-EA15-23	2587	17	2575	36	2559	79	1.3
LH15-EA15-24	2578	18	2033	100	1540	162	45.1
LH15-EA15-25	2765	18	1394	45	679	39	79.3
LH15-EA15-26	2662	17	2029	51	1466	76	50.1
~~LH15-EA15-27~~	~~2824~~	~~20~~	~~2458~~	~~34~~	~~2041~~	~~61~~	~~32.2~~
LH15-EA15-28	2664	17	2657	45	2648	103	0.7
LH15-EA15-29	2593	18	2172	50	1756	86	36.8
LH15-EA15-30	2674	18	2637	43	2589	96	3.9
LH15-EA15-31	2676	19	2666	38	2653	86	1.1
~~LH15-EA15-32~~	~~3111~~	~~45~~	~~1692~~	~~58~~	~~791~~	~~50~~	~~79.0~~
LH15-EA15-33	2710	17	2333	41	1927	73	33.3
LH15-EA15-34	2952	19	2017	84	1235	110	63.7
LH15-EA15-35	2633	19	2563	42	2476	92	7.2
LH15-EA15-36	2623	17	2570	39	2504	84	5.5
LH15-EA15-37	2811	28	2685	41	2520	85	12.5
LH15-EA15-38	2600	17	1939	44	1383	64	51.8
~~LH15-EA15-39~~	~~2893~~	~~19~~	~~2361~~	~~41~~	~~1796~~	~~68~~	~~43.3~~
LH15-EA15-40	2615	19	1788	65	1167	84	60.3
LH15-EA15-41	2607	18	2583	41	2553	91	2.5
LH15-EA15-43	2724	17	2626	39	2502	84	9.8
LH15-EA15-44	2741	22	2463	39	2141	74	25.6
LH15-EA15-45	2695	17	2660	40	2613	89	3.7
LH15-EA15-46	2612	21	2676	41	2762	96	-7.0
LH15-EA15-47	2598	21	2431	62	2237	127	16.4
LH15-EA15-48	2757	18	2368	65	1944	121	34.1
LH15-EA15-49	2832	19	1941	43	1220	54	62.3
LH15-EA15-50	2729	17	2705	41	2673	95	2.5

Table 4.8. (continued)

Spot name	Apparent Ages (Ma) $^{207}Pb^*/^{206}Pb^*$	2 σ	$^{207}Pb^*/^{235}U$	2 σ	$^{206}Pb^*/^{238}U$	2 σ	Disc (%)
LH15-EA15-51	2029	20	1976	35	1925	64	6.0
LH15-EA15-52	2656	17	2143	42	1649	68	42.8
LH15-EA15-53	2761	21	2321	51	1854	89	37.7
LH15-EA15-54	2630	17	2312	33	1970	59	29.1
LH15-EA15-55	2594	18	2552	35	2499	76	4.4
LH15-EA15-56	2596	17	1772	50	1159	63	60.3
LH15-EA15-57	2622	18	2375	45	2098	87	23.4
LH15-EA15-58	2681	17	2630	43	2564	95	5.3
LH15-EA15-59	2682	17	2024	36	1443	52	51.4
LH15-EA15-60	2798	32	1485	70	744	63	77.5
LH15-EA15-61	2610	25	2464	41	2291	81	14.5
LH15-EA15-64	2719	23	2596	51	2442	108	12.2
LH15-EA15-65	2614	17	2621	46	2630	106	-0.8
LH15-EA15-66	2603	17	2353	36	2077	68	23.6
LH15-EA15-67	2658	17	1935	44	1334	62	55.0
LH15-EA15-68	2466	20	2898	53	3560	150	-58.2
LH15-EA15-69	2731	23	2616	44	2470	92	11.5
LH15-EA15-70	2808	16	2776	40	2732	93	3.3
LH15-EA15-71	2669	17	1744	64	1081	77	64.4
LH15-EA15-72	2659	17	2634	37	2602	83	2.6
~~LH15-EA15-73~~	~~3180~~	~~19~~	~~2224~~	~~50~~	~~1339~~	~~66~~	~~63.8~~
LH15-EA15-74	2605	17	2569	36	2523	78	3.8
LH15-EA15-75	2709	19	2411	41	2074	78	27.4
LH15-EA15-76	2777	25	2513	64	2199	128	24.5
LH15-EA15-77	2737	21	2501	33	2221	64	22.2
LH15-EA15-78	2644	17	2430	46	2182	93	20.6
~~LH15-EA15-79~~	~~3347~~	~~33~~	~~1026~~	~~52~~	~~288~~	~~23~~	~~93.3~~
LH15-EA15-80	2628	23	2497	68	2338	145	13.1
LH15-EA15-81	2610	33	1945	51	1383	70	52.1
LH15-EA15-82	2708	17	2684	42	2652	96	2.5
LH15-EA15-83	2681	17	2545	60	2379	129	13.5
LH15-EA15-84	2026	19	1988	34	1951	64	4.3
LH15-EA15-85	2588	17	2142	63	1709	108	38.5
LH15-EA15-86	2712	18	2668	38	2609	85	4.6
LH15-EA15-87	2606	17	2564	42	2510	93	4.4
LH15-EA15-88	2705	17	2614	41	2499	90	9.2
LH15-EA15-89	2642	21	2622	38	2596	83	2.1
LH15-EA15-90	2675	19	2596	33	2496	70	8.1

Disc = Discordance relative to origin = 100% * (($^{207}Pb/^{206}Pb$ age - $^{206}Pb/^{238}U$ age)/($^{207}Pb/^{206}Pb$ age))

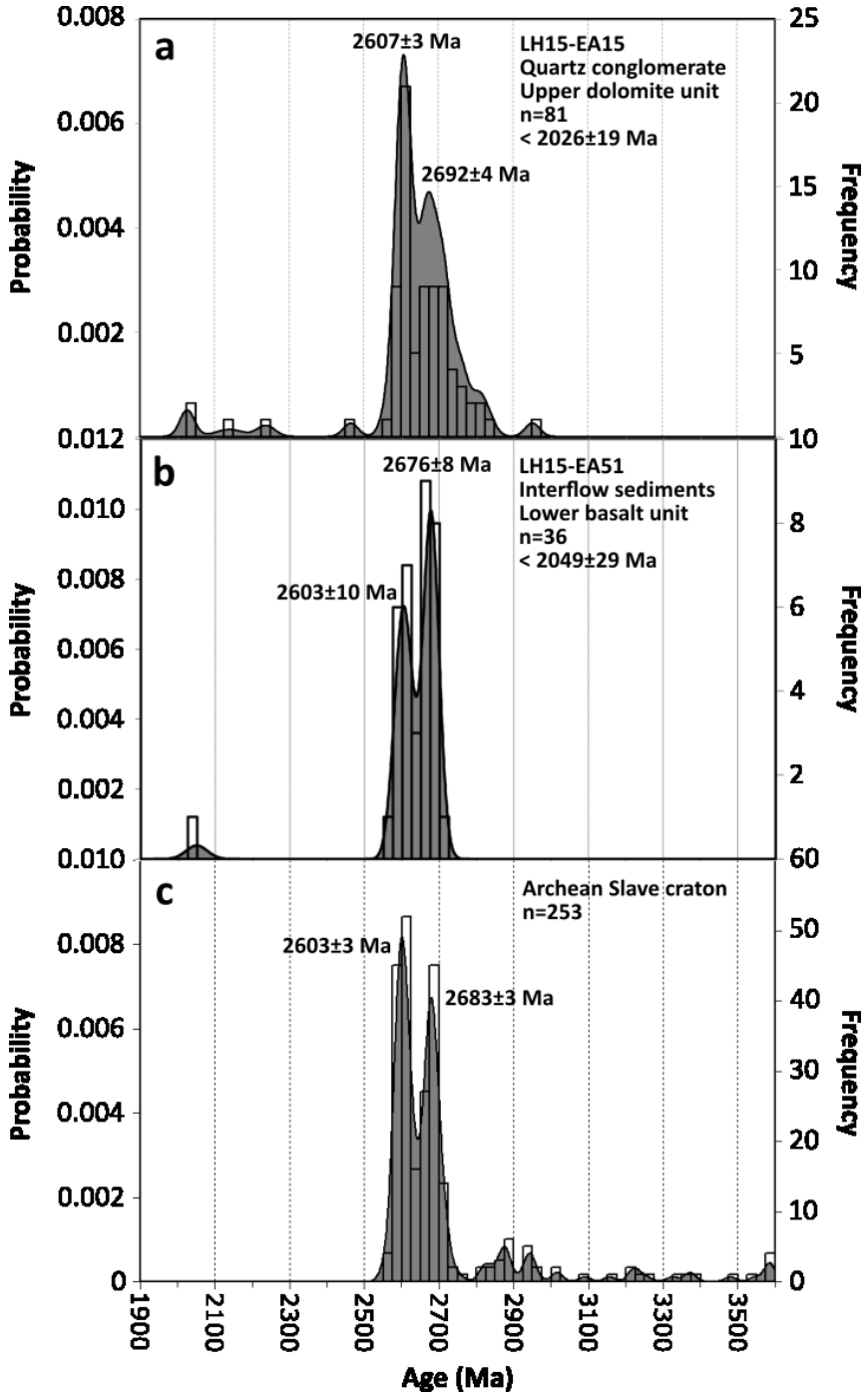

Figure 4.10. Probability distribution diagrams of detrital zircon $^{207}Pb/^{206}Pb$ ages of a) conglomerate sample LH15-EA15, b) interflow sediment sample LH15-EA51, with c) a summary of Archean igneous crystallization ages of the Slave craton (Geological Survey of Canada, 2013). Probability distribution of the Slave detrital zircon ages is based on an assigned error of ±15 Ma to allow comparison with detrital zircon ages. Data for LH15-EA51 were screened for discordance using a filter of ^{204}Pb > 1000 cps (7 analyses excluded).

4.3 Isotope analysis

4.3.1 Rb–Sr

Rubidium–strontium isotope analyses of Union Island Group mafic units are presented in Table 4.9 and Fig. 4.11. Measured present-day $^{87}Sr/^{86}Sr$ ratios of the samples range from 0.70716 to 0.71463, with $^{87}Rb/^{86}Sr$ ratios of 0.15–0.51. These present-day isotopic ratios overlap for the three units distinguished above (lower basalt, upper basalt, and diabase intrusions). On the Rb–Sr isochron plot, the lower basalt unit (n=5) plots along a slightly scattered trend; linear regression yields an imprecise Rb–Sr isochron age of 1403±880 Ma (MSWD=1527) with an initial $^{87}Sr/^{86}Sr$ ratio of 0.7032±0.0046 (2σ). Diabase sample LH14-14 plots approximately along this trend, suggesting compositional similarity with the lower basalt. Linear regression of the six points yields an errorchron age of 1538±930 Ma (MSWD=1533) and an initial $^{87}Sr/^{86}Sr$ ratio of 0.7029±0.0050 (2σ). Despite the imprecision associated with linear regression of data spanning a limited range of $^{87}Sr/^{86}Sr$ and $^{87}Rb/^{86}Sr$, our calculated initial $^{87}Sr/^{86}Sr$ ratios agrees with reported values of 0.7021–0.7030 for igneous clinopyroxene separates from the diabase sills (Goff et al., 1982).

Resetting of Rb–Sr systematics under low-grade metamorphism is well-documented for basaltic rocks (e.g., Cann, 1970; Wood et al., 1976; Page, 1978). Goff (1984) suggests that Rb–Sr systematics of rocks of the East Arm basin may have been affected by Rb-bearing metamorphic fluids that moved along the post-1.86 Ga McDonald Fault and/or the ca. 1.9 Ga Great Slave Lake shear zone. In Rb–Sr isochron space, Rb-addition shifts data points to the right (i.e. higher $^{87}Rb/^{86}Sr$ ratios). This is demonstrated in our data by a 2043 Ma reference isochron which, when anchored at any of the clinopyroxene initial $^{87}Sr/^{86}Sr_{(i)}$ ratios reported by Goff et al. (1982), plots to the left of the lower basalt unit and diabase samples from this study (Fig. 4.12). Furthermore, diabase sample LH14-14 and basalt sample LH15-EA20, which plot closest to this reference line, have low LOI values (3.4 wt% and 6.8 wt%, respectively), while samples with higher LOI values plot further to the right of the reference line. Therefore, Rb-addition during deformation and/or metamorphism is the most likely cause for the scattering of Rb–Sr data in these samples; samples LH14-14 and LH15-EA20 represent the least altered Rb–Sr compositions of the Union Island Group lower basalt.

Table 4.9. Rb–Sr analysis of Union Island Group samples. Shown for comparison are clinopyroxene analyses (UI102C, UI102A, UI63; marked by asterisk) reported in Goff et al. (1982). Initial $^{87}Sr/^{86}Sr_{(i)}$ ratio for samples analyzed in this study are calculated based on a U–Pb crystallization age of 2043 Ma.

UNIT/Sample	Rb (ppm)	Sr (ppm)	$^{87}Rb/^{86}Sr$	$^{87}Sr/^{86}Sr$	2 S.E.	$^{87}Sr/^{86}Sr_{(i)}$	Age from isochron (Ma)	$^{87}Sr/^{86}Sr_{(i)}$ from isochron
LOWER BASALT, DIABASE INTRUSIONS							1564	0.7029
LH14-14	32.1	218.9	0.42	0.71410	0.00002	0.7018		
UI79B	10.5	68.3	0.44	0.71098	0.00002	0.6981		
LH15-EA12	9.5	53.3	0.51	0.71463	0.00003	0.6997		
LH15-EA18	12.9	156.7	0.24	0.70716	0.00001	0.7003		
LH15-EA20	5.4	93.9	0.17	0.70741	0.00001	0.7026		
LH15-EA23	12.4	112.2	0.32	0.70954	0.00002	0.7003		
UPPER BASALT							1752	0.7059
UI39	18.8	213.3	0.26	0.71226	0.00002			
LH14-33	14.6	275.4	0.15	0.70973	0.00003			
CLINOPYROXENES IN DIABASE SILL*								
UI102C-cpx						0.7027		
UI102A-cpx						0.7021		
UI63-cpx						0.7030		

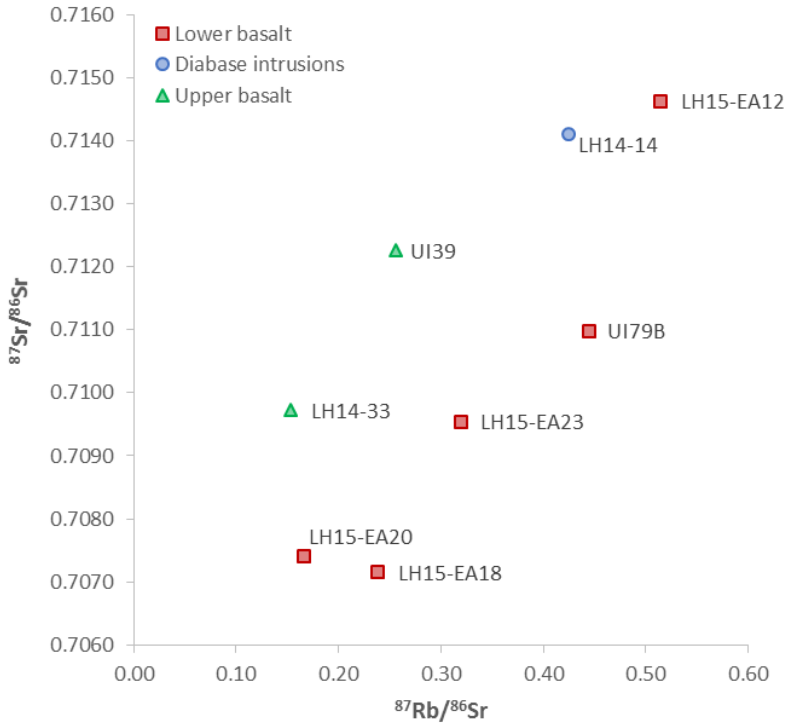

Figure 4.11. $^{87}Sr/^{86}Sr$ vs. $^{87}Rb/^{86}Sr$ plot for Union Island Group samples.

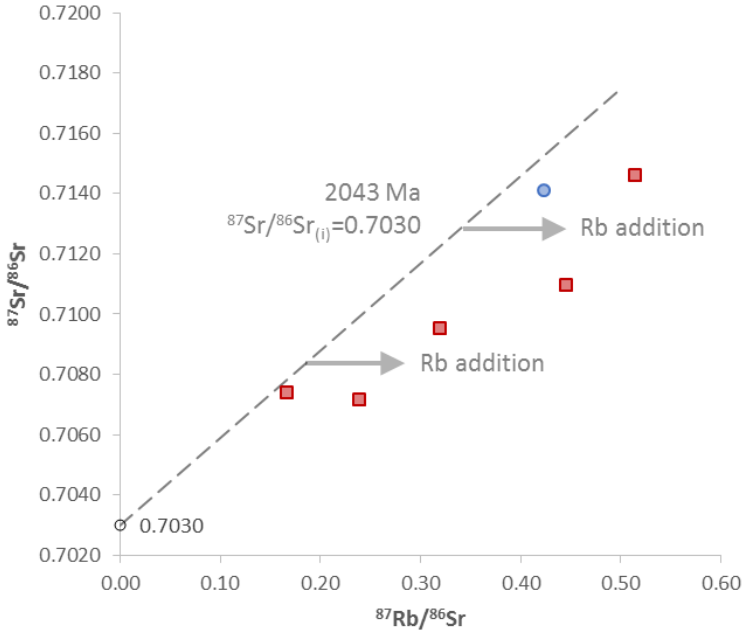

Figure 4.12. $^{87}Sr/^{86}Sr$ vs. $^{87}Rb/^{86}Sr$ plot of samples from the lower basalt unit and diabase intrusions, compared to a reference isochron of 2043 Ma anchored at an initial $^{87}Sr/^{86}Sr$ ratio of 0.7030, which is the highest value reported for clinopyroxenes from the diabase sills (Goff et al., 1982). Symbols as defined in Figure 4.11. Arrows indicate direction of data scatter expected from Rb addition during metamorphism.

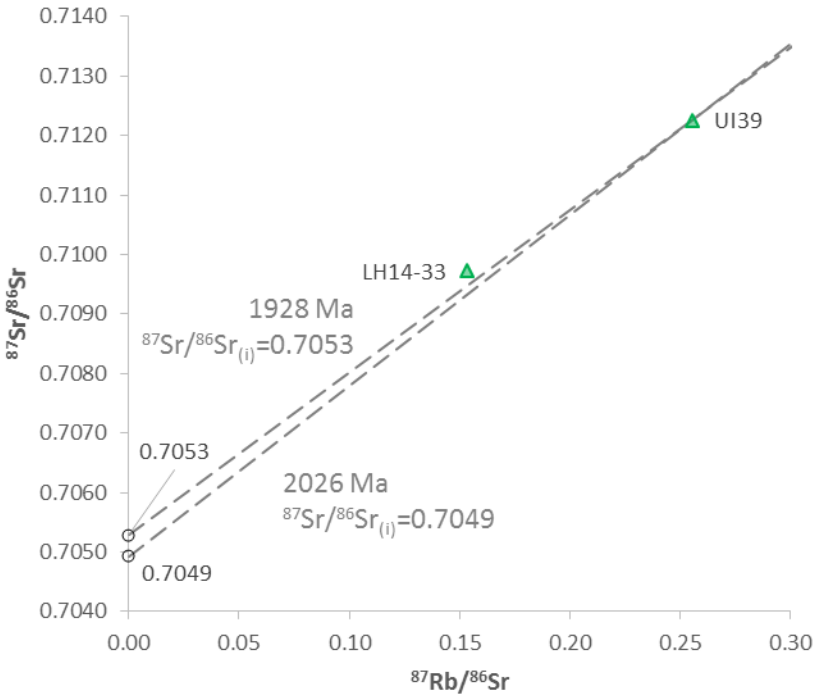

Figure 4.13. $^{87}Sr/^{86}Sr$ vs. $^{87}Rb/^{86}Sr$ plot of upper basalt samples, plotted with a reference isochrons of 2026 Ma and 1928 Ma, the lower and upper age limits for the upper basalt, anchored on sample UI39.

In contrast to the lower basalt unit, the upper basalt unit (n=2) has generally higher $^{87}Sr/^{86}Sr$ ratios for the same values of $^{87}Rb/^{86}Sr$. Although direct age dating is unavailable for the upper basalt unit at present, we estimate the initial Sr isotopic composition given the maximum age constraint of ca. 2026 Ma (sec. 4.2.3). A 2026 Ma reference isochron anchored on sample UI39, which has a lower LOI value (3.98 wt%), yields an initial $^{87}Sr/^{86}Sr$ ratio of 0.7049 (Fig. 4.13). This initial $^{87}Sr/^{86}Sr$ ratio would be higher if the age of the upper basalt unit is younger than 2026 Ma, and lower if $^{87}Rb/^{86}Sr$ ratios has been increased due to Rb addition during metamorphism.

4.3.2 Sm–Nd

Samarium–neodymium isotope analyses of Union Island Group mafic rocks are summarized in Table 10. Present-day $^{143}Nd/^{144}Nd$ ratios for all Union Island Group mafic rocks range from 0.511760–0.512186, with ε_{Nd} values between –8.8 and –17.1. Time-corrected (t=2.04 Ga) initial $^{144}Nd/^{143}Nd_{(i)}$ ratios for four lower basalt samples and one diabase feeder range between 0.51004–0.51015 ($\varepsilon_{Nd(t)}$: +1.1 to +3.2) and are indistinguishable. Based on the relatively large eruption age constraint range of 2026–1928 Ma, samples of the upper basalt have possible initial $^{144}Nd/^{143}Nd_{(i)}$ ratios ranging 0.51009–0.51011 ($\varepsilon_{Nd(i)}$: +1.5 – +2.0) at 2026 Ma, and 0.51019–0.51021 ($\varepsilon_{Nd(i)}$: +1.0 – +1.4) at 1928 Ma. A small shift of ~0.5 in estimated $\varepsilon_{Nd(i)}$ is associated with the age uncertainty. These values overlap with the mid- to low-$\varepsilon_{Nd(i)}$ range of the lower basalt and diabase feeders.

Table 4.10. Sm–Nd analysis for Union Island Group samples.

UNIT/Sample	Sm (ppm)	Nd (ppm)	$^{147}Sm/^{144}Nd$	$^{143}Nd/^{144}Nd$	$^{143}Nd/^{144}Nd_{(i)}$*	$\varepsilon Nd_{(i)}$*
LOWER BASALT						
KIA09-009	7.99	36.98	0.1306	0.511802	0.510043	1.1
LH15-EA09	7.39	36.86	0.1212	0.511760	0.510128	2.7
LH15-EA14	7.42	33.23	0.1350	0.511917	0.510098	2.1
UI68D	5.08	23.09	0.1330	0.511945	0.510155	3.2
DIABASE INTRUSIONS						
LH14-27	8.73	41.54	0.1271	0.511833	0.510123	2.6
UPPER BASALT						
LH14-34	4.47	17.21	0.1570	0.512186	0.510092	1.5
LH14-36	3.28	13.26	0.1495	0.512109	0.510114	2.0

* $^{143}Nd/^{144}Nd_{(i)}$ ratios and $\varepsilon_{Nd(i)}$ calculated using Sm decay constant of 6.54×10^{-12} yr^{-1} (Lugmair and Marti, 1978), with an assigned age of 2043 Ma for the lower basalt and diabase intrusions, and 2026 Ma for the upper basalt.

5 DISCUSSION

5.1 Timing of the Union Island Group mafic magmatism

Multiple metamorphic and structural overprints have complicated stratigraphic interpretations of the East Arm basin (Goff et al., 1982; Hoffman, 1981; Hoffman et al., 1977; Johnson, 1990). The 1928±11 Ma Wilson Island Group has previously been interpreted to be the oldest Proterozoic supracrustal package within the basin and is stratigraphically below the Union Island Group (Fig. 5.1a; Bowring et al., 1984; Hoffman, 1987, 1988a; Kjarsgaard et al., 2013), despite the important observation that the Union Island Group unconformably overlies Archean basement in a number of locations (Thorstad, 1976; Hoffman et al., 1977; this study, sec. 2.2.2). This existing stratigraphic interpretation is primarily based on correlating metamorphic fabrics, and that the Wilson Island Group has been metamorphosed to a higher grade than the rest of basin stratigraphy (Hoffman et al., 1977; Johnson, 1990). However, the geology preserved in the East Arm basin is deformed with numerous NE-trending faults, high strain gradients and complex folding. Clear evidence for primary stratigraphic contacts between the Wilson Island and Union Island groups have not been reported; the Wilson Island Group is structurally isolated from both the Union Island Group and the Archean basement. Although the Union Island Group deposition has previously been interpreted to post-date the Wilson Island Group (Fig. 5.1a), this stratigraphic relationship is equivocal. The lack of any preserved stratigraphic contact between these two supracrustal packages is a significant weakness in understanding the Paleoproterozoic geologic evolution of the basin. In order to address this uncertainty in the stratigraphic relationship, we have attempted to date mafic units within the East Arm basin that, based on field and geochemical criteria, are most likely a product of Union Island Group mafic magmatism.

Our key finding of the 2042.7±3.0 Ma U–Pb baddeleyite crystallization age of diabase intrusion LH14-27, which intrudes volcaniclastic beds interpreted to belong to be Union Island Group lower basalt unit, forces a reinterpretation of the stratigraphic relationship between the Wilson Island and Union Island groups. This diabase intrusion has compatible and incompatible trace-element abundances that exactly overlaps the composition of the Union Island Group lower basalt unit and is geochemically distinct from other Paleoproterozoic mafic intrusions in the East Arm basin. Sample LH14-27, together with the lower basalt unit and other East Arm basin diabase sills and dykes sampled in this study, are characterized by an alkaline composition (Fig. 4.2), high levels of

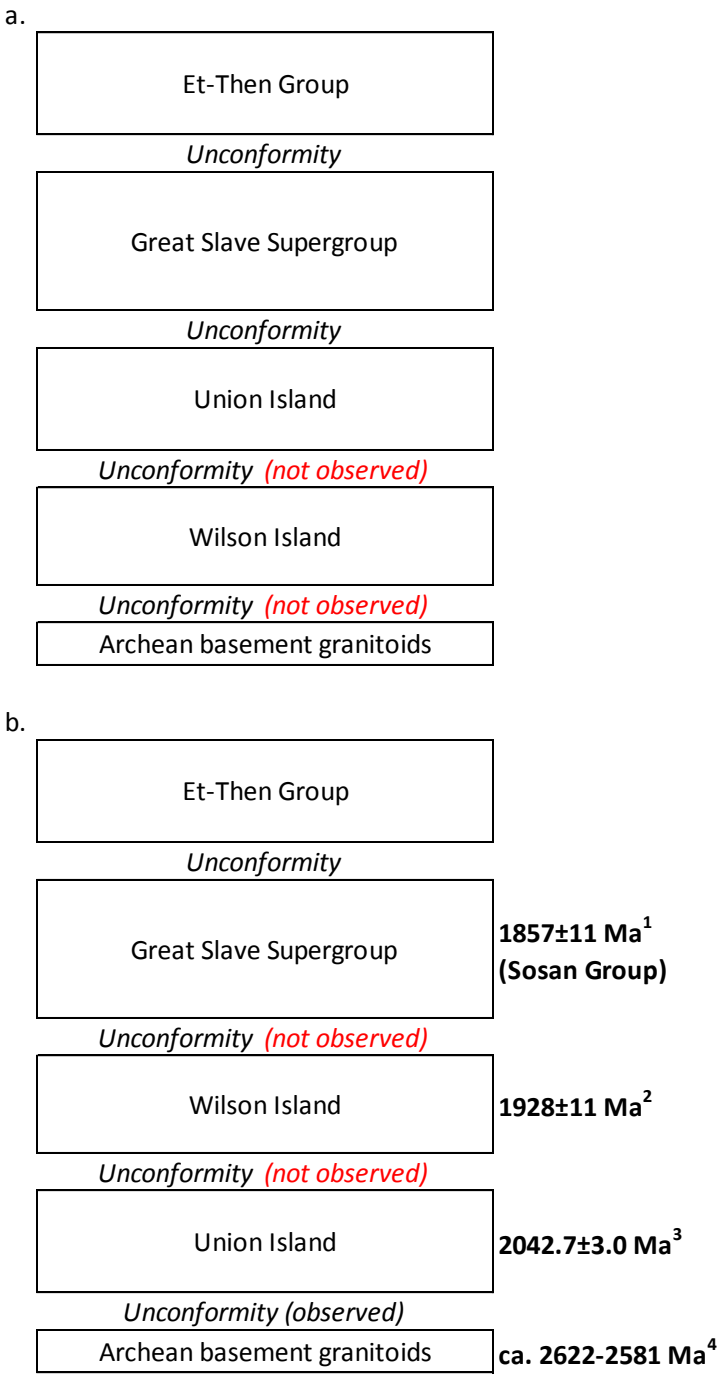

Figure 5.1. a) Stratigraphic model of the East Arm basin prior to this study, as adopted by Hoffman (1969, 1973), Hoffman et al. (1974, 1977), and Kjarsgaard et al. (2013a). b) Revised stratigraphic model based on U–Pb dating in this study, compared with U–Pb igneous ages from the rest of the basin and from the Archean basement. The Wilson Island Group is structurally isolated from the rest of the basin strata. Age data from [1]Bowring et al. (1984), [2]Kjarsgaard et al. (2013), [3]this study, and [4]Kjarsgaard et al. (2013b).

incompatible element enrichment, Zr/Nb ratios in the range of 7–8, and a lack of negative Nb anomalies on primitive mantle normalized multi-element plots. Such attributes are distinguished from the upper basalt package (Zr/Nb: 23–26) and other similar-trending regional mafic dyke swarms including the Malley (Zr/Nb: 13–17), Mackay (Zr/Nb: 13–19), and Hearne swarms (Zr/Nb: 18–26), plus the North Simpson Island dyke (Zr/Nb: 8–11), and the South Simpson Island dykes (Zr/Nb: 10–12). In a Zr vs. Nb plot (Fig. 4.4), the lower basalt unit forms a high Zr and Nb continuation of the trend defined by the diabase sills and dykes. Given the strong geochemical similarity and close stratigraphic association, we interpret many of the diabase sills and dykes investigated in this study to represent the feeder system for the lower basalt unit. The 2042.7±3.0 Ma crystallization age of for the diabase feeder LH14-27, therefore, represents a minimum age constraint for the Union Island Group lower basalt unit; it also places a minimum depositional age for the volcaniclastic sequence which the diabase intrudes.

Our age dating result demonstrates that the Union Island Group predates the 1928±11 Ma Wilson Island Group by over 100 million years. The Union Island Group therefore represents the earliest known record of volcanic activity and sedimentation in the East Arm basin (Fig. 5.1b). This is supported by our observations of a basal unconformity between the lower dolomite unit and the Slave craton basement (sec. 2.2.2), in addition to the prevalence of Archean basement ages in the detrital zircon record of sedimentary samples LH15-EA15 and LH15-EA51, and the absence of 2.0–1.9 Ga zircon ages from the Taltson and Thelon zones from these sedimentary samples (sec. 4.2). The youngest of these detrital zircons have indistinguishable $^{207}Pb/^{206}Pb$ ages of 2049±29 Ma, 2029±20 Ma, and 2026±19 Ma, which are consistent with our age constraint of 2042.7±3.0 Ma for the lower basalt unit. These young detrital zircons are unlikely to have originated from felsic plutons of the Taltson and Thelon zones (TTZ), for which the earliest known crystallization age is 1986±2.4 Ma (Bostock et al., 1987). It is therefore more plausible that these young zircons were derived from weathering of the lower volcanic package; zircons are observed in some of the lower basalt unit samples (sec. 3.4).

We note that the 2042.7±3.0 Ma crystallization age for diabase feeder LH14-27 is indistinguishable, with analytical uncertainties taken into account, from the 2038±3 Ma McKee Lake dykes (Pehrsson et al., 1993). Similar to the Union Island Group dykes, the McKee Lake dykes are 060°-trending and exhibit similar petrographic attributes such as a subophitic texture,

the replacement of clinopyroxene by chlorite and epidote, and the skeletal habit of titanite-mantled ilmenite (Pehrsson et al., 1993). We therefore propose that the McKee Lake dykes are an extension of the Union Island Group dykes and that, overall, diabase intrusions associated with the Union Island Group have a uniform age.

There exists no reliable radiometric age dating for the upper basalt unit. Although at present the two basalt packages of Union Island Group are not known to occur in one continuously exposed stratigraphic sequence, the upper basalt unit is interpreted to post-date the lower basalt unit based on the observation that it overlies the black shale unit whereas the upper basalt unit overlies the upper dolomite unit, which in turns overlies the black shale unit in the Union Island area (Thorstad, 1976; Hoffman et al., 1977). Consistent with this, we observed in fieldwork of this study a continuous section of black shale–upper dolomite–upper basalt on the south side of Camp Island. As the Wilson Island Group post-dates the Union Island Group in our revised stratigraphic model, the eruption age of the upper basalt unit is bracketed between 2026 Ma, the maximum deposition age of conglomerate LH15-EA15, and 1928 Ma, the age of felsic volcanism of the Wilson Island Group.

Detrital zircon dates from sedimentary samples LH15-EA15 and LH15-EA51 are dominated by Neoarchean ages and distinctively lack any zircons that indicate provenance from the 2.0–1.9 Ga TTZ. In contrast, sedimentary rocks of the younger Wilson Island Group, Great Slave Supergroup, and Et-Then Group show a prominent ca. 2.0–1.9 Ga detrital zircon population, interpreted to reflect significant erosion of the TTZ and westerly to northwesterly sediment transport into the East Arm basin (van Breemen et al., 2013; Shaulis et al., 2014). The absence of 2.0–1.9 Ga detrital zircons from the Union Island Group sedimentary rocks either reflects paleocurrent directions from the west or that the samples were deposited prior to the development of the TTZ. There are no available paleocurrent measurements of sedimentary units of the Union Island Group. If the latter interpretation is correct, then the upper age constraint for the upper basalt unit should be placed at 1986±2.4 Ma, the earliest age of magmatism in the TTZ (Bostock et al., 1987).

5.2 Eruption dynamics of the lower basalt unit

A unique feature of the lower basalt unit revealed in the detailed basalt stratigraphy transect is the identification of two geochemically distinct types of lava flows. The flows can be distinguished based on petrographic textures and HFSE enrichment levels (sec. 4.1.6). Higher levels of

incompatible element enrichment in type A lavas imply that it represents a more evolved composition relative to type B lavas. The alternating nature of the two lava types throughout the lower basalt sequence suggests close temporal association throughout the eruption history of the entire unit; there is no one-step transition from one composition to the other. Although inflation of a basalt flow by synvolcanic sills also may account for the interlayered nature of the two lava types, the presence of pillowed flows throughout the lower basalt unit precludes this. Cyclic geochemical variations in lava flows can be created by episodic recharge of magma into a fractionating chamber (Shervais et al., 2006). Magma erupted from a newly recharged chamber will be more primitive in composition (type B). Then, as the chamber continues to undergo fractional crystallization, the remaining liquid becomes more evolved prior to erupting (type A). We note, however, that the HFSE gap between the two lava types is very distinct (Fig. 4.8); no sample from the lower basalt unit records an intermediate composition between the two types, as is typically seen in lava packages showing cyclic geochemical variations (cf. Huijsmans and Barton, 1989; Shervais et al., 2006).

An alternative theory for the distinction between type A and B lavas in the lower basalt unit is that they reflect two consanguineous magma chambers that evolved slightly differently but were simultaneously eruptive (Fig. 5.2). Simultaneous activity of multiple magma chambers may be sustained by a complex plumbing system (Medynski et al., 2013), which is represented in the Union Island Group by the feeder sills and dykes. The evolution of two individual magma chambers is also supported by the observation that, in flows A_2 and B_2 (Fig. 4.7), Ta and Hf levels of the bottom-most samples (representing initial composition of each flow) are similar to those of the uppermost samples from layers A_1 and B_1 (representing final composition of previous flows), respectively. This reflects fractional crystallization occurring in both chambers, creating a decreasing HFSE trend for each chamber. The observed HFSE volcanistratigraphic profile results from interlayering between lavas from these two continuously evolving chambers (Fig. 5.2). If both type A and type B lavas were derived from a single chamber undergoing fractional crystallization with periodic recharge, one would expect progressive shifts from type B to type A flows instead of the observed step-like pattern (Fig. 4.7). Also, periodic recharge would cause more irregular shifts in HFSE composition between each flow. Therefore, the distinction of type A and type B lavas is best explained by two consanguineous magma chambers undergoing fractional crystallization, with chamber A having a slightly more evolved composition overall.

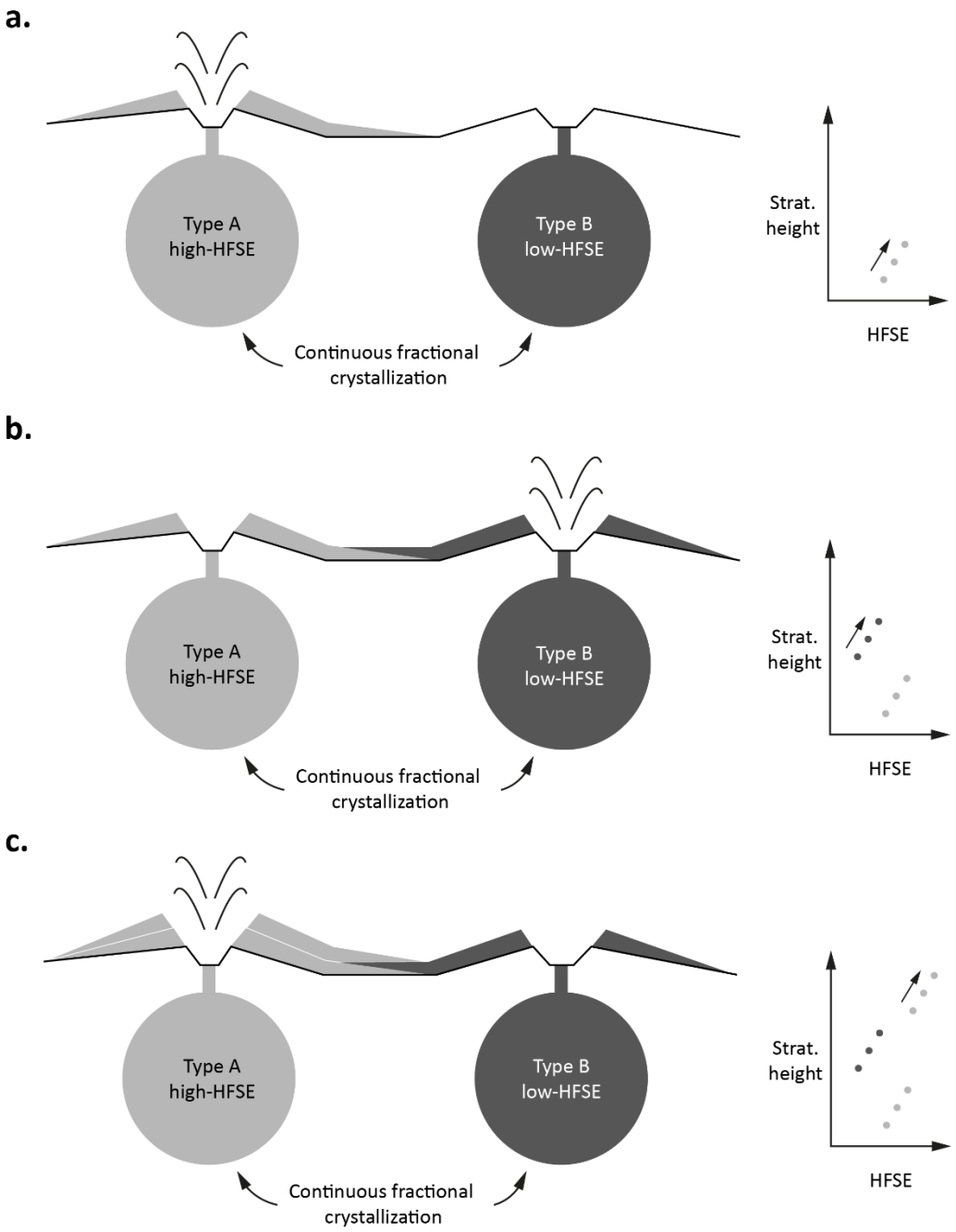

Figure 5.2. Simplified cartoon illustrating the two-chamber model for the origin of type A and B lavas in the lower basalt unit and of the observed HFSE variations with stratigraphy. a) Chamber A erupts, depositing high-HFSE type A lavas that show progressive enrichment in HFSE up-stratigraphy due to closed-system fractional crystallization. b) Chamber B erupts, depositing lavas with lower HFSE content but nevertheless showing similar HFSE enrichment up-stratigraphy. c) Chamber A erupts again, this time depositing lavas with higher HFSE content than the previous type A flow.

These two magma chambers contributed to most of the lavas of the lower basalt unit, as evidenced in the bimodal distribution of all lower basalt samples in Ta–Hf space (Fig. 4.8).

Fractionation mechanisms within the diabase sills and dykes

The diabase feeder sills and dykes, similar to the lower basalt unit, display a range of geochemical variations (section 4.1.7). One of the sampled sills displays a more evolved composition at the fine-grained margins compared to the more primitive centre. Assuming that the margins represent the first injected magma, their more evolved compositions can be explained by prior fractionation in a magma chamber that was poorly mixed. This more evolved magma was injected first into the black shale unit and the sill was subsequently inflated by the arrival of the less evolved. Alternatively, the more primitive sill centre may reflect a recharge event of the magma chamber by less evolved magma.

Dyke centre sample LH14-22A displays a negative Eu anomaly, which can be explained by flow segregation of plagioclase phenocrysts away from the dyke margin due to grain dispersive pressure (Komar, 1972). In contrast to the sill discussed above, the dyke margin has a more primitive composition than the centre, which is consistent with initial penetration by a primitive magma before inflation by magmas with more evolved compositions. The different emplacement mechanism suggests that this dyke may not have been physically linked to the sill discussed above.

5.3 Geochemical insights into the origin of the Union Island Group mafic magmatism

The two stratigraphically separate mafic magmatic packages of the Union Island Group are geochemically distinct (Table 5.1). The lower Union Island Group magmatism, consisting of the lower basalt unit and the diabase feeders, is marked by high incompatible element enrichment levels, low Zr/Nb ratios (7–10), and a large composition range. The upper Union Island Group magmatism (represented by the upper basalt unit), in contrast, displays a lower level of incompatible elements, higher Zr/Nb ratios (23–26), and a restricted composition range. These geochemical differences suggest that the upper package was produced by magmatic processes and sources distinct from those which produced the lower package. We evaluate the petrogenesis for these two temporally distinct volcanic events by comparing geochemical results with literature data, in addition to using geochemical modeling to assess the observed incompatible element compositions. Essentially, we ask the questions: 1) what magmatic processes contributed to the

Table 5.1. Geochemical summary of the Union Island Group mafic magmatism, sample LH14-14 (most primitive composition of the lower magmatism), and of select mantle reservoirs. For the lower and upper magmatism, ranges of values are denoted in brackets. OIB=ocean island basalt, N-MORB=normal mid-ocean ridge basalt, PM=primitive mantle, DM=depleted mantle. OIB and N-MORB data: Sun and McDonough (1989); PM data: McDonough and Sun (1995); DM data: Salters and Stracke (2004); East Arm basin Slave crust data: Janzen (2015).

	Lower magmatism	LH14-14	Upper magmatism	OIB	N-MORB	PM	DM	Average EAB Slave Crust
n	44		14[a]					8[b]
Ni (ppm)	20-260 (78)[c]	130	80-120 (103)	190[d]	149.5[e]	1960	1960	<20
Cr (ppm)	20-240 (66)[f]	240	220-330 (289)	324[d]	446[g]	2625	2500	<20
TiO_2 (wt%)	1.6-4.5 (2.8)	1.6	1.5-1.7 (1.6)	3.1	1.1	0.20	0.13	0.23
Zr (ppm)	108-438 (247)	108	83-101 (93)	280	74	10.5	7.94	133
Nb (ppm)	13-62 (33)	13	1.8-4.0 (3.4)	48	2.33	0.66	0.21	6.9
Zr/Nb	6.6-9.8 (7.5)	8.3	23-26 (24)[h]	5.8	31.8	16	38	21.5
Th/Nb	0.08-0.19 (0.12)	0.12	0.16-0.32 (0.21)	0.08	0.05	0.12	0.07	2.23
Nb/Hf	4.4-6.2 (5.3)	5.0	0.8-1.6 (1.3)	6.2	1.1	2.3	1.1	1.8
Gd/Yb_N	1.8-2.3 (2.1)[i]	2.4	2.0-2.4 (2.3)[j]	2.9	1.0	1.0	0.8	3.4
$\varepsilon_{Nd(i)}$	+1.1 - +3.2 (n=5)		+1.7 - +2.1 (n=2)			0	+7.5[k]	-6.0[l]
$^{87}Sr/^{86}Sr_{(i)}$	0.7021-0.7030[m]		> 0.7049			0.7021[n]	0.7019[k]	0.7048[o]-0.7069[p]

a. Includes eight analyses from Kjarsgaard et al. (2013a).
b. Janzen (2015).
c. excluding four samples falling below l.o.d. (20 ppm).
d. Fitton et al. (1991).
e. Hart et al. (1999).
f. excluding one sample falling below l.o.d. (20 ppm).
g. Klein (2004).
h. Excludes samples LH14-32, LH14-33, LH14-34, and LH14-36.
i. Excludes samples UI95D, LH15-EA11, and LH15-EA12, which show HREE remobilization under alteration (Appendix A).
j. Excludes sample UI35A, which shows REE remobilization under alteration (Appendix A).
k. Rehkämper and Hofmann (1997).
l. Average composition of southwest Slave craton Archean crust (n=51); Davis and Hegner (1992), Yamashita et al. (1999).
m. Clinopyroxene data (n=3) from Goff et al. (1982).
n. Bulk silicate earth (BSE); Workman and Hart (2005).
o. Composition of a felsic crust derived from a melt extracted from the BABI reservoir at 2.6 Ga, assuming a Rb/Sr ratio of 0.027 (Workman and Hart, 2005) in the melt.
p. Fort Enterprise Granite; McCulloch and Wasserburg (1978).

observed geochemical trends, and 2) what mantle and/or crustal components were involved the formation of these magmas?

5.3.1 Fractional crystallization

Low Ni and Cr contents, low Mg# values, and chondrite-normalized enrichment of incompatible elements indicate that both volcanic packages of the Union Island Group represent evolved basaltic liquids and do not represent a primary melt (Table 5.1). Primary basaltic magmas derived from single-stage partial melting of mantle reservoirs are typically associated with high Mg# (67–85), Cr (684–1711 ppm), and Ni (278–943 ppm) contents (Jaques and Green, 1980; Francis, 1985). These are significantly higher than the maximum values of Mg# 45, 240 ppm Cr, 260 ppm Ni of the lower magmatism, and Mg# 57, 330 ppm Cr, 120 ppm Ni of the upper magmatism.

The large range of incompatible element levels (e.g., Zr, Nb; Fig. 4.4) in the lower magmatism reflects extensive fractional crystallization. Incompatible elements are not significantly incorporated into major basalt-forming minerals and are therefore progressively enriched in an evolving liquid. The lack of significant variations in Ni, Cr (Figs 4.3f, g), and of large Eu anomalies suggests that neither olivine nor plagioclase were a significant fractionating phase during the eruptive stage. Similarly, the slightly increasing trend of TiO_2 versus Mg# (Fig. 4.3e) does not suggest significant fractionation of Ti-bearing oxide phases such as Ti-magnetite and ilmenite (Okamoto, 1979; Villemant et al., 1981). Clinopyroxene fractionation may have been responsible for some of the observed geochemical variations, as evidenced in positive correlation between Sc/Y ratio and Mg# (Fig. 5.3). In the most evolved samples (lowest Mg# and/or highest Zr), high enrichment of incompatible elements is reflected in the crystallization of late-stage accessory minerals, such as zircon (in high-Zr samples) and apatite (in high-P samples). Based on these enrichment trends, the most primitive magma composition of the lower magmatism is represented by sample LH14-14 which has the lowest incompatible element contents (e.g., 108 ppm Zr, 13 ppm Nb, 1.6 wt% TiO_2). Modeling using Zr and Nb contents shows that the entire range of incompatible element levels in the lower magmatism can be produced by ~80% fractional crystallization (Allègre and Minster, 1978) from this primitive composition (Fig. 5.4a).

While varying degrees of partial melting can also create variations in incompatible-element content, there is no evidence in the lower magmatism for significant fractionation between

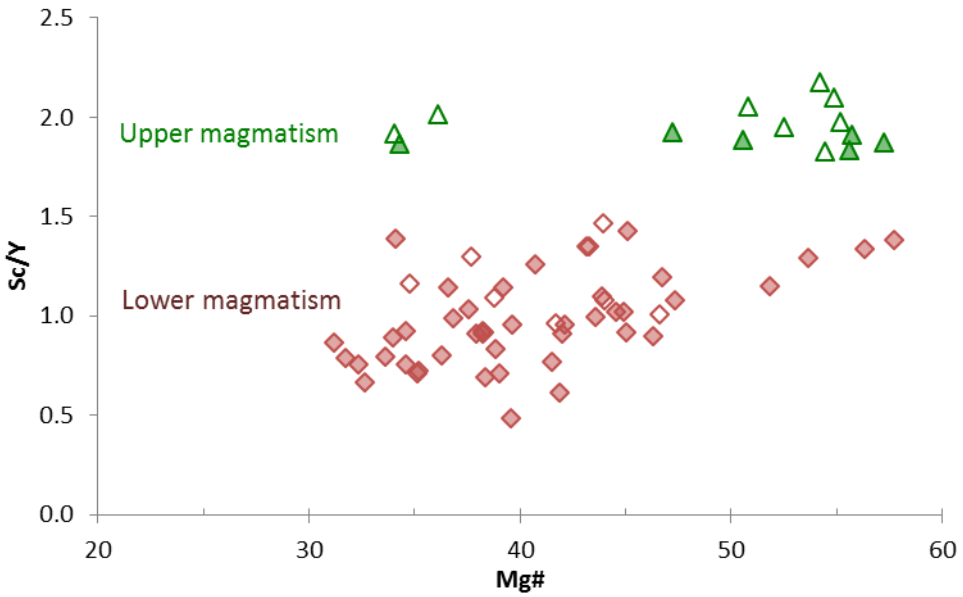

Figure 5.3. Sc/Y ratio vs. Mg# plot. The lower magmatism is shown as red diamonds and the upper magmatism as green triangles. Data from Kjarsgaard et al. (2013a) are shown as open symbols.

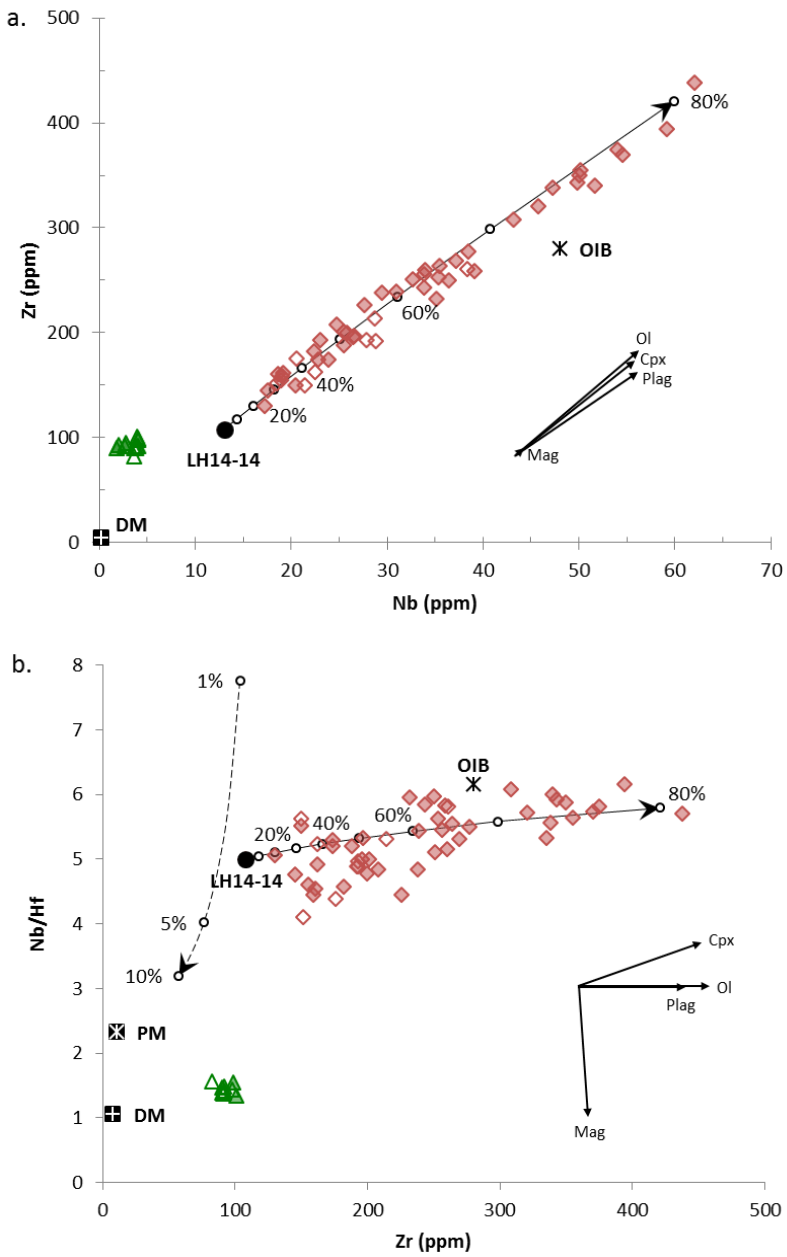

Figure 5.4. a) Zr vs. Nb plot illustrating fractional crystallization model (Allègre and Minster, 1978) with sample LH14-14 as starting composition. b) Nb/Hf vs. Zr plot comparing magma evolution path for a fractional crystallization model (solid curve) with that for an equilibrium partial melting model (dashed curve; Shaw, 1970). Symbols as defined in Figure 5.3. Inset shows melt evolution vectors resulting from 50% simple fractionation of each of the individual mineral phases. Partial melting assumes a primitive mantle (PM) source composition (McDonough and Sun, 1995). Points along the fractional crystallization curve are labelled at 10% intervals. Modeling parameters are summarized in Appendix B. Upper basalt samples LH14-32, LH14-33, LH14-34, and LH14-36 are not plotted in diagram B due to scattering in Nb/Hf ratios caused by Nb analytical imprecision.

individual incompatible elements; Nb/Hf (4.4–6.2) and Zr/Nb ratios (6.6–9.8) maintain a fairly narrow range over a large range of Zr levels (108–438; Table 5.1, Fig. 5.4b). Therefore we discount varying degrees of source partial melting as a significant factor of the observed variations in the lower magmatism.

Low levels of Cr, Ni, and Mg# in sample LH14-14 relative to primary basalt magmas indicates origin from a primary magma via fractional crystallization of olivine, clinopyroxene, and/or spinel. Modeling indicates that 30–40% fractional crystallization of olivine+clinopyroxene is required to produce the composition of LH14-14 from a primary basaltic magma; the addition of 2–5% spinel lowers that estimate to 10–15% (Fig. 5.5). In all scenarios, clinopyroxene is the dominant fractionating phase.

In contrast to the lower magmatism, incompatible-element levels in the upper magmatism are relatively constant regardless of Mg# (Fig. 4.3d, e, h). The lack of compositional variation indicates limited fractional crystallization during the eruptive stage (Fig. 5.4). Given the uniform composition of the upper magmatism, the low Mg#, Cr, and Ni values may be due to 1) fractional crystallization of a primary melt followed by extensive homogenization within the magma body prior to eruption, or 2) a mantle source composition that is evolved with respect to Mg#, Cr, and Ni.

5.3.2 Lithospheric contamination

In order to infer the geochemical composition of possible mantle sources that produced the Union Island Group magmatic packages, an evaluation of lithospheric contamination is necessary to determine to what extent these magmas reflect their source geochemistry. The Union Island Group basalts erupted over Archean felsic crust belonging to the Slave craton (Janzen, 2015), which overlies a long-lived (ca. 2.7 Ga) subcontinental lithospheric mantle (SCLM) that shows complex chemical heterogeneity (Griffin et al., 1999; Kopylova and Russell, 2000; Kopylova and Caro, 2004; Aulbach et al., 2013). Interaction with these chemically distinct lithospheric reservoirs can impart vastly different geochemical signatures to a primary magma during its evolution and ascent.

Positive $\varepsilon_{Nd(i)}$ values (+1.2 – +3.0) in both Union Island Group basalt packages suggests the involvement of a depleted mantle reservoir with time-integrated Nd depletion. The lower

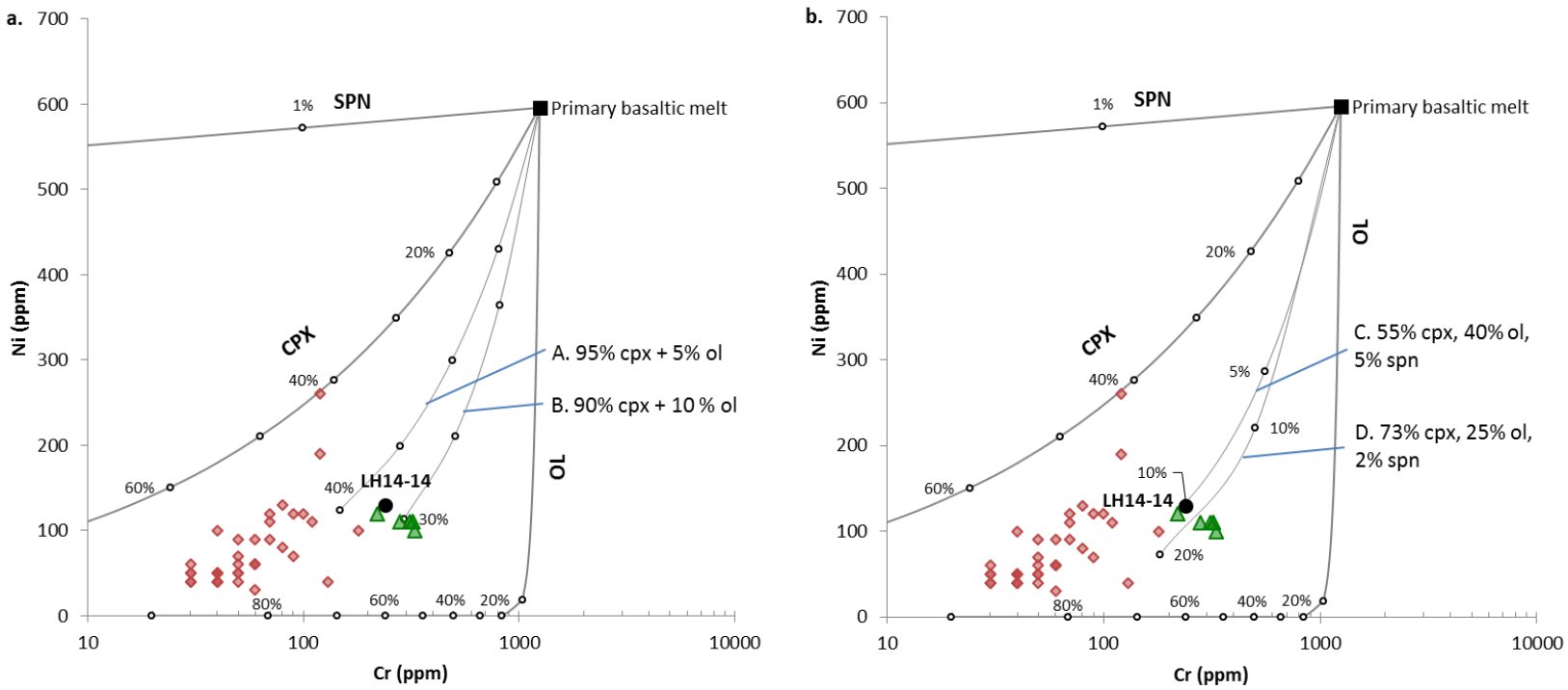

Figure 5.5. Ni vs. Cr plots showing evolution path of a primary basaltic melt (Francis, 1985) undergoing spinel (SPN), clinopyroxene (CPX), and olivine (OL) fractionation (bold curves), and fractionation of mixed mineral assemblages (A to D, fine curves). If no spinel is present in the crystallizing assemblage, the primitive composition of sample LH14-14 can be produced by 30–40% fractionation of predominantly clinopyroxene. If 2–5% spinel were present, the estimate is lowered to 10–15% fractional crystallization. Symbols as defined in Figure 5.3. Model parameters are summarized in Appendix B.

magmatism further displays a negative correlation between $\varepsilon_{Nd(i)}$ values and indices of magma fractionation (e.g., Zr; Fig. 5.6), which can be explained by 1) progressive assimilation of radiogenic crustal Nd from the Archean felsic crust, or 2) a progressively decreasing input of the depleted mantle reservoir in a magma source that is otherwise chondritic ($\varepsilon_{Nd(i)}$ = ~0; Table 5.1, Fig. 5.7)

Incompatible element data do not support a crustal contamination model for either magmatic package. Neoarchean granitoids, which dominate the southern Slave craton and occur as inliers in the East Arm basin, have high Nd levels (average 30 ppm) and $\varepsilon_{Nd(i)}$ values ranging from +1.2 to -12.7 (Davis and Hegner, 1992; Janzen, 2015; Yamashita et al., 1999). Given the very low Nd concentration of 0.713 ppm estimated for depleted mantle (Salters and Stracke, 2004), isotopic mixing between a basaltic melt derived from the depleted mantle and the Neoarchean crust would be dominated by the latter's unradiogenic composition. Secondly, such mixing would also result in a predominantly crustal signature in incompatible elements. However, Nb content of the lower basalt is much higher than Archean crustal levels (4–10 ppm; Janzen, 2015) and does not suggest crustal contamination of a depleted magma. A crustal signature is also absent from the upper basalt unit as evidenced in a characteristic chrondrite-normalized enrichment order of La>Th>Nb (Fig. 4.6) as opposed to the Th>La>Nb order typical of the Slave Neoarchean crust (Davis et al., 1994).

Incompatible element ratios Th/Yb and Nb/Yb further point to negligible crustal contamination in both magmatic packages of the Union Island Group. A plot of Th/Yb and Nb/Yb ratios shows that the lower magmatism does not lie on a mixing line between the most primitive basalt sample LH14-14 and the average composition of the basement crust in the East Arm basin (Fig. 5.8). Comparison with basalts from the well-characterized ca. 1100 Ma Midcontinent Rift system shows that the Union Island Group lower magmatism compositionally overlaps with the Osler Group lower suite, which has been interpreted to reflect mantle source compositions and contain negligible crustal contamination (Hollings et al., 2007). The upper Union Island Group magmatism has depleted $\varepsilon_{Nd(i)}$ values and does not record evidence of evolving magma compositions during the eruption stage; these geochemical attributes are inconsistent with the progressive and Nd-enriching nature of crustal contamination. Comparing with the Midcontinent Rift system, the upper Union Island Group magmatism is compositionally similar to uncontaminated group 6 basalts in the Mamainse Point Formation (Shirey et al., 1994). In contrast, basalts from groups 1 and 5 with

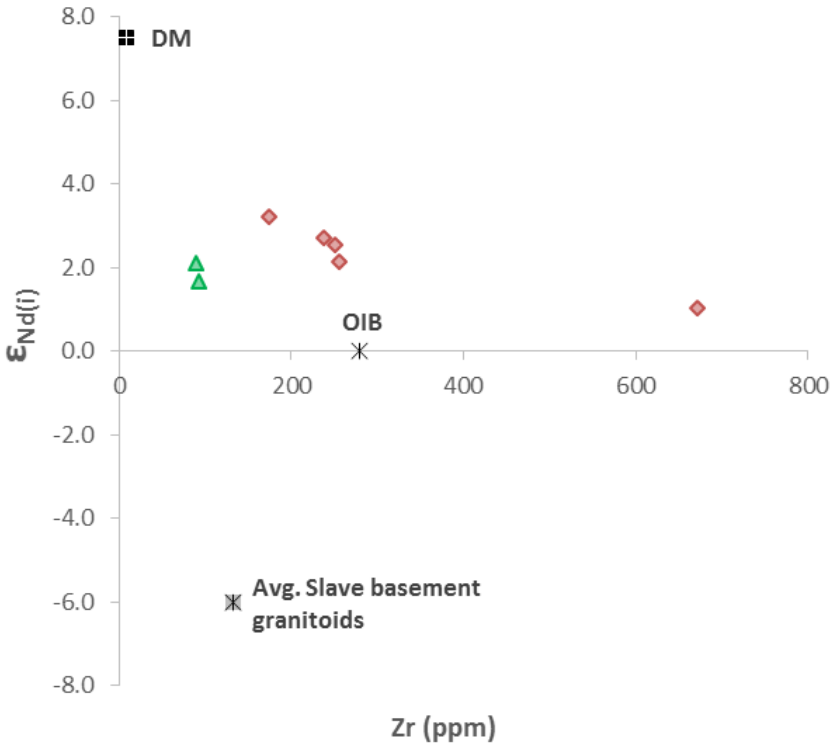

Figure 5.6. $\varepsilon_{Nd(i)}$ vs. Zr plot demonstrating negative correlation between initial (t=2.04 Ga) Nd isotopic composition and indices of magma fractionation in the lower magmatism (diamond symbols). Symbols as defined in Figure 5.3. Plotted for reference are the composition of possible mantle sources (DM: Rehkämper and Hofmann, 1997; Salters and Stracke, 2004; OIB: Sun and McDonough, 1989) and the average composition of Archean Slave granitoids in the East Arm basin (Davis and Hegner, 1992; Janzen, 2015; Yamashita et al., 1999). $\varepsilon_{Nd(i)}$ of the <2.03 Ga upper basalt is calculated at 2.04 Ga due to negligible shift in $\varepsilon_{Nd(i)}$ values.

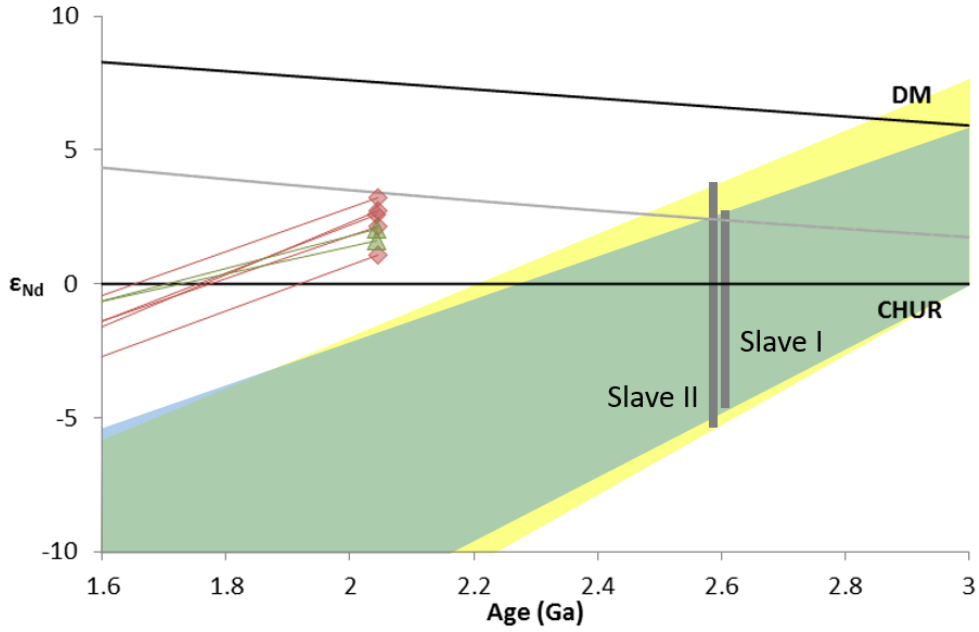

Figure 5.7. Plot of Nd isotopic composition evolution with time for Union Island Group magmatism; symbols as defined in Figure 5.3. Shown for comparison are Archean basement granitoids of Slave craton (types I and II, Davis and Hegner, 1992). DM: depleted mantle (Rehkämper and Hofmann, 1997). CHUR: Chondritic Uniform Reservoir (DePaolo and Wasserburg, 1976). The DM model of DePaolo (1981) is shown for comparison (grey curve).

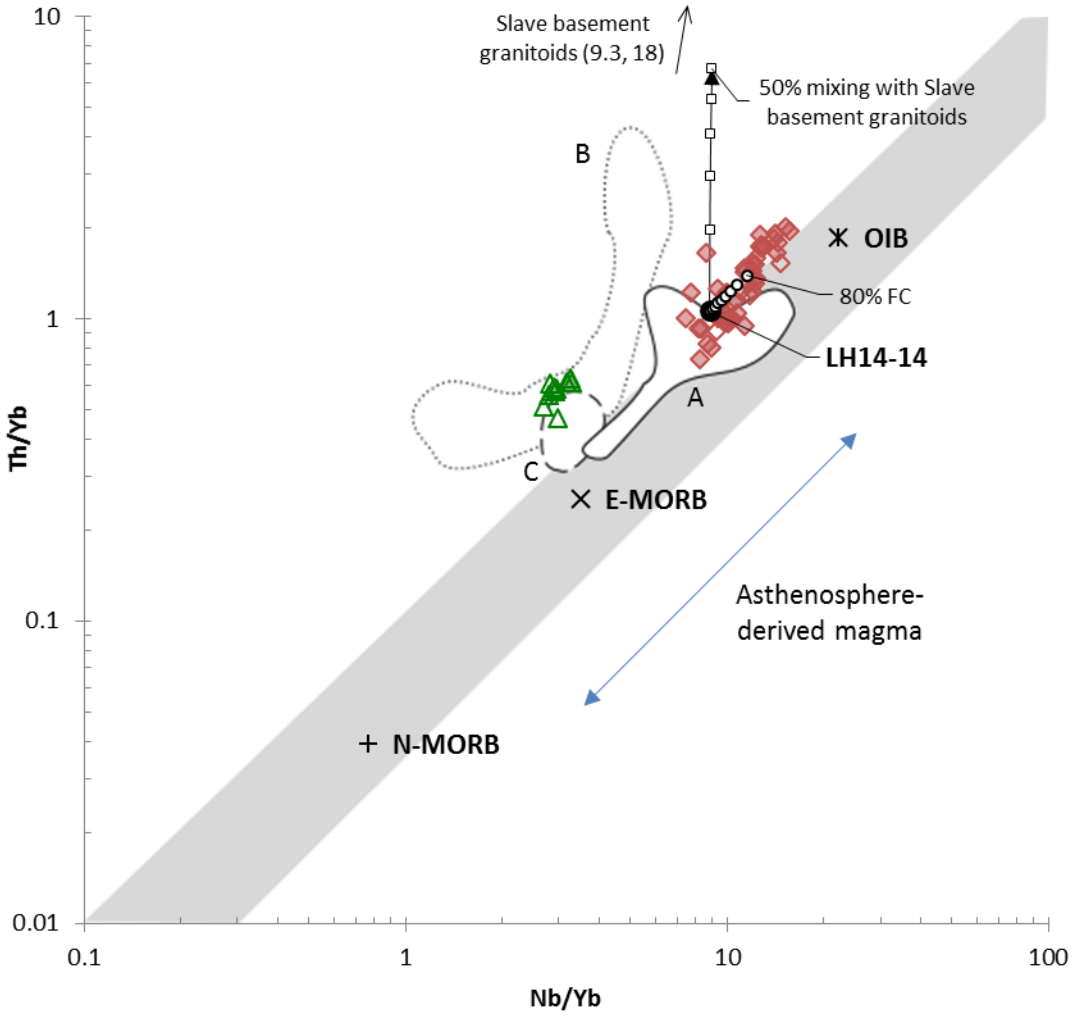

Figure 5.8. Nb/Yb vs. Th/Yb plot (after Pearce et al., 2008) for Union Island Group magmatic packages. Symbols as defined in Figure 5.3. Grey band represents composition range of uncontaminated magma derived from the asthenospheric mantle. Crustal contamination for the lower basalt is modeled by simple mixing (Langmuir, 1978) between primitive sample composition LH14-14 and the average composition of Slave Archean granitoids in the East Arm basin (Janzen, 2015); small squares mark 10% increments of bulk volume crustal input. Closed-system fractionation (Allègre and Minster, 1978) of sample LH14-14 is denoted by small circles; Th/Yb and Nb/Yb range of the lower basalt extends beyond that which can be explained by 80% fractional crystallization (Fig. 5.4; see main text). Shown for comparison are composition fields of basalts from the ca. 1100 Ma Midcontinent Rift system: A) uncontaminated basalts from the lower Osler Group (Hollings et al., 2007), B) contaminated basalts from the Mamainse Point Formation (groups 1 and 5; Shirey et al., 1994) and, C) uncontaminated basalts from the Mamainse Point Formation (Shirey et al., 1994). Upper basalt samples LH14-32, LH14-33, LH14-34, and LH14-36 are not plotted due to scattering in Nb/Yb ratios caused by Nb analytical imprecision.

inferred crustal contamination display a much wider range of Th/Yb and Nb/Yb ratios (Fig. 5.6) in addition to nearly all samples recording negative $\varepsilon_{Nd(i)}$ values. Based on these lines of evidence, we rule out crustal contamination as a significant process in modifying the geochemical signature of the Union Island Group magmas.

5.3.3 Mantle sources

Fractionated $(Gd/Yb)_N$ ratios (>2; Table 4.2) associated with both magmatic packages of the Union Island Group suggest that garnet, which heavily partitions HREE (e.g., Fujimaki et al., 1984; Johnson, 1998), was present as a residual phase in equilibrium with the source melt. Although residual amphibole also preferentially partitions HREE over LREE (to a lesser degree than garnet), D_{amph}/D_{melt} coefficients do not differ drastically for the heavier HREE (Chazot et al., 1995; McKenzie and O'Nions, 1991). Therefore, fractionated HREE profile exhibited by the Union Island Group magmatism suggests that residual garnet rather than amphibole in the source was the principal reason for the HREE depletion and high Gd/Yb ratios in the basalts.

Incompatible elements and isotopic data point to both magmatic packages as products of interaction between a chondritic asthenospheric mantle and a depleted mantle reservoir. Th/Yb and Nb/Yb ratios of the lower magmatism lie within the mantle array (Fig. 5.8), between the composition of ocean island basalts (OIB) and the depleted mantle (DM). As fractional crystallization causes only small variations in Th/Yb and Nb/Yb ratios (white circles in Fig. 5.8), the spread of the lower magmatism supports mixing between an enriched, OIB-like reservoir and a DM-like reservoir. An OIB signature in the lower magmatism is supported by the high incompatible element enrichment levels, similar incompatible element ratios (Table 5.1), and characteristic MORB-normalized multi-element profiles (Fig. 5.9). In addition, the extensive degree of fractional crystallization in lower magmatism is comparable to that observed in some modern OIB, such as Tristan da Cunha (le Roex et al., 1990).

Increasingly chondritic, OIB-like $\varepsilon_{Nd(i)}$ values of the lower Union Island Group magmatism are consistent with a rift origin. Ocean island basalts are generally envisioned to represent low-degree partial melts of an upwelling primitive, asthenospheric mantle with negligible interaction with the lithosphere and are associated with intraplate extensional settings (Hart et al., 1989; Pearce, 2008; Niu et al., 2011). An OIB component with varying degrees of interaction with other mantle and crustal reservoirs has been invoked for basalt generation in rift magma suites (e.g., Gibson et al.,

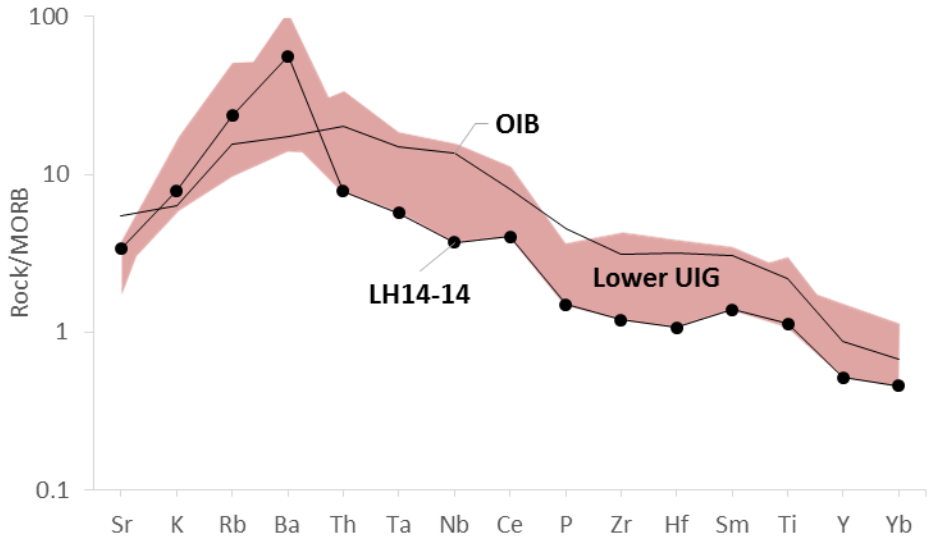

Figure 5.9. MORB-normalized incompatible element diagram (after Pearce, 1983). Shaded area represents enrichment range of the lower magmatism (Lower UIG; data screened by a filter of LOI < 5 wt% to minimize scattering in LILE due to alteration). The most primitive sample composition, LH14-14, displays lower HFSE enrichment compared to average ocean island basalt (OIB; Sun and McDonough, 1989). Normalization values from Wheatley and Rock (1988).

1992; Hart et al., 1989; Hollings et al., 2007; Thompson and Morrison, 1988). In the case of the Union Island Group, the negligible crustal influence on geochemistry is consistent with lithospheric thinning which accompanies asthenospheric upwelling during rift formation. Increasing asthenospheric input versus a waning contribution from a depleted mantle reservoir due to lithospheric thinning explains the $\varepsilon_{Nd(i)}$ shift from +3.2 to +1.1 in the lower magmatism. Furthermore, the lower magmatism shares similar Nb/Yb and Th/Yb ratios with initial phases of basaltic volcanism in several well-characterized rift systems, including the ca. 1100 Ma Midcontinent Rift, the ca. 45 Ma Afar Rift, and the ca. 31 Ma Rio Grande Rift (Figs 5.8, 5.10). These lines of evidence point to the lower Union Island Group magmatism as a rift basalt sequence.

Positive $\varepsilon_{Nd(i)}$ values of the upper magmatism are indistinguishable from those of the lower magmatism and suggest derivation also from the interaction between a chondritic reservoir and a depleted reservoir. DM-like Nb/Hf ratios (1.3–1.6) of the upper magmatism cannot be derived from partial melting of the primitive mantle alone (Fig. 5.11) and suggest prominent input from the depleted reservoir. Modeling results are consistent with shallow, high-degree partial melting which accounts for the tholeiitic character of the upper magmatism. However, the prominence of a DM signature in incompatible element ratios of the upper magmatism does not readily explain why it displays $\varepsilon_{Nd(i)}$ values similar to the lower magmatism. An $\varepsilon_{Nd(i)}$ vs. Zr/Y plot (Fig. 5.12) shows that the composition of both magmatic packages can be produced by mixing partial melts of varying degrees from the primitive and the depleted reservoirs. Melts involved in producing the upper magmatism are associated with larger degrees of partial melting (5% for PM, 20% for DM) than melts which produced the lower magmatism (3% for PM, 10% for DM); this is consistent with Nb/Hf modeling results (Fig. 5.11). The model suggests that the bulk volume input of a DM-like mantle decreased from 70% to 40% during the lower magmatism, while the upper magmatism contains ~60% DM input. The shift from a DM-dominant to a PM-dominant composition in the lower magmatism is consistent with an impinging asthenospheric mantle. The increased DM component in the upper magmatism may point to: 1) shallow decompression melting occurring mostly in the lithosphere, and/or 2) decreased melt production from the asthenospheric mantle.

A higher melt fraction is assigned to the depleted reservoir in our $\varepsilon_{Nd(i)}$–Zr/Y model due to the possibility of DM being eclogitic in composition (see below). In a mixture of eclogite and

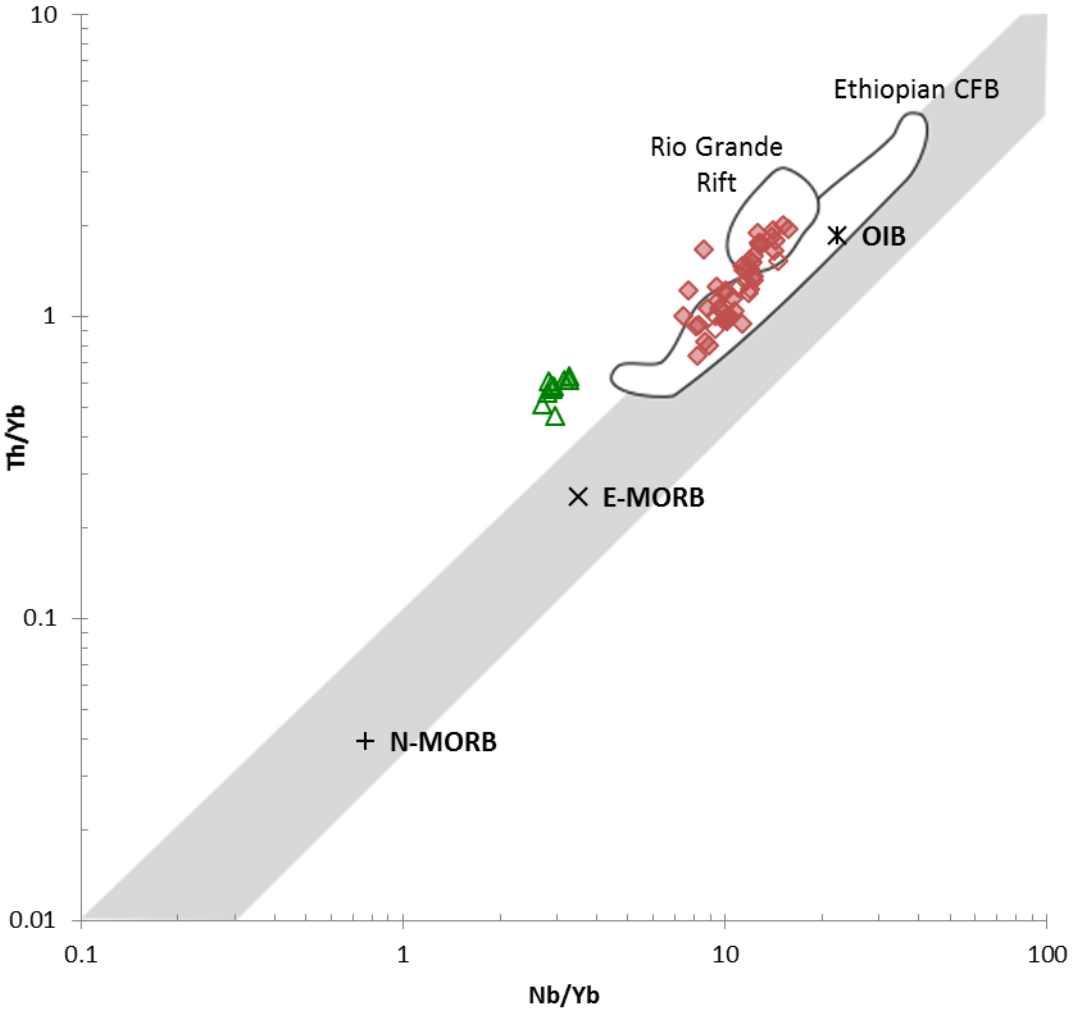

Figure 5.10. Nb/Yb vs. Th/Yb plot of the Union Island Group magmatic packages (after Pearce et al., 2008). Symbols as defined in Figure 5.3. Shown for comparison are composition fields for incipient rift basalt sequences from the ca. 31 Ma Rio Grande Rift (24-21 Ma Yarmony Mountain basalts, Leat et al., 1990) and from the ca. 45 Ma East African Rift system (45-11 Ma southern Ethiopian CFB, George and Rogers, 2002; HT-1, HT-2 basalts from northern Ethiopian CFB, Pik et al., 1999).

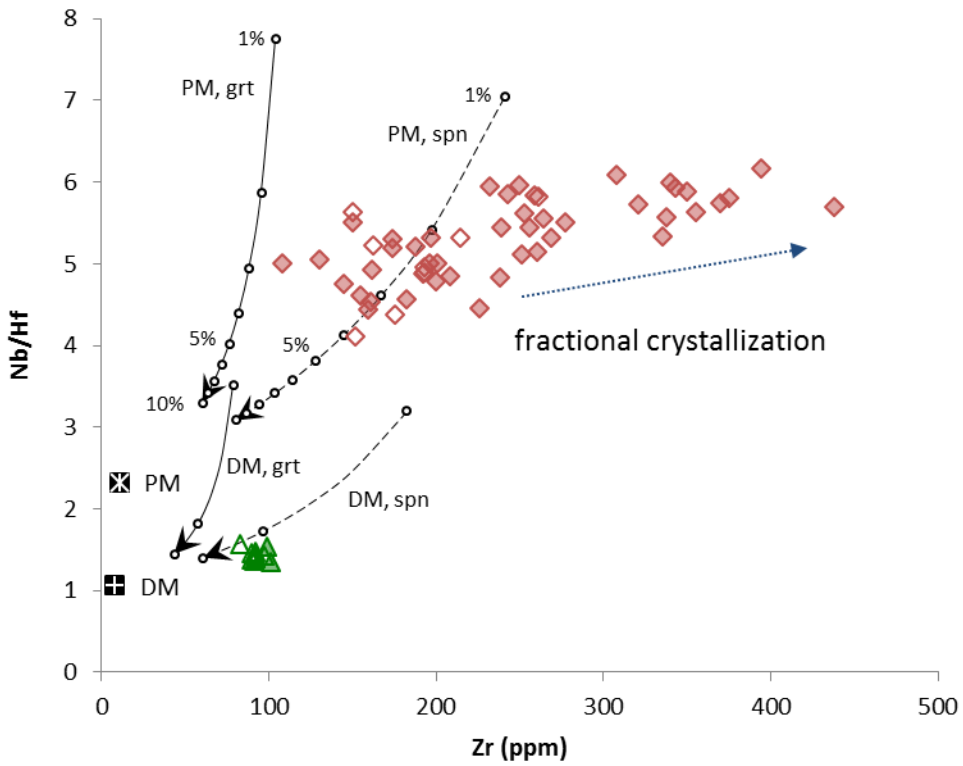

Figure 5.11. Nb/Hf vs. Zr plot of Union Island Group magmatic packages, with comparison between partial melting models. Symbols as defined in Figure 5.3. Magma evolution curves are calculated for 10% equilibrium partial melting (Shaw, 1970) under garnet-stable (grt; solid curves) and spinel-stable depths (spn; dashed curves), with the primitive mantle (PM; McDonough and Sun, 1995) and the depleted mantle (DM; Salters and Stracke, 2004) as source compositions. Dotted curve represents evolution vector of a magma undergoing fractional crystallization (see Figure 5.4b). Melting curves for PM are labelled at 1% increments; melting curves for DM are labelled at 1%, 5%, and 10%. Incompatible element patterns of the lower basalt are consistent with low-degree (1–5%) partial melting of a PM-dominant source at garnet-stable depths, while the upper basalt composition is consistent with higher degree (>5%) partial melting of a DM-dominant source. Upper basalt samples LH14-32, LH14-33, LH14-34, and LH14-36 are not plotted due to scattering in Nb/Hf ratios caused by Nb analytical imprecision.

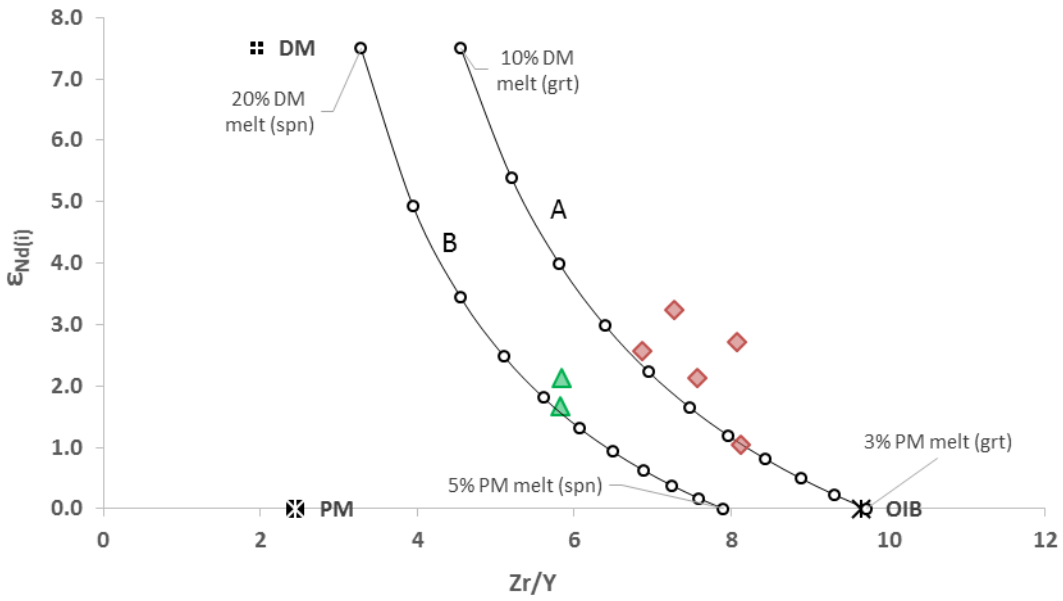

Figure 5.12. $\varepsilon_{Nd(i)}$ vs. Zr/Y plot for Union Island Group basalts. Symbols as defined in Figure 5.3. Simple mixing (Langmuir, 1978) is modeled for two source melt mixtures: A) 3% partial melt of the primitive mantle (PM; McDonough and Sun, 1995) plus 10% partial melt of the depleted mantle (DM; Salters and Stracke, 2004), both at garnet-stable depths. B) 5% partial melt of PM plus 20% partial melt of DM, both at spinel-stable depths. Curves are labelled at 10% bulk volume increments. Trend of the lower basalt is consistent with 40–70% DM input, while the upper basalt composition corresponds to ~60% DM input. Model parameters are summarized in Appendix B.

undepleted peridotite subjected to the same thermal regime, eclogite melts first and has a higher melt productivity (fraction of melt derived per degree of temperature rise above the solidus) than undepleted peridotite (Sobolev et al., 2005). Therefore, a PM–DM mixture undergoing partial melting will contain DM melts at a higher melt fraction than PM melts.

Proposed origins for the depleted mantle reservoir includes: 1) subcreted oceanic lithosphere at the base of the subcontinental lithosphere (SCLM; Heaman and Pearson, 2010), 2) fragments of subducted oceanic lithosphere in the upper mantle and/or in the transition zone (Kerr et al., 1995), and 3) parts of the upper mantle that have been depleted via prior extensive extraction of basaltic melts (Gast, 1968; Wood, 1979). The first two scenarios are supported by late Neoarchean to early Paleoproterozoic subduction-related granitoid magmatism that formed much of the basement crust in southern Slave craton (e.g., Davis et al., 2003). In the first scenario, if the depleted mantle component is represented by subcreted oceanic lithosphere, an upwelling asthenospheric mantle is required to interact with the Slave SCLM in order to produce the Union Island Group magmas. In this case, lithospheric thinning associated with rift extension would cause DM input in the magmas to progressively decrease; this is inconsistent with a persistent DM signature in the upper magmatism. The latter two scenarios suggest entrainment of the depleted reservoir during ascent of the primitive mantle through the asthenosphere, possibly within a plume head structure (Griffiths and Campbell, 1990). In a plume model, initial magmas are derived from the heterogeneous plume head. This is followed by melts from the more homogeneous plume core which contains less entrained mantle material, therefore carrying a more primitive signature. If the depleted mantle signature originated from upper mantle materials entrained in a plume head, then this heterogeneous plume head likely contributed to both the lower and upper magmatism such that a DM signature is present in both packages. We note, however, that modern active plumes are commonly associated with primary mantle magmas (e.g., picrites) and traceable plume tracks (e.g., the Hawaiian–Emperor seamount chain); neither of these has been observed in the Union Island Group or the regional record, suggesting some inconsistencies with a plume origin for the Union Island Group magmatism.

High-Th mantle reservoir

The Union Island Group magmatism display Th enrichment that is not readily explained by simple petrogenetic models. The upper magmatism has Th/Nb ratios higher than those of asthenospheric

magmas, as does the lower magmatism to a lesser extent (Table 5.1). Thorium is prominently enriched in the Archean granitoid crust in the East Arm basin, with high Th/Nb ratios ranging 1.5–3.6 (Janzen, 2015). However we found no evidence for significant crustal contamination in the Union Island Group magmas. The high Th levels therefore suggest input from a Th-enriched mantle reservoir.

An examination of mantle reservoirs suggests two tentative origins for this Th enrichment. First, it may be a feature of the primitive reservoir which is dominant in the most evolved compositions of the lower magmatism. Due to PM having higher concentrations of incompatible elements than DM, a PM reservoir with Th enrichment would contribute high-Th OIB-like melts in the lower magmatism, and at the same time cause significant Th/Nb enrichment in the DM-dominant upper magmatism even at a low PM to DM proportion in the melt mix. In contrast, if Th enrichment is an intrinsic feature of the depleted reservoir, mixing between this depleted reservoir and a primitive reservoir would produce more prominent Th enrichment in the least evolved (higher DM input) magmas in the lower magmatism, which is inconsistent with the observed trend.

Alternatively, the Th enrichment may represent a third mantle source that is not readily distinguished by Nd isotopic compositions. High Th/Nb ratios of the upper basalt are greater than those associated with PM and DM, and cannot be explained by partial melting of any mixture of the two reservoirs; partial melting produces melts with Th/Nb ratios lower than the melt source. While melting of metasomatic veins within the lithospheric mantle has been invoked to explain elevated Th/Nb ratios in Paleoproterozoic mafic magmas (Sandeman et al., 2013), input from such enriched components would produce melts with highly negative $\varepsilon_{Nd(i)}$ values according to the highly radiogenic Nd compositions of metasomatized peridotites in the Slave SCLM (Aulbach et al., 2013). Therefore, it is plausible that the upper basalt itself represents a Th-enriched but otherwise depleted reservoir that is distinct from the DM-like reservoir involved in generating the lower basalt.

Despite uncertainties in the origin of the Th enrichment, a similar signature has been observed in other Paleoproterozoic mafic magmatism in the Slave craton, including the 2.23 Ga Malley and 2.21 Ga Mackay dyke swarms (Ernst and Buchan, 2010; Fig. 5.13). Both swarms have been interpreted to reflect relatively uncontaminated asthenospheric magmas based on chondritic to slightly depleted $\varepsilon_{Nd(i)}$ values (0–+2; Davis, 1997). Older Paleoproterozoic mafic magmatism in

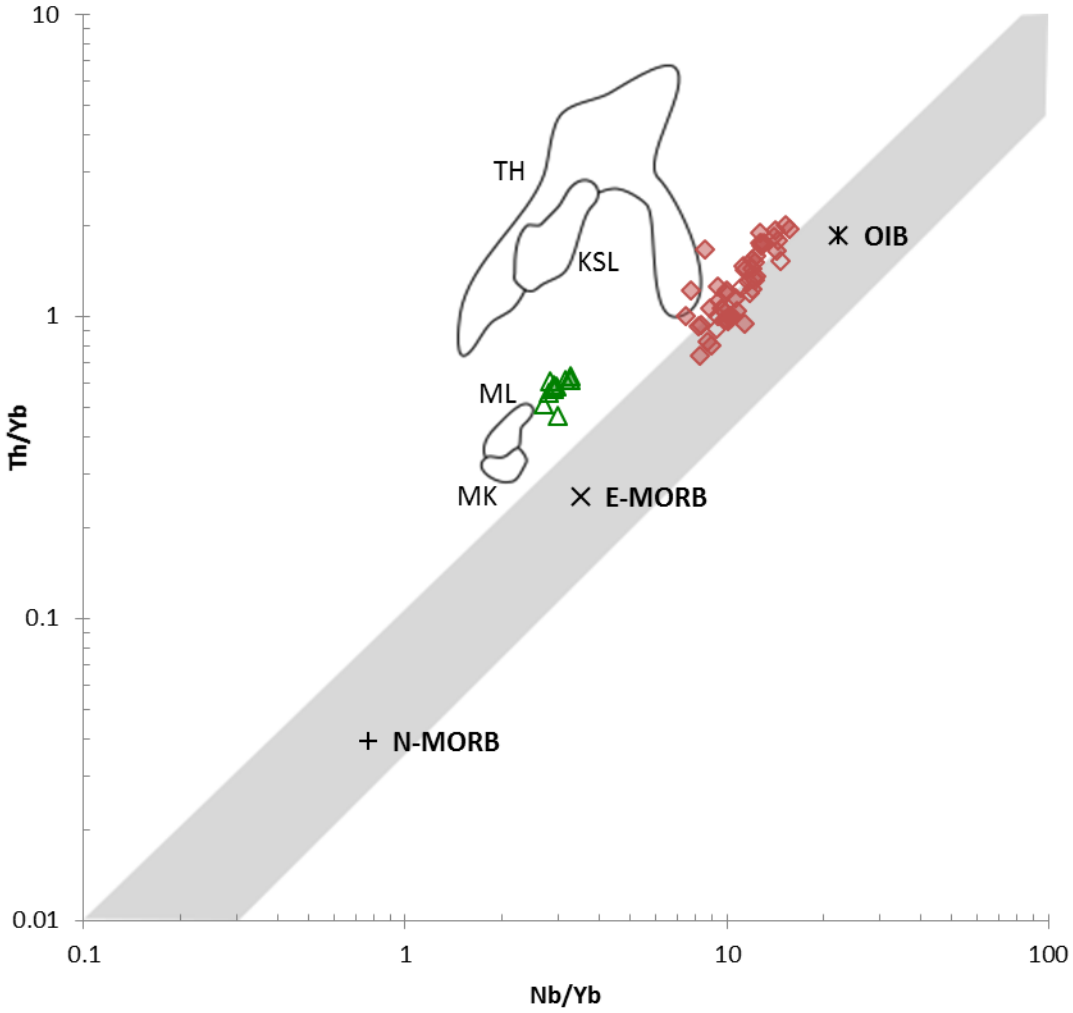

Figure 5.13. Nb/Yb vs. Th/Yb plot of the Union Island Group magmatic packages (after Pearce, 2008). Symbols as defined in Figure 5.3. High-Th/Nb deviation of the upper basalt from the mantle array (grey band) is compared with Paleoproterozoic mafic magmatism in the Slave craton, Hearne province, and the Superior craton. TH: Thessalon volcanics (ca. 2453 Ma; Ketchum et al., 2013). KSL: Kaminak dykes and Spi Lake basalts (ca. 2498 Ma; Sandeman and Ryan, 2008; Sandeman et al., 2013). ML: Malley dyke swarm (ca. 2231 Ma; Ernst and Buchan, 2010). MK: Mackay dyke swarm (ca. 2210 Ma; Ernst and Buchan, 2010). These Paleoproterozoic mafic magmatism are interpreted to have negligible or limited crustal contamination. Upper basalt samples LH14-32, LH14-33, LH14-34, and LH14-36 are not plotted due to scattering in Nb/Yb ratios caused by Nb analytical imprecision.

the Superior craton and Hearne province, including the ca. 2453 Ma Thessalon volcanics, the ca. 2498 Ma Kaminak dykes and the cogenetic Spi Lake basalts, have even higher Th/Nb ratios while lacking apparent evidence for crustal contamination (Ketchum et al., 2013; Sandeman et al., 2013; Fig. 5.13). Therefore, while incompatible element data do not provide a definitive explanation for the origin of the Th enrichment in the Union Island Group magmatism, it is a common feature shared by Paleoproterozoic extension intraplate magmatism and has existed in the Slave craton since at least 2.23 Ga.

5.4 Towards a revised tectonic model for the formation of the East Arm basin

Over the years, discussions regarding the tectonic evolution of the East Arm basin have been complicated by a general paucity of radiometric dating. Hoffman (1968, 1969, 1970) first proposed the East Arm basin as an orogenic fold-belt based on sedimentological studies of the Great Slave Supergroup and Et-Then Group. However, stratigraphic similarities with the Coronation margin in the Wopmay orogen to the west of the Slave craton were then used to promote a contrasting model, where the East Arm basin developed as a failed rift (i.e. the Athapuscow aulacogen; Hoffman, 1973). In the failed rift model, mafic magmas and basinal sequences of the Union Island Group represent the formation of a rift graben.

Uranium–lead dating by Bowring et al. (1984) provided the first robust age constraints for the ca. 1928 Ma Wilson Island Group, the ca. 1895 Ma Butte Island suite granites, and the ca. 1872–1861 Ma Compton laccoliths. These dates, along with field studies and evolving ideas about the Wopmay orogen, led Hoffman (1987, 1988b) to re-propose an orogenic model, where the East Arm basin formed as a spreading back-arc during the 1.99–1.91 Ga Slave-Rae collision. Recent work along the western Slave margin has called to question this ca. 1.9 Ga collisional origin for the East Arm basin. A newly identified 1.91–1.90 Ga rift sequence in the Hottah terrane, on the western Slave margin, has been correlated with coeval extension in the East Arm basin represented by the 1.91 Ga Hearne dykes and Blatchford monzodiorite stocks (Mumford and Cousens, 2014; Ootes et al., 2015), suggesting that the two margins may have been tectonically related. In addition, Mitchell et al. (2010) tentatively revisited the failed-rift East Arm basin model following the interpretation of a ca. 2.01 Ga rift-to-drift transition in the western Slave margin (Hoffman et al., 2011), suggesting a correlation between the Union Island Group and 2.01–2.03 Ga mafic magmatism across the Slave craton.

Our geochemical studies on mafic magmatism of the Union Island Group point to a rift origin for the East Arm basin based on the following lines of evidence:

1) A prominent OIB-like, asthenospheric component
2) Lack of crustal contamination
3) Similar incompatible element signatures to many incipient rift magmas across geologic time

The progression from flooded Archean crust to platform facies deposition (lower dolomite unit) then to basinal facies (black shale unit) is consistent with isostatic sinking during rift extension and lithospheric thinning. While the lack of significant crustal contamination is consistent with both magmatic packages originating in an extensional setting, this also places a constraint on the timing of the upper magmatism. The onset of subsequent tectonic/magmatic activity at the Slave–Rae boundary, as marked by felsic magmatism in the Taltson magmatic zone, began as early as ca. 1986 Ma (Bostock et al., 1987). Therefore, the Union Island Group upper basalt must have erupted between 2026 Ma (maximum deposition age of the upper dolomite unit) and 1986 Ma.

Overall, the evolution of the East Arm rift is summarized in seven stages (Fig. 5.14):

1) A rift basin forms in the present-day East Arm area under regional extension (Fig. 5.14A). The graben is first overlain by a shallow ocean (lower dolomite unit). Further isostatic sinking of the graben block causes sea level to rise (black shale unit).
2) The lower basalt erupts, sourced from low-degree partial melting of a mixed mantle source near the base of the lithosphere. The segregated melt ponds and undergoes extensive fractional crystallization. Asthenospheric input becomes more dominant with time. Eruptions were sustained by consanguineous mafic sills and dykes.
3) A hiatus in volcanic activity followed and was accompanied by sea level drop (upper dolomite unit), possibly due to inflation of the mafic sills.
4) Further extension causes shallow, high-degree decompression melting of what is largely the depleted mantle reservoir. A thinned lithosphere allows rapid eruption of the magma in a different volcanic centre (upper basalt unit; Fig. 5.14B).
5) Sea level rises (red/green mudstone unit).
6) Extension in the rift basin ceases.

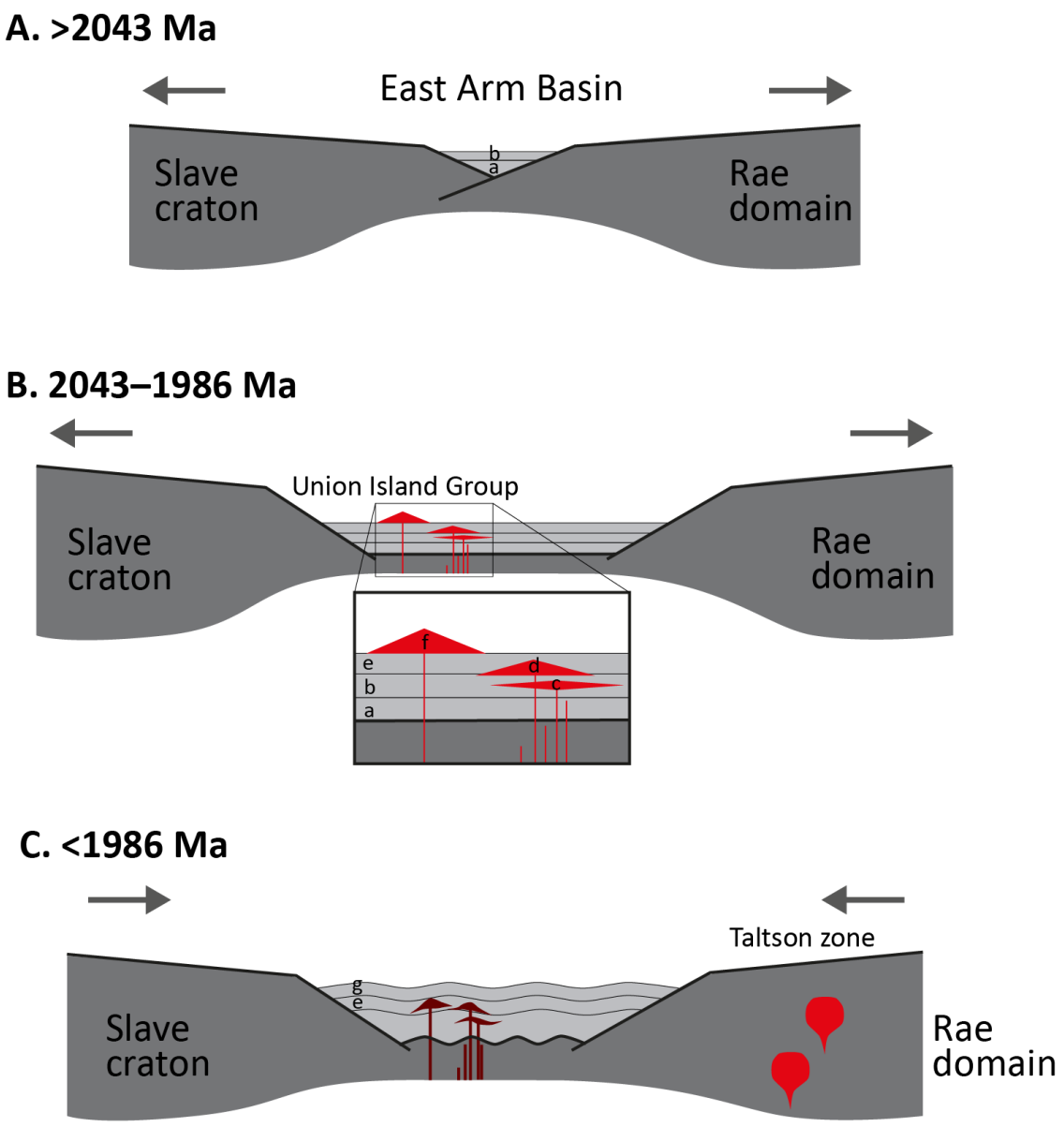

Figure 5.14. Simplified diagram showing the tectonic evolution of the East Arm rift. A) Regional extension forms a rift basin at some point prior to ca. 2043 Ma. B) Deposition of sedimentary strata of the Union Island Group (in grey; a: lower dolomite; b: black shale; e: upper dolomite), together with basaltic volcanism associated with both the lower and upper magmatism (in red; c: diabase intrusions, d: lower basalt; f: upper basalt), as the rift basin continued to extend. C) Extension of the rift ceased at some point prior to ca. 1986 Ma. By this point the uppermost sedimentary strata of the Union Island Group had been deposited (e: upper dolomite; g: red and green mudstones). The end of rifting was followed by regional compression, together with the emplacement of felsic plutons associated with tectonic activity in the Taltson magmatic zone (in red).

7) Tectonic compression initiates the emplacement of felsic plutons of the Taltson magmatic zone (Fig. 5.14C).

In light of the various tectonic interpretations formerly proposed for the East Arm basin, the timeline of the Union Island Group magmatism lends support to a contiguous Slave-Rae arrangement as early as 2.04 Ga. Comparison between well-characterized rift magmatic sequences through geologic time shows the total duration of volcanism rarely extends beyond 30 Myr before a passive margin is developed or the rift failed (Davis and Green, 1997; Storey et al., 2007; Sundvoll et al., 1990; Turner et al., 1994). Although the ~57 Myr time window for rift extension in the East Arm basin may have been sufficient for the development of a passive margin, seismic data shows no definitive evidence for subduction at the Slave-Rae lithospheric boundary (Snyder and Kjarsgaard, 2013), which would have been required to consume any oceanic crust produced prior to a hypothetical 2.0–1.9 Ga Slave–Rae collision. It has been demonstrated that the thinned lithosphere in a continental rift tends to focus deformation when subjected to a subsequent compressional regime and develop thick orogenic roots (Thompson et al., 2001). A 2.04–1.99 Ga failed rift model for the East Arm basin adequately explains the lack of continental-margin arc signatures in the Taltson granitoids and supports an intracratonic origin for the Taltson magmatic zone as proposed by Chacko et al. (2000) and De et al. (2000). The Slave craton and Rae domain therefore existed as one contiguous crustal unit as of 2.04 Ga.

5.4.1 A long-lived early Paleoproterozoic extensional regime in the Slave craton

The ca. 2043 Ma Union Island Group rift magmatism makes up part a long-lived extensional regime across the Slave craton during the 2.23–2.01 Ga period (Table 5.2, Fig. 5.15). Prior to the formation of the East Arm rift basin, the emplacement of numerous mafic dyke swarms and anorogenic alkaline intrusions in the southern Slave craton reflects repeated attempts at rifting, with the predominant E–NE dyke orientations indicating a prevalent crustal stress regime. It was along this southern margin that rifting finally occurred as the East Arm basin; incipient rift magmas of the Union Island Group were fed by dykes of a similar ENE orientation.

Rifting at the southern Slave margin was followed by the emplacement of the ca. 2023 Ma Lac de Gras dykes across Slave craton and the cogenetic 2026–2023 Ma Booth River intrusive complex in the Kilohigok Basin (Buchan et al., 2009; Davis et al., 2004; Roscoe et al., 1987). The Lac de Gras dykes have a highly enriched alkaline composition similar to the Union Island Group lower

Table 5.2. List of Paleoproterozoic igneous ages in the East Arm basin, Slave craton, Great Slave Lake shear zone, Kilohigok Basin, and Wopmay Orogen between 2250 Ma and 1900 Ma.

DOMAIN/Name	Age (Ma)	References
EAST ARM BASIN		
N. Simpson Island dyke	2219 ± 3.7	Mumford et al. (2012)
S. Simpson Island dyke*	2217 - 2198	this study
Union Island Group mafic magmatism	2043 ± 3	this study
Wilson Island Group felsic volcanism	1928 ± 11	Bowring et al. (1984)
Hearne dykes	1901 ± 4	Buchan et al. (2010)
SLAVE CRATON		
Malley dykes	2231 ± 2	Buchan et al. (2012)
Mackay dykes	2208 ± 5	LeCheminant and van Breemen (1994)
Dogrib dykes	2193 ± 2	Mitchell et al. (2014)
Blatchford Lake intrusive suite	2185 - 2176	Bowring et al. (1984), Sinclair et al. (1994), Mumford et al. (2012), Mumford (2013)
Big Spruce intrusive suite	2188 ± 16	Cavell and Baadsgaard (1986)
Duck Lake sill	2181 ± 2	Bleeker and Kamo (2003)
Squalus Lake intrusion	2180 ± 1	Villeneuve and van Breemen (1994)
Indin dykes	2126 - 2108	Buchan et al. (2016)
Lac de Gras dykes	2023 ± 2	Buchan et al. (2009)
GREAT SLAVE LAKE SHEAR ZONE		
McKee Lake dykes	2038 ± 3	Pehrsson et al. (1993)
Granite intrusions	1978 ± 5	van Breemen et al. (1990)
	1976 ± 5	van Breemen et al. (1990)
	1960	Hanmer et al. (1992)
	1924	Hanmer et al. (1992)
KILOHIGOK BASIN		
Booth River intrusive suite	2026 - 2023	Roscoe et al. (1987), Davis et al. (2004)
WOPMAY OROGEN		
Melville Group basalt	2014 ± 0.89	Hoffman et al. (2011)
Holly Lake met. complex (basalt)	1951 ± 15	Davis et al. (2015)
Hottah plutonic complex	1931 - 1902	Bowring (1984), Ootes et al. (2015)
Bell Island Bay Group	1906 - 1895	Ootes et al. (2015)
Grant subgroup	1903 - 1889	Ootes et al. (2015)

* $^{207}Pb/^{206}Pb$ ages from two baddeleyite analyses (Appendix C).

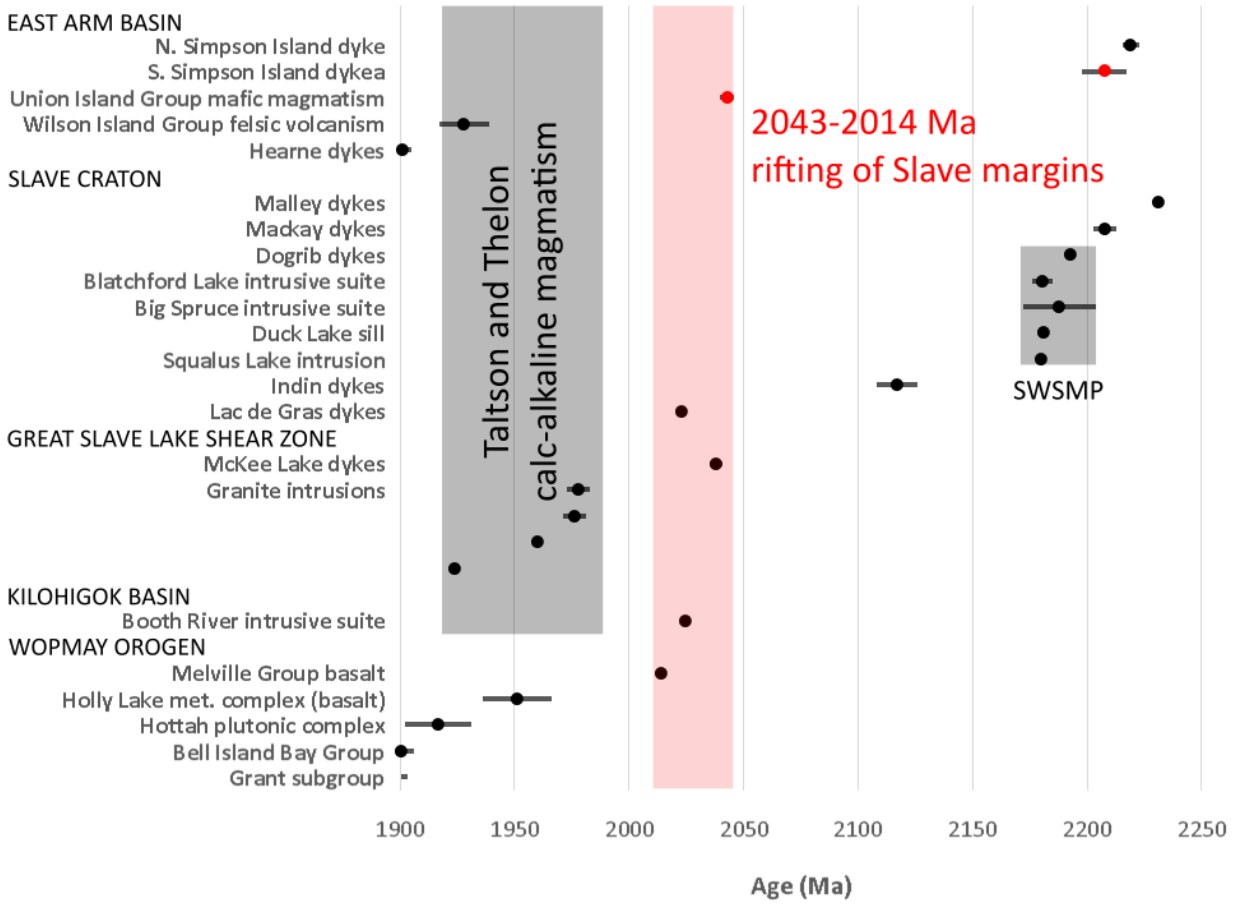

Figure 5.15. Diagram of Paleoproterozoic igneous ages in the East Arm basin, Slave craton, Great Slave Lake shear zone, Kilohigok Basin, and Wopmay Orogen between 2250 Ma and 1900 Ma (data summarized in Table 5.2). New geochronological data from this study are denoted by red circles. Red band indicates ca. 2043–2014 Ma rifting of Slave margins. Grey rectangles represent the ca. 2193–2164 Ma Southwest Slave magmatic province (SWSMP) and the ca. 1986–1920 Ma Taltson and Thelon calc-alkaline magmatism.

basalt. The ca. 2014 Ma Melville Group basalt marks rifting in the western Slave margin (Hoffman et al., 2011) and is the last known extension-related magmatism in the Slave craton prior to the ca. 1882 Ma onset of Wopmay orogen along the western margin and the ca. 1986 Ma onset of Taltson magmatism along the southern margin.

5.4.2 The break-up of the pre-Laurentia supercontinent

The ca. 2.04 Ga rifting of the southern Slave margin as part of the 2.23–2.01 Ga period of mafic magmatism across Slave craton is consistent with the inferred break-up of the Slave craton from its pre-Laurentia assembly during the 2.2–2.0 Ga period (Bleeker, 2003). In light of the Slave–Rae continuity inferred in this study, recently identified 2048–2032 Ma gabbroic to granitic assemblages (Davis et al., 2015) and a 2045 Ma mafic sill in the Rae domain (Percival et al., 2017) suggest contemporaneous tectonic activity in the Rae domain, although the origin of these magmas remain to be determined.

Mafic magmatism indicative of crustal extension contemporaneous with the East Arm rift are preserved in other pre-Laurentia crustal fragments: the 2072–2091 Ma Cauchon dykes and ca. 2069 Ma Lac Esprit dykes in the Superior craton (Buchan et al., 2007; Hall and Heaman, 2000; Heaman and Corkery, 1996), the ca. 2011 Ma Kennedy dykes in the Wyoming craton (Cox et al., 2000), the ca. 2038 Ma Korak sills in the Cape Smith belt (Machado et al., 1993), the 2036–2046 Ma Kangâmiut dykes in the North Atlantic craton (Nutman et al., 1999), and the ca. 2045 Ma Iglusuataliksuak dykes in the Nain province (Hamilton et al., 1998). The widespread nature of the 2.1–2.0 Ga regional extension signature supports a Laurentia-like supercontinent assembly in the early Paleoproterozoic ("Kenorland" of Williams et al., 1991) as opposed to the Slave-centric supercratonic arrangement of Sclavia (Bleeker, 2003; see also Pehrsson et al., 2013). Our findings in this study regarding the timing and origin of the Union Island Group mafic magmatism add to the increasing body of evidence for the breakup of this supercontinent at 2.1–2.0 Ga.

6 CONCLUSIONS

Our investigation into the origin of the Union Island Group mafic magmatism, integrating geochemical, geochronological, and tracer isotope information leads us to the following conclusions:

1) The first direct radiometric age determination for mafic magmatism in the Union Island Group is a U–Pb baddeleyite date of 2043±3 Ma; the age obtained for a diabase intrusion that is geochemically similar to the lower basalt flows and is thereby considered a feeder to these flows. This new age constraint for the Union Island Group volcanism indicates that it is oldest recognized stratigraphic package in the East Arm basin and that the basin formed much earlier than previously thought.

2) The 1928±11 Ma Wilson Island felsic volcanic rocks (Bowring et al., 1984) clearly post-dates the Union Island Group; this requires a major revision in the East Arm basin stratigraphy. This revised stratigraphy is consistent with field evidence that the Union Island Group unconformably overlies Slave basement.

3) The two basaltic volcanic packages of the Union Island Group experienced significant fractional crystallization of olivine±clinopyroxene prior to eruption (moderate to low Mg#) but have striking contrasting geochemical signatures. The lower basalt package has OIB-like affinities and displays substantial geochemical variation that can be attributed to fractional crystallization in deep-seated magma chambers. The upper basalt package has depleted mantle-like geochemical affinities and display a uniform composition. Both basaltic packages reflect an origin in an extensional setting with negligible crustal contamination.

4) Eruption of the Union Island Group basalts marked the formation of the East Arm basin as a rift basin between the Slave craton and the Rae domain. This rift ceased to be active prior to ~2.0 Ga and became the focus for deformation and magmatism during the subsequent Taltson and Thelon orogens.

5) The Slave craton and the Rae domain were a contiguous crustal unit as early as 2.04 Ga.

REFERENCES

Allègre, C.J., Minster, J.F., 1978. Quantitative models of trace element behavior in magmatic processes. Earth and Planetary Science Letters 38, 1–25.

Amelin, Y.V., Heaman, L.M., Semenov, V.S., 1995. U–Pb geochronology of layered mafic intrusions in the eastern Baltic Shield: implications for the timing and duration of Paleoproterozoic continental rifting. Precambrian Research 75, 31–46.

Ashton, K.E., Heaman, L.M., Lewry, J.F., Hartlaub, R.P., Shi, R., 1999. Age and origin of the Jan Lake Complex: a glimpse at the buried Archean craton of the Trans-Hudson Orogen. Canadian Journal of Earth Sciences 36, 185–208.

Aulbach, S., Griffin, W.L., Pearson, N.J., O'Reilly, S.Y., 2013. Nature and timing of metasomatism in the stratified mantle lithosphere beneath the central Slave craton (Canada). Chemical Geology 352, 153–169.

Badham, J.P.N., 1979. Geology and petrochemistry of lower Aphebian (2.4–2.0 Ga) alkaline plutonic and hypabyssal rocks in the East Arm of Great Slave Lake, Northwest Territories. Canadian Journal of Earth Sciences 16, 60–72.

Bleeker, W., 2003. The late Archean record: a puzzle in ca. 35 pieces. Lithos 71, 99–134.

Bleeker, W., Hall, B., 2007. The Slave Craton: geological and metallogenic evolution, in: Goodfellow, W.D. (Ed.), Mineral Resources of Canada: A Synthesis of Major Deposit-types, District Metallogeny, the Evolution of Geological Provinces, and Exploration Methods. Geological Survey of Canada Special Publication 5, pp. 849–879.

Bleeker, W., Kamo, S., 2003. A precise age for the Duke Lake sill and its relevance for fitting the Slave in a global Archean context, in: Program and Abstracts of Talks and Posters, 31st Yellowknife Geoscience Forum, pp. 7–8.

Bleeker, W., Hamilton, M.A., Söderlund, U., Ernst, R.E., 2008. Towards a complete magmatic event barcode for the Slave Craton; I, A precise U–Pb baddeleyite age for the Hearne swarm with

implications for a newly recognized Paleoproterozoic LIP across the Western Canadian Shield. Geological Association of Canada Abstract Volume 33, p. 23.

Bostock, H.H., van Breemen, O., Loveridge, W.D., 1987. Proterozoic geochronology in the Taltson Magmatic Zone, N.W.T., in: Radiogenic age and isotopic studies: Report 1. Geological Survey of Canada Paper 87-2, pp.73–80.

Bowring, S.A., Schmus, W.R.V., Hoffman, P.F., 1984. U–Pb zircon ages from Athapuscow aulacogen, East Arm of Great Slave Lake, N.W.T., Canadian Journal of Earth Sciences. 21, 1315–1324.

Buchan, K.L., Goutier, J., Hamilton, M.A., Ernst, R.E., Matthews, W.A., 2007. Paleomagnetism, U–Pb geochronology, and geochemistry of Lac Esprit and other dyke swarms, James Bay area, Quebec, and implications for Paleoproterozoic deformation of the Superior Province. Canadian Journal of Earth Sciences 44, 643–664.

Buchan, K.L., LeCheminant, A.N., van Breemen, O., 2009. Paleomagnetism and U–Pb geochronology of the Lac de Gras diabase dyke swarm, Slave Province, Canada: implications for relative drift of Slave and Superior provinces in the Paleoproterozoic. Canadian Journal of Earth Sciences 46, 361–379.

Buchan, K.L., Ernst, R.E., Bleeker, W., Davis, W.J., Villeneuve M., van Breemen, O., Hamilton, M., Söderlund, U., 2010. Proterozoic magmatic events of the Slave craton, Wopmay orogen and environs. Geological Survey of Canada Open File 5985.

Buchan, K.L., LeCheminant, A.N., van Breemen, O., 2012. Malley diabase dykes of the Slave craton, Canadian Shield: U–Pb age, paleomagnetism, and implications for continental reconstructions in the early Paleoproterozoic. Canadian Journal of Earth Sciences 49, 435–454.

Buchan, K.L., Mitchell, R.N., Bleeker, W., Hamilton, M.A., LeCheminant, A.N., 2016. Paleomagnetism of ca. 2.13–2.11 Ga Indin and ca. 1.885 Ga Ghost dyke swarms of the Slave craton: Implications for the Slave craton APW path and relative drift of Slave, Superior and Siberian cratons in the Paleoproterozoic. Precambrian Research 275, 151–175.

Canadian Certified Reference Materials Project, 1994. Certificate of Analysis, TDB-1.

Canadian Certified Reference Materials Project, 1997. Certificate of Analysis, WGB-1.

Canadian Geochronology Knowledgebase, 2013. Geological Survey of Canada. Earth Science Sector, Natural Resources Canada.

Cann, J.R., 1970. Rb, Sr, Y, Zr and Nb in some ocean floor basaltic rocks. Earth and Planetary Science Letters 10, 7–11.

Cavell, P.A., Baadsgaard, H., 1986. Geochronology of the Big Spruce Lake alkaline intrusion. Canadian Journal of Earth Sciences 23, 1–10.

Chacko, T., De, S.K., Creaser, R.A., Muehlenbachs, K., 2000. Tectonic setting of the Taltson magmatic zone at 1.9–2.0 Ga: a granitoid-based perspective. Canadian Journal of Earth Sciences 37, 1597–1609.

Chazot, G., Menzies, M.A., Harte, B., 1996. Determination of partition coefficients between apatite, clinopyroxene, amphibole, and melt in natural spinel lherzolites from Yemen: implications for wet melting of the lithospheric mantle. Geochimica et Cosmochimica Acta 60, 423–437.

Cox, D.M., Frost, C.D., Chamberlain, K.R., 2000. 2.01-Ga Kennedy dike swarm, southeastern Wyoming. Rocky Mountain Geology 35, 7–30.

Davis, D.W., Green, J.C., 1997. Geochronology of the North American Midcontinent rift in western Lake Superior and implications for its geodynamic evolution. Canadian Journal of Earth Sciences 34, 476–488.

Davis, W.J., 1997. U–Pb zircon and rutile ages from granulite xenoliths in the Slave province: Evidence for mafic magmatism in the lower crust coincident with Proterozoic dike swarms. Geology 25, 343–346.

Davis, W.J., Hegner, E., 1992. Neodymium isotopic evidence for the tectonic assembly of Late Archean crust in the Slave Province, northwest Canada. Contributions to Mineralogy and Petrology 111, 493–504.

Davis, W.J., Bleeker, W., 1999. Timing of plutonism, deformation, and metamorphism in the Yellowknife Domain, Slave Province, Canada. Canadian Journal of Earth Sciences 36, 1169–1187.

Davis, W.J., Fryers, B.J., King, J.E., 1994. Geochemistry and evolution of Late Archean plutonism and its significance to the tectonic development of the Slave craton. Precambrian Research 67, 207–241.

Davis, W.J., Jones, A.G., Bleeker, W., Grütter, H., 2003. Lithosphere development in the Slave craton: a linked crustal and mantle perspective. Lithos 71, 575–589.

Davis, W.J., Bleeker, W., Hulbert, L., Jackson, V., 2004. New geochronological results from the Slave Province Minerals and Geoscience Compilation and Synthesis Project. Yellowknife Geoscience Forum Abstracts Volume 2004, p. 20.

Davis, W.J., Pehrsson, S.J., Percival, J.A. 2015. Results of a U-Pb zircon geochronology transect across the southern Rae craton, Northwest Territories, Canada; Geological Survey of Canada, Open File 7655. 70 pp.

De, S.K., Chacko, T., Creaser, R.A., Muehlenbachs, K., 2000. Geochemical and Nd-Pb-O isotope systematics of granites from the Taltson Magmatic Zone, NE Alberta: implications for early Proterozoic tectonics in western Laurentia. Precambrian Research 102, 221–249.

DePaolo, D.J., 1981. Neodymium isotopes in the Colorado Front Range and crust–mantle evolution in the Proterozoic. Nature 291, 193–196.

DePaolo, D.J., Wasserburg, G.J., 1976. Nd isotopic variations and petrogenetic models. Geophysical Research Letters 3, 249–252.

Ernst, R.E., Buchan, K.L., with samples from Aspler, L.B., Baragar, W.R.A., Corkery, M.T., Davidson, A., et al., 2010. Geochemical database of Proterozoic intraplate mafic magmatism in Canada. Geological Survey of Canada, Open File 6016.

Fitton, J.G., James, D., Leeman, W.P., 1991. Basic magmatism associated with late Cenozoic extension in the western United States: Compositional variations in space and time. Journal of Geophysical Research: Solid earth, 96, 13693–13711.

Francis, D., 1985. The Baffin Bay lavas and the value of picrites as analogues of primary magmas. Contributions to Mineralogy and Petrology 89, 144–154.

Fujimaki H., Tatsumoto, M., Aoki K.I., 1984. Partition coefficients of Hf, Zr, and REE between phenocrysts and groundmasses. Journal of Geophysical Research 89, B662–B672.

Gast, P.W., 1968. Trace element fractionation and the origin of tholeiitic and alkaline magma types. Geochimica et Cosmochimica Acta 32, 1057–1086.

George, R., Rogers, N., 2002. Plume dynamics beneath the African plate inferred from the geochemistry of the Tertiary basalts of southern Ethiopia. Contributions to Mineralogy and Petrology 144, 286–304.

Gibson, S.A., Thompson, R.N., Leat, P.T., Dickin, A.P., Morrison, M.A., Hendry, G.L., Mitchell, J.G., 1992. Asthenosphere-derived magmatism in the Rio Grande rift, western USA: implications for continental break-up. Geological Society, London, Special Publications 68, 61–89.

Gladney, E.S., Roelandts, I., 1990. 1988 Compilation of Elemental Concentration Data for CCRMP Reference Rock Samples SY-2, SY-3 and MRG-1. Geostandards and Geoanalytical Research 14, 373–458.

Goff, S.P., 1984. The magmatic and metamorphic history of the East Arm, Great Slave Lake, N.W.T. PhD thesis, University of Alberta, Edmonton. 504 p.

Goff, S.P., Baadsgaard, H., Muehlenbachs, K., Scarfe, C.M., 1982. Rb–Sr isochron ages, magmatic 87Sr/86Sr initial ratios, and oxygen isotope geochemistry of the Proterozoic lava flows and intrusions of the East Arm of Great Slave Lake, Northwest Territories, Canada. Canadian Journal of Earth Sciences 19, 343–356.

Griffin, W.L., Doyle, B.J., Ryan, C.G., Pearson, N.J., Suzanne, Y.R., Davies, R., Kivi, K., Van Achterbergh, E., Natapov, L.M., 1999. Layered mantle lithosphere in the Lac de Gras area, Slave craton: composition, structure and origin. Journal of Petrology 40, 705–727.

Griffiths, R.W., Campbell, I.H., 1990. Stirring and structure in mantle starting plumes. Earth and Planetary Science Letters 99, 66–78.

Halls, H.C., Heaman, L.M., 2000. The paleomagnetic significance of new U-Pb age data from the Molson dyke swarm, Cauchon Lake area, Manitoba. Canadian Journal of Earth Sciences 37, 957–966.

Hamilton, M.A., Ryan, A.B., Emslie, R.F., Ermanovics, I.F., 1998. Identification of Paleoproterozoic anorthositic and monzonitic rocks in the vicinity of the Mesoproterozoic Nain Plutonic Suite, Labrador: U–Pb evidence. In Radiogenic age and isotopic studies, Report 11: Geological Survey of Canada, Current Research 1998-F, pp. 23–40.

Hanmer, S., Bowring, S., van Breemen, O., Parrish, R., 1992. Great Slave Lake shear zone, NW Canada: mylonitic record of Early Proterozoic continental convergence, collision and indentation. Journal of Structural Geology 14, 757–773.

Hart, W.K., WoldeGabriel, G., Walter, R.C. and Mertzman, S.A., 1989. Basaltic volcanism in Ethiopia: constraints on continental rifting and mantle interactions. Journal of Geophysical Research: Solid Earth 94, 7731–7748.

Hart, S.R., Blusztajn, J., Dick, H.J., Meyer, P.S., Muehlenbachs, K., 1999. The fingerprint of seawater circulation in a 500-meter section of ocean crust gabbros. Geochimica et Cosmochimica Acta 63, 4059–4080.

Heaman, L.M., 1997. Global mafic magmatism at 2.45 Ga: Remnants of an ancient large igneous province? Geology 25, 299–302.

Heaman, L.M., 2009. The application of U–Pb geochronology to mafic, ultramafic and alkaline rocks: an evaluation of three mineral standards. Chemical Geology 261, 43–52.

Heaman, L.M., Corkery, M.T., 1996. Proterozoic tectonic evolution of the eastern Trans-Hudson margin: Preliminary U–Pb results from the Split Lake block, Manitoba. Geological Association of Canada Program with Abstracts 21, A43.

Heaman, L.M., LeCheminant, A.N., 1993. Paragenesis and U-Pb systematics of baddeleyite (ZrO_2). Chemical Geology 110, 95–126.

Heaman, L.M., Pearson, D.G., 2010. Nature and evolution of the Slave Province subcontinental lithospheric mantle This article is one of a series of papers published in this Special Issue on the theme Lithoprobe—parameters, processes, and the evolution of a continent. Canadian Journal of Earth Sciences 47, 369–388.

Heaman, L.M., Erdmer, P., Owen, J.V., 2002. U–Pb geochronologic constraints on the crustal evolution of the Long Range Inlier, Newfoundland. Canadian Journal of Earth Sciences 39, 845–865.

Henderson, J.F., 1939. Taltson Lake, Northwest Territories. Geological Survey of Canada, "A" Series Map 525A, scale 1 inch = 4 miles.

Hoffman, P., 1968. Stratigraphy of the Lower Proterozoic Great Slave Supergroup, East Arm of Great Slave Lake, District of MacKenzie. Geological Survey of Canada. Paper 60–42, 93 p.

Hoffman, P.F., 1969. Proterozoic paleocurrents and depositional history of the East Arm fold belt, Great Slave Lake, Northwest Territories. Canadian Journal of Earth Sciences 6, 441–462.

Hoffman, P.F., 1973. Evolution of an Early Proterozoic Continental Margin: The Coronation Geosyncline and Associated Aulacogens of the Northwestern Canadian Shield. Philosophical Transactions of the Royal Society of London A: Mathematical, Physical and Engineering Sciences 273, 547-581.

Hoffman, P.F., 1981. Autopsy of Athapuscow aulacogen: a failed arm affected by three collisions, in: Campbell, F.H.A. (Ed.), Proterozoic Basins of Canada. Geological Survey of Canada, Paper 81-10, pp. 97–102.

Hoffman, P.F., 1987. Continental transform tectonics: Great Slave Lake shear zone (ca. 1.9 Ga), northwest Canada. Geology 15, 785–788.

Hoffman, P.F., 1988a. Geology and tectonics. East Arm of Great Slave Lake, Northwest Territories. Geologicl Survey of Canada Map 1628A, 2 sheets.

Hoffman, P.F., 1988b. United Plates of America, The Birth of a Craton: Early Proterozoic Assembly and Growth of Laurentia. Annual Review of Earth and Planetary Sciences 16, 543–603.

Hoffman, P.F., Burke, K.C.A., Dewey, J.F., 1974. Aulacogens and their genetic relation to geosynclines, with a Proterozoic example from Great Slave Lake, Canada, in: Dott, R.H., Shaver, R.H. (Eds.), Modern and Ancient Geosyncline Sedimentary. Society of Economic Paleontologists and Mineralogists, Special Publications 19, pp. 38–55.

Hoffman, P.F., Bell, I.R., Hildebrand, R.S., Thorstad, L., 1977. Geology of the Athapuscow Aulacogen, East Arm of Great Slave Lake, District of Mackenzie. Report of Activities, 77-1A, Geological Survey of Canada, Ottawa, Ont.

Hoffman, P.F., Bowring, S.A., Buchwaldt, R., Hildebrand, R.S., 2011. Birthdate for the Coronation paleocean: age of initial rifting in Wopmay orogen, Canada. Canadian Journal of Earth Sciences 48, 281–293.

Hollings, P., Fralick, P., Cousens, B., 2007. Early history of the Midcontinent Rift inferred from geochemistry and sedimentology of the Mesoproterozoic Osler Group, northwestern Ontario. Canadian Journal of Earth Sciences 44, 389–412.

Huijsmans, J.P., Barton, M., 1989. Polybaric geochemical evolution of two shield volcanoes from Santorini, Aegean Sea, Greece: evidence for zoned magma chambers from cyclic compositional variations. Journal of Petrology 30, 583–625.

Isley, A.E., Abbott, D.H., 1999. Plume-related mafic volcanism and the deposition of banded iron formation. Journal of Geophysical Research: Solid Earth 104, 15461–15477.

Jaffey, A.H., Flynn, K.F., Glendenin, L.E., Bentley, W.T., Essling, A.M., 1971. Precision measurement of half-lives and specific activities of ^{235}U and ^{238}U. Physical Review C 4, 1889–1906.

Janzen, M., 2015. Nature of Archean basement inliers, East Arm basin, NWT. B.Sc. thesis, University of Alberta, Edmonton.

Jaques, A.L., Green, D.H., 1980. Anhydrous melting of peridotite at 0–15 kb pressure and the genesis of tholeiitic basalts. Contributions to Mineralogy and Petrology 3, 287–310.

Johnson, B.J., 1990. Stratigraphy and structure of the Early Proterozoic Wilson Island Group, East Arm thrust-fold belt, N.W.T. Canadian Journal of Earth Sciences 27, 552–569.

Johnson, K.T., 1998. Experimental determination of partition coefficients for rare earth and high-field-strength elements between clinopyroxene, garnet, and basaltic melt at high pressures. Contributions to Mineralogy and Petrology 133, 60–68.

Kerr, A.C., Thompson, R.N., Bernstein, S., 1995. High-pressure fractionation in rift-related basaltic magmatism: Faeroe plateau basalts. Geology 23, 671–672.

Ketchum, K.Y., Heaman, L.M., Bennett, G., Hughes, D.J., 2013. Age, petrogenesis and tectonic setting of the Thessalon volcanic rocks, Huronian Supergroup, Canada. Precambrian Research 233, 144–172.

Kjarsgaard, B.A., Pearson, D.G., DuFrane, A., and Heaman, L.M., 2013a. Proterozoic geology of the east arm basin wth emphasis on Paleoproterozoic magmatic rocks, Thaidene Nene MERA study area, in: Wright, D.F., Ambrose, E.J., Lemkow, D., and Bonham-Carter, G. (Eds.), Mineral and energy resource assessment of the proposed Thaidene Nene National Park Reserve in the area of the east arm of Great Slave Lake, Northwest Territories. Geological Survey of Canada Open File 7196, pp. 51–92.

Kjarsgaard, B.A., Tella, S., Lemkow, D., 2013b. Bedrock geology of the proposed Thaidene Nene National Park Reserve in the area of the East Arm of Great Slave Lake, Northwest Territories, in: Wright, D.F., Ambrose, E.J., Lemkow, D., and Bonham-Carter, G. (Eds.), Mineral and energy resource assessment of the proposed Thaidene Nene National Park Reserve in the area of the east arm of Great Slave Lake, Northwest Territories. Geological Survey of Canada Open File 7196, 1 sheet.

Klein, E.M., 2004. Geochemistry of the Igneous Oceanic Crust, in: Holland, H.D., Turekian, K.K. (Eds.), Treatise on Geochemistry. Elsevier, Amsterdam, pp. 433–463.

Komar, P.D., 1972. Flow differentiation in igneous dikes and sills: profiles of velocity and phenocryst concentration. Geological Society of America Bulletin 83, 3443–3448.

Kopylova, M.G., Caro, G., 2004. Mantle xenoliths from the southeastern Slave craton: evidence for chemical zonation in a thick, cold lithosphere. Journal of Petrology 45, 1045–1067.

Kopylova, M.G., Russell, J.K., 2000. Chemical stratification of cratonic lithosphere: constraints from the Northern Slave craton, Canada. Earth and Planetary Science Letters 181, 71–87.

Kuehner, S.M., 1986. Mafic dykes of the East Antarctic shield: experimental, geochemical and petrological studies focusing on the Proterozoic evolution of the crust and the mantle. PhD thesis, University of Tasmania, Hobart. 345 p.

Langmuir, C.H., Vocke, R.D., Hanson, G.N., Hart, S.R., 1978. A general mixing equation with applications to Icelandic basalts. Earth and Planetary Science Letters,37, 380–392.

Le Roex, A.P., Cliff, R.A., Adair, B.J.I., 1990. Tristan da Cunha, South Atlantic: geochemistry and petrogenesis of a basanite-phonolite lava series. Journal of Petrology 31, 779–812.

Leat, P.T., Thompson, R.N., Morrison, M.A., Hendry, G.L., Dickin, A.P., 1990. Geochemistry of mafic lavas in the early Rio Grande rift, Yarmony Mountain, Colorado, USA. Chemical Geology 81, 23–43.

LeCheminant, A.N., Heaman, L.M., 1989. Mackenzie igneous events, Canada: Middle Proterozoic hotspot magmatism associated with ocean opening. Earth and Planetary Science Letters 96, 38–48.

LeCheminant, A.N., van Breemen, O., 1994. U–Pb ages of Proterozoic dyke swarms, Lac de Gras area, NWT: evidence for progressive break-up of an Archean supercontinent. Geological Association of Canada/Mineralogical Association of Canada, Program with Abstracts 19, p. A-62.

Ludwig, K.R., 2003. Isoplot 3.00: A geochronological toolkit for Microsoft Excel. Berkeley Geochronology Center Spececial Publication 4. 71 pp.

Lugmair, G.W., Marti, K., 1978. Lunar initial $^{143}Nd/^{144}Nd$: differential evolution of the lunar crust and mantle. Earth and Planetary Science Letters 39, 349–357.

Machado, N., David, J., Scott, D.J., Lamothe, D., Philippe, S., Gariépy, C., 1993. U–Pb geochronology of the western Cape Smith Belt, Canada: new insights on the age of initial rifting and arc magmatism. Precambrian Research 63, 211–223.

McCulloch, M.T., Wasserburg, G.J., 1978. Sm-Nd and Rb-Sr chronology of continental crust formation. Science 200, 1003–1011.

McDonough, W.F., Sun, S.-s., 1995. The composition of the Earth. Chemical Geology 120, 223–253.

McKenzie, D., O'Nions, R.K., 1991. Partial melt distributions from inversion of rare Earth element concentrations. Journal of Petrology 32, 1021–1091.

Medynski, S., Pik, R., Burnard, P., Williams, A., Vye-Brown, C., Ferguson, D., Blard, P.H., France, L., Yirgu, G., Seid, J.I., Ayalew, D., 2013. Controls on magmatic cycles and development of rift topography of the Manda Hararo segment (Afar, Ethiopia): insights from cosmogenic ^{3}He investigation of landscape evolution. Earth and Planetary Science Letters 367, 133–145.

Menzies, M., Seyfried, W.E., 1979. Basalt-seawater interaction: trace element and strontium isotopic variations in experimentally altered glassy basalt. Earth and Planetary Science Letters 44, 463–472.

Mitchell, R.N., Hoffman, P.F., Evans, D.A., 2010. Coronation loop resurrected: Oscillatory apparent polar wander of Orosirian (2.05–1.8 Ga) paleomagnetic poles from Slave craton. Precambrian Research 179, 121–134.

Mitchell, R.N., Bleeker, W., van Breemen, O., LeCheminant, T.N., Peng, P., Nilsson, M.K., Evans, D.A., 2014. Plate tectonics before 2.0 Ga: Evidence from paleomagnetism of cratons within supercontinent Nuna. American Journal of Science 314, 878–894.

Mumford, T.R., 2013. Petrology of the Blatchford Lake Intrusive Suite, Northwest Territories, Canada. PhD thesis, Carleton University, Ottawa. 239 p.

Mumford, T.R., Cousens, B.L., 2014. Constraints on the relationships between Paleoproterozoic intrusions and dyke swarms, East Arm of Great Slave Lake, N.W.T. Canadian Journal of Earth Sciences 51, 419–438.

Mumford, T. R., Ketchum, J., Falck, H. & Heaman, L., 2012. New geochemical, geochronological, and isotopic data of the Blachford Lake Intrusive Suite and the Simpson Island Dyke. Northwest Territories Geoscience Office, NWT Open File 2102-005, 41 p.

Niu, Y., Wilson, M., Humphreys, E.R., O'Hara, M.J., 2011. The origin of intra-plate ocean island basalts (OIB): the lid effect and its geodynamic implications. Journal of Petrology 52, 1443–1468.

Nutman, A.P., Kalsbeek, F., Marker, M., van Gool, J.A., Bridgwater, D., 1999. U–Pb zircon ages of Kangâmiut dykes and detrital zircons in metasediments in the Palaeoproterozoic Nagssugtoqidian Orogen (West Greenland): Clues to the pre-collisional history of the orogen. Precambrian Research 93, 87–104.

Okamoto, K., 1979. Geochemical study on magmatic differentiation of Asama Volcano, central Japan. Journal of the Geological Society of Japan 85, 525–535.

Ootes, L., Davis, W.J., Jackson, V.A., van Breemen, O., 2015. Chronostratigraphy of the Hottah terrane and Great Bear magmatic zone of Wopmay Orogen, Canada, and exploration of a terrane translation model. Canadian Journal of Earth Sciences 52, 1062–1092.

Page, R.W., 1978. Response of U–Pb zircon and Rb-Sr total-rock and mineral systems to low-grade regional metamorphism in Proterozoic igneous rocks, Mount Isa, Australia. Journal of the Geological Society of Australia 25, 141–164.

Pearce, J.A., 1983. Role of the sub-continental lithosphere in magma genesis at active continental margins, in: Hawkesworth, C.J., Norry, M.J. (Eds.), Continental Basalts and Mantle Xenoliths. Shiva Publications, Nantwich, Cheshire, pp. 230–249.

Pearce, J.A., 1996. A user's guide to basalt discrimination diagrams. Trace element geochemistry of volcanic rocks: applications for massive sulphide exploration. Geological Association of Canada, Short Course Notes 12, pp. 79–113.

Pearce J.A., 2008. Geochemical fingerprinting of oceanic basalts with applications to ophiolite classification and the search for Archean oceanic crust. Lithos 100, 14–48.

Pehrsson, S.J., van Breemen, O., and Hanmer, S., 1993. Ages of diabase dyke intrusions, Great Slave Lake shear zone, Northwest Territories. In Radiogenic age and isotopic studies, Report 7. Geological Survey of Canada, Paper 93-2, pp. 23–28.

Percival, J.A., Davis, W.J., Hamilton, M.A., 2016. U–Pb Zircon Geochronology and Depositional History of the Montresor group, Rae Province, Nunavut, Canada. Canadian Journal of Earth Sciences. DOI: 10.1139/cjes-2016-0170.

Pik, R., Deniel, C., Coulon, C., Yirgu, G., Marty, B., 1999. Isotopic and trace element signatures of Ethiopian flood basalts: evidence for plume–lithosphere interactions. Geochimica et Cosmochimica Acta 63, 2263–2279.

Rehkämper, M., Hofmann, A.W., 1997. Recyclced ocean crust and sediment in Indian Ocean MORB. Earth and Planetary Science Letters 147, 93–106.

Reinhardt, E.W., 1970. Geology of the Thubun Lakes, District of Mackenzie. Geological Survey of Canada, Preliminary Map 9-1969.

Roscoe S.M., Henderson, M.N., Hunt, P.A., van Breemen, O. 1987. U–Pb zircon age of an alkaline granite body in the Booth River Intrusive Suite, N.W.T., in Radiogenic age and isotopic studies: Report 1. Geological Survey of Canada, Paper 87-2, pp 95–100.

Salters, V.J.M., Stracke, A., 2004. Composition of the depleted mantle. Geochemistry, Geophysics, Geosystems 5, Q05B07.

Sandeman, H.A., Ryan, J.J., 2008. The Spi Lake Formation of the central Hearne domain, western Churchill Province, Canada: an axial intracratonic continental tholeiite trough above the cogenetic Kaminak dyke swarm. Canadian Journal of Earth Sciences 45, 745–767.

Sandeman, H.A., Heaman, L.M., LeCheminant, A.N., 2013. The Paleoproterozoic Kaminak dykes, Hearne craton, western Churchill Province, Nunavut, Canada: Preliminary constraints on their age and petrogenesis. Precambrian Research 232, 119–139.

Sarkar, C., Pearson, D.G., Heaman, L.M., Woodland, S.J., 2015. Precise Pb isotope ratio determination of picogram-size samples: A comparison between multiple Faraday collectors equipped with 10^{12} Ω amplifiers and multiple ion counters. Chemical Geology 395, 27–40.

Shaulis, B.J., Heaman, L.M., Ootes, L., Martel, E., Chacko, T., 2014. An update on the detrital zircon record from the Paleoproterozoic East Arm basin, Great Slave Lake, NWT, in: 42nd Annual Yellowknife Geoscience Forum Abstracts, pp. 101–102.

Shaw, D.M., 1970. Trace element fractionation during anatexis. Geochimica et Cosmochimica Acta 34, 237–243.

Shervais, J.W., Vetter, S.K., Hanan, B.B., 2006. Layered mafic sill complex beneath the eastern Snake River Plain: Evidence from cyclic geochemical variations in basalt. Geology 34, 365–368.

Shirey, S.B., Berg, J.H., Carlson, R.W., 1994. Temporal changes in the sources of flood basalts: isotopic and trace element evidence from the 1100 Ma old Keweenawan Mamainse Point Formation, Ontario, Canada. Geochimica et Cosmochimica Acta 58, 4475–4490.

Simonetti, A., Heaman, L.M., Hartlaub, R.P., Creaser, R.A., MacHattie, T.G., Böhm, C., 2005. U–Pb zircon dating by laser ablation-MC-ICP-MS using a new multiple ion counting Faraday collector array. Journal of Analytical Atomic Spectrometry 20, 677–686.

Sinclair, W.D., Hunt, P.A., Birkett, T.C., 1994. U–Pb zircon and monazite ages of the Grace Lake Granite, Blatchford Lake Intrusive Suite, Slave Province, Northwest Territories. Geological Survey of Canada, Current Research 1994-F, pp. 15–20.

Skelhorn, R.R., Henderson, P, Walsh, J.N., Longland, P.J.N., 1979. The chilled margin of the Ben Buie layered gabbro, Isle of Mull. Scottish Journal of Geology 15, 161–167.

Snyder, D.B., Kjarsgaard, B.A., 2013. Mantle roots of major Precambrian shear zones inferred from structure of the Great Slave Lake shear zone, northwest Canada. Lithospher 5, 539–546.

Sobolev, A.V., Hofmann, A.W., Sobolev, S.V., Nikogosian, I.K., 2005. An olivine-free mantle source of Hawaiian shield basalts. Nature 434, 590–597.

Stacey J.S., Kramers, J.D., 1975. Approximation of terrestrial lead isotope evolution by a two-stage model. Earth and Planetary Science Letters 26, 207–221.

Stern, R.A., Bodorkos, S., Kamo, S.L., Hickman, A.H., Corfu, F., 2009. Measurement of SIMS instrumental mass fractionation of Pb isotopes during zircon dating. Geostandards and Geoanalytical Research 33, 145–168.

Stockwell, C.H., 1932. Great Slave Lake-Coppermine River area, NWT. Geological Survey Summary Report, Pt C, pp. 37–63.

Stockwell, C.H., 1936a. Great Slave Lake, eastern portion (west half), District of Mackenzie, Northwest Territories. Geological Survey of Canada, Map 377A (with marginal notes), Scale 1 in. = 4 mi.

Stockwell, C.H., 1936b. Great Slave Lake, eastern portion (east half), District of Mackenzie, Northwest Territories. Geological Survey of Canada, Map 378A (with marginal notes), Scale 1 in. = 4 mi.

Stockwell, C.H., Brown, I.C., Barnes, F.Q., Wright, G.M., 1968. Geology, Christie Bay, District of Mackenzie, Northwest Territories. Geological Survey of Canada, Map 1122A.

Storey, M., Duncan, R.A., Tegner, C., 2007. Timing and duration of volcanism in the North Atlantic Igneous Province: Implications for geodynamics and links to the Iceland hotspot. Chemical Geology 241, 264–281.

Sun, S.-s., McDonough, W.F., 1989. Chemical and isotopic systematics of oceanic basalts: implications for mantle composition and processes, in: Saunders, A.D., Norry, M.J. (Eds.), Magmatism in the Ocean Basins. Geological Society Special Publication 42, pp. 313–345.

Sundvoll, B., Neumann, E.R., Larsen, B.T., Tuen, E., 1990. Age relations among Oslo Rift magmatic rocks: implications for tectonic and magmatic modelling. Tectonophysics 178, 67–87.

Thompson, A.B., Schulmann, K., Jezek, J., Tolar, V., 2001. Thermally softened continental extensional zones (arcs and rifts) as precursors to thickened orogenic belts. Tectonophysics 332, 115–141.

Thompson, R.N., Morrison, M.A., 1988. Asthenospheric and lower-lithospheric mantle contributions to continental extensional magmatism: an example from the British Tertiary Province. Chemical Geology 68, 1–15.

Thorstad, L., 1976. Structure, stratigraphy and petrology of the Union Island group, East Arm of Great Slave Lake, NWT. Unpublished B.Sc. thesis, University of British Columbia, Vancouver. 55 p.

Turner, S., Regelous, M., Kelley, S., Hawkesworth, C., Mantovani, M., 1994. Magmatism and continental break-up in the South Atlantic: high precision ^{40}Ar–^{39}Ar geochronology. Earth and Planetary Science Letters 121, 333–348.

Upton, B.G.J., Stephenson, D., Martin, A.R., 1985. The Tugtutôq older giant dyke complex: mineralogy and geochemistry of an alkali gabbro-augite-syenite-foyaite association in the Gardar Province of South Greenland. Mineralogical Magazine 49, 624–642.

van Breemen, O., Hanmer, S.K., Parrish, R.R., 1990. Archean and Proterozoic mylonites along the southeastern margin of the Slave structural province, Northwest Territories. Geological Survey of Canada Paper 89-2, 55–61.

van Breemen, O., Davis, W.J. and King, J.E., 1992. Temporal distribution of granitoid plutonic rocks in the Archean Slave Province, northwest Canadian Shield. Canadian Journal of Earth Sciences 29, 2186–2199.

van Breemen, O., Kjarsgaard, B.A., Tella, S., Lemkow, D., Aspler, L., 2013. U–Pb detrital zircon geochronology of clastic sedimentary rocks of the Paleoproterozoic Nonacho and East Arm basins, East Arm MERA study area, Chapter 4, in: Wright, D.F., Ambrose, E.J., Lemkow, D., and Bonham-Carter, G. (Eds.), Mineral and energy resource assessment of the proposed Thaidene Nene National Park Reserve in the area of the east arm of Great Slave Lake, Northwest Territories. Geological Survey of Canada Open File 7196, pp. 95–118.

Villeneuve, M.E., van Breemen, O., 1994. A compilation of U–Pb age data from the Slave Province. Geological Survey of Canada Open File 2972, p. 53.

Villemant, B., Jaffrezic, H., Joron, J.L., Treuil, M., 1981. Distribution Coefficients of Major and Trace-Elements - Fractional Crystallization in the Alkali Basalt Series of Chaine-Des-Puys (Massif Central, France). Geochimica et Cosmochimica Acta 45, 1997–2016.

Wheatley, M., Rock, N.M., 1988. SPIDER; a Macintosh program to generate normalized multi-element "spidergrams". American Mineralogist 73, 919–921.

Williams, H., Hoffman, P.F., Lewry, J.F., Monger, J.W., Rivers, T., 1991. Anatomy of North America: thematic geologic portrayals of the continent. Tectonophysics 187, 117–134.

Wood, D.A., 1979. A variably veined suboceanic upper mantle—genetic significance for mid-ocean ridge basalts from geochemical evidence. Geology 7, 499–503.

Wood, D.A., Gibson, I.L., Thompson, R.N., 1976. Elemental mobility during zeolite facies metamorphism of the Tertiary basalts of eastern Iceland. Contributions to Mineralogy and Petrology 55, 241–254.

Workman, R.K., Hart, S.R., 2005. Major and trace element composition of the depleted MORB mantle (DMM). Earth and Planetary Science Letters 231, 53–72.

Yamashita, K., Creaser, R.A., Stemler, J.U., Zimaro, T.W., 1999. Geochemical and Nd–Pb isotopic systematics of late Archean granitoids, southwestern Slave Province, Canada: constraints for granitoid origin and crustal isotopic structure. Canadian Journal of Earth Sciences 36, 1131–1147.

Appendix A Anomalous remobilization of rare earth elements during alteration of the Union Island Group basalts

Several samples from the Union Island Group basalts display fractionation between rare earth elements (REE) and the rest of high field strength elements (HFSE; Fig. A1; Table A1). In the lower basalt unit, samples LH15-EA11 and UI95D display depletion of both LREE and HREE relative to Th, Nb, Ta, Zr, Hf, and Ti ($Nd/Zr_N = 0.6$, 0.8, respectively, compared to 1.3 for average lower basalt unit; $Ti/Gd_N = 1.3$, 1.3, respectively, compared to 0.9 for average lower basalt unit). Sample LH15-EA06 displays only LREE depletion, with an elevated Ta/La_N ratio of 2.5 compared to an average of 1.4 for the lower basalt unit. In the upper basalt unit, sample UI35A is depleted in REE relative to Nb, Ta, Zr, Hf, and Ti (Fig. A1b). As the enrichment patterns of Nb, Ta, Zr, Hf, and Ti of these samples closely follows those of their respective units, the REE in these samples were likely selectively remobilized at some point after crystallization.

Humphris (2013) defined REE mobility in igneous rocks as being dependent on 1) the distribution of REE within mineral phases, 2) the susceptibility of these mineral phases to fluid alteration, 3) the concentration of REE in the fluids, and 4) the formation of secondary, alteration minerals that may capture mobilized REE. Since distribution coefficients for most REE in major mineral phases in basalt (i.e. olivine, clinopyroxene, plagioclase, oxide phases) is less than unity (e.g., Fujimaki et al., 1984), we can surmise that REE would have been most enriched in late-stage liquid phases which crystallized to form interstitial glass, provided that REE-concentrating accessory mineral phases such as zircon, allanite, and titanite did not form as part of the primary igneous assemblage. In this scenario, significant mobilization of REE may occur during breakdown of basaltic glass, which is commonly observed in fluid alteration of seafloor basalt (e.g., Bonatti, 1965). In comparison, other HFSE such as Ta, Nb, Zr, Hf, and Ti are more strongly partitioned into oxide phases than REE (Lemarchand et al., 1987; Nielsen et al., 1992; Zach and Brumm, 1998); therefore whole-rock abundance of these five elements would be less disturbed during breakdown of basaltic glass. Palagonitization of basalt glass has been demonstrated to cause selective enrichment or depletion of REE in ocean floor basalts depending on water/rock ratios and exposure times (Ludden and Thompson, 1978; Staudigel and Hart, 1983). Therefore, breakdown of basaltic glass and the selected removal of REE from the rock by alteration fluids can explain the depletion of REE relative to other HFSE in some samples from the lower and upper basalt units.

Of all Union Island Group basalt samples, only LH15-EA12 displays anomalous REE enrichment relative to other HFSE. LH15-EA12 shares similar petrographic attributes as the REE-depleted LH15-EA11, collected only 10m away, except that the former contains large (up to 10 mm) xenocrysts of altered plagioclase and clinopyroxene. Considering that REE are more strongly partitioned into clinopyroxene relative to other primary basaltic minerals (Fujimaki et al., 1984), the enriched REE trend in LH15-EA12 was likely derived from clinopyroxene xenocrysts plucked from a partly crystallized magma during liquid ascent. This is supported by the higher enrichment of HREE in LH15-EA12 relative to average lower basalt unit compared to only moderate enrichment of LREE; this is consistent with higher partition coefficients of HREE than LREE in clinopyroxene (Fujimaki et al., 1984).

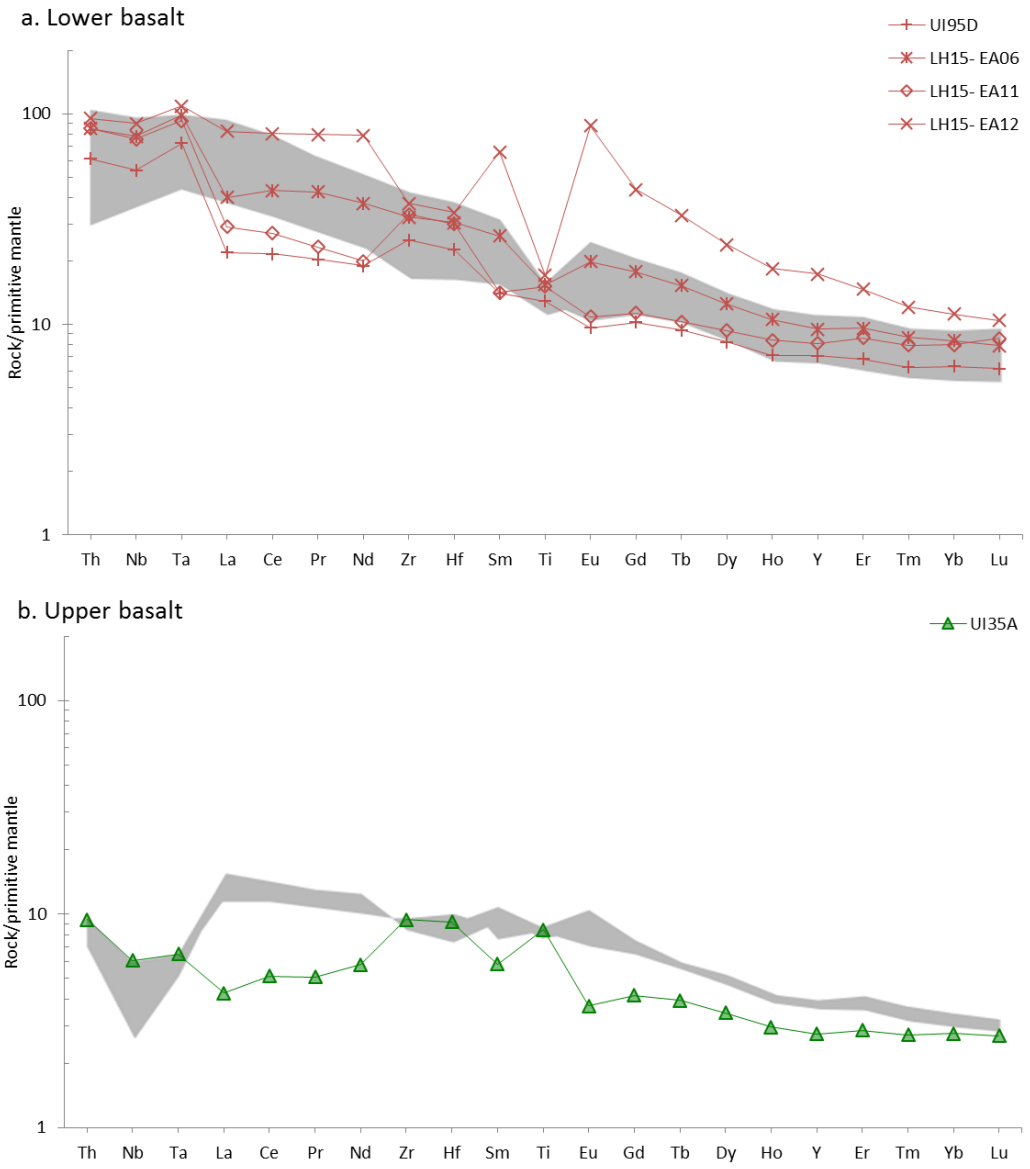

Figure A.1. Incompatible element multi-element plots for samples from the lower basalt and upper basalt units that show anomalous REE enrichment trends. Normalization is made to primitive pyrolite mantle (McDonough and Sun, 1995). Shaded area represents the remainder of the dataset from this study.

Table A.1. Normalized HFSE ratios for Union Island Group basalt samples showing anomalous REE trends, compared with their respective unit averages. Ratios are taken between REE and non-REE HFSE with similar degrees of incompatibility (Figure A.1). Normalization is made to primitive pyrolite mantle (McDonough and Sun, 1995).

Unit/Sample	Ta/La_N	Nd/Zr_N	Ti/Gd_N
Lower basalt (n=25)	**1.4**	**1.3**	**0.9**
UI95D	3.3	0.8	1.3
LH15-EA06	2.5	1.2	0.9
LH15-EA11	3.2	0.6	1.3
LH15-EA12	1.3	2.1	0.4
Upper basalt (n=6)	**0.4**	**1.3**	**1.2**
UI35A	1.5	0.6	2.0

References

Bonatti, E., 1965. Palagonite, hyaloclastites and alteration of volcanic glass in the ocean. Bulletin Volcanologique 28, 257–269.

Fujimaki H., Tatsumoto, M., Aoki K.I., 1984. Partition coefficients of Hf, Zr, and REE between phenocrysts and groundmasses. Journal of Geophysical Research 89, B662–B672.

Humphis, S.E., 2013. The mobility of rare earth elements in the crust, in: Henderson, P. (Ed.), Rare Earth Element Geochemistry. Elsevier, Amsterdam, Netherlands, pp. 317–342.

Lemarchand, F., Villemant, B., Calas, G., 1987. Trace element distribution coefficients in alkaline series. Geochimica et Cosmochimica Acta 51, 1071–1081.

Ludden, J.N., Thompson, G., 1978. Behaviour of rare earth elements during submarine weathering of tholeiitic basalt. Nature 274, 147–149.

McDonough, W.F., Sun, S.-s., 1995. The composition of the Earth. Chemical Geology 120, 223–253.

Nielsen, R.L., Gallahan, W.E., Newberger, F., 1992. Experimentally determined mineral-melt partition coefficients for Sc, Y and REE for olivine, orthopyroxene, pigeonite, magnetite and ilmenite. Contributions to Mineralogy and Petrology 110, 488–499.

Staudigel, H., Hart, S.R., 1983. Alteration of basaltic glass: Mechanisms and significance for the oceanic crust-seawater budget. Geochimica et Cosmochimica Acta 47, 337–350.

Zach, T., Brumm, R., 1998. Ilmenite/liquid partition coefficients of 26 trace elements determined through ilmenite/clinopyroxene partitioning in garnet pyroxene, in: 7th International Kimberlite Conference. Gurney, J.J., Gurney, J.L., Pascoe, M.D., Richardson, S.H. (Eds.). Red Roof Design, Cape Town, pp. 986–988.

Appendix B Parameters for petrological modeling

1 Fractional crystallization

Modeling for closed-system fractional crystallization in a magma body follows the principle of Rayleigh fractionation, after the approach of Allègre and Minster (1978). Assuming that the bulk partition coefficient of the element of interest, $\overline{D}^i$, remains constant during crystallization of the magma, the concentration of the element in the evolving liquid is defined as:

$$C_l^i = C_{0,l}^i f^{\overline{D}^i - 1} \quad \text{(Eq. 1)}$$

where $C_{0,l}^i$ is the initial magma concentration of the element *i*, and *f* is the weight proportion of residual magma. Bulk partition coefficient of the element is defined as:

$$\overline{D}^i = \sum_a D_{a-l}^i X_a \quad \text{(Eq. 2)}$$

where D_{a-l}^i is the partition coefficient of element *i* between mineral *a* and the liquid, and X_a is the weight fraction of the crystallizing mineral *a*. For modeling fractional crystallization in the lower basalt unit and its diabase feeders, a mafic crystallizing assemblage of 10% olivine+58% clinopyroxene+30% plagioclase+2% magnetite was applied; the values are based on CIPW norm calculation of mineral modes of the most primitive sample composition LH14-14.

2 Partial melting

Partial melting of mantle sources is modeled by the equilibrium melting formula after Shaw (1970). The concentration of an element *i* in the liquid is defined as:

$$C_l^i = \frac{C_{0,l}^i}{\overline{D}^i + F(1 - \overline{D}^i)} \quad \text{(Eq. 3)}$$

where *F* is the weight fraction of the melt. This assumes that the melt is in equilibrium with residual solid phases, in contrast to a fractional melting model where melts are separated from residual solids before equilibrium is reached. In modeling geochemical parameters used in this study, we found negligible difference between the equilibrium melting model and the fractional melting model, and thus preferred the former for its simpler formulation.

Bulk distribution coefficient, $\overline{D}^i$, is defined similarly as in equation 2, with X_a representing the weight fraction of the mineral in the melt assemblage. In this study we model melting of mantle peridotites at different depths using garnet lherzolite (60% olivine, 20% orthopyroxene, 10% clinopyroxene, 10% garnet) and spinel lherzolite (53% olivine, 27% orthopyroxene, 17% clinopyroxene, 3% spinel) as the melt assemblages (Kinzler, 1997; Walter, 1998).

3 Isotopic mixing

Determination of the isotopic ratio of a mixture of two magmas with known isotopic ratios follows the formulation of DePaolo and Wasserburg (1979):

$$(\epsilon_x)_{mix} = \frac{X_1[x^s]_1(\epsilon_x)_1 + (1 - X_1)[x^s]_2(\epsilon_x)_2}{X_1[x^s]_1 + (1 - X_1)[x^s]_2} \quad \text{(Eq. 4)}$$

where x denotes the element in question, ϵ_x represents the isotopic ratio of interest ($^{143}Nd/^{144}Nd$ in this study), $[x^s]_i$ is the concentration of the stable isotope x^s (^{144}Nd in this study) in component i, and X_i is the weight fraction of component i in the mixture.

4 Distribution coefficients

Distribution coefficients of elements used in petrological modeling are presented in tables B.1 and B.2.

Table B.1. Liquid-mineral distribution coefficients used in fractional crystallization modeling in this study.

	Olivine	Clinopyroxene	Plagioclase	Magnetite	Spinel
Cr	2.8 (Villemant et al., 1981)	5.3 (Villemant et al., 1981)	–	–	252 (Wijbran et al., 2015)
Ni	34 (Villemant et al., 1981)	2.5 (Villemant et al., 1981)	–	–	5 (Wijbran et al., 2015)
Zr	0.06 (Villemant et al., 1981)	0.123 (Zach and Brumm, 1998)	0.2 (Villemant et al., 1981)	0.9 (Nielsen et al., 1992)	–
Nb	0.01 (McKenzie and O'Nions, 1991)	0.05 (McKenzie and O'Nions, 1991)	0.01 (McKenzie and O'Nions, 1991)	0.905 (Nielsen et al., 1992)	–
Yb	0.0313 (Fujimaki et al., 1984)	0.3209 (Fujimaki et al., 1984)	0.0855 (Aignertorres et al., 2007)	0.018 (Lemarchand et al., 1987)	–
Hf	0.01 (McKenzie and O'Nions, 1991)	0.233 (McKenzie and O'Nions, 1991)	0.01 (McKenzie and O'Nions, 1991)	0.16 (Lemarchand et al., 1987)	–
Th	0.03 (Villemant et al., 1981)	0.04 (Villemant et al., 1981)	0.07 (Villemant et al., 1981)	0.1 (Lemarchand et al., 1987)	–

Table B.2. Liquid-mineral distribution coefficients used in partial melting modeling in this study.

	Olivine	Orthopyroxene	Clinopyroxene	Spinel	Garnet
Y	0.0036 (Nielsen et al., 1992)	0.384 (Salters and Longhi, 1999)	0.715 (Hack et al., 1994)	0.002 (Elkins et al., 2008)	3.48 (Salters and Longhi, 1999)
Zr	0.011 (Fujimaki et al., 1984)	0.0245 (Salters and Longhi, 1999)	0.1155 (Salters and Longhi, 1999)	0.06 (Horn et al., 1994)	0.688 (Salters and Longhi, 1999)
Nb	0.01 (McKenzie and O'Nions, 1991)	0.00165 (Salters and Longhi, 1999)	0.0077 (Zach and Brumm, 1998)	0.08 (Horn et al., 1994)	0.021 (Salters and Longhi, 1999)
Nd	0.001 (McKenzie and O'Nions, 1991)	0.0068 (McKenzie and O'Nions, 1991)	0.21 (McKenzie and O'Nions, 1991)	0.01 (McKenzie and O'Nions, 1991)	0.087 (McKenzie and O'Nions, 1991)
Hf	0.01 (McKenzie and O'Nions, 1991)	0.01 (McKenzie and O'Nions, 1991)	0.233 (McKenzie and O'Nions, 1991)	0.05 (Horn et al., 1994)	0.23 (McKenzie and O'Nions, 1991)

References

Aignertorres, M., Blundy, J., Ulmer, P., Pettke, T., 2007. Laser Ablation ICPMS study of trace element partitioning between plagioclase and basaltic melts: an experimental approach. Contributions to Mineralogy and Petrology 153, 647–667.

Allègre, C.J., Minster, J.F., 1978. Quantitative models of trace element behavior in magmatic processes. Earth and Planetary Science Letters 38, 1–25.

DePaolo, D.J., Wasserburg, G.J., 1979. Petrogenetic mixing models and Nd–Sr isotopic patterns. Geochimica et Cosmochimica Acta 43, 615–627.

Elkins, L., Gaetani, G., Sims, K., 2008. Partitioning of U and Th during garnet pyroxenite partial melting: Constraints on the source of alkaline ocean island basalts. Earth and Planetary Science Letters 265, 270–286.

Hack, P.J., Nielsen, R.L., Johnston, A.D., 1994. Experimentally determined rare-Earth element and Y partitioning behavior between clinopyroxene and basaltic liquids at pressures up to 20 kbar. Chemical Geology 117, 89–105.

Horn, I., Foley, S.F., Jackson, S.E., Jenner, G.A., 1994. Experimentally determined partitioning of high field strength- and selected transition elements between spinel and basaltic melt. Chemical Geology 117, 193–218.

Kinzler, R.J., 1997. Melting of mantle peridotite at pressures approaching the spinel to garnet transition: Application to mid-ocean ridge basalt petrogenesis. Papers on Chemistry and Physics of Mineral and Rocks Volcanology 102, 853–874.

McKenzie, D., O'Nions, R.K., 1991. Partial melt distributions from inversion of rare Earth element concentrations. Journal of Petrology 32, 1021–1091.

Salter, V., Longhi, J., 1999. Trace element partitioning during the initial stages of melting beneath mid-ocean ridges. Earth and Planetary Science Letters 166, 15–30.

Shaw, D.M., 1970. Trace element fractionation during anatexis. Geochimica et Cosmochimica Acta 34, 237–243.

Villemant, B., Jaffrezic, H., Joron, J.L., Treuil, M., 1981. Distribution coefficients of major and trace-elements - fractional crystallization in the alkali basalt series of Chaine-Des-Puys (Massif Central, France). Geochimica et Cosmochimica Acta 45, 1997–2016.

Walter, M.J., 1998. Melting of garnet peridotite and the origin of komatiite and depleted lithosphere. Journal of Petrology 39, 29–60.

Appendix C U–Pb geochronology of the South Simpson Island dykes, East Arm Basin, N.W.T.

1 INTRODUCTION

The following is a summary of U–Pb geochronology and whole-rock geochemisty studies of the ENE-trending South Simpson Island diabase dyke ("Mid-Aphebian diabase dykes" of Goff et al., 1982, Goff, 1984, and Hoffman et al., 1977) in the East Arm basin. Prior to 2014 and 2015 fieldwork on the Union Island Group, no dykes associated with the Union Island Group mafic units have been identified in the East Arm basin. The East Arm basin and its surrounding region, particularly the Slave craton, are cut by several alkaline intrusions and mafic dyke swarms of Paleoproterozoic age (sec. 2.1 of main text). Several of these dyke swarms have similar E to NE trends, including the ca. 2231 Ma Malley dykes, ca. 2210 Ma Mackay dykes, ca. 2219 Ma North Simpson Island dyke ("Simpson Island dyke" or "Easter Island dyke" in previous reports; interpreted to be a Mackay dyke by Kjarsgaard et al., 2013b), the ca. 2193 Ma Dogrib dykes, and the ca. 1901 Ma Hearne dykes (Table 2.1, Fig. 2.1 of main text).

The South Simpson Island diabase dykes are located ~10 km south of the North Simpson Island dyke (Fig. C.1). The largest dyke is ~# km in length, ~100 m in width, and has a trend of 045°–050°. At least four smaller, 10–30 m wide dykes occur within ~4 km south of the main dyke and trend 060–070. All of these dykes intrude Archean basement granitoids, and the main dyke terminates at an unconformity where the basement is overlain by sedimentary rocks of the ca. 1857 Ma Sosan Group of the Great Slave Supergroup (Kjarsgaard et al., 2013a). Small, geochemically correlated diabase dykes crosscut both the North Simpson Island dyke and the surrounding basement (Fig. C.1; Goff, 1984); these have a similar NE–ENE trend.

The South Simpson Island dykes have an alkaline composition. Based on geochemical similarities and available stratigraphic constraints, Goff (1984) suggested that the South Simpson Island dykes and the Union Island Group lower basalts represent mafic magmatism during the same extensional event. The precise age relationship between the two, however, was unavailable as mafic rocks were not typically amenable to conventional geochronology methods of the time. We therefore conducted a U–Pb baddeleyite geochronology study of the South Simpson Island dykes with the goal of resolving its timing relative to regional Paleoproterozoic extensional magmatism.

Furthermore, we test the proposed geochemical similarity between the South Simpson Island dykes and the Union Island Group lower basalt by re-analysis of archive samples for trace elements and rare earth elements which were not analyzed in the original study by Goff (1984).

2 METHODOLOGY

Six samples of the South Simpson Island dykes were selected from the East Arm thesis collection of S. Goff (1984) archived at the Department of Earth and Atmospheric Sciences, University of Alberta. Samples were selected based on lack of weathering and alterations, and volume available for analysis. Sample locations are summarized in Fig. C.1; field coordinates for these samples are unavailable. Four samples (SD1, SD3, SD4, SD7) are from the main dyke on South Simpson Island; SD3 is from the dyke center, SD1 is from near the dyke margin, and SD4 and SD7 are from the dyke margin. Two samples (S4A, S4C) are from a small dyke which intrudes the Archean basement immediately north of the North Simpson Island dyke.

All samples were analyzed for whole-rock abundance of major, minor, and trace elements via ICP (major, minor, and some trace elements) and ICP-MS analysis (trace elements) of lithium borate infused glasses at the Activation Laboratories Ltd., Ancaster, ON. The analytical package 4LITHORES was selected for all samples. Analytical precision associated with this method is summarized in section 3.3.1 of the main text.

Sample SD3 was selected for the U–Pb ID-TIMS study as it had the highest sample volume (~500 mL) available for analysis. Baddeleyite separation, U–Pb purification, and TIMS analysis follow the same protocols as those for sample LH14-27, summarized in sections 3.2 and 3.3.3 of the main text. Approximately ~40 baddeleyite grains were separated from ~500 g of crushed sample; these ranged from 20 μm to 80 μm in size and are brown to dark brown. Due to the low number of baddeleyite fragments large enough for precise U–Pb analysis, only two fractions of grains were chosen for analysis. Fraction #1 was a single, ~80 μm fragment. Fraction #2 consisted of four 40–60 μm fragments.

Petrography

Diabase of the South Simpson Island dykes displays a crystallization order of olivine>plagioclase> metal oxides>clinopyroxene. Euhedral olivine (2–5 modal %) is entirely replaced by chlorite and dolomite. Plagioclase (60–70 modal %) are marginally altered to albite and more than half

sericitized. The oxide phase (< 5 modal %), identified as ulvospinel by Goff (1984), contains ilmenite exsolution lamellae. Titanaugite (10–30 modal %) may form intergranular or ophitic textures with plagioclase and is altered to epidote, chlorite, and actinolite. Trace amount of brown biotite occurs interstitially and is associated with chlorite. Apatite is an accessory phase.

Baddeleyite occurs mostly in chloritized interstices as singular, 80–300 μm long blades (Fig. C.2) or as 20–30 μm clusters. Fractures are observed only in the smaller population.

3 RESULTS AND DISCUSSIONS

3.1 Geochronology

Uranium–lead analyses of two baddeleyite fractions from sample SD3 is presented in Table C.1. Both analyses are 5.7% discordant. Fraction 1 yielded a $^{207}Pb/^{206}Pb$ age of 2197.7±2.9 Ma (5.7% discordant), while fraction 2 yielded a $^{207}Pb/^{206}Pb$ age of 2216.8±2.1 Ma (5.7% discordant). Regression of the two analyses yields an imprecise errorchron with an upper intercept of 2492±450 Ma and a lower intercept of 1763±480 Ma. As the South Simpson Island dykes crosscut the ca. 2219 Ma North Simpson Island dyke, a ca. 2492 Ma age for the South Simpson Island dykes is not possible. $^{207}Pb/^{206}Pb$ ages of both baddeleyite fractions postdate the North Simpson Island dyke and more likely represent the true crystallization age of the diabase.

It is unlikely that two crystallization ages exists for sample SD3. Inherited baddeleyite has yet to be reported in any rock type, therefore the grains separated from sample SD3 for dating are primary. The ~19 Myr difference in $^{207}Pb/^{206}Pb$ ages of the two baddeleyite fractions more likely resulted from scattering due to Pb loss. For comparison, analysis of eight baddeleyite fractions from the Union Island Group diabase feeder LH14-27 (sec. 4.2 of main text) yielded individual $^{207}Pb/^{206}Pb$ ages across a range of ~27 Myr. Therefore, the two $^{207}Pb/^{206}Pb$ ages of the two baddeleyite fractions from sample SD3 are approximations of the true crystallization age of the diabase.

The two $^{207}Pb/^{206}Pb$ ages for diabase dyke SD3 demonstrate that the South Simpson Island dykes predate the Union Island Group mafic magmatism by at least ~150 Myr. Although additional analyses are required to yield a precise U–Pb age for diabase dyke SD3, the age constraint defined by the two $^{207}Pb/^{206}Pb$ ages correlate with regional dyke emplacements. The younger, 2197.7±2.9 Ma age of fraction 1 is indistinguishable from the 2193±2 Ma age of the Dogrib dykes (Mitchell et al., 2014), while the older, 2216.8±2.1 Ma age of fraction 2 is indistinguishable from the

2219±3.7 Ma age of the North Simpson Island dyke (Mumford et al., 2012b) which the South Simpson Island dykes intrude. Although comparison with possibly contemporaneous regional dykes do not further constrain the emplacement age of the South Simpson Island dykes, the ca. 2217–2198 Ma $^{207}Pb/^{206}Pb$ age range of the two baddeleyite fractions demonstrates that the South Simpson Island dykes are not genetically related to the ca. 2043 Ma Union Island Group lower magmatism.

3.2 Geochemistry

According to new analyses in this study (Table C.2), the South Simpson Island diabase dykes are classified as subalkaline basalt nearing the alkaline-subalkaline boundary (Nb/Y = 0.8; Fig. C.4). The diabase has Mg# ranging 42–59 and Al_2O_3 ranging 14–16 wt%. The two dykes sampled display distinct TiO_2 levels, with the main South Simpson Island dyke (SD) ranging 2.5–2.7 wt% and the North Simpson Island dykelet (S4) having higher levels, at 4.0–4.1 wt%. Chromium and nickel contents range 80–190 ppm and 50–120 ppm, respectively. The lack of high Mg#, Cr, or Ni content suggests that these diabase samples do not represent primitive melts. The dykes have moderate Zr (150–251 ppm) and Nb (14–28 ppm) levels. Chrondrite-normalized rare earth element diagram (Fig. C.5a) shows that the South Simpson Island dykes are enriched in REE, with LREE over HREE enrichment and moderately fractionated LREE (La/Sm_N: 1.1–1.8) and HREE (Gd/Yb_N: 2.2–2.5) profiles. Slight positive Eu anomalies are present in two samples. One sample from the North Simpson Island dykelet, S4A, shows much higher REE enrichment levels (La_N = 267, compared with 47–99 for the others samples). Normalized multi-element spidergram show that sample S4A contains negative anomalies of Nb, Ta, Zr, and Hf that are distinct from all other samples (Fig. C5b).

Comparison with other mafic dykes in the region from the 2.22–2.20 Ga period show that the South Simpson Island dykes are more enriched in incompatible elements than the Mackay and Dogrib swarms, but have similar enrichment levels as ultramafic samples from the differentiated North Simpson Island dyke (Fig. C.6). The South Simpson Island dykes have Zr/Nb slightly higher than the Union Island Group lower magmatism. Incompatible element ratios of Th/Yb and Nb/Yb show that both the South Simpson Island dykes and the North Simpson Island dyke plot along the mantle array while the Mackay and Dogrib swarms plot on a separate trend marked by Th enrichment relative to Nb. The North Simpson Island dyke plots in a tight cluster coincident with

average ocean island basalt (OIB) composition, whereas the South Simpson Island dykes define a linear trend between E-MORB and OIB compositions. The South Simpson Island dykes display lower Th/Yb and Nb/Yb ratios than the Union Island Group lower magmatism.

Previous work have suggested a link between the North Simpson Island dyke and the ca. 2193–2164 Ma Southwest Slave magmatic province (SWSMP) based on lithology and geochemistry (Badham, 1979; Mumford et al., 2012a; Mumford et al., 2012b; Mumford, 2013). Mumford (2013) proposed that the compositional range of the SWSMP and the North Simpson Island dyke can be produced by interaction of a melt of metasomatic veins with the depleted subcontinental lithospheric mantle (SCLM). Although our geochronology results suggest that the South Simpson Island dykes are in a similar age range as the SWSMP, the North Simpson Island dyke, and the older Mackay and Malley swarms, distinct differences in incompatible element trends suggest that the South Simpson Island dykes were not cogenetic with any of these magmatism. The close spatial associations between the South Simpson Island dykes and the North Simpson Island dyke may reflect a common magmatic event. There is a need for further evaluation of the tectonic relationship between these dykes and other 2.23–2.19 Ga igneous intrusions in the southern Slave craton.

The NE–ENE trends of the 2.23–2.19 mafic dyke swarms are similar to ca. 2.04 Ga diabase dykes of the Union Island Group, which marked the formation of the East Arm rift. This similarity in dyke trend suggests a long-lived extensional regime in the southern Slave craton leading up to the ca. 2.04 Ga rift basin formation.

4 CONCLUSIONS

Uranium–lead ID-TIMS analysis of two baddeleyite fractions from a South Simpson Island diabase dyke yielded discordant $^{207}Pb/^{206}Pb$ ages of 2197.7±2.9 Ma and 2216.8±2.1 Ma. A geochemical comparison with the 2219±3.7 Ma North Simpson Island dyke and the 2193±2 Ma Dogrib dykes does not suggest a comagmatic relationship with either intrusive event. Although the South Simpson Island dykes have a similar orientation as the ca. 2043 Ma Union Island Group dykes, the former is older by ~150 Myr and the two events are geochemically distinct.

Figure C.1. Geologic map of the South Simpson Island dykes. Modified after Goff (1984). A precise location for samples S4A and S4C is unavaialble.

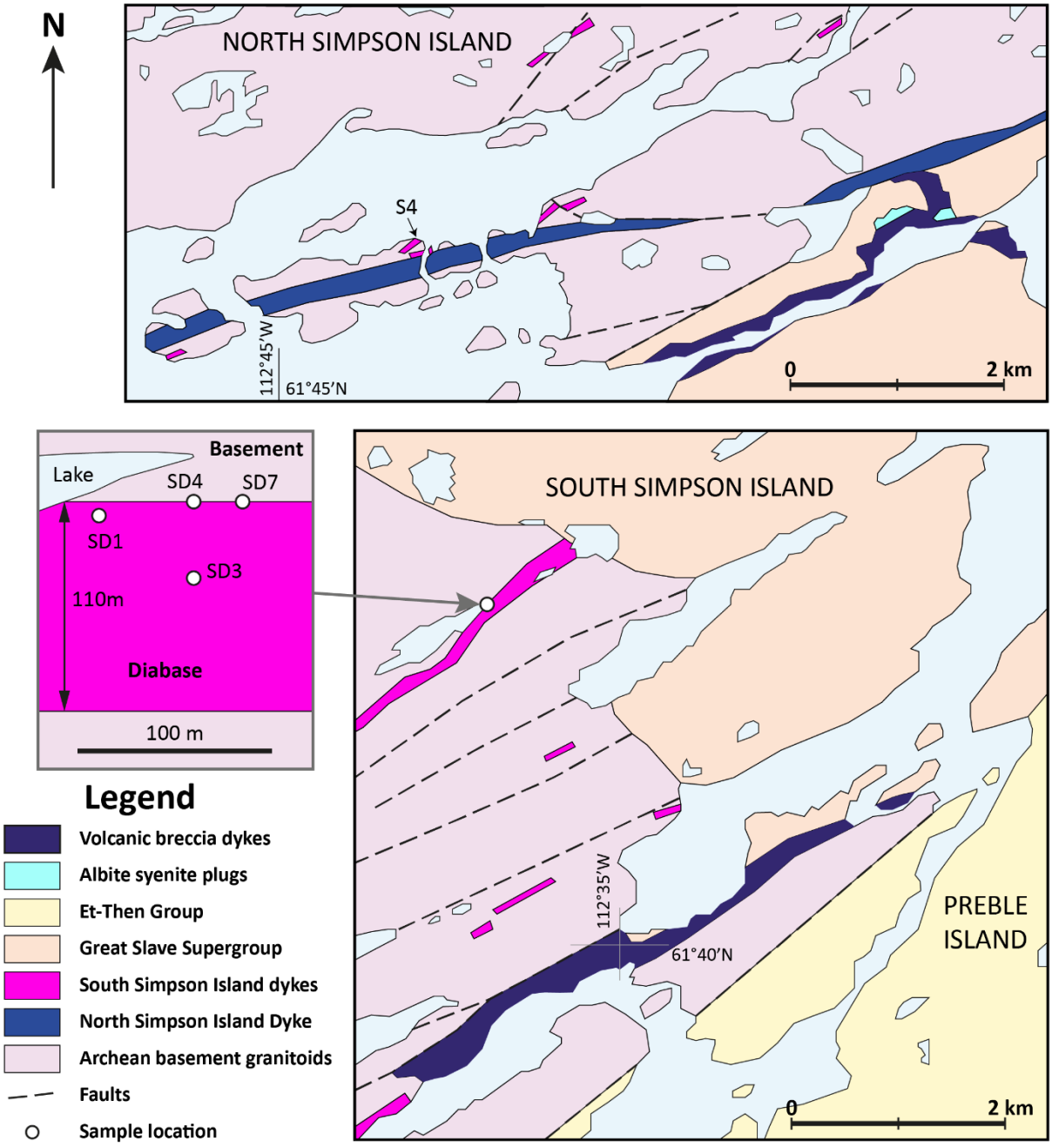

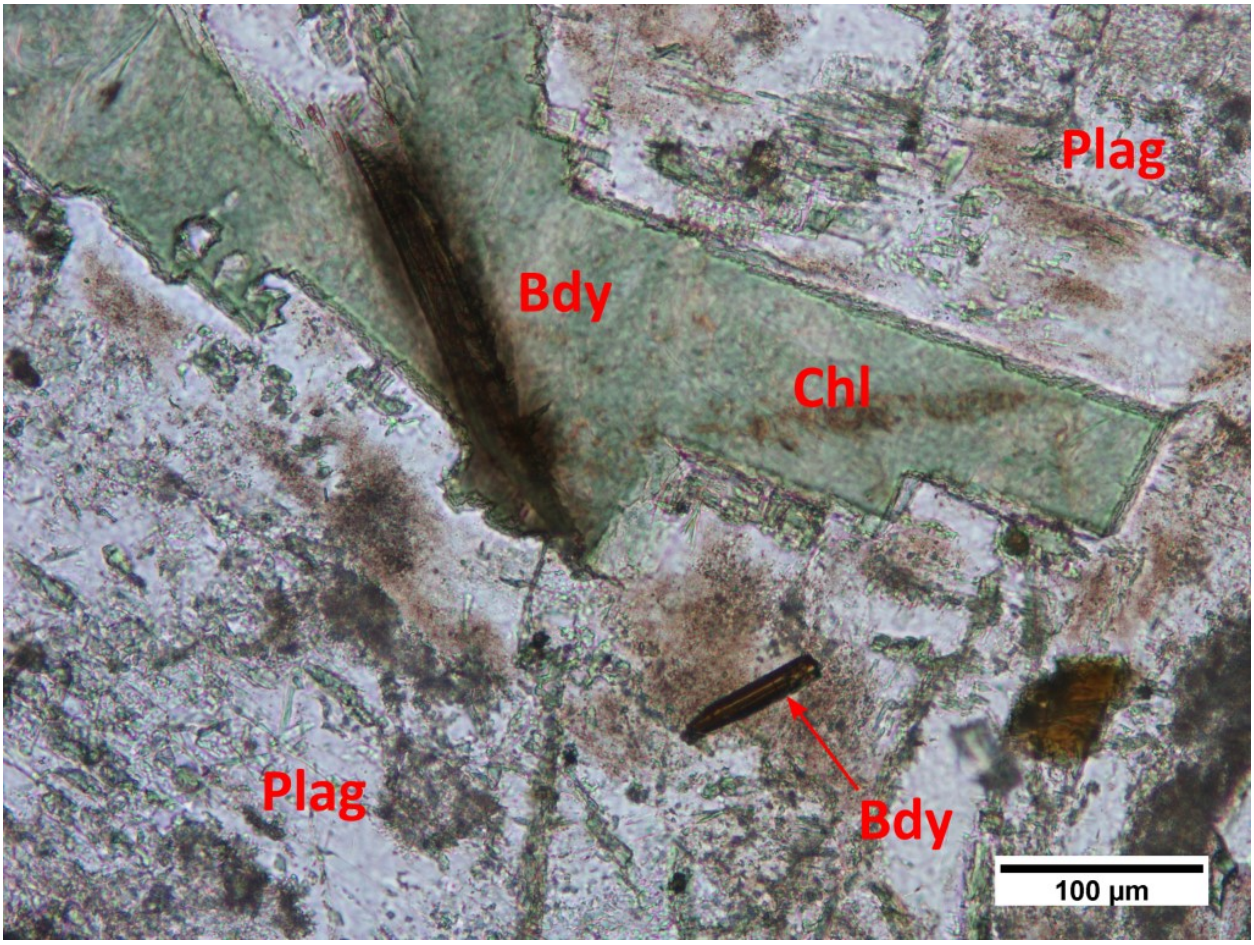

Figure C.2. Photomicrograph of pristine, euhedral baddeleyites in the South Simpson Island diabase dykes. Sample SD3.

Table C.1. TIMS U–Pb analysis of baddeleyite fractions for diabase dyke SD3. Associated errors are given in 1σ.

Fraction	Weight (µg)	U (ppm)	Th (ppm)	Pb (ppm)	Th/U	TCPb (pg)	$^{206}Pb/^{204}Pb$	$^{206}Pb/^{238}U$	$^{207}Pb/^{235}U$	$^{207}Pb/^{206}Pb$	$^{206}Pb/^{238}U$ (Ma)	$^{207}Pb/^{235}U$ (Ma)	$^{207}Pb/^{206}Pb$ (Ma)	%Disc
1(1)	0.5	191	31	75	0.16	1.4	1653	0.3829 ± 12	7.267 ± 27	0.13764 ± 2	2089.9 ± 5.6	2144.7 ± 3.3	2197.7 ± 2.9	5.7
2(4)	0.5	263	28	103	0.11	1.4	2276	0.3872 ± 10	7.429 ± 21	0.13916 ± 2	2109.9 ± 4.5	2164.5 ± 2.6	2216.8 ± 2.1	5.7

All atomic ratios are corrected for spike (composition), estimated blank (0.5 pg U, 1.0 pg Pb), and initial common lead (Stacey and Kramers, 1975).

Number in parentheses refers to the number of baddeleyite grains analysed; TCPb refers to total common Pb present in the analysis.

Age calculations based on decay constants of Jaffey et al. (1971); $^{206}Pb/^{238}U$ and $^{207}Pb/^{206}Pb$ ages corrected for initial disequilibrium in $^{230}Th/^{238}U$ using a Th/U (magma) ratio of 3.

Model Th/U ratio estimated from radiogenic $^{208}Pb/^{206}Pb$ ratio and $^{207}Pb/^{235}U$ age.

Figure C.3. Concordia plot of U–Pb baddeleyite results for diabase dyke SD3.

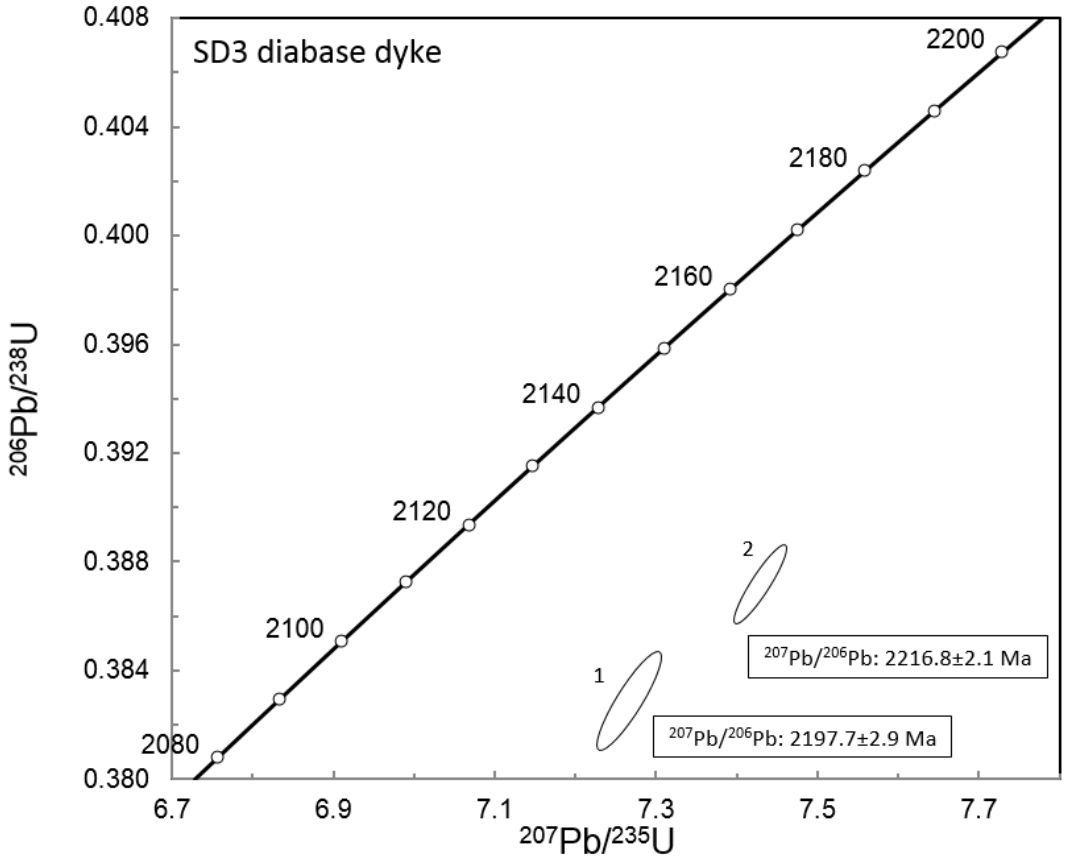

Table C.2. Whole-rock geochemistry data of South Simpson Island dykes. Analytical methods are described in chapter 3 of main text.

		Sample Number						
Analyte	Method	SD1	SD3	SD4	SD7	S4C	S4A	Detection limit
SiO_2 (%)	FUS-ICP	42.92	48.04	47.41	43.86	44.93	45.84	0.01
Al_2O_3	FUS-ICP	16.25	15.63	14.91	15.12	12.66	13.89	0.01
$Fe_2O_{3(T)}$	FUS-ICP	13.7	14.13	12.61	13.88	15.88	15.34	0.01
MnO	FUS-ICP	0.12	0.19	0.24	0.09	0.21	0.18	0.001
MgO	FUS-ICP	9.81	5.14	8.22	9.88	7.56	5.49	0.01
CaO	FUS-ICP	2.08	7.57	5.36	2.65	6.21	6.88	0.01
Na_2O	FUS-ICP	2.05	3.22	3.44	3.87	2.87	2.46	0.01
K_2O	FUS-ICP	3.48	1.31	1	0.38	1	0.86	0.01
TiO_2	FUS-ICP	2.55	2.48	2.50	2.69	4.17	4.02	0.001
P_2O_5	FUS-ICP	0.25	0.42	0.26	0.26	0.32	0.4	0.01
LOI	FUS-ICP	5.79	2.44	3.62	5.84	3.36	4.71	0.01
Total	FUS-ICP	99	100.6	99.57	98.53	99.17	100.1	
Sc (ppm)	FUS-ICP	31	21	32	33	33	30	1
Be	FUS-ICP	2	2	3	2	2	2	1
V	FUS-ICP	350	288	350	357	483	451	5
Cr	FUS-MS	190	80	190	180	120	120	20
Co	FUS-MS	59	43	52	60	53	60	1
Ni	FUS-MS	120	50	80	90	60	60	20
Cu	FUS-MS	< 10	40	60	20	40	40	10
Zn	FUS-MS	120	130	100	80	210	80	30
Ga	FUS-MS	23	27	24	24	25	28	1
Ge	FUS-MS	1.6	1.3	1.4	1.3	1.8	1.3	0.5
As	FUS-MS	< 5	< 5	< 5	< 5	< 5	< 5	5
Rb	FUS-MS	52	31	31	10	26	28	1
Sr	FUS-ICP	240	355	328	106	277	292	2
Y	FUS-MS	27.8	35.9	25.1	25.8	28.3	34.5	0.5
Zr	FUS-ICP	150	251	155	165	204	183	1
Nb	FUS-MS	13.6	21.4	14.3	14.7	19.9	27.7	0.2
Mo	FUS-MS	< 2	< 2	< 2	< 2	< 2	2	2
Ag	FUS-MS	< 0.5	< 0.5	< 0.5	< 0.5	< 0.5	< 0.5	0.5
In	FUS-MS	< 0.1	0.1	< 0.1	< 0.1	0.1	0.1	0.1
Sn	FUS-MS	1	2	1	2	2	2	1
Sb	FUS-MS	< 0.2	< 0.2	< 0.2	< 0.2	< 0.2	< 0.2	0.2
Cs	FUS-MS	1.4	0.7	1	0.7	0.8	3	0.1
Ba	FUS-ICP	1460	301	328	74	325	243	3

Table C.2. (continued)

		Sample Number						
Analyte	Method	SD1	SD3	SD4	SD7	S4C	S4A	Detection limit
La	FUS-MS	15.8	23.4	13.9	11.1	18.6	63.2	0.05
Ce	FUS-MS	38.3	56.9	34.9	36.5	46.5	131	0.05
Pr	FUS-MS	5.32	7.86	4.82	5.85	6.27	14.9	0.01
Nd	FUS-MS	24.4	35.5	22.3	28.3	28.9	58.4	0.05
Sm	FUS-MS	6.26	8.78	5.48	6.47	6.64	11.6	0.01
Eu	FUS-MS	2.99	2.69	1.88	2.74	2.48	4.01	0.01
Gd	FUS-MS	6.18	8.06	5.63	6.03	6.94	9.9	0.01
Tb	FUS-MS	0.94	1.23	0.91	0.94	1.03	1.35	0.01
Dy	FUS-MS	5.36	7.3	5.29	5.24	5.75	7.43	0.01
Ho	FUS-MS	0.99	1.36	0.91	0.97	1.04	1.26	0.01
Er	FUS-MS	2.57	3.68	2.54	2.66	2.82	3.41	0.01
Tm	FUS-MS	0.367	0.48	0.366	0.351	0.385	0.441	0.01
Yb	FUS-MS	2.29	3.06	2.15	2.14	2.29	2.77	0.01
Lu	FUS-MS	0.379	0.467	0.334	0.304	0.346	0.407	0.002
Hf	FUS-MS	4.1	6.3	4.3	4.3	5.5	5	0.1
Ta	FUS-MS	0.86	1.37	0.86	0.91	1.22	1.75	0.01
Tl	FUS-MS	< 0.05	< 0.05	< 0.05	< 0.05	< 0.05	0.21	0.05
Pb	FUS-MS	< 5	< 5	< 5	< 5	< 5	34	5
Bi	FUS-MS	< 0.1	< 0.1	< 0.1	< 0.1	< 0.1	< 0.1	0.1
Th	FUS-MS	1.01	1.83	0.99	1.09	1.69	6.54	0.05
U	FUS-MS	0.22	0.48	0.25	0.3	0.41	0.81	0.01
Mg#*		59	42	56	59	49	41	

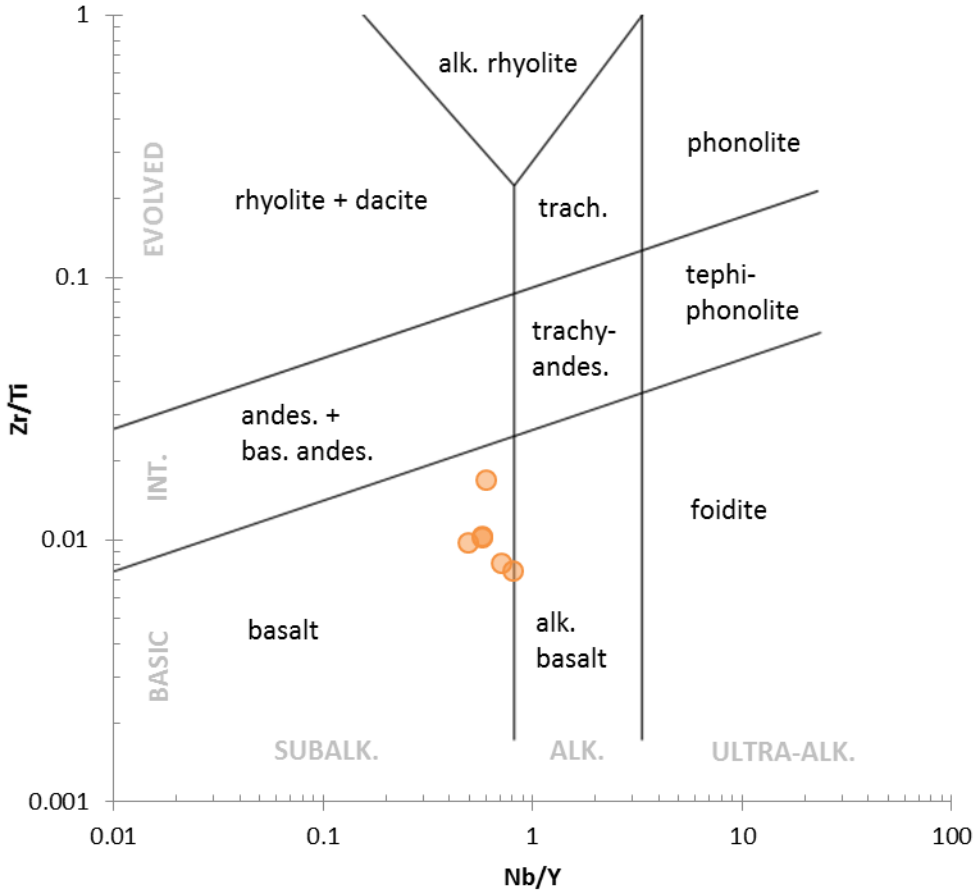

Figure C.4. Zr/Ti vs. Nb/Y igneous classification (Pearce, 1996) of the South Simpson Island diabase dykes.

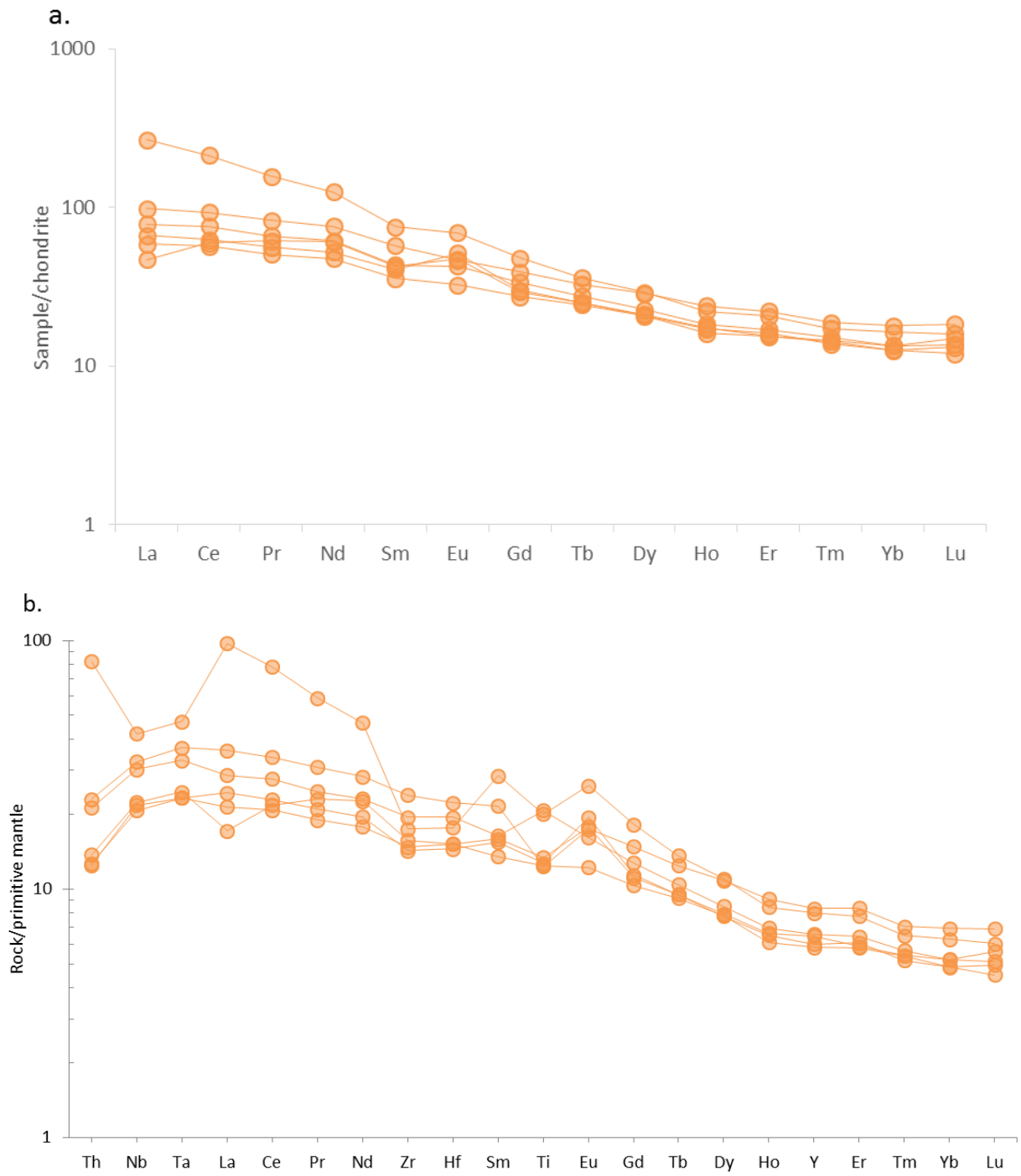

Figure C.5. a) Chondrite-normalized rare earth element plot and b) incompatible element multi-element plot for the South Simpson Island dykes. Normalization is made to chondrite (Sun and McDonough, 1989) and to primitive (pyrolite) mantle (McDonough and Sun, 1995), respectively.

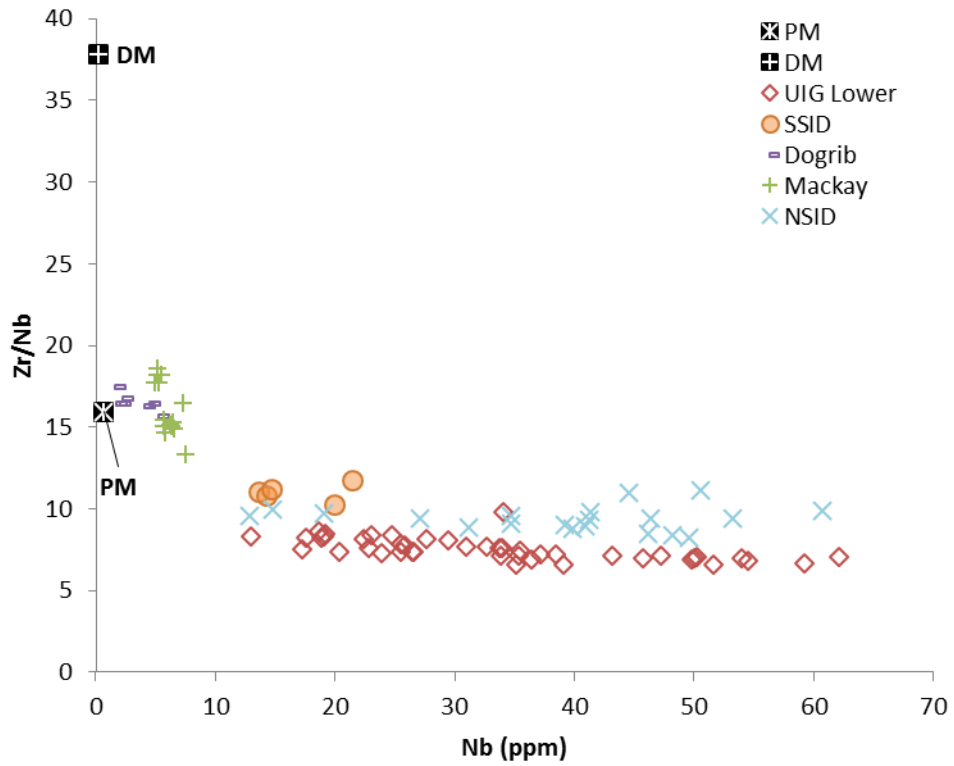

Figure C.6. Zr/Nb vs. Nb plot of the South Simpson Island dykes (SSID), compared with other Paleoproterozoic regional mafic magmatism: North Simpson Island dyke (NSID; Mumford, 2013), Mackay dykes (Ernst and Buchan, 2010), Dogrib dykes (Ernst and Buchan, 2010), and Union Island Group lower magmatism (UIG Lower; this study). Shown for reference are the estimated composition of the primitive mantle (PM; McDonough and Sun, 1995) and the depleted mantle (DM; Salters and Stracke, 2004).

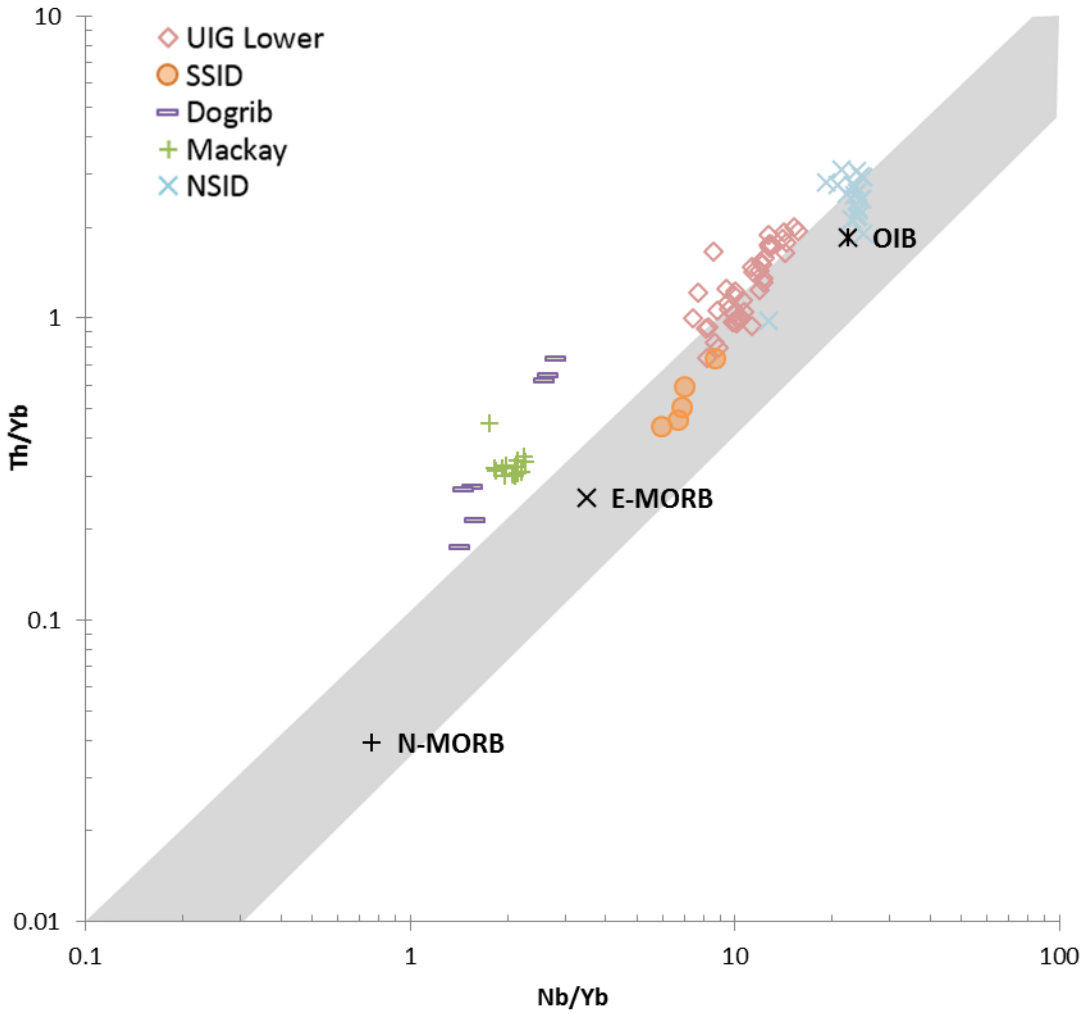

Figure C.7. Nb/Yb vs. Th/Yb plot (after Pearce et al., 2008) of the South Simpson Island dykes (SSID), compared with other Paleoproterozoic regional mafic magmatism: North Simpson Island dyke (NSID; Mumford, 2013), Mackay dykes (Ernst and Buchan, 2010), Dogrib dykes (Ernst and Buchan, 2010), and Union Island Group lower magmatism (UIG Lower; this study). Grey band represents composition range of uncontaminated magma derived from the asthenospheric mantle.

References

Badham, J.P.N., 1979. Geology and petrochemistry of lower Aphebian (2.4–2.0 Ga) alkaline plutonic and hypabyssal rocks in the East Arm of Great Slave Lake, Northwest Territories. Canadian Journal of Earth Sciences 16, 60–72.

Ernst, R.E., Buchan, K.L., with samples from Aspler, L.B., Baragar, W.R.A., Corkery, M.T., Davidson, A., et al., 2010. Geochemical database of Proterozoic intraplate mafic magmatism in Canada. Geological Survey of Canada, Open File 6016.

Goff, S.P., 1984. The magmatic and metamorphic history of the East Arm, Great Slave Lake, N.W.T. PhD thesis, University of Alberta, Edmonton. 504 p.

Goff, S.P., Baadsgaard, H., Muehlenbachs, K., Scarfe, C.M., 1982. Rb–Sr isochron ages, magmatic $^{87}Sr/^{86}Sr$ initial ratios, and oxygen isotope geochemistry of the Proterozoic lava flows and intrusions of the East Arm of Great Slave Lake, Northwest Territories, Canada. Canadian Journal of Earth Sciences 19, 343–356.

Hoffman, P.F., Bell, I.R., Hildebrand, R.S., Thorstad, L., 1977. Geology of the Athapuscow Aulacogen, East Arm of Great Slave Lake, District of Mackenzie. Report of Activities, 77-1A. Geological Survey of Canada, Ottawa, ON, pp. 117–129.

Jaffey, A.H., Flynn, K.F., Glendenin, L.E., Bentley, W.T., Essling, A.M., 1971. Precision measurement of half-lives and specific activities of ^{235}U and ^{238}U. Physical Review C 4, 1889–1906.

Kjarsgaard, B.A., Pearson, D.G., DuFrane, A., and Heaman, L.M., 2013a. Proterozoic geology of the east arm basin wth emphasis on Paleoproterozoic magmatic rocks, Thaidene Nene MERA study area, in: Wright, D.F., Ambrose, E.J., Lemkow, D., and Bonham-Carter, G. (Eds.), Mineral and energy resource assessment of the proposed Thaidene Nene National Park Reserve in the area of the east arm of Great Slave Lake, Northwest Territories. Geological Survey of Canada Open File 7196, pp. 51–92.

Kjarsgaard, B.A., Tella, S., Lemkow, D., 2013b. Bedrock geology of the proposed Thaidene Nene National Park Reserve in the area of the East Arm of Great Slave Lake, Northwest Territories, in: Wright, D.F., Ambrose, E.J., Lemkow, D., and Bonham-Carter, G. (Eds.), Mineral and energy resource assessment of the proposed Thaidene Nene National Park Reserve in the area of the east arm of Great Slave Lake, Northwest Territories. Geological Survey of Canada Open File 7196, 1 sheet.

Mitchell, R.N., Bleeker, W., van Breemen, O., LeCheminant, T.N., Peng, P., Nilsson, M.K., Evans, D.A., 2014. Plate tectonics before 2.0 Ga: Evidence from paleomagnetism of cratons within supercontinent Nuna. American Journal of Science 314, 878–894.

Mumford, T.R., 2013. Petrology of the Blatchford Lake Intrusive Suite, Northwest Territories, Canada. PhD thesis, Carleton University, Ottawa. 239 p.

Mumford, T.R., Cousens, B.L., Falck, H., Cairns, S., 2012a. Geochemistry and Sm–Nd isotope systematics of ca. 2180 Ma intrusions in the southwestern Slave magmatic province. Northwest Territories Geoscience Office, NWT Open File 2012-007, 22 p.

Mumford, T.R., Ketchum, J., Falck, H., Heaman, L., 2012b. New geochemical, geochronological, and isotopic data of the Blachford Lake Intrusive Suite and the Simpson Island Dyke. Northwest Territories Geoscience Office, NWT Open File 2102-005, 41 p.

Pearce, J.A., 1996. A user's guide to basalt discrimination diagrams. Trace element geochemistry of volcanic rocks: applications for massive sulphide exploration. Geological Association of Canada, Short Course Notes 12, pp. 79–113.

Pearce J.A., 2008. Geochemical fingerprinting of oceanic basalts with applications to ophiolite classification and the search for Archean oceanic crust. Lithos 100, 14–48.

Salters, V.J.M., Stracke, A., 2004. Composition of the depleted mantle. Geochemistry, Geophysics, Geosystems 5, Q05B07.

Stacey J.S., Kramers, J.D., 1975. Approximation of terrestrial lead isotope evolution by a two-stage model. Earth and Planetary Science Letters 26, 207–221.

Sun, S.-s., McDonough, W.F., 1989. Chemical and isotopic systematics of oceanic basalts: implications for mantle composition and processes, in: Saunders, A.D., Norry, M.J. (Eds.), Magmatism in the Ocean Basins. Geological Society Special Publication 42, pp. 313–345.